

**PREPARATIVE MASS SPECTROMETRY: INSTRUMENTATION AND
APPLICATIONS**

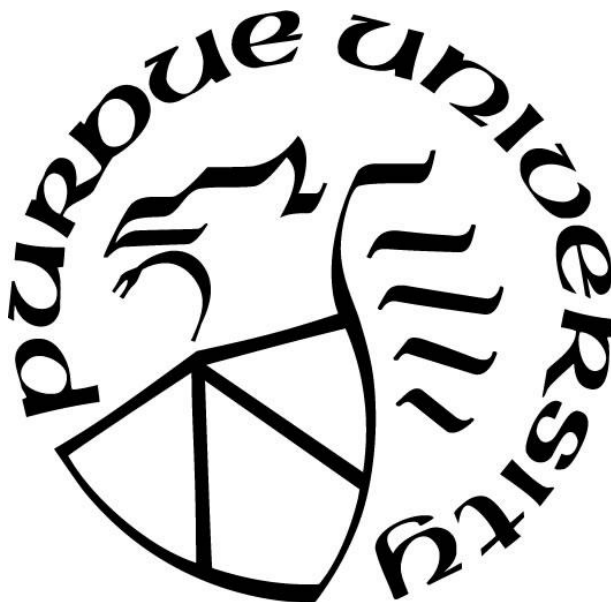
by
Pei Su

A Dissertation

Submitted to the Faculty of Purdue University

In Partial Fulfillment of the Requirements for the degree of

Doctor of Philosophy



Department of Chemistry

West Lafayette, Indiana

December 2020

THE PURDUE UNIVERSITY GRADUATE SCHOOL
STATEMENT OF COMMITTEE APPROVAL

Dr. Julia Laskin, Chair

Department of Chemistry

Dr. R. Graham Cooks

Department of Chemistry

Dr. Mingji Dai

Department of Chemistry

Dr. Scott McLuckey

Department of Chemistry

Approved by:

Dr. Christine Hrycyna

献给我的父母

Dedicated to my parents.

ACKNOWLEDGMENTS

First and foremost, I would like to thank Prof. Julia Laskin for mentoring and guidance throughout my last three and a half years at Purdue. I started with barely any experience in instrumentation in the lab as your first graduate student in the ion soft landing research and all the progress I have made would not have happened without you. I felt truly motivated getting into new scientific endeavors and I believe that everything I have learned from you will be a solid foundation for my future career.

I must express my thanks to Prof. Zheng Ouyang and Prof. Yu Xia, who were my research advisors for my first two years at Purdue. Thanks for all the mentorship and support provided to me as a young graduate student. I still remember the time I entered the program with barely any knowledge in mass spectrometry. You have provided me with excellent opportunities in research and networking which are exceptionally valuable in my life. Additionally, I would like to thank my thesis committee members, especially Prof. R. Graham Cooks, for continuous support and mentoring.

My parents, Mr. Mu Su and Mrs. Li Chen, my elder brother, Mr. Bo Su, for the thoughtful and warm support for all my endeavors over these years. I am grateful to have you as role-models, and I know you are always there to be together with me getting through the unusual times. My grandparents, aunts, uncles, and young cousins, please receive my gratitude for always being supportive and best wishes to all of you.

I must acknowledge the friendship and scientific collegiality of all members and alumni of the J. Laskin Group with whom I have spent my time at Purdue. In particular, I must express my thanks to Dr. Jonas Warneke, who was an Alexander von Humboldt research scholar in the Laskin lab, for always being a dear friend, a great mentor, a source of bright ideas and scientific motivation, and an excellent collaborator after you have started an independent career as a “Freigeist” junior research group leader at Universität Leipzig, Germany. In addition, I must express my thanks to Andrew Smith, who was working with me as an undergraduate student and post-bachelor scholar, for being a dear friend and co-worker. I also want to thank Dr. Venkateshkumar Prabhakaran and Dr. Grant Johnson for the mentorship during my time at Pacific Northwest National Laboratory,

Dr. Ruichuan Yin for his friendship and help. I cannot wait to thank Daisy Unsihuay and Hugo Samayoa, for the great time we spent in the lab (and in particular for bringing me to your tremendously-fun Latino parties!); Michael Espenship, Solita Wilson, Manxi Yang, for all the scientific and non-science-related chatters; Hilary Brown, Daniela Mesa-Sanchez, Courtney Huffstutler, Miranda Weigand, Jyothsna Padmakumar Bindu, Habib Gholipour, Hang Hu, Xiangtang Li, for great collaborations and valuable discussions.

I also must express my thanks to members of Prof. Ouyang and Prof. Xia's lab at Purdue and Tsinghua University. In particular, I thank Dr. Wenpeng Zhang for the mentorship, Dr. Fan Pu, Dr. Xiao Wang, Dr. Sarju Adhikari, and Zishuai Li for being great lab mates and dear friends. Dr. Leelyn Chong, Dr. Elissia Franklin, Jia Ren, Dr. Ran Zou, Pengqing Yu, please, receive my heartfelt thanks as well.

I cannot skip my thanks to my friends at Purdue. Thanks, Dake, for being a great roommate (and a real chef!), it has been almost a decade since our college time at Fudan University. Zhuoer, Fan, Aaron (Tse-Hong), Tina (Changqin), Chen, Ruoxing, thanks for all the unforgettable happy moments we spent together as a group of friends at Purdue and best wishes to all of you.

TABLE OF CONTENTS

LIST OF TABLES	9
LIST OF FIGURES	10
LIST OF SCHEMES.....	17
LIST OF ABBREVIATIONS.....	18
ABSTRACT.....	20
CHAPTER 1. INTRODUCTION	21
1.1 Synopsis	21
1.2 Phenomena in Ion-Surface Collisions.....	22
1.2.1 Soft Landing of Ions	23
1.2.2 Charge Retention by Soft-Landed Ions	24
1.3 Instrumentation	26
1.3.1 Ionization Sources	26
1.3.2 Mass Analyzers.....	27
1.3.3 Ambient Soft Landing	28
1.4 Surface Characterization Techniques for Soft-Landed Ions.....	29
1.5 References.....	30
CHAPTER 2. DESIGN AND PERFORMANCE OF A DUAL POLARITY INSTRUMENT FOR ION SOFT LANDING.....	38
2.1 Introduction.....	38
2.2 Experimental Section.....	40
2.2.1 Instrumentation	40
2.2.2 Chemicals	44
2.2.3 FSAM Surface Preparation.....	44
2.2.4 Surface Characterization.....	44
2.3 Results and Discussion	45
2.3.1 Characterizations of Mass-Selected Ion Beams	45
2.3.2 Ion Kinetic Energy Distributions (KED).....	47
2.3.3 Two Modes of Ion Soft Landing Experiments	50
2.3.4 Protecting Soft-Landed Cations Using Weakly-Coordinating Anions.....	51

2.3.5	Preparation of Charge-Balanced Ionic Layers.....	54
2.4	Conclusions.....	57
2.5	References.....	58
CHAPTER 3. PREPARATIVE MASS SPECTROMETRY USING A ROTATING WALL		
MASS ANALYZER.....		
3.1	Introduction.....	64
3.2	Experimental Section.....	65
3.2.1	Instrumentation.....	65
3.3	Results and Discussion.....	70
3.3.1	Analytical Expression for the Deposition Radius.....	70
3.3.2	Calibration.....	74
3.3.3	Mass Resolution.....	79
3.3.4	Deposition of High- m/z Nanoclusters.....	87
3.3.5	High-Throughput Deposition of Multicomponent Mixtures.....	92
3.4	Conclusions.....	97
3.5	References.....	97
CHAPTER 4. IN SITU SPECTROELECTROCHEMISTRY FOR UNDERSTANDING		
STRUCTURAL TRANSFORMATIONS OF PRECISELY DEFINED IONS AT		
ELECTROCHEMICAL INTERFACES.....		
4.1	Introduction.....	105
4.2	Experimental Section.....	107
4.3	Results and Discussion.....	109
4.4	Conclusions.....	124
4.5	References.....	125
CHAPTER 5. GAS PHASE FRAGMENTATION OF HOST-GUEST COMPLEXES OF		
CYCLODEXTRINS AND POLYOXOMETALATES.....		
5.1	Introduction.....	129
5.2	Experimental Sections.....	131
5.2.1	Chemicals.....	131
5.2.2	Synthesis.....	131
5.2.3	MS Experiments.....	132

5.3	Results and Discussion	133
5.3.1	ESI-MS of tungsten CD-POM complexes.....	134
5.3.2	Gas Phase fragmentation Pathways	135
5.3.3	Isotopic Labeling Experiments and Statistical Modeling.....	145
5.4	Conclusions.....	151
5.5	References.....	152
CHAPTER 6.	GAS PHASE REACTIVITY OF $[\text{Mo}_6\text{X}_{14}]^{2-}$ (X=Cl, Br, I) DIANIONS	159
6.1	Introduction.....	159
6.2	Experimental Section	160
6.3	Results and Discussion	161
6.3.1	In-Source Collision-Induced Dissociation.....	162
6.3.2	Reaction Pathways Probed by Ion-Trap CID	163
6.4	Conclusions.....	173
6.5	References.....	174
APPENDIX I:	ANALYTICAL EXPRESSION FOR PREDICTING THE DEPOSITION RING USING ROTATING WALL MASS ANALYZER.....	179
APPENDIX II:	STEP-BY-STEP FOR STATISTICAL MODELING OF MULTIPLE WATER ELIMINATION PROCESS OF ISOTOPICALLY-LABELED $[\Gamma\text{-CD-W}_6\text{POM}]^{2-}$ COMPLEX	184
PUBLICATIONS.....		190

LIST OF TABLES

Table 2.1 Typical ion currents of $\text{Ru}(\text{bpy})_3^{2+}$ and WPOM^{3-} obtained on the surface in ESI(+/-) and ESI $\times 2$ mode.	46
Table 3.1 m/z of the major oligomers observed in the spectrum (I to VIII) in Figure 2.6.....	75
Table 3.2 m/z of the major oligomers observed in the spectrum (I to VIII) in Figure 2.7.....	77
Table 3.3 Experimentally-determined radii of the ubiquitin ions and the values predicted using calibrated Equation 3.1 along with the corresponding relative errors.	78
Table 4.1 Calculated electrochemical parameters in the CV studies of WPOM anions at a scan rate of 0.5 mV s^{-1} . The $E_{\text{p, red}}$ and $E_{\text{p, ox}}$ refer to reduction and re-oxidation peak potentials; $E_{1/2, \text{ red}}$ and $E_{1/2, \text{ ox}}$ refer to reduction and re-oxidation half-wave peak potentials.	113
Table 4.2 IR band assignments to different charge states of reduced WPOM from the spectroelectrochemistry experiments in the range of $1000\text{-}800 \text{ cm}^{-1}$	124

LIST OF FIGURES

- Figure 1.1 Physical and chemical processes associated with ion-surface collisions at chemically-relevant energies. Reproduced with permission from Ref [3]. Copyright 2012, American Chemical Society..... 23
- Figure 1.2 Schematic drawing of the lateral time-of-flight mas analyzer. Reproduced with permission from Ref [77]. Copyright 1999, American Institute of Physics. 27
- Figure 1.3 Schematic diagram of the electrospray emitter, drying tube, and electrostatic deflectors used for ambient soft landing .Reproduced from Ref [80]. with permission. Copyright 2011, American Chemical Society. 28
- Figure 2.1 Schematic drawing of the dual polarity ion soft landing instrument showing the dual polarity ESI interface (1), high pressure ion funnel (HPF, 2), low pressure ion funnel (LPF, 3), bent flatapole ion guide (4), quadrupole mass filter (5), einzel lens (6) and surface (7). Direct current (DC) voltages on the tandem ion funnel system are shown with Roman numerals: I, HPF repeller in; II, HPF repeller out; III, HPF funnel in; IV, HPF funnel out; V, LPF funnel in; VI, LPF lens; VII, LPF funnel out; VIII, conductance limit. The pressure in each vacuum region is marked in red. Typical DC voltages used for transmission of ions of both polarities in the tandem ion funnel region are shown in the bottom left table. 41
- Figure 2.2 Ion current stabilities of mass-selected $\text{Ru}(\text{bpy})_3^{2+}$ and WPOM^{3-} in ESI $\times 2$ or ESI(+/-) modes over one hour time period..... 46
- Figure 2.3 One-dimensional ion beam profiles of +3.1 nA $\text{Ru}(\text{bpy})_3^{2+}$ and -4.6 nA WPOM^{3-} obtained using IonCCD..... 47
- Figure 2.4 KEDs of $\text{Ru}(\text{bpy})_3^{2+}$ (a) and WPOM^{3-} (b) obtained at different values of the flatapole bias. The most probable KE (KE_{mp}) and FWHM and are shown for each curve. 48
- Figure 2.5 Ion kinetic energy distributions (KEDs) of $\text{Ru}(\text{bpy})_3^{2+}$ (a) and WPOM^{3-} (b) acquired at different voltages on the conductance limit (V_{cl}). The flatapole bias was kept at +14 V/-14 V for $\text{Ru}(\text{bpy})_3^{2+}$ and WPOM^{3-} , respectively. The FWHM and most probable kinetic energy (KE_{mp}) of each KED plot was shown on the top left corner of each figure. 49
- Figure 2.6 KEDs of $\text{Ru}(\text{bpy})_3^{2+}$ (a) and WPOM^{3-} (b) obtained at different values of the flatapole bias. The most probable KE (KE_{mp}) and FWHM and are shown for each curve. 51
- Figure 2.7 (a) Visible absorption spectra of $\text{B}_{12}\text{Cl}_{12}^{2-}/\text{NRH}^+$ surfaces. Optical images of the surfaces are shown on the right: (b) neutral red only, (c) LBL, and (d) fast polarity switching. . 52
- Figure 2.8 (a) Visible spectra of 1 mM Neutral Red in methanol (red) and in a solution of 10 mM NaOH in methanol (yellow). Optical images of the solutions are shown on the right: (b) NR in methanol, (c) NR in 10 mM NaOH in methanol. 53
- Figure 2.9 (a) Visible spectra of solutions of 1 mM Neutral Red in methanol (red) and in a solution of 10 mM NaOH in methanol (yellow) dropcasted onto FSAM surfaces. Optical images of the

dropcasted spots are shown on the right: (b) NR in methanol, (c) NR in 10 mM NaOH in methanol. 54

Figure 2.10 IRRAS spectra of the MoPOM³⁻/Ru(bpy)₃²⁺ surfaces prepared by LBL (A and B), fast polarity switching (C), MoPOM³⁻ only (D) and Ru(bpy)₃²⁺ only (E). The cartoon pictures of surface A through E are shown in the corresponding figures, illustrating the surfaces were prepared in either LBL or fast polarity switching modes. The combination of bands, reproduced by Gaussian curve fitting, are shown in each of the figures with color coding. A scale bar showing the absorbance is marked on the top left of the figure. 56

Figure 3.1 (a) A cross-section view of the RWMA from SIMION simulations showing the equipotential lines (red) at $\theta = 0^\circ$ and $\theta = 30^\circ$. The black arrows indicate the direction of the electric field. The equipotential lines inside the RWMA are evenly spaced indicating that a homogeneous rotating field is constructed in the central region of the RWMA. (b) A schematic drawing of the ion soft landing instrument composed of a high-transmission ESI interface, an einzel lens, the RWMA and an IonCCD/surface. The left bottom corner shows the schematic drawing of the RWMA fabricated in our lab, and a diagram showing the phases of the sinusoidal rf waveforms applied to the eight electrodes. This panel is adopted from ref. [51] and presented here for clarity. (c) Cross-sectional view of the electrode geometry used in SIMION simulations including a conductance limit plate, einzel lens, RWMA, and IonCCD/surface. The red, green, and blue traces indicate the ion trajectories of 12000 ions of $m/z=253.2$, $m/z=329.2$, $m/z=470.3$, respectively, at a kinetic energy of 20 eV. 67

Figure 3.2 (a) A schematic diagram of the RWMA and a collector plate used to derive Eq. 1. The ion entering the RWMA at (0,0,0) at time t_0 along the cylinder's central axis is radially dispersed by the rotating field and exits the RWMA at (x_1, y_1, z_1) . The length of this region and time the ion spends in this region are denoted as D_1 and t_1 , respectively. Next, the ion travels through the field-free region along its velocity vector attained at (x_1, y_1, z_1) and lands onto the collector plate at (x_2, y_2, z_2) . The length of this region and time the ion spends in this region are denoted as D_2 and t_2 , respectively. (b) A projection of the collector plate perpendicular to the central axis showing the ring deposition pattern formed by a continuous ion beam; r is the radius of the ring. 71

Figure 3.3 Deposition radius as a function of distance from the RWMA entrance for an ion of $m/z=253.2$, $E_k=35$ eV/charge with RWMA operating at $f=70$ kHz, 10 V_{p-p} 72

Figure 3.4 (a) Plots of the deposition radius as a function of m/z for singly-charged ions of the same E_k (35 eV) and at several frequencies of the rotating field shown in different colors. (b) Simulated RWMA mass spectra containing four signals ($m/z = 200, 400, 600,$ and 800) extracted from the plots shown in panel (a) at different frequencies shown using the same color coding as in panel (a). The heights of the bars in the simulated spectra indicate the m/z 73

Figure 3.5 The rotating electric field strength along the main axis of the RWMA. The location of the RWMA relative to the plot is shown in the figure. 75

Figure 3.6 Negative ESI-MS spectrum of PAM ($M_n=1500$); m/z of the major oligomers observed in the spectrum (I to VIII) are listed in Table 2.1. 75

Figure 3.7 Plots of the calibrated deposition radii vs m/z at $f=70$ kHz (solid) and $f=50$ kHz (dashed). The experimental data points are shown for PAM calibrants (filled circles), organic dyes (open triangles), and PDMS oligomers (open diamonds). The r values were calculated using Eq. 1 using

the effective rotating field strength (E) and length of the field (D_I) obtained from the calibration.	77
Figure 3.8 (a) An ESI mass spectrum of 5 μ M ubiquitin in 49:49:1:1 methanol/H ₂ O/CH ₃ COOH/glycerol (v/v/v/v) showing a distribution of charge states ranging from 7+ to 13+. (b) An IonCCD profile of ubiquitin ions separated by the RWMA operated at a frequency of $f=40$ kHz. The charge state assignment of each peak is labeled in the profile.	79
Figure 3.9 (a) IonCCD profile of a mixture of the three dyes acquired using RWMA operated at $f=70$ kHz, $10 V_{0-p}$ at different kinetic energies. (b) The FWHMs of the peaks in the profiles shown in (a) and the corresponding values of mass resolution (c).	80
Figure 3.10 Experimental IonCCD profiles (black) and simulated profiles (red) using sums of best-fit Lorentzian distributions of the beam of the dye mixture at different kinetic energies.	82
Figure 3.11 Kinetic energy distributions of the dyes at 20 eV (a) and 50 eV (b). The black and red traces represent the experimental first derivative of the retarding voltage plot and the Gaussian-fitted curve, respectively.	83
Figure 3.12 Experimental beam profiles (top black trace) and the corresponding profiles generated using SIMION simulations (light grey bars) of the three dyes at kinetic energies of 20 eV (a) and 50 eV (b). Yellow, green, and blue areas/curves on the top/bottom of each panel represent Lorentzian profiles obtained from the best fit of the underlying peaks of DASPE ⁺ (m/z 253.2), MG ⁺ (m/z 329.2) and VBB ⁺ (m/z 470.3), respectively.	85
Figure 3.13 Simulated FWHM of the deposition ring of DASPE ⁺ (m/z 253.2) with Gaussian-shaped KEDs of 0.2 eV, 1 eV and 2 eV FWHM centered at 20 eV/charge and various initial beam widths (0 mm, 0.5 mm, 1 mm, 1.5 mm and 2 mm).	86
Figure 3.14 a) Gold atom arrangement in an atomic structure of Au ₁₄₄ (SCH ₂ Ph) ₆₀ ⁸¹ and the IonCCD beam profile showing Au ₁₄₄ (SC ₄ H ₉) ₆₀ ⁿ⁺ (n=1,2,3) separated by RWMA at $f=6/7/8/10$ kHz, $10 V_{0-p}$ when the IonCCD was positioned 1'' after RWMA. The charge states of Au ₁₄₄ (SC ₄ H ₉) ₆₀ are labelled on top of the peaks. b) TEM images of Au ₁₄₄ (SC ₄ H ₉) ₆₀ ⁺ deposited onto graphene-coated Cu grid acquired at 300 kV acceleration voltage, scale bar: 20 nm. c) An expanded view of an area of the TEM image highlighted with the yellow-squared area in panel b) containing monodisperse Au ₁₄₄ (SC ₄ H ₉) ₆₀ ⁺ clusters, scale bar: 10 nm. d) A cluster size distribution extracted from the TEM image in b). e) A representative HRTEM image of an individual Au ₁₄₄ (SC ₄ H ₉) ₆₀ ⁺ cluster acquired at 300 kV acceleration voltage. f) HRTEM image of the cluster shown in E) after electron beam irradiation. Scale bar=1 nm.	88
Figure 3.15 Deposition radius of Au ₁₄₄ (SC ₄ H ₉) ₆₀ ⁿ⁺ (n=1,2,3) from SIMION simulations, analytical expression (equation 10), and experiments at $f=70$ kHz, $V_{0-p}=10$ V with the IonCCD positioned 1'' away from RWMA.	89
Figure 3.16 a) SIMION simulations of the native charge state distribution of Apoferritin (480 kDa) ⁸³ separated by RWMA operating at $f=10$ kHz, $V_{0-p}=10$ V. The collecting plate is positioned 3'' away from the RWMA. The kinetic energy of the ions is 5 eV/charge. The scale bar in the picture is 5 mm. b) Deposition radius of different charge states of Apoferritin extracted from SIMION simulations presented in (a).	90

Figure 3.17 Schematic diagram of the TEM grid holder used for Au ₁₄₄ (SC ₄ H ₉) ₆₀ cluster deposition. 1: grounded mask with a 3 mm diameter aperture in the center; 2: TEM grid; 3: current collector; 4: PEEK adapter connected to a XYZ positioner.	90
Figure 3.18 STEM image of deposited Au ₁₄₄ (SC ₄ H ₉) ₆₀ ⁺ on graphene-coated Cu grid. The average cluster diameter is labeled. Scale bar: 10 nm.....	91
Figure 3.19 Representative HRTEM images of individual Au ₁₄₄ (SC ₄ H ₉) ₆₀ ⁺ on graphene-coated Cu grid showing fcc-like Au core arrangement. Scale bar=1 nm.	92
Figure 3.20 (a) IonCCD beam profile of the PAM oligomers with RWMA operating at f=70 kHz, V _{0-p} =10 V with the IonCCD positioned 2'' after RWMA; peaks corresponding to different oligomers are marked in the figure. (b) Nano-DESI line scan along the deposition region showing extracted ion signals for different oligomers (colored lines) and total ion signal (black line).	94
Figure 3.21 Contact angles of the (a) hydrophobic FSAM surface covered with hydrophilic PAM oligomers and (b) hydrophilic gold surface covered with hydrophobic PDMS oligomers. The x coordinate of the plot corresponds to the distance between the point of measurement and the edge of the surface. The grey dashed lines are shown to guide the eye.	95
Figure 3.22 Full-width-at-half-maximum (FWHM) of the nano-DESI profiles of PAM oligomers II through VI on the left side (blue bars) and right side (red bars) of the line scan in Figure 2.20.	95
Figure 3.23 A positive mode ESI-MS spectrum of PDMS (Mn~580); m/z of the major oligomers observed in the spectrum (I to XI) are listed in the table.....	96
Figure 3.24 IonCCD beam profile of the PDMS oligomers with RWMA operating at f=50 kHz, V _{0-p} =10 V; peaks corresponding to different oligomers are marked in the figure.....	96
Figure 4.1 in situ vacuum-compatible electrochemical cell using a nanoporous ionic liquid membrane. WE=working electrode, CE=counter electrode, RE=reference electrode.	106
Figure 4.2 A photographic image of the three-electrode cell assembly and schematic drawing of the IR light beam used for IRRAS measurements. WE = working electrode, CE = counter electrode, RE = reference electrode. The electrolyte membrane covers all three electrodes.	108
Figure 4.3 (a) Nyquist plot obtained from the potentiostatic EIS of the <i>in situ</i> spectroelectrochemical cell (Frequency range: 100 kHz to 1 Hz, amplitude: 10 mV). Inset: the equivalent circuit model used to fit the EIS data, R _e - electrolyte resistance, R _{ct} - charge transfer resistance, C _{dl} - double layer capacitance, R _m - porous membrane resistance, C _m - double layer capacitance derived at porous membrane, and Z _w - Warburg impedance). (b) CV of the blank spectroelectrochemical cell before soft landing experiments acquired at scan rate of 50 mV s ⁻¹	111
Figure 4.4 <i>In situ</i> CV of soft-landed PW ₁₂ O ₄₀ ³⁻ anions in the potential range between -2100 and -100 mV. CV measurements were performed after 3 × 10 ¹⁵ ions were deposited onto the cell. Scan rate: 0.5 mV s ⁻¹ . The reduction portion of the CV curve showing potential regions outlined with red dashed lines and labeled with numbers on top along with key electron transfer processes examined spectroelectrochemically. The potentials used in the IRRAS measurements are marked with blue dots on the CV curve.....	112

Figure 4.5 <i>In situ</i> IR spectra of the electrochemical cell obtained at different ion coverages. The IR spectrum of the initial blank cell is used as the baseline. The top spectrum represents the WPOM soft-landed on a bare Au surface for comparison.	115
Figure 4.6 IRRAS spectra of <i>in situ</i> spectroelectrochemical cell obtained at different potentials during reduction processes indicated on the left side in the range of 3000-700 cm^{-1}	116
Figure 4.7 IRRAS spectra of <i>in situ</i> spectroelectrochemical cell obtained at different potentials during re-oxidation processes indicated on the left side in the range of 3000-700 cm^{-1}	117
Figure 4.8 Chronoamperometry during the spectroelectrochemistry experiments. The measurements are shown in consecutive 1800-sec segments (including 600 sec equilibration and 1200 sec IRRAS measurement time).	118
Figure 4.9 (a) <i>In situ</i> IRRAS spectrum of WPOM anions soft-landed on a bare gold surface. (b) Representative IRRAS spectrum acquired at -2.1 V shown to illustrate new features that appear during the spectroelectrochemical measurements. The red dashed line indicates the IR baseline. <i>In situ</i> IRRAS spectra obtained at different potentials during the (c) reduction and (d) oxidation processes of WPOM. The potential regions I-VI and the corresponding charge states of the reduced WPOM species are marked on the right.	119
Figure 4.10 (a) Fitted IR spectra obtained during the reduction process in the wavenumber range between 1000 to 800 cm^{-1} . Bar graphs showing the intensities of the positive (b) and negative (c) bands in the W=O _i region obtained from curve fitting as a function of the potential applied to the WE. The potential regions (I-VI) and charge states of the reduced WPOM at each potential are marked to facilitate understanding.	122
Figure 4.11 Experimental and curve-fitted IRRAS spectra at different potentials in the reduction process marked on the top left side of each plot. In each plot, experimental spectrum is shown in black and the best fit curve is shown in red. The sum of squares in each curve fitting is indicated on the top right.	124
Figure 5.1 ESI-MS spectra of solutions containing (a) $[\gamma\text{-CD} + \text{W}_{12}\text{POM}]^{3-}$ and (b) $[\gamma\text{-CD} + \text{W}_6\text{POM}]^{2-}$	134
Figure 5.2 ESI-MS spectra of solutions containing (a) $[\alpha\text{-CD} + \text{W}_{12}\text{POM}]^{3-}$ and (b) $[\beta\text{-CD} + \text{W}_{12}\text{POM}]^{2-}$	135
Figure 5.3 (a) HCD (CE = 45) and (b) low-energy CID (CE = 17) spectra of Keggin CD-W ₁₂ POM complexes under same conditions. The precursor ion signal in each spectrum is marked with an asterisk.	137
Figure 5.4 (a) CID spectrum of $[\alpha\text{-CD} + \text{W}_{12}\text{POM}]^{3-}$ complex with 10× magnified lower <i>m/z</i> region. The fragments observed in the low <i>m/z</i> region is confirmed as the subsequent fragments of [CD - H] ⁻ by CID spectrum of [CD - H] ⁻ (b).....	138
Figure 5.5 (a) CID spectrum of $[\alpha\text{-CD} + \text{W}_{12}\text{POM}]^{3-}$ complex with 10× magnified lower <i>m/z</i> region. The fragments observed in the low <i>m/z</i> region is confirmed as the subsequent fragments of [CD - H] ⁻ by CID spectrum of [CD - H] ⁻ (b).....	140
Figure 5.6 A region of low-energy CID spectra of $[\gamma\text{-CD} + \text{W}_6\text{POM}]^{2-}$ showing multiple water losses at (a) CE = 16, (b) CE = 19, and (c) CE = 22. The precursor ion signal in each spectrum is	

marked with an asterisk. The red ruler on top of the panel shows the corresponding number of water losses.	141
Figure 5.7 Expanded m/z range of the MS^3 spectra showing further multiple water loss peaks from the $[\gamma\text{-CD} + W_6POM]^{2-}$ complex (CE = 17 eV). The parent peak in each of the MS^3 spectrum isolated from the MS^2 of $[\gamma\text{-CD} + W_6POM]^{2-}$ is marked with an asterisk. The red ruler on top of the panel shows the corresponding number of water losses from the original complex.	142
Figure 5.8 (a) Low-energy CID spectra of Lindqvist CD- Mo_6POM complexes at CE = 17. The precursor ion signal in each spectrum is marked with an asterisk. (b) Expanded m/z range of the spectra showing multiple water loss peaks. The red ruler on top of each spectrum shows the corresponding number of water losses.	143
Figure 5.9 Expanded m/z range of the spectra showing the $[CD + W_2O_6 - H - xH_2O]^-$ fragments produced from low-energy CID experiments of $[\alpha\text{-CD} + W_6POM]^{2-}$ (a), $[\beta\text{-CD} + W_6POM]^{2-}$ (b), and $[\gamma\text{-CD} + W_6POM]^{2-}$ (c).	144
Figure 5.10 ESI-MS spectrum of a solution of $[\gamma\text{-CD} + W_6POM]^{2-}$ in 50:50 (v/v) CD_3OD/D_2O solvent showing the isotopic envelopes of $[\gamma\text{-CD-H}]^-$, $[\gamma\text{-CD} + Cl]^-$, and $[\gamma\text{-CD} + W_6POM]^{2-}$ after three hours of H/D exchange.	146
Figure 5.11 Experimental (a) and simulated (b and c) distributions of water losses from $m/z = 1365$ isolated from the isotopic pattern of deuterium-exchanged $[\gamma\text{-CD} + W_6POM]^{2-}$. Panel (b) shows a simulated spectrum obtained assuming that all of the 24 -OH groups are available for the water loss channel; panel (c) shows a simulated spectrum obtained assuming that only 16 -OH groups participate in the water loss channel. The red ruler shows the corresponding number of water losses.	147
Figure 5.12 ESI-MS spectrum of a solution of ^{18}O -exchanged $[\gamma\text{-CD} + W_6POM]^{2-}$ in 50:50 (v/v) acetonitrile/ $H_2^{18}O$ solvent showing W_6POM^{2-} and $[\gamma\text{-CD} + W_6POM]^{2-}$	149
Figure 5.13 Experimental (a) and simulated (b, c and d) distributions of water losses from $m/z = 1369.5$ isolated from the isotopic pattern of ^{18}O -exchanged $[\gamma\text{-CD} + W_6POM]^{2-}$. (b-d) Simulated spectra obtained assuming that different number of oxygen atoms participate in the water loss channel: (b) only the oxygen atoms of W_6POM^{2-} ; (c) a total of 35 oxygen atoms of both W_6POM^{2-} and 16 secondary hydroxyl groups of $\gamma\text{-CD}$; (d) a total of 43 oxygen atoms of W_6POM^{2-} and all 24 hydroxyl groups of $\gamma\text{-CD}$. The red ruler shows the corresponding number of water losses..	150
Figure 6.1 Geometry of octahedral hexanuclear molybdenum $[Mo_6X^i_8X^a_6]^{2-}$ (X = F, Cl, Br, I) cluster anions.	159
Figure 6.2 ESI-MS spectra of TBA salt of $[Mo_6X_{14}]^{2-}$ (X=Cl (a), Br (b) and I (c)) in acetonitrile, showing the doubly-charged $[Mo_6X_{14}]^{2-}$ as the predominant species.	162
Figure 6.3 In-source CID spectra, showing an overview of molecular fragment ions and their reaction products with background gases for a) $[Mo_6Cl_{14}]^{2-}$, b) $[Mo_6Br_{14}]^{2-}$ and c) $[Mo_6I_{14}]^{2-}$. All observed fragments are singly charged. Adducts with H_2O and O_2 are marked with red and blue arrows, respectively. Multiple arrows in (b) and (c) indicate the number of O_2 added. Fragment ions which have not reacted with background gas molecules are marked with a black dotted line and their molecular formula is abbreviated by [Number of Mo atoms, Number of halogen atoms].	163

Figure 6.4 Ion-trap CID mass spectra of $[\text{Mo}_x\text{Cl}_y]^-$ clusters: (a) $[\text{Mo}_6\text{Cl}_{13}]^-$ (b) $[\text{Mo}_6\text{Cl}_{12}]^-$ (c) $[\text{Mo}_6\text{Cl}_{11}]^-$ (d) $[\text{Mo}_5\text{Cl}_{10}]^-$ (e) $[\text{Mo}_5\text{Cl}_9]^-$ (f) $[\text{Mo}_5\text{Cl}_8]^-$ (g) $[\text{Mo}_4\text{Cl}_8]^-$ (h) $[\text{Mo}_4\text{Cl}_7]^-$ (i) $[\text{Mo}_4\text{Cl}_6]^-$ (j) $[\text{Mo}_3\text{Cl}_6]^-$ (k) $[\text{Mo}_3\text{Cl}_5]^-$ (l) $[\text{Mo}_2\text{Cl}_5]^-$ (m) $[\text{Mo}_2\text{Cl}_4]^-$ (n) $[\text{Mo}_2\text{Cl}_3]^-$. Parent ions, generated via in-source CID, are marked by *. Fragment ions which have not reacted with background gas molecules are marked with a blue, dotted line and their molecular formula is abbreviated by [Number Mo atoms, Number halogen atoms]. The red arrow indicates the reaction with water and green arrow indicates the reaction with O_2 , while dotted line indicates the corresponding adducts. 164

Figure 6.5 Ion-trap CID mass spectra of $[\text{Mo}_x\text{Br}_y]^-$ clusters: (a) $[\text{Mo}_6\text{Br}_{13}]^-$ (b) $[\text{Mo}_6\text{Br}_{12}]^-$ (c) $[\text{Mo}_6\text{Br}_{11}]^-$ (d) $[\text{Mo}_6\text{Br}_{10}]^-$ (e) $[\text{Mo}_6\text{Br}_9]^-$ (f) $[\text{Mo}_6\text{Br}_8]^-$ (g) $[\text{Mo}_6\text{Br}_7]^-$ (h) $[\text{Mo}_6\text{Br}_6]^-$ (i) $[\text{Mo}_6\text{Br}_5]^-$ (j) $[\text{Mo}_6\text{Br}_4]^-$ (k) $[\text{Mo}_6\text{Br}_3]^-$ (l) $[\text{Mo}_6\text{Br}_2]^-$. Parent ions, generated via in-source CID, are marked by *. Fragment ions which have not reacted with background gas molecules are marked with a blue, dotted line and their molecular formula is abbreviated by [Number Mo atoms, Number halogen atoms]. The red arrow indicates the reaction with dioxygen, while dotted line indicates the corresponding adducts. Multiple arrows indicate the number of O_2 added. 167

Figure 6.6 Ion-trap CID mass spectra of $[\text{Mo}_x\text{I}_y]^-$ clusters: (a) $[\text{Mo}_6\text{I}_{13}]^-$ (b) $[\text{Mo}_6\text{I}_{12}]^-$ (c) $[\text{Mo}_6\text{I}_{11}]^-$ (d) $[\text{Mo}_6\text{I}_{10}]^-$ (e) $[\text{Mo}_6\text{I}_9]^-$. Parent ions, generated via in-source CID, are marked by *. Fragment ions which have not reacted with background gas molecules are marked with a blue, dotted line and their molecular formula is abbreviated by [Number Mo atoms, Number halogen atoms]. The red arrow indicates the reaction with dioxygen, while dotted line indicates the corresponding adducts. Multiple arrows indicate the number of O_2 added. We note that (a) and (b) are acquired under extended mass range on the LTQ-XL instrument. 169

Figure 6.7 Ion-trap CID mass spectra of $[\text{Mo}_6\text{X}_{14}]^{2-}$ clusters: (a) $[\text{Mo}_6\text{Cl}_{14}]^{2-}$ (b) $[\text{Mo}_6\text{Br}_{14}]^{2-}$ (c) $[\text{Mo}_6\text{I}_{14}]^{2-}$. Parent ions are marked by *. The red arrows indicate the loss of X^- 171

Figure 6.8 Examples of isolation of $[\text{Mo}_6\text{In}(\text{O}_2)_y]^-$ adducts in the ion trap: (a) $[\text{Mo}_6\text{I}_9(\text{O}_2)]^-$, (b) $[\text{Mo}_6\text{I}_8(\text{O}_2)]^-$, (c) $[\text{Mo}_6\text{I}_8(\text{O}_2)_2]^-$. Parent ions are marked by *. The red and blue arrows indicate the mass difference between two peaks corresponding to I^- loss and O_2 addition, respectively. 173

LIST OF SCHEMES

Scheme 5.1 Cyclodextrins (α , β , and γ -CD) and POM anions (Keggin $W_{12}POM^{3-}$, Lindqvist W_6POM^{2-}) used in this study.	133
Scheme 5.2 Major fragmentation pathways observed for the CD-POM host-guest complexes in the gas phase.	136
Scheme 6.1 Gas-phase fragmentation pathways of $[Mo_6X_{14}]^{2-}$ ($X=Cl, Br$ and I) ions by ion-trap CID experiments. Molecular formulae of the ions are abbreviated by [Number Mo atoms, Number halogen atoms]. Singly charged ions are written black, doubly charged ions red. Arrows mark the fragmentation pathways evidenced by ion-trap CID.	170

LIST OF ABBREVIATIONS

AFM	Atomic Force Microscopy
CD	Cyclodextrin
CID	Collision Induced Dissociation
Da	Dalton
DC	Direct Current
DESI	Desorption Electrospray Ionization
DFT	Density Functional Theory
EEI	Electrode-Electrolyte Interface
EIS	Electrochemical Impedance Spectroscopy
ESI	Electrospray Ionization
FSAM	Fluorinated Self-Assembled Monolayer
FWHM	Full Width at Half Maximum
eV	Electron-volt
GI-SAXS	Grazing-Incidence Small Angle X-ray Scattering
HCD	Higher-Energy Collisional Dissociation
HDX	Hydrogen Deuterium Exchange
HRTEM	High-Resolution Transmission Electron Microscopy
IL	Ionic Liquid
IRRAS	Infrared Reflection Absorption Spectroscopy
KED	Kinetic Energy Distribution
LBL	Layer by Layer
LDI	Laser Desorption Ionization
MACS	Matrix Assembly Cluster Source
MS	Mass Spectrometry
<i>m/z</i>	mass-to-charge ratio
Nano-DESI	Nanospray Desorption Electrospray Ionization
NIR	Near Infrared
NMR	Nuclear Magnetic Resonance

PAM	Polyacrylamide
PDMS	Polydimethylsiloxane
POM	Polyoxometalate
RF	Radio Frequency
RWMA	Rotating Wall Mass Analyzer
SAM	Self-Assembled Monolayer
SEM	Scanning Electron Microscopy
SHG	Second Harmonic Generation
SID	Surface Induced Dissociation
SIMS	Secondary Ion Mass Spectrometry
SPE	Screen-Printed Electrode
STEM	Scanning Transmission Electron Microscopy
STM	Scanning Tunneling Microscopy
STS	Scanning Tunneling Spectroscopy
TEM	Transmission Electron Microscopy
TOF	Time of Flight
TPD	Temperature Programmed Desorption
TPR	Temperature Programmed Reaction
UPS	Ultraviolet Photoelectron Spectroscopy
XAS	X-ray Absorption Spectroscopy
XAFS	X-ray Absorption Fine Structure
XPS	X-ray Photoelectron Spectroscopy
XRD	X-ray Diffraction

ABSTRACT

Ion soft landing is a preparative mass spectrometry technique that enables intact deposition of polyatomic ions onto surfaces. The ability to select ions with well-defined mass, charge, and kinetic energy, along with precise control over size, shape, and position of the ion beam in the deposition process distinguishes ion soft landing from traditional synthetic and surface preparation approaches. A wide range of projectile ions including molecular ions, non-covalent complexes, clusters, and ionic fragments generated in the gas phase have been used in soft-landing studies to address both the fundamental questions related to ion-surface interactions and enable applications of hyperthermal beams.

Since the first soft landing instrument was implemented by Cooks and co-workers in 1977, significant advances have been achieved in preparative mass spectrometry instrumentation. Current instrument development efforts are focused on obtaining high ion currents, increasing the experimental throughput, and developing capabilities for layer-by-layer deposition. In chapter 2 and 3, two novel instrumentation approaches are introduced, which improve the ion flux and experimental throughput of ion soft landing research. In particular, soft landing of ions of both polarities enables the bottom-up construction of ionic materials. Meanwhile, a rotating wall mass analyzer substantially increases the mass range of mass-selective deposition and disperses multiple species on the same surface thereby increasing the experimental throughput. These instrumentation developments open up the opportunities to explore research topics in the field of catalysis, energy storage and production, biology, and quantum sciences.

In chapter 4, I describe a novel *in situ* spectroelectrochemistry approach for studying structural changes of electroactive species during electrochemical processes. In these experiments, ion soft landing is used to prepare well-defined ions at electrochemical interfaces. In addition, understanding of the gas-phase properties of cluster ions is important for their application in ion soft landing research. Ions can be prepared in the proper physical and chemical state via gas-phase chemistry approaches, and the favorable properties and reactivities of ions can thereby be harnessed using ion soft landing. In chapter 5 and 6, gas phase properties of host-guest complexes of cyclodextrins and polyoxometalates and molybdenum halide clusters are discussed.

CHAPTER 1. INTRODUCTION

1.1 Synopsis

Ions are important components of many classes of materials including electrolytes, ionic crystals, and polymers. The unique physical and chemical properties of these materials originate from their ionic building blocks. Mass spectrometry (MS) has been used for investigating the chemistry and physics of isolated gaseous ions, ion-ion and ion-matter interactions. Except for its wide analytical applications, MS is also ideally-suited as a preparative tool for the deposition of well-defined ions onto surfaces and substrates under controlled conditions. The first study of ion-surface collisions was conducted by J.J. Thompson in early 1900s, which provided a “permanent record of the position of the rays”.¹ Subsequent studies of ion-surface collisions have provided a detailed description of the relevant physical and chemical processes. Of particular interest are processes leading to trapping of ions on surfaces during collision, which have been developed into a distinct scientific field of ion soft landing. Ion soft landing refers to the deposition of ions onto surfaces, which preserves their structural integrity, and in specific cases, physical properties (e.g., ionic charge), chemical reactivity, and even biological activity.²⁻⁵

In a typical preparative MS (ion soft landing) experiment, atomic or molecular ions produced from ionization sources are transferred into vacuum through ion optics, mass-selected using a mass analyzer, and deposited onto a substrate under controlled conditions.^{6,7} Recent developments in the field of preparative MS enable a high-coverage deposition using bright ion beams, which opens up opportunities to investigate ion-ion and ion-neutral chemistry on surfaces.^{8,9} Interesting macroscopic phenomena have been observed in ionic layers prepared using high-coverage deposition, which are not observed at sub-monolayer surface coverages.¹⁰ In particular, interactions of individual ions with surfaces at sub-monolayer coverage are replaced with collective phenomena at high coverages, which result in self-organization of the deposited layers.^{11,12} This has led us to think about two fundamentally important aspects associated with preparative deposition of ions. On the one hand, careful preparation of gaseous ions with desired physical and chemical properties is important for predicting their properties following a collision with a surface. It is therefore important to understand the structure, dynamics and chemical reactivity of gaseous ions. On the other hand, understanding of the physical and chemical processes

accompanying ion-surface collisions including ion-ion and ion-neutral interactions on surfaces is essential to the rational design and fabrication of functional ionic architectures of interest to energy storage, catalysis, and biology. These studies often employ a variety of surface characterization techniques. In particular, *in situ* techniques are favorable since they allow the real-time characterization of the ionic layer during its growth. X-ray spectroscopy,^{13,14} temperature programmed desorption (TPD),¹⁵ infrared and Raman spectroscopy,¹⁶⁻¹⁸ and electrochemical techniques^{19,20} have been used to study the structure and dynamics of ions and their local environment. Soft-landed ions have been also extensively investigated using *ex situ* surface-characterization techniques such as optical spectroscopy,^{8,10} electron microscopy,^{21,22} and ambient ionization MS.^{21,23}

Herein, a series of studies focused on the characterization of structures and reactivity of gas-phase polyatomic ions and their interactions in the condensed phase layers prepared by soft landing of mass-selected ions is presented. We start by describing two developments of preparative MS instrumentation. The development of a dual polarity deposition instrument opens up opportunities for preparing previously inaccessible layered architectures using ions of both positive and negative polarities. Meanwhile, the rotating wall mass analyzer enables high-throughput dispersive deposition of ions over a much wider mass range than what is accessible using a quadrupole mass filter or any commercial mass spectrometer. Our studies employ several interesting molecular clusters including polyoxometalates (POMs), halogenated *closo*-borates, and transition metal chalcogenide clusters that display distinct electronic, optical and magnetic properties determined by their molecular structures and composition. Studies of their gas-phase properties as isolated species are first presented, followed by demonstrations of how the favorable properties of these clusters can be harnessed in the condensed-phase using preparative MS.

1.2 Phenomena in Ion-Surface Collisions

Physical and chemical processes associated with ion-surface collisions are summarized in Figure 1.1. Ion-surface collisions at energies exceeding 1 keV result in physical sputtering and implantation.³ Meanwhile, ion scattering, surface-induced dissociation (SID) of ions, charge transfer to and from the surface, ion deposition (soft and reactive landing), and chemical sputtering are the dominant processes at hyperthermal kinetic energies (<100 eV).^{3,24} The key processes

observed at kinetic energies below 20 eV include ion scattering, charge transfer, and ion soft landing.^{7,25,26} In ion soft landing, the projectile ion is trapped on the surface. SID becomes a dominant process for ion-surface collisions at higher kinetic energies (20-60 eV).²⁷⁻²⁹ In addition, two other processes commonly take place in the same energy range: 1) ion reactive landing, in which ions or their fragments formed following the collision are covalently bound to the surface; 2) reactive scattering, in which projectile ions pick up a chemical group from the surface prior to scattering.³⁰⁻³² Collision energies exceeding 100 eV typically result in ion shattering generating a large number of fragment ions.³³⁻³⁵

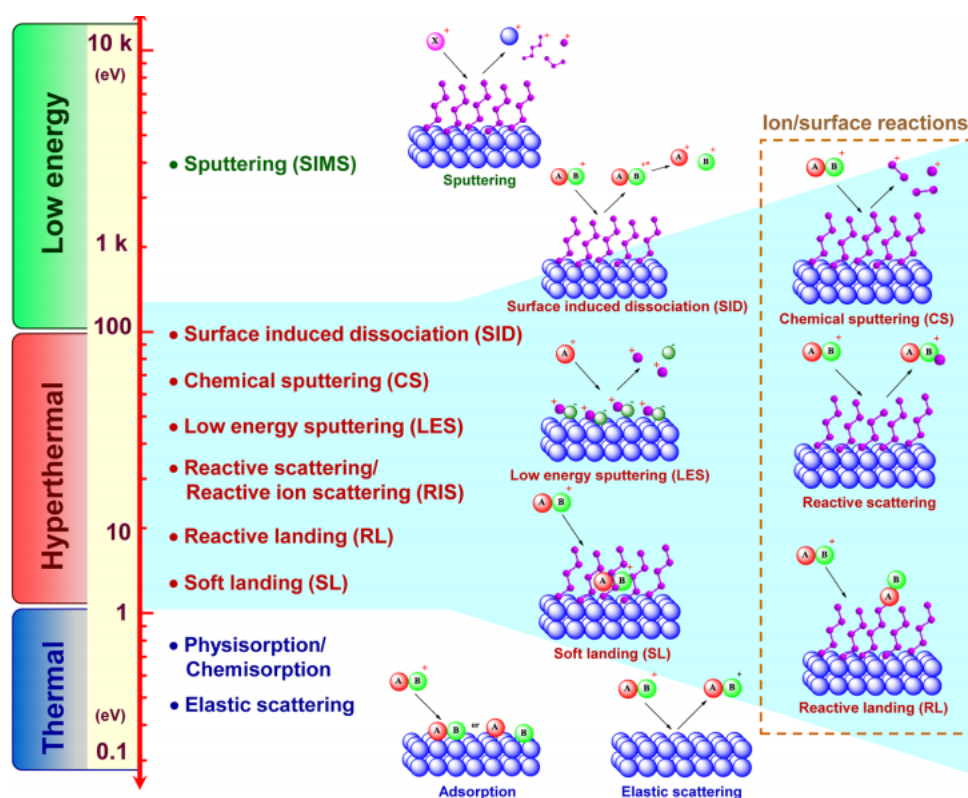


Figure 1.1 Physical and chemical processes associated with ion-surface collisions at chemically-relevant energies. Reproduced with permission from Ref [3]. Copyright 2012, American Chemical Society.

1.2.1 Soft Landing of Ions

Of particular interest to this chapter is the ion soft landing process, which results in deposition of intact projectile ions on the surface. In addition to the kinetic energy of the ions discussed earlier, the soft landing process is also determined by the structure of the ion and

properties of the surface.^{6,36} Specifically, collisions of ions with harder surfaces facilitate fragmentation at relatively low kinetic energies.^{37,38} At the same time, due to the larger number of vibrational degrees of freedom, large ions may remain intact at higher vibrational excitations than small ions.³⁹ In addition, when chemical reactions between projectile ions and surfaces take place resulting in reactive landing, the reaction efficiency is largely determined by the reactivity of the ions and/or the presence of reactive functional groups on surfaces.^{18,31,40,41}

1.2.2 Charge Retention by Soft-Landed Ions

The fate of soft-landed ions is determined by both the intrinsic properties of the projectile ions and the deposition target. Although neutralization of ions is a dominant process in collisions with conductive surfaces, partial or complete retention of ionic charge may occur when ions are soft landed onto thin insulating films assembled on top of an underlying conductive surface. In particular, organic thin films such as self-assembled monolayers (SAMs)^{37,42,43} or Langmuir-Blodgett films⁴⁴ have been extensively employed for studying soft- and reactive-landing of organic ions, organometallic complexes, and biomolecular ions, while thin metal oxide films on top of metal surfaces are typically used as substrates for studying bare metal clusters.⁴⁵

SAMs are well-organized thin organic films on solid substrates that may be terminated with various functional groups, thereby making them ideal targets for examining the physical and chemical processes accompanying soft- and reactive-landing of ions. Efficient charge retention by soft-landed ions was first discovered using gold surface covered with a fluorinated SAM (FSAM).⁴⁶ Subsequent studies provide a comprehensive picture of the mechanisms of charge reduction by soft-landed ions. Neutralization of soft-landed cations is attributed to the interfacial electron transfer from a conductive substrate through the insulating layer. In contrast, charge loss by protonated molecules (peptides, proteins) on surfaces occurs via the loss of ionizing protons.²⁶

The following equation may be used to estimate the total accumulated potential, ΔV , resulting from the soft landing of charged ions on top of a thin insulating SAM layer:

$$\Delta V = \frac{ZeN_{ions}d}{A\epsilon\epsilon_0}$$

(Equation 1.1)

Where Z is the charge state of the ion, e is the elementary charge, N_{ions} is the number of ions soft landed on the surface, d is the thickness of the SAM film, A is the area of the deposition spot, ϵ_0 is the vacuum permittivity, ϵ is the permittivity of the SAM. The potential across the SAM layer increases with the number and charge density of soft-landed ions and the thickness of the insulating layer. The properties of the SAM also have a pronounced effect on the electron tunneling rate across the layer. For example, efficient electron tunneling through alkylthiol layers (HSAM) and SAMs terminated with carboxyl groups (COOH-SAM) has been observed at very low applied potentials. In contrast, due to the presence of a large interfacial dipole on an FSAM surface, electron transfer from the conductive Au surface across the insulating SAM layer is quite inefficient. Nevertheless, once a sufficient charge is accumulated on the surface generating ~ 1 V potential, electron tunneling through the FSAM becomes quite efficient and the deposited ions are neutralized.

In contrast, stable anions often demonstrate a higher propensity towards charge retention on surfaces.⁴⁷ This is due to the relatively high electron detachment barrier for either partial charge reduction or complete neutralization. Recent spectroscopic investigations on multilayered deposition of electronically stable dodecaborate and polyoxometalate anions on Au-FSAM surface indicate efficient charge retention by anions independent of ion coverages.⁸ Chemical analysis of the soft-landed layer indicates the presence of co-adsorbed hydrocarbon molecules in the layer from the instrument background. More surprisingly, the soft-landed layer undergoes an unexpected macroscopic self-organization on the surface upon exposure to the laboratory air. These results were rationalized as follows:¹¹ electrostatic attraction of the soft-landed anions by the image charge from the conductive substrate plays an important role in stabilizing the layer. Destabilization of the layer by charge repulsion between adjacent anions in the layer is further mitigated through co-adsorption of neutral molecules. Destabilization and self-organization of the layer take place upon exposure to the laboratory environment as the electrostatic stabilization by the image charge dissipates over time. The decay of the stabilizing electrostatic interaction in the layer is accompanied by complex chemistry including partial oxidation of neutral molecules and water uptake from the environment.

1.3 Instrumentation

1.3.1 Ionization Sources

Starting from the first system built by Cooks and co-workers in 1977,⁴⁸ the applications of ion soft landing have been tightly linked to the development of custom-designed instrumentation.^{4,7,25,49} In particular, ion soft landing has benefited from the development of ionization sources and high transmission ion optics. In particular, a number of ionization approaches, such as electron impact ionization,^{50,51} electrospray ionization (ESI),⁵²⁻⁵⁵ magnetron sputtering and gas aggregation,⁵⁶⁻⁶¹ laser desorption ionization (LDI),⁶²⁻⁶⁶ are employed to make ions ranging from atomic ions, hydrocarbon fragments, peptides, metal oxides, metallic nanoparticles, to even polymer beads, protein complexes and virus capsids. Continuous ionization sources are usually preferred over pulsed systems due to the ability to produce higher ion fluxes with high duty cycles.

ESI is one of the most widely used ionization techniques in ion soft landing experiments due to its ability to generate a broad range of molecular ions and the ease of operation.^{67,68} By applying a high voltage to a liquid containing the analytes of interest, charged droplets are produced from the end of an ESI capillary. Ions are subsequently formed when the charged droplets are desolvated and transferred into downstream components of the instrument. Recent advances in ESI-based soft landing instrumentation focused on the improved transfer of charged droplets into the vacuum system and more efficient desolvation of the droplets at the atmospheric interface. Heated inlet capillary coupled to electrodynamic ion funnel interface has been used as the frontend of ion soft landing instrument to efficiently transfer ESI-generated ions into the higher vacuum region.⁶⁹ It has been shown that enhanced ion current in the nanoampere range can be produced by either increased inner diameter⁹ or precisely shaped heated inlet capillary.⁷⁰

Alternatively, a nonthermal magnetron sputtering source combined with gas aggregation has been used to generate charged nanoparticles and nanoclusters of different size, composition, and structure that are not readily accessible using traditional synthetic approaches. A few recent developments enable the production of high-intensity cluster beams.^{71,72} In particular, the sputtering process can be multiplexed with multiple metal targets positioned at controlled locations in the same aggregation region.⁷³

1.3.2 Mass Analyzers

Quadrupole mass analyzer is the most widely employed mass analyzer in current preparative mass spectrometry systems.⁷⁴ The quadrupole mass analyzer was first invented by Wolfgang Paul and Helmut Steinwedel in 1953.⁷⁵ It is composed of four parallel rods in an ideally hyperbolic geometry. Out-of-phase radio frequency electric potentials are applied to the two pairs of rods with a direct current offset voltage applied between one pair of rods and the other. Under typical operation mode, only ions of a certain mass-to-charge ratio (m/z) will reach the detector for a given ratio of voltages. Quadrupole mass filters used in preparative mass spectrometers transmits only one m/z at a time.

Another mass analyzer widely employed in the nanocluster deposition community is the lateral time-of-flight mass analyzer shown in Figure 1.2.^{76,77} It was first developed at the University of Birmingham. The principle for mass selection in this system is to laterally displace an ion beam by an orthogonal pulsed acceleration, let it drift for some time, and stop the perpendicular movement by an orthogonal pulsed deceleration. Ions of different masses are dispersed into parallel beams with different lateral displacements. The mass separation does not depend on the kinetic energy of the ion beam. It is particularly advantageous for the size selection and deposition of nanoclusters due to its unlimited mass range and has a resolution of $m/\Delta m=20-50$.

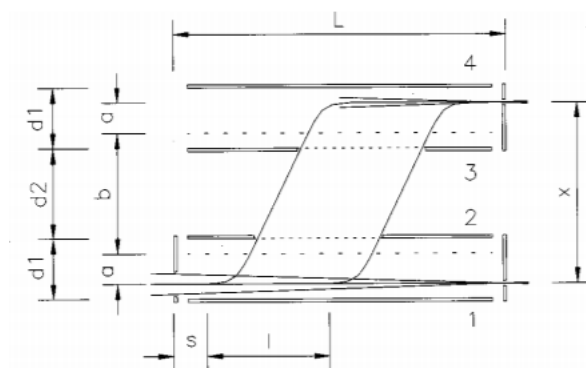


Figure 1.2 Schematic drawing of the lateral time-of-flight mas analyzer. Reproduced with permission from Ref [78]. Copyright 1999, American Institute of Physics.

Furthermore, mass-dispersive devices such as sector⁷⁸ and distance-of-flight mass spectrometers⁷⁹ enable spatial separation and simultaneous deposition of ions of different m/z on

a surface, which is beneficial to the throughput of ion soft landing experiments. However, most of these ideas are still limited to conceptual developments.

1.3.3 Ambient Soft Landing

Ambient soft landing is a simplified ion soft landing technique that has been used for the deposition of ions at atmospheric pressure.^{80,81} By using ambient soft landing technique, certain advantages of soft landing of mass-selected ions in vacuum may be reproduced with simpler instrumentation and substantially reduced cost. In a typical ambient soft landing system (Figure 1.3), charged droplet generated using ESI are pneumatically passed through a heated drying tube to ensure efficient droplet desolvation. The polarity of ions is then selected using electrostatic deflectors, and the desolvated polarity-selected ions are soft landed onto a surface in the open air. In contrast to traditional in-vacuum ion soft landing experiments, where ions are selected by their mass-to-charge ratio, here the ions to be deposited are selected through the choice of a chemical compound that produces mainly one ionic species in a given charge state during ESI. Ambient soft landing is a more accessible ion deposition approach that has a number of advantages compared to conventional solution-based preparation methods, such as drop casting and spin coating, since it eliminates neutral molecules and counterions from the surface.

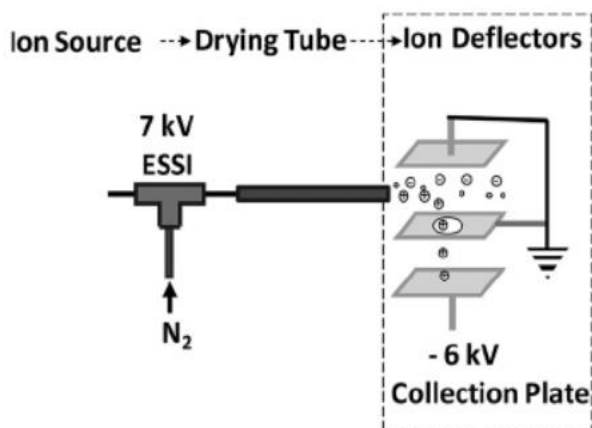


Figure 1.3 Schematic diagram of the electrospray emitter, drying tube, and electrostatic deflectors used for ambient soft landing .Reproduced from Ref [80]. with permission. Copyright 2011, American Chemical Society.

1.4 Surface Characterization Techniques for Soft-Landed Ions

A variety of surface characterization techniques capable of detecting small amounts of materials have been successfully applied in conjunction with ion soft landing experiments to obtain an understanding of the properties of soft-landed ions. In particular, low-energy chemical sputtering,^{50,82,83} LDI,⁸⁴ desorption electrospray ionization (DESI),⁸⁵ and secondary ion mass spectrometry (SIMS)⁸⁶⁻⁹⁰ have been employed either for *in situ* or *ex situ* characterizations. For example, TOF-SIMS is sensitive enough to detect soft-landed ions down to approximately 0.05% surface coverage.⁸⁷ In addition, *in situ* SIMS has been employed to study charge reduction kinetics of soft-landed ions on different substrates and the reactivity of ions with surfaces and gaseous molecules.^{26,88,91,92} Transmission electron microscopy (TEM), scanning tunneling microscopy (STM) enable high spatial resolution imaging of individual molecules, clusters, and their assemblies on surfaces.⁹³⁻⁹⁵ The binding energy between soft-landed ions and the surface may be derived from temperature-programmed desorption (TPD) experiments.¹⁷ *In situ* Raman^{16,96} and infrared spectroscopy have been coupled to soft landing systems for real-time structural characterization of ions. Grazing-incidence infrared reflection-absorption spectroscopy (IRRAS) have been used to probe the structures of peptides,⁸⁸ proteins,⁹⁷ and anionic metal oxide clusters⁴⁷ at 1×10^{12} - 10^{13} and higher surface coverages. In addition, the morphology of ionic layers deposited on surfaces may be characterized using atomic force microscopy (AFM) and scanning electron microscopy (SEM).^{10,98,99} The morphology and reactivity may also be probed by grazing incidence small-angle X-ray scattering (GI-SAXS) and temperature programmed reaction (TPR).¹⁵ Furthermore, the electronic properties of soft-landed ions and clusters have been investigated using X-ray photoelectron spectroscopy (XPS),⁶⁵ ultraviolet photoelectron spectroscopy (UPS),¹⁰⁰ and scanning tunneling spectroscopy (STS).¹⁰¹ have enabled the structural characterization of soft-landed layers using NMR and XRD.⁶ High-coverage deposition is also advantageous for studying the electrochemical properties of soft-landed ions. Both *ex situ* rotating disc electrode measurements^{102,103} and *in situ* analysis using an ionic-liquid-based solid-state membrane electrochemical cell have been used to study the electrochemical properties of interest to applications in electrocatalysis, energy storage, and energy production.¹⁹

1.5 References

- (1) Thomson, J. J. XXVI. Rays of positive electricity. *The London, Edinburgh, and Dublin Philosophical Magazine and Journal of Science* **1911**, *21*, 225-249.
- (2) Laskin, J.; Johnson, G. E.; Warneke, J.; Prabhakaran, V. From Isolated Ions to Multilayer Functional Materials Using Ion Soft-Landing. *Angewandte Chemie International Edition* **2018**, DOI: 10.1002/anie.201712296.
- (3) Cyriac, J.; Pradeep, T.; Kang, H.; Souda, R.; Cooks, R. Low-energy ionic collisions at molecular solids. *Chem. Rev.* **2012**, *112*, 5356-5411.
- (4) Verbeck, G.; Hoffmann, W.; Walton, B. Soft-landing preparative mass spectrometry. *Analyst* **2012**, *137*, 4393-4407.
- (5) Rauschenbach, S.; Stadler, F. L.; Lunedei, E.; Malinowski, N.; Koltsov, S.; Costantini, G.; Kern, K. Electrospray ion beam deposition of clusters and biomolecules. *small* **2006**, *2*, 540-547.
- (6) Johnson, G. E.; Gunaratne, D.; Laskin, J. Soft-and reactive landing of ions onto surfaces: Concepts and applications. *Mass Spectrom. Rev.* **2016**, *35*, 439-479.
- (7) Johnson, G. E.; Hu, Q.; Laskin, J. Soft Landing of Complex Molecules on Surfaces. *Ann. Rev. Anal. Chem.* **2011**, *4*, 83-104.
- (8) Su, P.; Hu, H.; Warneke, J.; Belov, M. E.; Anderson, G. A.; Laskin, J. Design and Performance of a Dual-Polarity Instrument for Ion Soft Landing. *Anal. Chem.* **2019**, *91*, 5904-5912.
- (9) Gunaratne, K. D. D.; Prabhakaran, V.; Ibrahim, Y. M.; Norheim, R. V.; Johnson, G. E.; Laskin, J. Design and performance of a high-flux electrospray ionization source for ion soft landing. *Analyst* **2015**, *140*, 2957-2963.
- (10) Warneke, J.; McBriarty, M. E.; Riechers, S. L.; China, S.; Engelhard, M. H.; Aprà, E.; Young, R. P.; Washton, N. M.; Jenne, C.; Johnson, G. E. Self-organizing layers from complex molecular anions. *Nat. Commun.* **2018**, *9*, 1-10.
- (11) Warneke, J.; McBriarty, M. E.; Riechers, S. L.; China, S.; Engelhard, M. H.; Aprà, E.; Young, R. P.; Washton, N. M.; Jenne, C.; Johnson, G. E.; Laskin, J. Self-organizing layers from complex molecular anions. *Nat. Commun.* **2018**, *9*, 1889.
- (12) Laskin, J.; Johnson, G. E.; Warneke, J.; Prabhakaran, V. From Isolated Ions to Multilayer Functional Materials Using Ion Soft Landing. *Angew. Chem. Int. Ed.* **2018**, *57*, 16270-16284.
- (13) Zachary, A. M.; Bolotin, I. L.; Asunskis, D. J.; Wroble, A. T.; Hanley, L. Cluster beam deposition of lead sulfide nanocrystals into organic matrices. *ACS applied materials & interfaces* **2009**, *1*, 1770-1777.

- (14) Kaden, W. E.; Wu, T.; Kunkel, W. A.; Anderson, S. L. Electronic structure controls reactivity of size-selected Pd clusters adsorbed on TiO₂ surfaces. *Science* **2009**, *326*, 826-829.
- (15) Tyo, E. C.; Yin, C.; Di Vece, M.; Qian, Q.; Kwon, G.; Lee, S.; Lee, B.; DeBartolo, J. E.; Seifert, S. n.; Winans, R. E. Oxidative dehydrogenation of cyclohexane on cobalt oxide (Co₃O₄) nanoparticles: the effect of particle size on activity and selectivity. *ACS Catal.* **2012**, *2*, 2409-2423.
- (16) Cyriac, J.; Wleklinski, M.; Li, G.; Gao, L.; Cooks, R. G. In situ Raman spectroscopy of surfaces modified by ion soft landing. *Analyst* **2012**, *137*, 1363-1369.
- (17) Nagaoka, S.; Matsumoto, T.; Okada, E.; Mitsui, M.; Nakajima, A. Room-temperature isolation of V (benzene)₂ sandwich clusters via soft-landing into n-alkanethiol self-assembled monolayers. *J. Phys. Chem. B* **2006**, *110*, 16008-16017.
- (18) Wang, P.; Hadjar, O.; Laskin, J. Covalent Immobilization of Peptides on Self-Assembled Monolayer Surfaces Using Soft-Landing of Mass-Selected Ions. *J. Am. Chem. Soc.* **2007**, *129*, 8682-8683.
- (19) Prabhakaran, V.; Johnson, G. E.; Wang, B.; Laskin, J. In situ solid-state electrochemistry of mass-selected ions at well-defined electrode–electrolyte interfaces. *Proc. Natl. Acad. Sci.* **2016**, *113*, 13324-13329.
- (20) Su, P.; Prabhakaran, V.; Johnson, G. E.; Laskin, J. In Situ Infrared Spectroelectrochemistry for Understanding Structural Transformations of Precisely Defined Ions at Electrochemical Interfaces. *Anal. Chem.* **2018**, *90*, 10935-10942.
- (21) Su, P.; Hu, H.; Unsihuay, D.; Zhang, D.; Dainese, T.; Diaz, R. E.; Lee, J.; Gunaratne, D. K.; Wang, H.; Maran, F.; Mei, J.; Laskin, J. Preparative Mass Spectrometry Using a Rotating-Wall Mass Analyzer. *Angew. Chem. Int. Ed.* **2020**, *59*, 7711-7716.
- (22) Vats, N.; Rauschenbach, S.; Sigle, W.; Sen, S.; Abb, S.; Portz, A.; Dürr, M.; Burghard, M.; van Aken, P.; Kern, K. Electron microscopy of polyoxometalate ions on graphene by electrospray ion beam deposition. *Nanoscale* **2018**, *10*, 4952-4961.
- (23) Peng, W.-P.; Goodwin, M. P.; Nie, Z.; Volný, M.; Ouyang, Z.; Cooks, R. G. Ion Soft Landing Using a Rectilinear Ion Trap Mass Spectrometer. *Anal. Chem.* **2008**, *80*, 6640-6649.
- (24) Johnson, G. E.; Gunaratne, D.; Laskin, J. Soft- and reactive landing of ions onto surfaces: Concepts and applications. *Mass Spectrom. Rev.* **2016**, *35*, 439-479.
- (25) Grill, V.; Shen, J.; Evans, C.; Cooks, R. G. Collisions of ions with surfaces at chemically relevant energies: instrumentation and phenomena. *Rev. Sci. Instrum.* **2001**, *72*, 3149-3179.
- (26) Laskin, J.; Wang, P.; Hadjar, O. Soft-landing of peptide ions onto self-assembled monolayer surfaces: an overview. *PCCP* **2008**, *10*, 1079-1090.

- (27) Wysocki, V. H.; Joyce, K. E.; Jones, C. M.; Beardsley, R. L. Surface-induced dissociation of small molecules, peptides, and non-covalent protein complexes. *J. Am. Soc. Mass. Spectrom.* **2011**, *19*, 190-208.
- (28) Dongré, A. R.; Jones, J. L.; Somogyi, Á.; Wysocki, V. H. Influence of peptide composition, gas-phase basicity, and chemical modification on fragmentation efficiency: evidence for the mobile proton model. *J. Am. Chem. Soc.* **1996**, *118*, 8365-8374.
- (29) Cooks, R. G.; Ast, T.; Mabud, M. A. Collisions of polyatomic ions with surfaces. *Int. J. Mass Spectrom. Ion Processes* **1990**, *100*, 209-265.
- (30) Cooks, R.; Ast, T.; Pradeep, T.; Wysocki, V. Reactions of ions with organic surfaces. *Acc. Chem. Res.* **1994**, *27*, 316-323.
- (31) Johnson, G. E.; Laskin, J. Preparation of Surface Organometallic Catalysts by Gas-Phase Ligand Stripping and Reactive Landing of Mass-Selected Ions. *Chemistry – A European Journal* **2010**, *16*, 14433-14438.
- (32) Wang, P.; Laskin, J. Helical peptide arrays on self-assembled monolayer surfaces through soft and reactive landing of mass-selected ions. *Angew. Chem. Int. Ed.* **2008**, *47*, 6678-6680.
- (33) Ast, T.; Riederer Jr, D.; Miller, S.; Morris, M.; Cooks, R. Collisions of fluorocarbon ions at solid surfaces: Electronic excitation, surface-induced dissociation and chemical sputtering. *Org. Mass Spectrom.* **1993**, *28*, 1021-1033.
- (34) Xirouchaki, C.; Palmer, R. Pinning and implantation of size-selected metal clusters: a topical review. *Vacuum* **2002**, *66*, 167-173.
- (35) Winograd, N.; Garrison, B. J. Biological cluster mass spectrometry. *Annual review of physical chemistry* **2010**, *61*, 305-322.
- (36) Gologan, B.; Green, J. R.; Alvarez, J.; Laskin, J.; Cooks, R. G. Ion/surface reactions and ion soft-landing. *PCCP* **2005**, *7*, 1490-1500.
- (37) Morris, M.; Riederer Jr, D.; Winger, B.; Cooks, R.; Ast, T.; Chidsey, C. Ion/surface collisions at functionalized self-assembled monolayer surfaces. *Int. J. Mass Spectrom. Ion Processes* **1992**, *122*, 181-217.
- (38) Cohen, S. R.; Naaman, R.; Sagiv, J. Translational energy transfer from molecules and atoms to adsorbed organic monolayers of long-chain amphiphiles. *Phys. Rev. Lett.* **1987**, *58*, 1208.
- (39) Laskin, J.; Futrell, J. H. Activation of large ions in FT-ICR mass spectrometry. *Mass Spectrom. Rev.* **2005**, *24*, 135-167.
- (40) Laskin, J.; Hu, Q. Reactive Landing of Gramicidin S and Ubiquitin Ions onto Activated Self-Assembled Monolayer Surfaces. *J. Am. Soc. Mass. Spectrom.* **2017**, *28*, 1304-1312.

- (41) Wang, P.; Laskin, J. Helical Peptide Arrays on Self-Assembled Monolayer Surfaces through Soft and Reactive Landing of Mass-Selected Ions. *Angew. Chem. Int. Ed.* **2008**, *47*, 6678-6680.
- (42) Miller, S.; Luo, H.; Pachuta, S.; Cooks, R. Soft-landing of polyatomic ions at fluorinated self-assembled monolayer surfaces. *Science* **1997**, *275*, 1447-1450.
- (43) Luo, H.; Miller, S. A.; Cooks, R. G.; Pachuta, S. J. Soft landing of polyatomic ions for selective modification of fluorinated self-assembled monolayer surfaces. *Int. J. Mass Spectrom. Ion Processes* **1998**, *174*, 193-217.
- (44) Bittner, A. Clusters on soft matter surfaces. *Surf. Sci. Rep.* **2006**, *61*, 383-428.
- (45) Heiz, U.; Bullock, E. Fundamental aspects of catalysis on supported metal clusters. *J. Mater. Chem.* **2004**, *14*, 564-577.
- (46) Miller, S. A.; Luo, H.; Pachuta, S. J.; Cooks, R. G. Soft-Landing of Polyatomic Ions at Fluorinated Self-Assembled Monolayer Surfaces. *Science* **1997**, *275*, 1447-1450.
- (47) Gunaratne, K. D. D.; Prabhakaran, V.; Andersen, A.; Johnson, G. E.; Laskin, J. Charge retention of soft-landed phosphotungstate Keggin anions on self-assembled monolayers. *PCCP* **2016**, *18*, 9021-9028.
- (48) Franchetti, V.; Solka, B. H.; Baitinger, W. E.; Amy, J. W.; Cooks, R. G. Soft landing of ions as a means of surface modification. *Int. J. Mass Spectrom. Ion Phys.* **1977**, *23*, 29-35.
- (49) Gologan, B.; Takáts, Z.; Alvarez, J.; Wiseman, J. M.; Talaty, N.; Ouyang, Z.; Cooks, R. G. Ion soft-landing into liquids: Protein identification, separation, and purification with retention of biological activity. *J. Am. Soc. Mass. Spectrom.* **2004**, *15*, 1874-1884.
- (50) Pradeep, T.; Feng, B.; Ast, T.; Patrick, J. S.; Cooks, R. G.; Pachuta, S. J. Chemical modification of fluorinated self-assembled monolayer surfaces by low energy reactive ion bombardment. *J. Am. Soc. Mass. Spectrom.* **1995**, *6*, 187-194.
- (51) Wijesundara, M. B. J.; Fuoco, E.; Hanley, L. Preparation of Chemical Gradient Surfaces by Hyperthermal Polyatomic Ion Deposition: A New Method for Combinatorial Materials Science. *Langmuir* **2001**, *17*, 5721-5726.
- (52) Feng, B.; Wunschel, D. S.; Masselon, C. D.; Pasa-Tolic, L.; Smith, R. D. Retrieval of DNA using soft-landing after mass analysis by ESI-FTICR for enzymatic manipulation. *J. Am. Chem. Soc.* **1999**, *121*, 8961-8962.
- (53) Ouyang, Z.; Takáts, Z.; Blake, T. A.; Gologan, B.; Guymon, A. J.; Wiseman, J. M.; Oliver, J. C.; Davisson, V. J.; Cooks, R. G. Preparing Protein Microarrays by Soft-Landing of Mass-Selected Ions. *Science* **2003**, *301*, 1351-1354.
- (54) Hauptmann, N.; Hamann, C.; Tang, H.; Berndt, R. Soft-landing electrospray deposition of the ruthenium dye N3 on Au (111). *J. Phys. Chem. C* **2013**, *117*, 9734-9738.

- (55) Volný, M.; Tureček, F. High efficiency in soft landing of biomolecular ions on a plasma-treated metal surface: are double-digit yields possible? *J. Mass Spectrom.* **2006**, *41*, 124-126.
- (56) Cheng, H.-P.; Landman, U. Controlled deposition, soft landing, and glass formation in nanocluster-surface collisions. *Science* **1993**, *260*, 1304-1307.
- (57) Barnes, M. C.; Kumar, S.; Green, L.; Hwang, N.-M.; Gerson, A. R. The mechanism of low temperature deposition of crystalline anatase by reactive DC magnetron sputtering. *Surf. Coat. Technol.* **2005**, *190*, 321-330.
- (58) Pratontep, S.; Carroll, S.; Xirouchaki, C.; Streun, M.; Palmer, R. Size-selected cluster beam source based on radio frequency magnetron plasma sputtering and gas condensation. *Rev. Sci. Instrum.* **2005**, *76*, 045103.
- (59) Tanemura, S.; Miao, L.; Wunderlich, W.; Tanemura, M.; Mori, Y.; Toh, S.; Kaneko, K. Fabrication and characterization of anatase/rutile-TiO₂ thin films by magnetron sputtering: a review. *Science and Technology of Advanced Materials* **2005**, *6*, 11-17.
- (60) Navamathavan, R.; Yang, E.-J.; Lim, J.-H.; Hwang, D.-K.; Oh, J.-Y.; Yang, J.-H.; Jang, J.-H.; Park, S.-J. Effects of electrical bias stress on the performance of ZnO-based TFTs fabricated by RF magnetron sputtering. *J. Electrochem. Soc.* **2006**, *153*, G385.
- (61) Hartmann, H.; Popok, V.; Barke, I.; von Oeynhausen, V.; Meiwes-Broer, K.-H. Design and capabilities of an experimental setup based on magnetron sputtering for formation and deposition of size-selected metal clusters on ultra-clean surfaces. *Rev. Sci. Instrum.* **2012**, *83*, 073304.
- (62) Honea, E.; Ogura, A.; Peale, D.; Felix, C.; Murray, C.; Raghavachari, K.; Sprenger, W.; Jarrold, M.; Brown, W. Structures and coalescence behavior of size-selected silicon nanoclusters studied by surface-plasmon-polariton enhanced Raman spectroscopy. *J. Chem. Phys.* **1999**, *110*, 12161-12172.
- (63) Messerli, S.; Schintke, S.; Morgenstern, K.; Sanchez, A.; Heiz, U.; Schneider, W.-D. Imaging size-selected silicon clusters with a low-temperature scanning tunneling microscope. *Surface science* **2000**, *465*, 331-338.
- (64) Pauwels, S.; Boucart, N.; Dierckx, B.; Van Vlierberghe, P. In *Tilte2000*; International Society for Optics and Photonics.
- (65) Kaden, W. E.; Wu, T.; Kunkel, W. A.; Anderson, S. L. Electronic Structure Controls Reactivity of Size-Selected Pd Clusters Adsorbed on TiO₂ Surfaces. *Science* **2009**, *326*, 826-829.
- (66) Wepasnick, K. A.; Smith, B. A.; Bitter, J. L.; Fairbrother, D. H. Chemical and structural characterization of carbon nanotube surfaces. *Analytical and bioanalytical chemistry* **2010**, *396*, 1003-1014.
- (67) Fenn, J. B.; Mann, M.; Meng, C. K.; Wong, S. F.; Whitehouse, C. M. Electrospray ionization—principles and practice. *Mass Spectrom. Rev.* **1990**, *9*, 37-70.

- (68) Fenn, J. B.; Mann, M.; Meng, C. K.; Wong, S. F.; Whitehouse, C. M. Electrospray ionization for mass spectrometry of large biomolecules. *Science* **1989**, *246*, 64-71.
- (69) Bernier, L.; Taesch, M.; Rauschenbach, S.; Reiss, J. Transfer conditions and transmission bias in capillaries of vacuum interfaces. *Int. J. Mass Spectrom.* **2020**, *447*, 116239.
- (70) Pauly, M.; Sroka, M.; Reiss, J.; Rinke, G.; Albarghash, A.; Vogelgesang, R.; Hahne, H.; Kuster, B.; Sesterhenn, J.; Kern, K.; Rauschenbach, S. A hydrodynamically optimized nano-electrospray ionization source and vacuum interface. *Analyst* **2014**, *139*, 1856-1867.
- (71) Cai, R.; Cao, L.; Griffin, R.; Chansai, S.; Hardacre, C.; Palmer, R. E. Scale-up of cluster beam deposition to the gram scale with the matrix assembly cluster source for heterogeneous catalysis (propylene combustion). *AIP Adv.* **2020**, *10*, 025314.
- (72) Palmer, R. E.; Cao, L.; Yin, F. Note: Proof of principle of a new type of cluster beam source with potential for scale-up. *Rev. Sci. Instrum.* **2016**, *87*, 046103.
- (73) Martínez, L.; Díaz, M.; Román, E.; Ruano, M.; Llamosa P, D.; Huttel, Y. Generation of nanoparticles with adjustable size and controlled stoichiometry: recent advances. *Langmuir* **2012**, *28*, 11241-11249.
- (74) Miller, P. E.; Denton, M. B. The quadrupole mass filter: basic operating concepts. *J. Chem. Educ.* **1986**, *63*, 617.
- (75) Paul, W.; Steinwedel, H. A new mass spectrometer without a magnetic field. *Zeitschrift fuer Naturforschung (West Germany) Divided into Z. Naturforsch., A, and Z. Naturforsch., B: Anorg. Chem., Org. Chem., Biochem., Biophys.* **1953**, *8*.
- (76) Issendorff, B. v.; Palmer, R. E. A new high transmission infinite range mass selector for cluster and nanoparticle beams. *Rev. Sci. Instrum.* **1999**, *70*, 4497-4501.
- (77) Roy, C.; Sebok, B.; Scott, S. B.; Fiordaliso, E. M.; Sørensen, J. E.; Bodin, A.; Trimarco, D. B.; Damsgaard, C. D.; Vesborg, P. C. K.; Hansen, O.; Stephens, I. E. L.; Kibsgaard, J.; Chorkendorff, I. Impact of nanoparticle size and lattice oxygen on water oxidation on NiFeO_xHy. *Nat. Catal.* **2018**, *1*, 820-829.
- (78) Mayer, P. S.; Tureček, F.; Lee, H.-N.; Scheidemann, A. A.; Olney, T. N.; Schumacher, F.; Štřop, P.; Smrčina, M.; Pátek, M.; Schirlin, D. Preparative Separation of Mixtures by Mass Spectrometry. *Anal. Chem.* **2005**, *77*, 4378-4384.
- (79) Enke, C. G.; Ray, S. J.; Graham, A. W.; Dennis, E. A.; Hieftje, G. M.; Carado, A. J.; Barinaga, C. J.; Koppelaar, D. W. Distance-of-Flight Mass Spectrometry: A New Paradigm for Mass Separation and Detection. *Ann. Rev. Anal. Chem.* **2012**, *5*, 487-504.
- (80) Badu-Tawiah, A. K.; Wu, C.; Cooks, R. G. Ambient Ion Soft Landing. *Anal. Chem.* **2011**, *83*, 2648-2654.

- (81) Li, A.; Baird, Z.; Bag, S.; Sarkar, D.; Prabhath, A.; Pradeep, T.; Cooks, R. G. Using Ambient Ion Beams to Write Nanostructured Patterns for Surface Enhanced Raman Spectroscopy. *Angew. Chem. Int. Ed.* **2014**, *53*, 12528-12531.
- (82) Shen, J.; Grill, V.; Evans, C.; Cooks, R. G. Chemical modification of fluorinated self-assembled monolayer surfaces using low-energy ion beams for halogen and pseudohalogen transfer. *J. Mass Spectrom.* **1999**, *34*, 354-363.
- (83) Wade, N.; Pradeep, T.; Shen, J.; Cooks, R. G. Covalent chemical modification of self-assembled fluorocarbon monolayers by low-energy CH_2Br_2^+ ions: a combined ion/surface scattering and X-ray photoelectron spectroscopic investigation. *Rapid Communications in Mass Spectrometry* **1999**, *13*, 986-993.
- (84) Takáts, Z.; Wiseman, J. M.; Gologan, B.; Cooks, R. G. Mass Spectrometry Sampling Under Ambient Conditions with Desorption Electrospray Ionization. *Science* **2004**, *306*, 471-473.
- (85) Peng, I. X.; Ogorzalek Loo, R. R.; Shiea, J.; Loo, J. A. Reactive-Electrospray-Assisted Laser Desorption/Ionization for Characterization of Peptides and Proteins. *Anal. Chem.* **2008**, *80*, 6995-7003.
- (86) Denault, J. W.; Evans, C.; Koch, K. J.; Cooks, R. G. Surface modification using a commercial triple quadrupole mass spectrometer. *Anal. Chem.* **2000**, *72*, 5798-5803.
- (87) Alvarez, J.; Cooks, R. G.; Barlow, S. E.; Gaspar, D. J.; Futrell, J. H.; Laskin, J. Preparation and in situ characterization of surfaces using soft landing in a Fourier transform ion cyclotron resonance mass spectrometer. *Anal. Chem.* **2005**, *77*, 3452-3460.
- (88) Hadjar, O.; Wang, P.; Futrell, J. H.; Dessiaterik, Y.; Zhu, Z.; Cowin, J. P.; Iedema, M. J.; Laskin, J. Design and performance of an instrument for soft landing of biomolecular ions on surfaces. *Anal. Chem.* **2007**, *79*, 6566-6574.
- (89) Johnson, G. E.; Lysonski, M.; Laskin, J. In situ reactivity and TOF-SIMS analysis of surfaces prepared by soft and reactive landing of mass-selected ions. *Anal. Chem.* **2010**, *82*, 5718-5727.
- (90) Nie, Z.; Li, G.; Goodwin, M. P.; Gao, L.; Cyriac, J.; Cooks, R. G. In situ SIMS analysis and reactions of surfaces prepared by soft landing of mass-selected cations and anions using an ion trap mass spectrometer. *J. Am. Soc. Mass. Spectrom.* **2009**, *20*, 949-956.
- (91) Hadjar, O.; Futrell, J. H.; Laskin, J. First Observation of Charge Reduction and Desorption Kinetics of Multiply Protonated Peptides Soft Landed onto Self-Assembled Monolayer Surfaces. *J. Phys. Chem. C* **2007**, *111*, 18220-18225.
- (92) Johnson, G. E.; Priest, T.; Laskin, J. Coverage-Dependent Charge Reduction of Cationic Gold Clusters on Surfaces Prepared Using Soft Landing of Mass-Selected Ions. *J. Phys. Chem. C* **2012**, *116*, 24977-24986.

- (93) Tyo, E. C.; Vajda, S. Catalysis by clusters with precise numbers of atoms. *Nat. Nanotechnol.* **2015**, *10*, 577-588.
- (94) Deng, Z.; Thontasen, N.; Malinowski, N.; Rinke, G.; Harnau, L.; Rauschenbach, S.; Kern, K. A Close Look at Proteins: Submolecular Resolution of Two- and Three-Dimensionally Folded Cytochrome c at Surfaces. *Nano Lett.* **2012**, *12*, 2452-2458.
- (95) Wu, X.; Delbianco, M.; Anggara, K.; Michnowicz, T.; Pardo-Vargas, A.; Bharate, P.; Sen, S.; Pristl, M.; Rauschenbach, S.; Schlickum, U.; Abb, S.; Seeberger, P. H.; Kern, K. Imaging single glycans. *Nature* **2020**, *582*, 375-378.
- (96) Volný, M.; Sengupta, A.; Wilson, C. B.; Swanson, B. D.; Davis, E. J.; Tureček, F. Surface-enhanced Raman spectroscopy of soft-landed polyatomic ions and molecules. *Anal. Chem.* **2007**, *79*, 4543-4551.
- (97) Hu, Q.; Laskin, J. Secondary Structures of Ubiquitin Ions Soft-Landed onto Self-Assembled Monolayer Surfaces. *J. Phys. Chem. B* **2016**, *120*, 4927-4936.
- (98) Goldby, I.; Kuipers, L.; Von Issendorff, B.; Palmer, R. Diffusion and aggregation of size-selected silver clusters on a graphite surface. *Appl. Phys. Lett.* **1996**, *69*, 2819-2821.
- (99) Davila, S. J.; Birdwell, D. O.; Verbeck, G. F. Drift tube soft-landing for the production and characterization of materials: Applied to Cu clusters. *Rev. Sci. Instrum.* **2010**, *81*, 034104.
- (100) Räder, H. J.; Rouhanipour, A.; Talarico, A. M.; Palermo, V.; Samorì, P.; Müllen, K. Processing of giant graphene molecules by soft-landing mass spectrometry. *Nature materials* **2006**, *5*, 276-280.
- (101) Bettac, A.; Köller, L.; Rank, V.; Meiwes-Broer, K. Scanning tunneling spectroscopy on deposited platinum clusters. *Surface science* **1998**, *402*, 475-479.
- (102) Pepi, F.; Ricci, A.; Tata, A.; Favero, G.; Frasconi, M.; Delle Noci, S.; Mazzei, F. Soft landed protein voltammetry. *Chem. Commun.* **2007**, 3494-3496.
- (103) Proch, S.; Wirth, M.; White, H. S.; Anderson, S. L. Strong effects of cluster size and air exposure on oxygen reduction and carbon oxidation electrocatalysis by size-selected Pt_n (n ≤ 11) on glassy carbon electrodes. *J. Am. Chem. Soc.* **2013**, *135*, 3073-3086.

CHAPTER 2. DESIGN AND PERFORMANCE OF A DUAL POLARITY INSTRUMENT FOR ION SOFT LANDING

2.1 Introduction

Soft landing of mass-selected ions refers to the process of depositing intact polyatomic ions onto substrates with precisely controlled composition, charge state, and kinetic energy.¹⁻⁶ By eliminating solvent molecules, impurities, and counterions, ion soft landing provides an opportunity to explore the properties of well-defined ionic species on solid and liquid supports, which in turn facilitates molecular level understanding of the structure and reactivity of isolated ions and their assemblies in the condensed-phase. The ability to control the size, shape, and position of the ion beam makes ion soft landing a promising tool for surface modification and preparation of functional materials of interest to both fundamental investigations and practical applications in chemistry, physics, materials science, and biology.⁷⁻¹⁰ For example, soft landing of mass-selected ions has been used to examine peptide and protein conformations¹¹⁻¹⁴ and redox-activity¹⁵ on surfaces, prepare protein and peptide arrays,^{16,17} deposit molecular magnets,¹⁸ organometallic complexes¹⁹⁻²² and catalytically active nanoclusters onto surfaces,^{20,23-27} explore covalent immobilization of biomolecules^{28,29} and modification of polymer films,³⁰ self-assembled monolayers (SAMs),³¹ and carbon-based materials such as graphene³² and carbon nanotubes.³³

Starting from the first system built by Cooks and co-workers in 1977,³⁴ the applications of ion soft landing have been tightly linked to the development of custom-designed instrumentation. In particular, ion soft landing has benefited from the development of ionization sources and high transmission ion optics. Electrospray ionization (ESI) is one of the most widely used approaches for continuously generating ions from solution in an ambient environment. Ion currents in the nanoampere range have been obtained by either using a funnel-shaped heated inlet³⁵ or large inner diameter inlet combined with a tandem electrodynamic ion funnel system.³⁶ Comparable ion currents of charged nanoclusters have been obtained using magnetron sputtering combined with gas aggregation.^{37,38} More recently, substantial improvement to milliamp-scale currents were achieved using a Matrix Assembly Cluster Source (MACS), which generates nanoclusters with a tunable mean diameter.^{27,39} Furthermore, the development of ambient and benchtop ion soft landing instruments has significantly advanced the scalability of this technique for applied

research.⁴⁰⁻⁴³ The development of high-flux ion deposition capabilities has established ion soft landing as a promising approach for the rational design of electrical energy storage devices,⁴⁴ preparation of catalytic substrates,^{45,46} and opened up new directions for designing two-dimensional or multilayered three-dimensional ionic assemblies.⁴⁷

High-coverage deposition of ions of one polarity typically examined in these studies, revealed a number of interesting physical and chemical phenomena which have not been observed at low coverages.⁴⁷ Specifically, accumulation of ionic species on conductive surfaces produces charged layers balanced by the image charge on the surface.^{47,48} Although cations readily lose their charge at relatively high coverages,^{49,50} stable anions remain charged⁵¹ even when more than one layer is deposited on the surface. As a result, anion deposition generates charge-imbalanced anionic layers stabilized by strong electrostatic binding of the anions to the surface due to the presence of the induced image charge.⁴⁷ Recently, we have demonstrated that such high coverage layers are further stabilized by co-adsorption of neutral molecules from the background of the vacuum system.⁴⁷ This process produces liquid-like layers which often undergo spontaneous dewetting upon exposure to laboratory air. This self-organization process is controlled by the properties of the anions, co-adsorbed neutral molecules, surface, and environmental conditions. The final morphology of the resulting layer is mainly determined by the weaker interfacial forces as the image charge dissipates over time under ambient conditions. Controlling the degree of charge imbalance in the ionic layer potentially determines the final architecture of the ion assembly. Furthermore, charge balanced layers which may be prepared by co-depositing positive and negative ions, are promising for studying ion-ion interactions on surfaces and enables bottom-up design of novel ion-based materials.

Herein, we describe the design and performance of a first dual-polarity ion soft landing instrument, which may be used to generate both charge-balanced and charge-imbalanced layers. Employing a dual-polarity high-flux ESI source, we demonstrate the utility of this instrument for either sequential layer-by-layer (LBL) deposition of ions of different polarities or almost simultaneous deposition of positive and negative ions through fast switching between polarities. We demonstrate that fast polarity switching deposition of anions and cations may be used to control the structures of these building blocks and tailor their interactions on surfaces. Furthermore, we present the first evidence that weakly coordinating anions may be used to protect protonated

molecules from losing the ionizing protons to the surface. These findings open up unique opportunities for the bottom-up assembly of layered functional materials using ion soft-landing.

2.2 Experimental Section

The newly-designed ion soft landing instrument is shown schematically in Figure 2.1. The instrument is equipped with a high-transmission dual polarity electrospray (ESI) interface (Spectrograph, LLC) composed of two orthogonal injection ESI sources (1), a tandem RF ion funnel system (2, 3), and a bent flatapole ion guide (4). The two ion funnels and the bent flatapole ion guide are housed in three differentially pumped aluminum vacuum chambers. All the electrical components are powered by a custom-designed Modular Intelligent Power Sources (MIPS) system (GAA Custom Engineering, LLC).

2.2.1 Instrumentation

2.2.1.1 Dual Polarity ESI Interface. Ions of both polarities were produced by +/- ESI of 150 μM solutions of selected analytes in methanol. The major ionic species generated using negative and positive ESI of the sodium phosphotungstate tribasic hydrate and tris(2,2'-bipyridyl)dichlororuthenium(II) hexahydrate solutions are $\text{PW}_{12}\text{O}_{40}^{3-}$ and $\text{Ru}(\text{bpy})_3^{2+}$, respectively. Solutions were filled into separate gas-tight syringes (Hamilton Robotics, Reno, NV) and introduced into the ESI source through two fused silica capillaries (Polymicro Technologies, Phoenix, AZ, 100 μm ID, 360 μm OD, 1' length) using two syringe pumps (Cole-Palmer, Vernon Hills, IL) at a typical flow rate of 60 $\mu\text{L h}^{-1}$. Charged microdroplets were produced by applying a ± 3 kV voltage to the syringe needles.

In the dual polarity ESI interface, charged droplets produced by +/- ESI are transferred into the vacuum system through two 100 mm long heated stainless steel inlet tubes (1/16" OD, 0.04" ID) mounted on the opposite sides of the first vacuum chamber. The heated inlets are mounted orthogonally to the instrument axis with one inlet positioned ~5 mm downstream from another one to improve gas dynamics in the chamber. Orthogonal injection of ions has been shown to efficiently decouple ion transfer from gas flow dynamics and eliminate neutral molecules introduced into the vacuum system through the heated inlet.⁵² Two cartridge heaters (Omega Engineering, Inc., Stamford, CT) and thermocouples maintain the inlets at temperatures in the

range of 25-200 °C which are independently optimized to ensure efficient desolvation of the ESI droplets. The vacuum side of the heated capillaries protrude into the first section of the first ion funnel by ~1 mm through two cutouts.

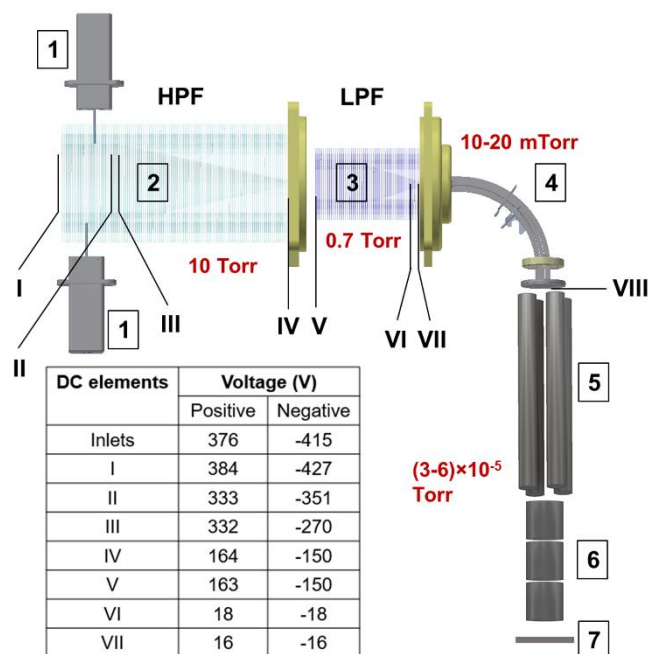


Figure 2.1 Schematic drawing of the dual polarity ion soft landing instrument showing the dual polarity ESI interface (1), high pressure ion funnel (HPF, 2), low pressure ion funnel (LPF, 3), bent flatpole ion guide (4), quadrupole mass filter (5), einzel lens (6) and surface (7). Direct current (DC) voltages on the tandem ion funnel system are shown with Roman numerals: I, HPF repeller in; II, HPF repeller out; III, HPF funnel in; IV, HPF funnel out; V, LPF funnel in; VI, LPF lens; VII, LPF funnel out; VIII, conductance limit. The pressure in each vacuum region is marked in red. Typical DC voltages used for transmission of ions of both polarities in the tandem ion funnel region are shown in the bottom left table.

2.2.1.2 Tandem Ion Funnel System. The tandem ion funnel system composed of two printed circuit board radio frequency (RF) ion funnels is described in detail elsewhere.^{36,52,53} Briefly, a high-pressure ion funnel (HPF) is mounted in a vacuum chamber differentially pumped to 10 Torr by a dry-compression multi-stage Roots vacuum pump (ECODRY 65 plus, 32 cubic feet per minute (cfm), Leybold GmbH, Cologne, Germany). The HPF is composed of a stainless steel repeller plate on top and a stack of 113 ring electrodes. The first 28 electrodes have identical inner diameters (ID) of 50.8 mm (2 inches) while the IDs of the following 85 electrodes decrease linearly from 50.8 mm to 2.5 mm (0.1 inch). The last plate of the HPF acts as a conductance limit

between the first and second vacuum chambers. The total length of the HPF is 5.7". A low-pressure ion funnel (LPF) is mounted in the second vacuum chamber differentially pumped to 0.7 Torr by a second ECODRY 65 plus vacuum pump. The LPF is composed of 96 ring electrodes and has a total length of 4.3". The first 24 ring electrodes have the same ID of 25.4 mm (1 inch) while the IDs of the following 72 ring electrodes decrease linearly from 25.4 mm to 2.3 mm (0.09 inch). An additional square-bracket-shaped electrode (denoted as lens) is inserted between the last two electrodes of the LPF.

Both ion funnels are powered by RF high-Q heads connected to the MIPS system. The resonant frequencies are ~ 740 kHz and ~ 860 kHz and peak-to-peak voltages are ~ 270 V and ~ 135 V for the HPF and LPF, respectively. Separate DC voltages are applied to the entrance and exit plates of each ion funnel and axial DC potential gradients are generated using a series of 0.5 M Ω resistors connected between neighboring electrodes. The DC gradient in the HPF funnel is divided into two regions: a repeller region (the first 24 electrodes) and funnel region (the following 92 electrodes). The voltages applied to the two ESI inlets are slightly lower than the voltage applied to the HPF repeller plate, which improves ion transmission. Typical DC voltages used for transmission of ions of both polarities are shown in Figure 2.1.

2.2.1.3 Bent Flatapole. The third vacuum chamber in the ion soft landing system houses a bent flatapole ion guide (4) described in detail elsewhere.^{54,55} The chamber is pumped down to 10-20 mTorr using a 90 L/s turbomolecular pump (TURBOVAC 90 I, Leybold GmbH, Cologne, Germany). The ECODRY 65 plus used for the second vacuum chamber backs the turbomolecular pump. The 90° bend of the flatapole rods effectively decouples the ion beam from the molecular beam present on the axis of the tandem ion funnel system. The flatapole is powered by a separate high-Q head connected to the MIPS system. The RF waveform applied to the flatapole rods has a frequency of ~ 1.88 MHz and peak-to-peak voltage of ~ 120 V; a typical DC bias of $\pm(15-35)$ V is applied to the flatapole rods for transferring positive and negative ions, respectively. Collisional cooling of ions in the flatapole RF field produces an ion beam focused to less than 2 mm at the flatapole exit.^{52,56} A stainless steel plate with a 2 mm aperture positioned at the end of the flatapole serves as a conductance limit (CL) separating the third and fourth differentially pumped regions of the vacuum system.

2.2.1.4 Soft Landing Chamber. A modular aluminum 6×6×12 inch rectangular chamber (Ideal Vacuum Products, Albuquerque, NM) serves as the fourth differentially pumped vacuum region of the new soft landing instrument. The chamber is sealed using vacuum cube plate flanges equipped with patterned openings for different types of fittings and configured with multiple 1/4"-20 threaded holes for mounting custom components inside the vacuum system. The fourth chamber is differentially pumped to $(3-6) \times 10^{-5}$ Torr by a 350 L/s turbomolecular pump (TURBOVAC 350 I, Leybold GmbH, Cologne, Germany) backed by the ECODRY 65 plus used to pump the second vacuum chamber.

2.2.1.5 Quadrupole Mass Filter. A quadrupole mass filter (5) with 9.5 mm rod diameter (Extrel CMS, Pittsburgh, PA) is mounted inside the soft landing chamber using custom-built aluminum brackets. The entrance plate is placed 2 mm away from the conductance limit. The quadrupole mass filter has an operating frequency of 868 kHz and is powered by an RF amplifier module controlled by MIPS. MIPS provides both the RF and DC voltages necessary to operate the quadrupole in the RF/DC mode.

An einzel lens (6) was constructed using three cylindrical elements (3/4" ID, 0.75" length) and mounted after the exit plate of the quadrupole mass filter for focusing of the ion beam on the deposition surface (7). Ion beam characterization was performed using an IonCCD^{57,58} (OI Analytical, Pelham, AL) position sensitive detector mounted at a variable distance from the einzel lens. The integration times for detection of anionic and cationic beams are 20 and 5 ms, respectively. The shorter integration time used for detecting negative ions is used because of the lower saturation limit of the IonCCD towards anions.⁵⁷ During soft landing experiments, ion current on the surface was measured using a picoammeter (RBD Instruments, Bend, OR) operated at a typical sampling rate of 300 ms.

2.2.1.6 Kinetic Energy Distribution Measurement. The kinetic energy distribution (KED) of the ions exiting the flatpole was measured using a stainless steel plate mounted 5 mm away from the conductance limit. The plate was connected to the picoammeter and biased using one of the DC voltages provided by MIPS. This configuration allows us to apply the retarding voltage (V_r) to the collector plate while measuring the ion current. A uniform electric field close to the plate was created by mounting a stainless steel mesh (part No. 9230T51, McMaster Carr,

Elmhurst, IL) ~2 mm in front of the plate. The mesh was kept at 0 V throughout the experiment. Ion current detected on the plate was measured as a function of V_r . Each data point was acquired by averaging the ion current for 10 s. The integrated retarding potential curve was obtained by plotting the ion current as a function of V_r . KED was obtained by taking a first derivative of the retarding potential plot.⁵⁹

2.2.2 Chemicals

Tris(2,2'-bipyridyl)dichlororuthenium(II) hexahydrate ($\text{Ru}(\text{bpy})_3\text{Cl}_2 \cdot 6\text{H}_2\text{O}$, CAS: 50525-27-4), Neutral Red ($\text{C}_{15}\text{H}_{17}\text{ClN}_4$, CAS: 553-24-2), sodium phosphotungstate tribasic hydrate ($\text{Na}_3[\text{PW}_{12}\text{O}_{40}] \cdot x \text{H}_2\text{O}$, CAS: 12026-98-1), sodium phosphomolybdate hydrate ($\text{Na}_3[\text{PMo}_{12}\text{O}_{40}] \cdot x \text{H}_2\text{O}$, CAS: 1313-30-0) and 1H,1H,2H,2H-perfluorodecanethiol (FSAM, $\text{CF}_3(\text{CF}_2)_7\text{CH}_2\text{CH}_2\text{SH}$, CAS: 34143-74-3) were purchased from Sigma-Aldrich (St. Louis, MO) and were used to demonstrate the instrument performance.

2.2.3 FSAM Surface Preparation

An FSAM on a gold surface was prepared as follows: a 10×10 mm gold coated silicon wafer (100 nm Au layer and 5 nm Ti adhesion layer, Platypus Technologies, Madison, WI) was ultrasonically washed in methanol, cleaned by a UV Ozone cleaner and immersed in a glass scintillation vial containing a 15 mM solution of FSAM in methanol. The monolayer was allowed to assemble for at least 12 h and then ultrasonically washed for 5 min in methanol. The surface was subsequently rinsed with methanol, dried under nitrogen and mounted on the sample holder in the soft landing chamber.

2.2.4 Surface Characterization

Infrared reflection absorption spectroscopy (IRRAS) measurements were performed using a Bruker Tensor II FTIR spectrometer (Bruker Optics, Billerica, MA) equipped with a liquid nitrogen cooled mercury-cadmium-telluride (MCT) detector. Surfaces were mounted onto an 80° reflection unit in the chamber of the spectrometer. IRRAS spectra were acquired at a spectral resolution of 4 cm^{-1} using p-polarized light. Each spectrum was collected by averaging 2000 scans

corresponding to a 5-minute acquisition time. The experimental IRRAS plots were processed using water subtraction and baseline-correction options of the OPUS software.

Visible spectroscopy characterization of on the surfaces was performed using a R600-8-VisNIR reflectance probe connected to a BLK-CXR spectrometer and a SL1 Tungsten-Halogen visible-NIR light source (Stellarnet, Tampa, FL). Visible spectrum of a clean Au-FSAM surface was used as the reference. The spectra were collected using the SpectraWiz software.

Visible spectroscopy characterization of solutions was performed using an QP450-1-XSR optical fiber patch cords connected to USB2000+UV-VIS spectrometer and a DH-2000-DUV-TTL Deuterium Halogen light source (Ocean Optics, Largo, FL). Visible spectrum of methanol was used as the reference. The spectra were collected using the OceanView software.

Extraction ESI-MS analysis of the surface was performed by dissolving the deposited material with 80 μL methanol and analyzed using Q-Exactive HF-X Hybrid Quadrupole-Orbitrap Mass Spectrometer (Thermo Fisher Scientific GmbH, Bremen, Germany). Sample was introduced into the MS inlet by direct infusion from a capillary (50 μm ID, 150 μm OD) at a flow rate of ~ 0.5 $\mu\text{L}/\text{min}$. Typical mass spectrometer conditions on Q-Exactive were as follows: electrospray voltage: ± 3 kV, capillary temperature: 250 $^{\circ}\text{C}$, RF funnel level: 100. Mass spectra were acquired over 150-2000 m/z at 240000 resolution (m/z 400).

2.3 Results and Discussion

2.3.1 Characterizations of Mass-Selected Ion Beams

The new ion soft landing instrument described in this study enables either LBL or fast switching deposition of ions of both polarities, which closely mimics co-deposition. A doubly-charged cation ($\text{Ru}(\text{bpy})_3^{2+}$) and a triply-charged anion ($\text{PW}_{12}\text{O}_{40}^{3-}$, WPOM^{3-}) were used as representative ions to demonstrate the instrument performance. The instrument schematically shown in Figure 2.1 is equipped with two ESI interfaces. Each interface can generate either positive or negative ions independently. We operate the soft landing instrument in two distinct modes. In the first mode, one ESI interface is used to generate positive ions and the other interface generates negative ions. In the second mode, both interfaces are used to generate ions of the same polarity in order to improve the total ion current. We refer to these two modes of operation as

ESI(+/-) and ESI×2, respectively. Typical mass-selected ion currents obtained on surfaces for $\text{Ru}(\text{bpy})_3^{2+}$ and WPOM^{3-} in both modes are listed in Table 2.1. The ESI×2 mode improves the ion current by ~ 75% for both positive and negative ions. Stable ion currents obtained in this study (Figure 2.2) are comparable to previously published data³⁶ and can be further improved using a larger ID heated inlet.

Table 2.1 Typical ion currents of $\text{Ru}(\text{bpy})_3^{2+}$ and WPOM^{3-} obtained on the surface in ESI(+/-) and ESI×2 mode.

Condition	$\text{Ru}(\text{bpy})_3^{2+}$		WPOM^{3-}	
	ESI(+/-)	ESI×2	ESI(+/-)	ESI×2
Current (nA)	+3.1	+5.3	-4.6	-8.2

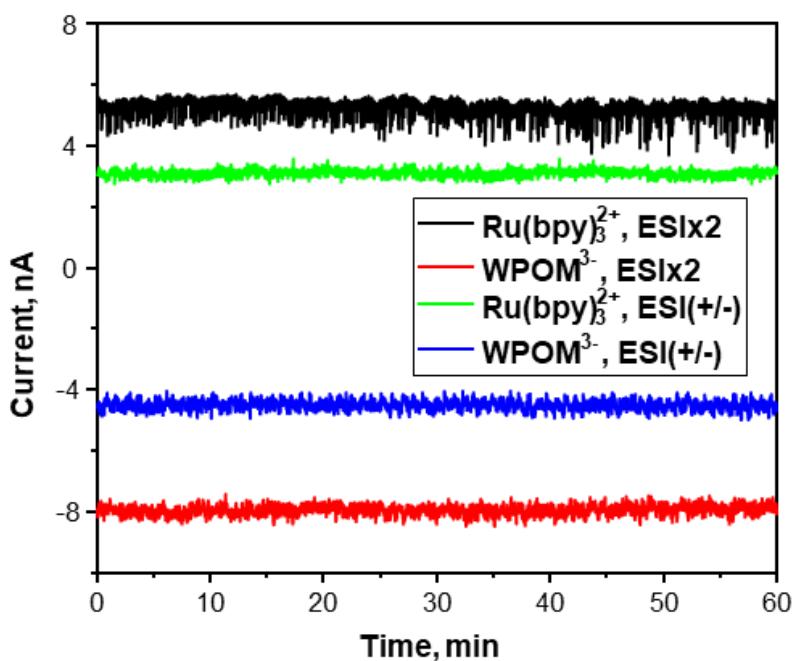


Figure 2.2 Ion current stabilities of mass-selected $\text{Ru}(\text{bpy})_3^{2+}$ and WPOM^{3-} in ESI×2 or ESI(+/-) modes over one hour time period.

The position and shape of the ion beams of both polarities were characterized using a position sensitive IonCCD detector mounted 3 mm away from the einzel lens. The voltages on the einzel lens were optimized to obtain the tightest focusing and best overlap between $\text{Ru}(\text{bpy})_3^{2+}$ and WPOM^{3-} ion beams. The best voltage combinations of the einzel lens were 0 V/120 V/0 V and 0

V/-100 V/0 V for the negative and positive ion beam, respectively. The one-dimensional ion beam profiles of $\text{Ru}(\text{bpy})_3^{2+}$ and WPOM^{3-} obtained under the best focusing conditions are shown in Figure 2.3. The full widths at half maximum (FWHM) are 1.5 and 2.2 mm for the positive and negative ion beam, respectively. The lower signal intensity obtained for the negative ion beam is

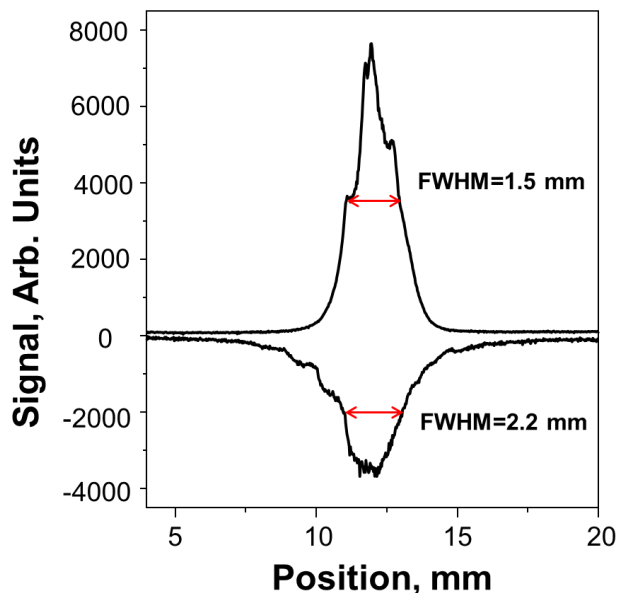


Figure 2.3 One-dimensional ion beam profiles of +3.1 nA $\text{Ru}(\text{bpy})_3^{2+}$ and -4.6 nA WPOM^{3-} obtained using IonCCD.

attributed to the lower anion saturation limit of the IonCCD.⁵⁷ The ion beam profiles shown in Figure 2.3 indicate good alignment and co-location of the positive and negative ion beams, which is important for both LBL and fast polarity switching experiments.

2.3.2 Ion Kinetic Energy Distributions (KED)

Precise control over the kinetic energy of the ions during deposition is an important capability of ion soft-landing. Depending on their kinetic energy, ions undergo different processes upon collisions with surfaces.^{1,60,61} Preserving the structural integrity of the soft-landed ions during the deposition process is critically important to understanding their intrinsic properties on the surface. In this study, we used a retarding potential analysis to determine the KEDs of WPOM^{3-} and $\text{Ru}(\text{bpy})_3^{2+}$ ions exiting the collisional flatapole. Previous studies demonstrated that the most probable kinetic energy, KE_{mp} , of the ions in comparable soft landing systems is determined by

the DC offset applied to the collisional quadrupole. This was attributed to the efficient collisional cooling of ions prior to their transfer into the high vacuum region of the instrument.

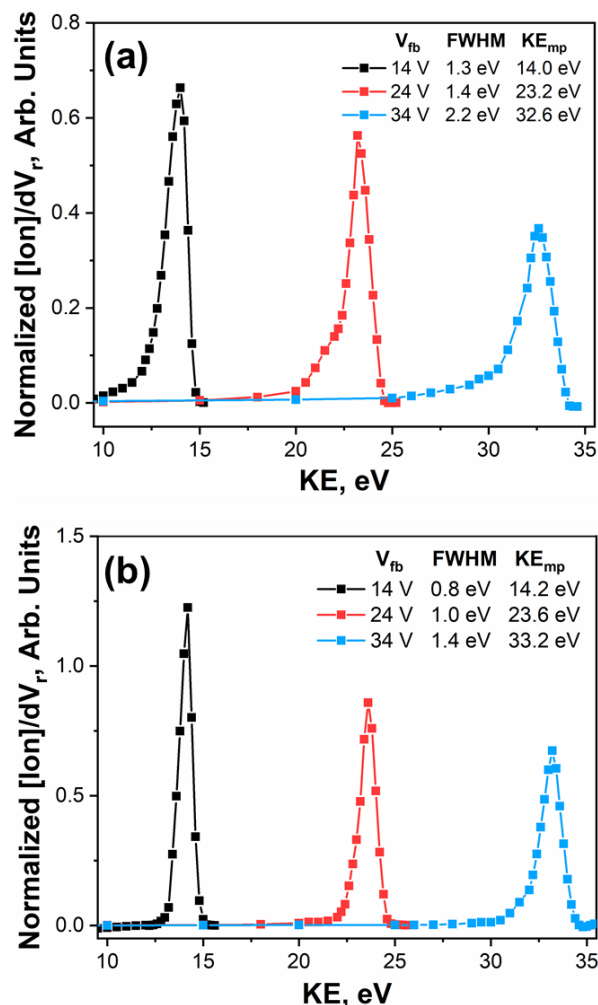


Figure 2.4 KEDs of Ru(bpy)₃²⁺ (a) and WPOM³⁻ (b) obtained at different values of the flatapole bias. The most probable KE (KE_{mp}) and FWHM and are shown for each curve.

KEDs of Ru(bpy)₃²⁺ and WPOM³⁻ acquired at three different values of the flatapole bias are shown in Figure 2.4. The difference between the flatapole bias and the voltage applied to the conductance limit was kept at +1 and -1 V for anions and cations, respectively. The narrowest KEDs for both Ru(bpy)₃²⁺ and WPOM³⁻ with FWHM of 1.3 and 0.8 eV, respectively were obtained at the lowest flatapole bias of ±14 V. At higher flatapole bias voltages, the KEDs become slightly broader. Furthermore, as shown in Figure 2.5, KEDs become broader with larger DC gradients between the flatapole bias and the voltage applied to the conductance limit. The broadening of the

KED could be attributed to ion-molecule collisions with the background gas during ion beam acceleration at the end of the flatapole, which become more important with an increasing in the voltage gradient in this region. These results demonstrate that narrow KEDs may be obtained using a mild voltage gradient at the exit of the flatapole region. In the soft landing experiments described in the following sections the kinetic energy of the ions was controlled by the flatapole bias and the voltage difference at the end of the flatapole region was minimized to ensure good transmission and a narrow KED.

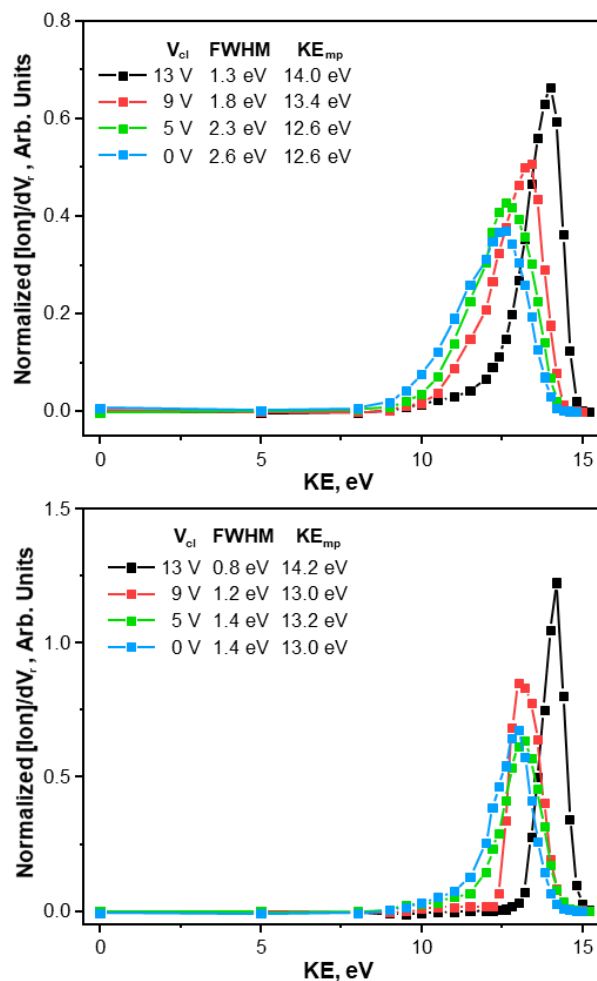


Figure 2.5 Ion kinetic energy distributions (KEDs) of Ru(bpy)₃²⁺ (a) and WPOM³⁻ (b) acquired at different voltages on the conductance limit (V_{cl}). The flatapole bias was kept at +14 V/-14 V for Ru(bpy)₃²⁺ and WPOM³⁻, respectively. The FWHM and most probable kinetic energy (KE_{mp}) of each KED plot was shown on the top left corner of each figure.

2.3.3 Two Modes of Ion Soft Landing Experiments

The flexible design of the dual-polarity ion soft-landing instrument described in this study enables deposition of positive and negative ions on the same surface using two distinct modes of operation. In mode one, ions of each polarity are delivered to the surface in sequential long segments of deposition. This results in an LBL assembly of ions with opposite polarity. In mode two, relatively short ion bursts of different polarities are produced using fast electronic switching between positive and negative ion beams. Mode two mimics ion co-deposition and presents a relatively simple alternative to merging two continuous ion beams of opposite polarity in the same instrument. The fast polarity switching capability of the instrument was evaluated by depositing $\text{PMo}_{12}\text{O}_{40}^{3-}$ (MoPOM^{3-}) and $\text{Ru}(\text{bpy})_3^{2+}$ in small alternating deposition segments, which were initiated by a custom-designed automated MIPS interface. A plot of the ion current as a function of time obtained in four deposition segments of MoPOM^{3-} and $\text{Ru}(\text{bpy})_3^{2+}$ is shown in Figure 2.6(a).

The one-dimensional ion beam profiles acquired over the corresponding time period are shown as a 3D waterfall plot in Figure 2.6(b). Each of the deposition segments lasts for 16 s and the ion current is stable for both ion beams. The length of the deposition segments can be varied independently for positive and negative ion beams, which enables control of the number of ions delivered to the surface in each segment. This capability is important for preparing layers with different amount of charge imbalance.

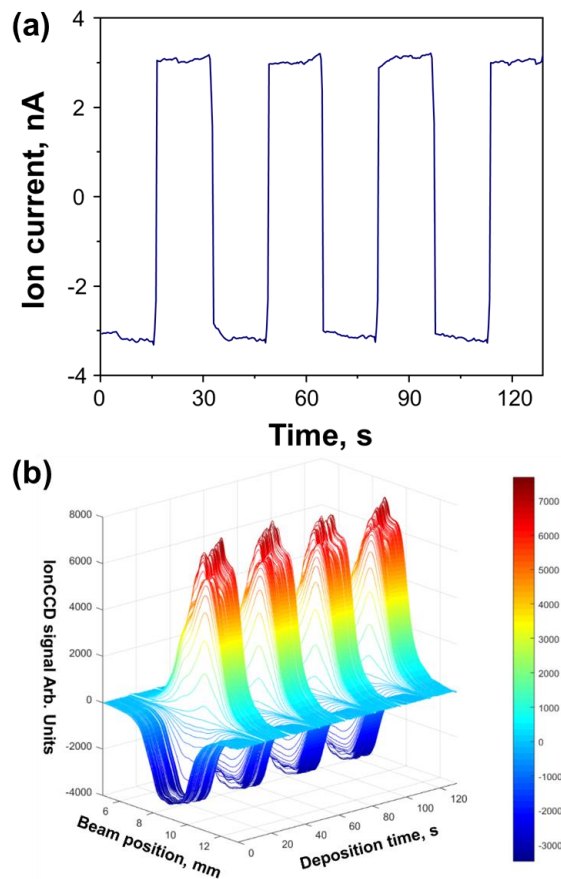


Figure 2.6 KEDs of $\text{Ru}(\text{bpy})_3^{2+}$ (a) and WPOM^{3-} (b) obtained at different values of the flatpole bias. The most probable KE (KE_{mp}) and FWHM and are shown for each curve.

2.3.4 Protecting Soft-Landed Cations Using Weakly-Coordinating Anions

The first model system was designed to test the hypothesis that weakly coordinating stable anions may be used to protect the charge of cations deposited on a surface. Since its initial demonstration,⁶² charge retention by soft-landed ions has attracted considerable attention and been examined using self-assembled monolayer (SAM) surfaces.^{49,63,64} Efficient charge retention by certain soft-landed anions has been attributed to the high energy barrier for electron detachment. In contrast, soft-landed cations more readily lose their charge on the surface. Specifically, charge loss by native cations is attributed to electron tunneling from the surface. Meanwhile, protonated molecules lose one or more of the ionizing protons to the surface. Preserving the charge of cations on surfaces is important for controlling their structures and reactivity.

In this study, we used dianionic chlorinated dodecaborate ($B_{12}Cl_{12}^{2-}$) anions to protect protonated molecules on a surface. The $B_{12}Cl_{12}^{2-}$ anions were selected due to their chemical stability and extremely weak proton affinity, which is attributed to the strong diprotic acidity of the corresponding acid $H_2B_{12}Cl_{12}$.^{65,66} In this experiment, we deposited 1×10^{14} $B_{12}Cl_{12}^{2-}$ and 1×10^{14} protonated Neutral Red (NRH^+) on SAMs of 1H,1H,2H,2H-perfluorodecanethiol (FSAM) using both LBL and fast polarity switching modes. This corresponds to ~ 20 monolayer coverage for each of the deposited species. LBL was achieved by depositing a layer of 1×10^{14} $B_{12}Cl_{12}^{2-}$ followed by a layer of 1×10^{14} NRH^+ . The deposition time was 3 and 2.25 hours for $B_{12}Cl_{12}^{2-}$ and NRH^+ layers, respectively. In contrast, in the fast polarity switching experiment the same overall coverage was achieved by alternating between the $B_{12}Cl_{12}^{2-}$ and NRH^+ ion beams in segments of 10 and 8 s, respectively. The length of the segments was selected to deliver $\sim 1 \times 10^{11}$ ions, which corresponds to $\sim 1\%$ monolayer coverage, over a $2 \text{ mm} \times 2 \text{ mm}$ deposition area. The total coverage corresponds to a 1:1 stoichiometry of anions and cations producing a charge imbalanced layer. A layer of 1×10^{14} NRH^+ on FSAM surface also was prepared for comparison. The surfaces were characterized using visible absorption spectroscopy.

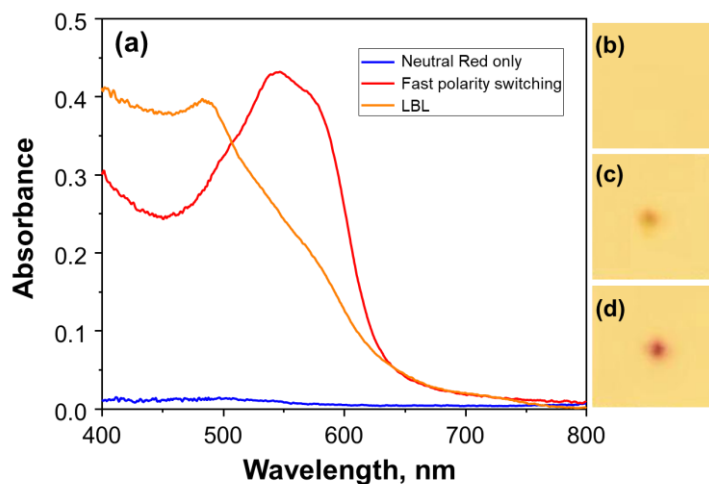


Figure 2.7 (a) Visible absorption spectra of $B_{12}Cl_{12}^{2-}/NRH^+$ surfaces. Optical images of the surfaces are shown on the right: (b) neutral red only, (c) LBL, and (d) fast polarity switching.

The visible spectra and optical images of the three surfaces are shown in Figure 2.7. The optical images demonstrate substantial differences in the visual appearance of the deposited spots. Specifically, almost no color was observed for the 1×10^{14} NRH^+ spot. Meanwhile, the LBL spot

showed an orange color and the spot obtained using fast switching appeared red. Visible spectra obtained for the three surfaces corroborate this observation. Specifically, two absorption bands observed in the visible spectrum of the LBL spot correspond to the combination of orange (major peak at ~480 nm) and red (minor peak at ~600 nm). In contrast, the major absorption peaks observed for the fast polarity switching deposition of $B_{12}Cl_{12}^{2-}/NRH^+$ appear at ~550 and ~600 nm corresponding to the deeper red color. Finally, no substantial absorption of visible light was observed for the NRH^+ spot. These observations may be compared to the known color of neutral red in solution. In particular, neutral red shows a red color in its protonated form and turns yellow when the solution is basic (Figure 2.8). A dropcasted sample was also prepared for comparison (Figure 2.9). We infer that the deeper red color of the deposition spot

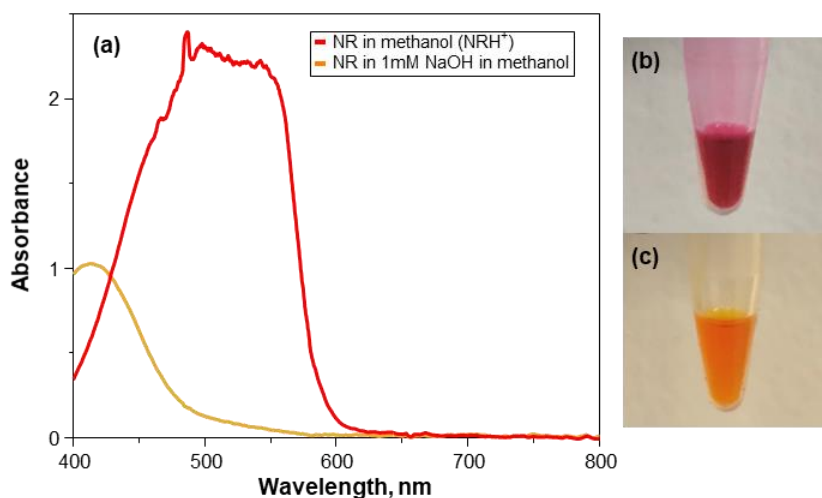


Figure 2.8 (a) Visible spectra of 1 mM Neutral Red in methanol (red) and in a solution of 10 mM NaOH in methanol (yellow). Optical images of the solutions are shown on the right: (b) NR in methanol, (c) NR in 10 mM NaOH in methanol.

prepared using fast polarity switching indicates more efficient charge retention by NRH^+ ions on the surface. Meanwhile, LBL deposition results in less efficient charge retention and neutralization of the neutral red is observed in the absence of the protecting anions. Although the mechanism of charge retention for systems prepared using multilayer deposition are not well-understood, several factors may contribute to the reduced charge retention of the LBL deposition. For example, co-adsorption of neutral molecules with $B_{12}Cl_{12}^{2-}$ anions described in our previous study⁴⁷ may alter

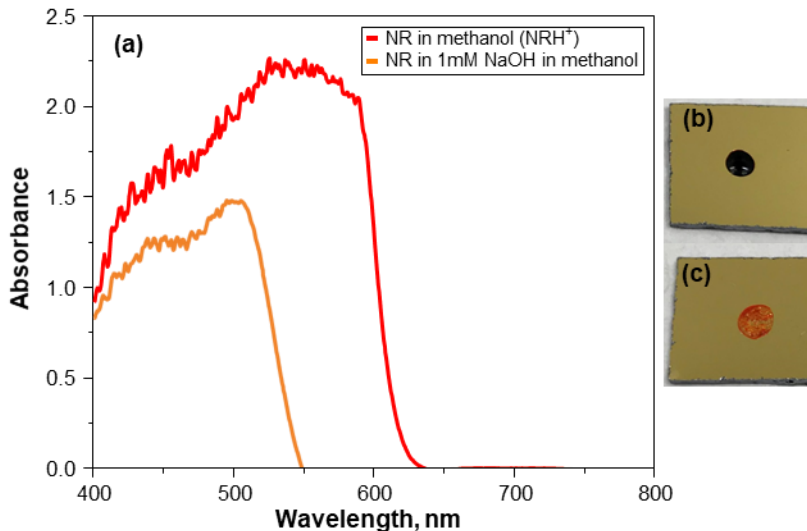


Figure 2.9 (a) Visible spectra of solutions of 1 mM Neutral Red in methanol (red) and in a solution of 10 mM NaOH in methanol (yellow) dropcasted onto FSAM surfaces. Optical images of the dropcasted spots are shown on the right: (b) NR in methanol, (c) NR in 10 mM NaOH in methanol.

the properties of the anionic protecting layer. Furthermore, multiple layers of NRH^+ present in the LBL spot may facilitate charge reduction. To the best of our knowledge, this is the first evidence of using weakly coordinating stable anions for protecting the ionizing protons of soft-landed cations.

2.3.5 Preparation of Charge-Balanced Ionic Layers

In another demonstration experiment, we explored the feasibility of bottom-up construction of charge-balanced ionic layers using dual polarity ion soft landing. We deposited MoPOM^{3-} and $\text{Ru}(\text{bpy})_3^{2+}$ on an FSAM surface using both LBL and fast polarity switching modes. We selected MoPOM^{3-} and $\text{Ru}(\text{bpy})_3^{2+}$ as model systems for negative and positive ions due to their well-understood charge retention properties on FSAM.^{51,67} MoPOM^{3-} and $\text{Ru}(\text{bpy})_3^{2+}$ are widely used in the fabrication of hybrid electrochemiluminescent nanocomposites by solution-phase approaches.^{68,69} MoPOM^{3-} shows distinct IR bands in the wavenumber region of $1100\text{-}800\text{ cm}^{-1}$ and the positions of the bands are strongly affected by the charge state of the anion and the presence of counter cations.^{51,70} Herein, we use the position of the terminal $\text{Mo}=\text{O}_t$ band of MoPOM^{3-} as a reporter of the ionic interactions in different multilayered architectures prepared by dual polarity ion soft landing.

The results of these experiments are summarized in Figure 2.10. Two LBL assemblies of MoPOM³⁻ and Ru(bpy)₃²⁺ ions were prepared in our experiments. These experiments were designed to obtain charge-balanced layers. Surface A was prepared using one-segment deposition of 1×10¹⁴ MoPOM³⁻ anions on FSAM followed by one-segment deposition of 1.5×10¹⁴ Ru(bpy)₃²⁺. Surface B was prepared by switching the order of the deposition, *i.e.*, first depositing 1.5×10¹⁴ Ru(bpy)₃²⁺ cations on FSAM followed by 1×10¹⁴ MoPOM³⁻ anions. Surface C was prepared using fast polarity switching, in which ion deposition was alternated between positive and negative ions to achieve similar total coverage of the ions as that obtained for surfaces A and B by LBL. Each of the short deposition segments delivered 1×10¹¹ MoPOM³⁻ followed by 1.5×10¹¹ Ru(bpy)₃²⁺ to the surface. For comparison, we prepared two FSAM surfaces containing the corresponding ions of one polarity, *i.e.*, 1×10¹⁴ MoPOM³⁻ (Surface D) and 1.5×10¹⁴ Ru(bpy)₃²⁺ (Surface E).

Ex situ infrared reflection absorption spectroscopy (IRRAS) of the surfaces was performed immediately after ion deposition. IRRAS spectra of surfaces A through D acquired with an FSAM surface as a background are shown in Figure 2.10. IR bands of MoPOM³⁻ were assigned based on our previous study.⁵¹ Specifically, the bands at 983 and 1067 cm⁻¹ are assigned to the terminal Mo=O_t stretching vibration and asymmetric coupling of P-O and Mo=O_t stretching modes (shown as P-O in Figure 2.10), respectively. The two bands at 887 and 827 cm⁻¹ are assigned to the vibrational stretching of the two types of bridging oxygen atoms, Mo-O_{b2}-Mo and Mo-O_{b1}-Mo, respectively. The IR bands of Ru(bpy)₃²⁺ were assigned based on the literature values.⁷¹

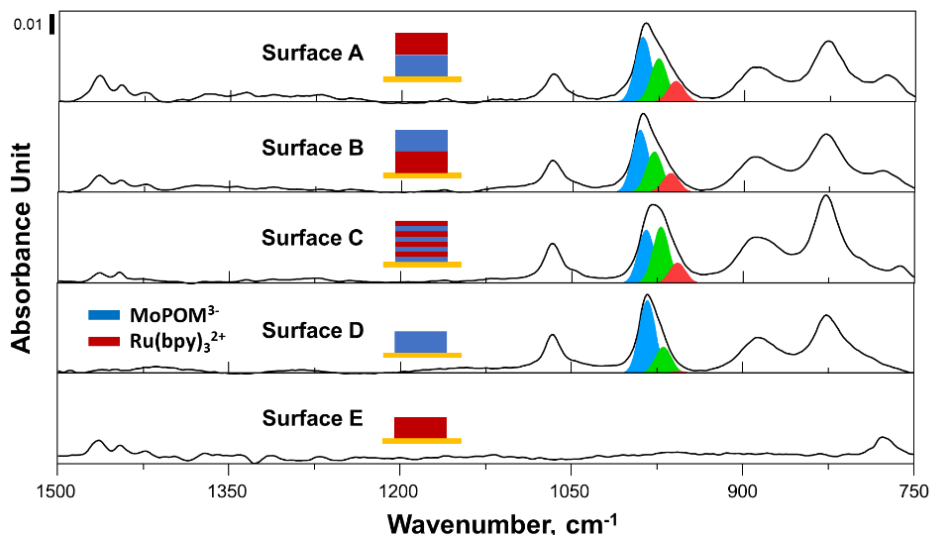


Figure 2.10 IRRAS spectra of the MoPOM³⁻/Ru(bpy)₃²⁺ surfaces prepared by LBL (A and B), fast polarity switching (C), MoPOM³⁻ only (D) and Ru(bpy)₃²⁺ only (E). The cartoon pictures of surface A through E are shown in the corresponding figures, illustrating the surfaces were prepared in either LBL or fast polarity switching modes. The combination of bands, reproduced by Gaussian curve fitting, are shown in each of the figures with color coding. A scale bar showing the absorbance is marked on the top left of the figure.

We observe that the positions of the P-O, Mo-O_{b2}-Mo and Mo-O_{b1}-Mo bands remain unchanged on all the surfaces containing MoPOM³⁻. In contrast, the terminal Mo=O_t band shows a systematic shift depending on the mode of deposition. It has been demonstrated that the terminal Mo=O_t band becomes broader and shifts towards lower wavenumbers when MoPOM³⁻ is soft landed onto an NH₃⁺-terminated SAM as compared to an FSAM.⁵¹ This is attributed to the attractive electrostatic interactions between the negatively charged MoPOM³⁻ ions and the positively charged NH₃⁺ moieties on the surface, which weaken the M=O bonds. We hypothesize that electrostatic interactions play a similar role when anions and cations are co-deposited in our soft-landing experiments. Fitting of the terminal Mo=O_t band performed as described in our previous study,⁷⁰ provides additional insights into the observed shifts. The simulated bands are shown in Figure 2.10. The terminal Mo=O_t band was successfully reproduced by a combination of three Gaussian distributions referred to as blue, green and red band at ~987, 974 and ~960 cm⁻¹, respectively, consistent with the color coding in Figure 2.6.

The blue and green bands, which appear in all the spectra may be attributed to the different charge states of the MoPOM anions as described in our previous study.⁵¹ In that work, the higher wavenumber feature (the blue band) was assigned to Mo=O_t band of MoPOM²⁻ produced by

charge loss of MoPOM³⁻ in the deposited layer. The green band at lower wavenumbers was assigned to the Mo=O_t band of intact MoPOM³⁻ ions. This band is most abundant in the spectrum of the surface prepared by fast polarity switching deposition, which indicates better charge retention of MoPOM³⁻ on this surface. An additional feature (red band) is observed in the presence of Ru(bpy)₃²⁺ on the surface. This band may be attributed to the electrostatic interactions between MoPOM³⁻ and Ru(bpy)₃²⁺ ions, which may contribute to the observed red-shifting of the band due to weakening of the Mo=O_t bond. The largest red shift of this band is observed for the surface prepared using fast polarity switching, which indicates stronger electrostatic interactions in this system as compared to surfaces prepared by LBL. We propose that fast polarity switching deposition of ions on the same surface results in more efficient charge retention and better ionic complexation in the layer.

2.4 Conclusions

In this study, we present the design and capabilities of a high-flux dual-polarity ion soft landing instrument for deposition of mass-selected cations and anions on surfaces. The instrument was systematically characterized in terms of the intensity and shape of the ion beam, kinetic energy distribution of ions, and the polarity switching capabilities. We demonstrate the ability of LBL or fast polarity switching deposition of cations and anions on the same surface with precise control over the ionic composition, kinetic energy, beam shape, and total charge deposited on the surface. The newly developed fast polarity switching capability enables experiments, which closely approximate simultaneous co-deposition of two ions beams of different polarities in a compact and relatively inexpensive instrument design. We found that fast polarity switching is the most effective approach for protecting soft-landed protonated molecules from neutralization by co-depositing them with weakly-coordinating anions. Furthermore, we provided spectroscopic evidence of the enhanced charge retention by native anions and better ionic complexation with cations on surfaces prepared using fast polarity switching compared to LBL. These novel capabilities of the newly-designed dual polarity ion soft landing instrument open up intriguing opportunities for the rational design and fabrication of ionic assemblies with different degrees of charge imbalance, which cannot be achieved using other deposition techniques.

2.5 References

- (1) Grill, V.; Shen, J.; Evans, C.; Cooks, R. G. Collisions of ions with surfaces at chemically relevant energies: instrumentation and phenomena. *Rev. Sci. Instrum.* **2001**, *72*, 3149-3179.
- (2) Johnson, G. E.; Hu, Q.; Laskin, J. Soft landing of complex molecules on surfaces. *Ann. Rev. Anal. Chem.* **2011**, *4*, 83-104.
- (3) Cyriac, J.; Pradeep, T.; Kang, H.; Souda, R.; Cooks, R. Low-energy ionic collisions at molecular solids. *Chem. Rev.* **2012**, *112*, 5356-5411.
- (4) Verbeck, G.; Hoffmann, W.; Walton, B. Soft-landing preparative mass spectrometry. *Analyst* **2012**, *137*, 4393-4407.
- (5) Johnson, G. E.; Gunaratne, D.; Laskin, J. Soft-and reactive landing of ions onto surfaces: Concepts and applications. *Mass Spectrom. Rev.* **2016**, *35*, 439-479.
- (6) Rauschenbach, S.; Ternes, M.; Harnau, L.; Kern, K. Mass spectrometry as a preparative tool for the surface science of large molecules. *Ann. Rev. Anal. Chem.* **2016**, *9*, 473-498.
- (7) Heiz, U.; Bullock, E. Fundamental aspects of catalysis on supported metal clusters. *J. Mater. Chem.* **2004**, *14*, 564-577.
- (8) Rauschenbach, S.; Stadler, F. L.; Lunedei, E.; Malinowski, N.; Koltsov, S.; Costantini, G.; Kern, K. Electrospray ion beam deposition of clusters and biomolecules. *small* **2006**, *2*, 540-547.
- (9) Vajda, S.; White, M. G. Catalysis applications of size-selected cluster deposition. *ACS catalysis* **2015**, *5*, 7152-7176.
- (10) Laskin, J.; Johnson, G. E.; Prabhakaran, V. Soft Landing of Complex Ions for Studies in Catalysis and Energy Storage. *J. Phys. Chem. C* **2016**, *120*, 23305-23322.
- (11) Wang, P.; Laskin, J. Helical peptide arrays on self-assembled monolayer surfaces through soft and reactive landing of mass-selected ions. *Angew. Chem. Int. Ed.* **2008**, *47*, 6678-6680.
- (12) Hu, Q.; Laskin, J. Secondary Structures of Ubiquitin Ions Soft-Landed onto Self-Assembled Monolayer Surfaces. *J. Phys. Chem. B* **2016**, *120*, 4927-4936.
- (13) Deng, Z.; Thontasen, N.; Malinowski, N.; Rinke, G.; Harnau, L.; Rauschenbach, S.; Kern, K. A close look at proteins: submolecular resolution of two-and three-dimensionally folded cytochrome c at surfaces. *Nano Lett.* **2012**, *12*, 2452-2458.
- (14) Longchamp, J.-N.; Rauschenbach, S.; Abb, S.; Escher, C.; Latychevskaia, T.; Kern, K.; Fink, H.-W. Imaging proteins at the single-molecule level. *Proc. Natl. Acad. Sci.* **2017**, *114*, 1474-1479.
- (15) Pepi, F.; Ricci, A.; Tata, A.; Favero, G.; Frasconi, M.; Delle Noci, S.; Mazzei, F. Soft landed protein voltammetry. *Chem. Commun.* **2007**, 3494-3496.

- (16) Ouyang, Z.; Takáts, Z.; Blake, T. A.; Gologan, B.; Guymon, A. J.; Wiseman, J. M.; Oliver, J. C.; Davisson, V. J.; Cooks, R. G. Preparing protein microarrays by soft-landing of mass-selected ions. *Science* **2003**, *301*, 1351-1354.
- (17) Blake, T. A.; Ouyang, Z.; Wiseman, J. M.; Takáts, Z.; Guymon, A. J.; Kothari, S.; Cooks, R. G. Preparative linear ion trap mass spectrometer for separation and collection of purified proteins and peptides in arrays using ion soft landing. *Anal. Chem.* **2004**, *76*, 6293-6305.
- (18) Kahle, S.; Deng, Z.; Malinowski, N.; Tonnoir, C. n.; Forment-Aliaga, A.; Thontasen, N.; Rinke, G.; Le, D.; Turkowski, V.; Rahman, T. S. The quantum magnetism of individual manganese-12-acetate molecular magnets anchored at surfaces. *Nano Lett.* **2011**, *12*, 518-521.
- (19) Nagaoka, S.; Matsumoto, T.; Ikemoto, K.; Mitsui, M.; Nakajima, A. Soft-landing isolation of multidecker V₂(benzene)₃ complexes in an organic monolayer matrix: an infrared spectroscopy and thermal desorption study. *J. Am. Chem. Soc.* **2007**, *129*, 1528-1529.
- (20) Johnson, G. E.; Laskin, J. Preparation of Surface Organometallic Catalysts by Gas-Phase Ligand Stripping and Reactive Landing of Mass-Selected Ions. *Chem. Eur. J.* **2010**, *16*, 14433-14438.
- (21) Peng, W.-P.; Johnson, G. E.; Fortmeyer, I. C.; Wang, P.; Hadjar, O.; Cooks, R. G.; Laskin, J. Redox chemistry in thin layers of organometallic complexes prepared using ion soft landing. *PCCP* **2011**, *13*, 267-275.
- (22) Hauptmann, N.; Hamann, C.; Tang, H.; Berndt, R. Soft-landing electrospray deposition of the ruthenium dye N3 on Au (111). *J. Phys. Chem. C* **2013**, *117*, 9734-9738.
- (23) Kaden, W. E.; Wu, T.; Kunkel, W. A.; Anderson, S. L. Electronic structure controls reactivity of size-selected Pd clusters adsorbed on TiO₂ surfaces. *Science* **2009**, *326*, 826-829.
- (24) Tyo, E. C.; Vajda, S. Catalysis by clusters with precise numbers of atoms. *Nat. Nanotech.* **2015**, *10*, 577.
- (25) Lünskens, T.; Heister, P.; Thämer, M.; Walenta, C. A.; Kartouzian, A.; Heiz, U. Plasmons in supported size-selected silver nanoclusters. *PCCP* **2015**, *17*, 17541-17544.
- (26) Ha, M.-A.; Baxter, E. T.; Cass, A. C.; Anderson, S. L.; Alexandrova, A. N. Boron switch for selectivity of catalytic dehydrogenation on size-selected Pt clusters on Al₂O₃. *J. Am. Chem. Soc.* **2017**, *139*, 11568-11575.
- (27) Xu, J.; Murphy, S.; Xiong, D.; Cai, R.; Wei, X.; Heggen, M.; Barborini, E.; Vinati, S.; Dunin-Borkowski, R. E.; Palmer, R. E. Cluster Beam Deposition of Ultrafine Cobalt and Ruthenium Clusters for Efficient and Stable Oxygen Evolution Reaction. *ACS Appl. Energy Mater.* **2018**, *1*, 3013-3018.
- (28) Wang, P.; Hadjar, O.; Gassman, P. L.; Laskin, J. Reactive landing of peptide ions on self-assembled monolayer surfaces: an alternative approach for covalent immobilization of peptides on surfaces. *PCCP* **2008**, *10*, 1512-1522.

- (29) Laskin, J.; Hu, Q. Reactive Landing of Gramicidin S and Ubiquitin Ions onto Activated Self-Assembled Monolayer Surfaces. *J. Am. Soc. Mass. Spectrom.* **2017**, *28*, 1304-1312.
- (30) Wijesundara, M. B.; Fuoco, E.; Hanley, L. Preparation of chemical gradient surfaces by hyperthermal polyatomic ion deposition: a new method for combinatorial materials science. *Langmuir* **2001**, *17*, 5721-5726.
- (31) Qin, X.; Tzvetkov, T.; Jacobs, D. C. Reaction of 5– 40 eV Ions with Self-Assembled Monolayers. *J. Phys. Chem. A* **2006**, *110*, 1408-1415.
- (32) Dubey, G.; Urcuyo, R.; Abb, S.; Rinke, G.; Burghard, M.; Rauschenbach, S.; Kern, K. Chemical modification of graphene via hyperthermal molecular reaction. *J. Am. Chem. Soc.* **2014**, *136*, 13482-13485.
- (33) Pepi, F.; Tata, A.; Garzoli, S.; Giacomello, P.; Ragno, R.; Patsilnakos, A.; Fusco, M. D.; D'Annibale, A.; Cannistraro, S.; Baldacchini, C.; Favero, G.; Frasconi, M.; Mazzei, F. Chemically Modified Multiwalled Carbon Nanotubes Electrodes with Ferrocene Derivatives through Reactive Landing. *J. Phys. Chem. C* **2011**, *115*, 4863-4871.
- (34) Franchetti, V.; Solka, B.; Baitinger, W.; Amy, J.; Cooks, R. Soft landing of ions as a means of surface modification. *Int. J. Mass Spectrom. Ion Phys.* **1977**, *23*, 29-35.
- (35) Pauly, M.; Sroka, M.; Reiss, J.; Rinke, G.; Albarghash, A.; Vogelgesang, R.; Hahne, H.; Kuster, B.; Sesterhenn, J.; Kern, K. A hydrodynamically optimized nano-electrospray ionization source and vacuum interface. *Analyst* **2014**, *139*, 1856-1867.
- (36) Gunaratne, K. D. D.; Prabhakaran, V.; Ibrahim, Y. M.; Norheim, R. V.; Johnson, G. E.; Laskin, J. Design and performance of a high-flux electrospray ionization source for ion soft landing. *Analyst* **2015**, *140*, 2957-2963.
- (37) Heiz, U.; Schneider, W.-D. Size-Selected Clusters on Solid Surfaces. *Critical Reviews in Solid State and Materials Sciences* **2001**, *26*, 251-290.
- (38) Zhang, C.; Tsunoyama, H.; Akatsuka, H.; Sekiya, H.; Nagase, T.; Nakajima, A. Advanced nanocluster ion source based on high-power impulse magnetron sputtering and time-resolved measurements of nanocluster formation. *J. Phys. Chem. A* **2013**, *117*, 10211-10217.
- (39) Palmer, R.; Cao, L.; Yin, F. Note: Proof of principle of a new type of cluster beam source with potential for scale-up. *Rev. Sci. Instrum.* **2016**, *87*, 046103.
- (40) Badu-Tawiah, A. K.; Wu, C.; Cooks, R. G. Ambient ion soft landing. *Anal. Chem.* **2011**, *83*, 2648-2654.
- (41) Li, A.; Baird, Z.; Bag, S.; Sarkar, D.; Prabhath, A.; Pradeep, T.; Cooks, R. G. Using ambient ion beams to write nanostructured patterns for surface enhanced raman spectroscopy. *Angew. Chem. Int. Ed.* **2014**, *53*, 12528-12531.

- (42) Hou, J.; Zheng, Q.; Badu-Tawiah, A. K.; Xiong, C.; Guan, C.; Chen, S.; Nie, Z.; Wang, D.; Wan, L. Electrospray soft-landing for the construction of non-covalent molecular nanostructures using charged droplets under ambient conditions. *Chem. Commun.* **2016**, *52*, 13660-13663.
- (43) Johnson, G. E.; Prabhakaran, V.; Browning, N. D.; Mehdi, B. L.; Laskin, J.; Kottke, P. A.; Fedorov, A. G. DRILL Interface Makes Ion Soft Landing Broadly Accessible for Energy Science and Applications. *Batteries & Supercaps* **2018**, *1*, 97-101.
- (44) Prabhakaran, V.; Mehdi, B. L.; Ditto, J. J.; Engelhard, M. H.; Wang, B.; Gunaratne, K. D. D.; Johnson, D. C.; Browning, N. D.; Johnson, G. E.; Laskin, J. Rational design of efficient electrode–electrolyte interfaces for solid-state energy storage using ion soft landing. *Nat. Commun.* **2016**, *7*, 11399.
- (45) Nesselberger, M.; Roefzaad, M.; Hamou, R. F.; Biedermann, P. U.; Schweinberger, F. F.; Kunz, S.; Schloegl, K.; Wiberg, G. K.; Ashton, S.; Heiz, U. The effect of particle proximity on the oxygen reduction rate of size-selected platinum clusters. *Nat. Mater.* **2013**, *12*, 919.
- (46) Popescu, R.; Schneider, R.; Gerthsen, D.; Böttcher, A.; Löffler, D.; Weis, P.; Kappes, M. Coarsening of mass-selected Au clusters on amorphous carbon at room temperature. *Surf. Sci.* **2009**, *603*, 3119-3125.
- (47) Warneke, J.; McBriarty, M. E.; Riechers, S. L.; China, S.; Engelhard, M. H.; Apra, E.; Young, R. P.; Washton, N. M.; Jenne, C.; Johnson, G. E.; Laskin, J. Self-organizing layers from complex molecular anions. *Nat. Commun.* **2018**, *9*, 1889.
- (48) Laskin, J.; Johnson, G. E.; Warneke, J.; Prabhakaran, V. From Isolated Ions to Multilayer Functional Materials Using Ion Soft-Landing. *Angew. Chem. Int. Ed.* **2018**, DOI: 10.1002/anie.201712296.
- (49) Hadjar, O.; Futrell, J. H.; Laskin, J. First observation of charge reduction and desorption kinetics of multiply protonated peptides soft landed onto self-assembled monolayer surfaces. *J. Phys. Chem. C* **2007**, *111*, 18220-18225.
- (50) Johnson, G. E.; Priest, T.; Laskin, J. Coverage-dependent charge reduction of cationic gold clusters on surfaces prepared using soft landing of mass-selected ions. *J. Phys. Chem. C* **2012**, *116*, 24977-24986.
- (51) Gunaratne, K. D. D.; Johnson, G. E.; Andersen, A.; Du, D.; Zhang, W.; Prabhakaran, V.; Lin, Y.; Laskin, J. Controlling the charge state and redox properties of supported polyoxometalates via soft landing of mass-selected ions. *J. Phys. Chem. C* **2014**, *118*, 27611-27622.
- (52) Belov, M. E.; Damoc, E.; Denisov, E.; Compton, P. D.; Horning, S.; Makarov, A. A.; Kelleher, N. L. From protein complexes to subunit backbone fragments: a multi-stage approach to native mass spectrometry. *Anal. Chem.* **2013**, *85*, 11163-11173.
- (53) Ibrahim, Y. M.; Baker, E. S.; Danielson, W. F.; Norheim, R. V.; Prior, D. C.; Anderson, G. A.; Belov, M. E.; Smith, R. D. Development of a new ion mobility time-of-flight mass spectrometer. *Int. J. Mass spectrom.* **2015**, *377*, 655-662.

- (54) Rose, R. J.; Damoc, E.; Denisov, E.; Makarov, A.; Heck, A. J. High-sensitivity Orbitrap mass analysis of intact macromolecular assemblies. *Nat. Methods* **2012**, *9*, 1084.
- (55) Peng, W.-P.; Goodwin, M. P.; Nie, Z.; Volný, M.; Ouyang, Z.; Cooks, R. G. Ion soft landing using a rectilinear ion trap mass spectrometer. *Anal. Chem.* **2008**, *80*, 6640-6649.
- (56) Tolmachev, A. V.; Udseth, H. R.; Smith, R. D. Radial stratification of ions as a function of mass to charge ratio in collisional cooling radio frequency multipoles used as ion guides or ion traps. *Rapid Commun. Mass Spectrom.* **2000**, *14*, 1907-1913.
- (57) Hadjar, O.; Johnson, G.; Laskin, J.; Kibelka, G.; Shill, S.; Kuhn, K.; Cameron, C.; Kassin, S. IonCCD™ for direct position-sensitive charged-particle detection: from electrons and keV ions to hyperthermal biomolecular ions. *J. Am. Soc. Mass. Spectrom.* **2011**, *22*, 612-623.
- (58) Johnson, G. E.; Hadjar, O.; Laskin, J. Characterization of the ion beam focusing in a mass spectrometer using an IonCCD™ detector. *J. Am. Soc. Mass. Spectrom.* **2011**, *22*, 1388-1394.
- (59) Chantry, P.; Schulz, G. Kinetic-energy distribution of negative ions formed by dissociative attachment and the measurement of the electron affinity of oxygen. *Phys. Rev.* **1967**, *156*, 134.
- (60) Jacobs, D. C. Reactive collisions of hyperthermal energy molecular ions with solid surfaces. *Annu. Rev. Phys. Chem.* **2002**, *53*, 379-407.
- (61) Laskin, J.; Wang, P.; Hadjar, O. Soft-landing of peptide ions onto self-assembled monolayer surfaces: an overview. *PCCP* **2008**, *10*, 1079-1090.
- (62) Miller, S.; Luo, H.; Pachuta, S.; Cooks, R. Soft-landing of polyatomic ions at fluorinated self-assembled monolayer surfaces. *Science* **1997**, *275*, 1447-1450.
- (63) Johnson, G. E.; Priest, T.; Laskin, J. Charge retention by gold clusters on surfaces prepared using soft landing of mass selected ions. *ACS nano* **2011**, *6*, 573-582.
- (64) Gunaratne, K. D. D.; Prabhakaran, V.; Andersen, A.; Johnson, G. E.; Laskin, J. Charge retention of soft-landed phosphotungstate Keggin anions on self-assembled monolayers. *PCCP* **2016**, *18*, 9021-9028.
- (65) Jenne, C.; Keßler, M.; Warneke, J. Protic Anions $[H(B_{12}X_{12})]^{-}$ (X= F, Cl, Br, I) That Act as Brønsted Acids in the Gas Phase. *Chem. Eur. J.* **2015**, *21*, 5887-5891.
- (66) Avelar, A.; Tham, F. S.; Reed, C. A. Superacidity of boron acids $H_2(B_{12}X_{12})(X= Cl, Br)$. *Angew. Chem. Int. Ed.* **2009**, *48*, 3491-3493.
- (67) Laskin, J.; Wang, P. Charge retention by organometallic dications on self-assembled monolayer surfaces. *Int. J. Mass Spectrom.* **2014**, *365-366*, 187-193.

- (68) Li, Y.; Yang, X.; Yang, F.; Wang, Y.; Zheng, P.; Liu, X. Effective immobilization of Ru(bpy)₃²⁺ by functional composite phosphomolybdic acid anion on an electrode surface for solid-state electrochemiluminescence to sensitive determination of NADH. *Electrochimica Acta* **2012**, *66*, 188-192.
- (69) Li, Y.; Zhu, H.; Yang, X. [Ru(bpy)₃]²⁺ nanocomposites containing heteropolyacids: Simple preparation and stable solid-state electrochemiluminescence detection application. *Talanta* **2009**, *80*, 870-874.
- (70) Su, P.; Prabhakaran, V.; Johnson, G. E.; Laskin, J. In Situ Infrared Spectroelectrochemistry for Understanding Structural Transformations of Precisely Defined Ions at Electrochemical Interfaces. *Anal. Chem.* **2018**, *90*, 10935-10942.
- (71) Omberg, K. M.; Schoonover, J. R.; Treadway, J. A.; Leasure, R. M.; Dyer, R. B.; Meyer, T. J. Mid-infrared spectrum of [Ru(bpy)₃]²⁺. *J. Am. Chem. Soc.* **1997**, *119*, 7013-7018.

CHAPTER 3. PREPARATIVE MASS SPECTROMETRY USING A ROTATING WALL MASS ANALYZER

3.1 Introduction

The deposition of well-defined polyatomic species onto surfaces is a powerful approach for the precisely-controlled preparation of interfaces for materials design and synthesis.¹⁻⁴ Mass spectrometry (MS) is a powerful preparative tool due to its ability to generate mass- and charge-selected polyatomic ions in the gas phase and deposit them onto surfaces under controlled conditions.^{5,6} Gentle deposition of ions on surfaces with or without the retention of charge in a process referred to as ion soft landing⁷⁻⁹ helps preserve the structure and, in specific cases, the reactivity of the ion.¹⁰⁻¹⁷ Furthermore, the ability to control surface coverage, spot size, and pattern makes ion soft landing particularly advantageous for the preparation of coatings, thin films, and selective doping of materials.¹⁸⁻²⁰ Ion soft landing has been employed to prepare protein and peptide arrays,²¹⁻²³ nanocluster-based catalysts,²⁴⁻³⁰ electrochemical interfaces,^{31,32} self-organizing layers,³³⁻³⁶ optical^{37,38} and magnetic thin films.³⁹⁻⁴¹

A majority of preparative MS instruments utilize quadrupole⁴²⁻⁴⁶ and lateral time-of-flight analyzers^{47,48} as mass filtering devices. Despite the significant advances in soft landing instrumentation,⁴⁹⁻⁵³ mass filtering limits the deposition to one species at a time and requires specialized high-voltage electronics. The broader application of preparative MS will benefit from the development of simple, low-cost, and compact instruments. Ambient soft landing systems have been developed to address this need and improve the scalability of the technique.⁵⁴⁻⁵⁶ However, the ability to deposit mass-selected ions in a high-throughput manner is still limited. Furthermore, mass-filtering devices traditionally used in soft landing experiments are limited to lower mass ions ($m/z < 4000$), which hinders their application to nanomaterials design and protein structure characterization.

Herein, we address some of these limitations by introducing a straightforward approach for mass-selected ion deposition using a rotating wall mass analyzer (RWMA, Figure 1A). RWMA enables dispersive deposition of ions with different m/z onto distinct locations on a surface by separating them in space. This device has a theoretically unlimited mass range and enables

deposition of ions originating from multicomponent mixtures onto substrates in a high-throughput manner. We present a systematic study of the RWMA employed specifically for ion soft landing experiments using a combination of experiments and simulations. We present a modified analytical equation for predicting the deposition radius for a specific m/z and discuss factors that affect the separation of multicomponent mixtures. In addition, we have developed a universal mass calibration of the RWMA using a series of oligomer ions. Finally, we present a systematic study of the factors affecting mass resolution of the RWMA. Although the performance characteristics of the RWMA are discussed in the context of hyperthermal ion deposition, the same principles of operation can be used for the separation of higher-kinetic energy ions for other types of applications. RWMA is well-suited for applied research since it separates ions using low rf voltages ($\leq 10 V_{0-p}$) and kilohertz frequencies provided by inexpensive waveform generators, making ion soft landing accessible to the broader scientific community. Although RWMA has been previously employed as a mass analyzer,^{57,58} it is used as a preparative device for the first time in this study. Furthermore, the small size of RWMA is advantageous to the development of miniature preparative MS instrumentation.

3.2 Experimental Section

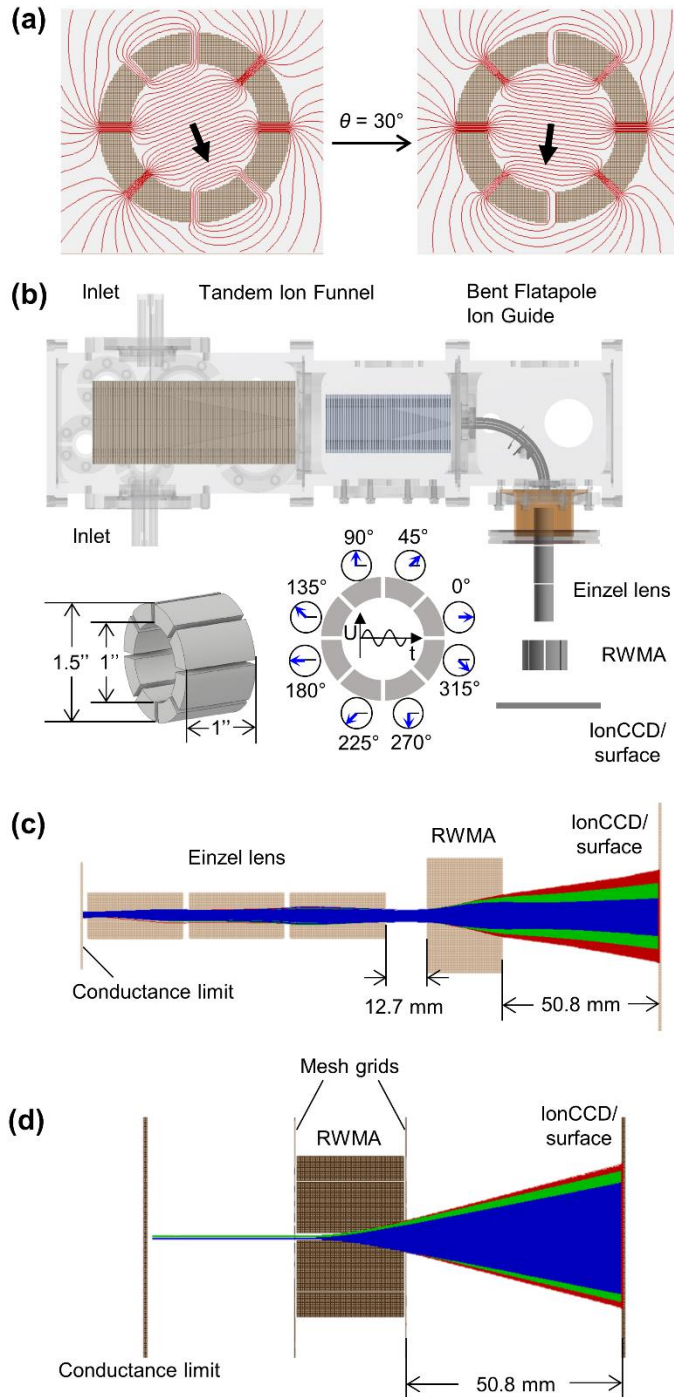
3.2.1 Instrumentation

The RWMA constructed in our laboratory is comprised of a stainless steel cylinder (1.5'' outer diameter, 1'' inner diameter, 1'' length) segmented lengthwise into eight arc-shaped electrodes (Figure 3.1(b)). The length of the RWMA was selected to facilitate the separation of hyperthermal ions (≤ 100 eV). The eight electrodes are connected to eight identical sinusoidal rf voltages generated using four dual-channel Rigol DG1022Z arbitrary waveform generators (Beaverton, OR). Typically, we use sinusoidal waveforms with a frequency in the range of 5-100 kHz and $\leq 10 V_{0-p}$ amplitude. A constant-strength rotating electric field is constructed by applying the rf voltages to the eight electrodes with a 45° phase shift between each waveform (Figure 3.1(a)).⁵⁹ The four waveform generators are synchronized to lock the phases of the waveforms using the following procedure: first, the function generators are connected through the 10MHz in/out ports using BNC cables; next, one of the function generators is designated as the internal clock, to which the other three units are synchronized. To construct the rotating field, the frequency

and amplitude of each waveform are first selected; then one of the waveforms is designated as the reference phase (start phase=0°). The initial phases of the remaining waveforms are adjusted accordingly (start phase=45°, 90°, 135°, 180°, 225°, 270°, 315°) by monitoring them on an oscilloscope (Figure 3.1(b)).

The instrument configuration for ion soft landing experiments using the RWMA described in our previous study¹⁴ is shown in Figure 3.1(b). It is composed of a high-transmission ESI interface described elsewhere,¹⁴ einzel lens, RWMA, and IonCCD (OI Analytical, Pelham, AL) detector/collector surface. Briefly, ions produced using ESI are transferred through the dual ion funnel system and subjected to collisional focusing in the bent flatpole. The ion beam is subsequently transferred into the high vacuum region (5×10^{-5} Torr), focused by the einzel lens (three 12.7 mm-long cylinders spaced by 0.65 mm gaps), spatially separated using the RWMA, and collected on a detector/surface. The rf and dc voltage settings of the high-transmission ESI interface used in this study are similar to the ones reported in our previous publication.⁶⁰ Typical rf levels for high-pressure funnel (HPF), low-pressure funnel (LPF) and bent flatpole are ~270 V, ~135 V and ~400 V, respectively. Typical DC settings for positive and negative ions are: 376/-385 V (Inlet), 384/-400 V (HPF Repeller In), 333/-355 V (HPF Repeller Out), 332/-354 V (HPF Funnel In), 164/-150 V (HPF Funnel Out), 163/-149 V (LPF Funnel In), 28/-28 V (LPF Lens), 32/-32 V (LPF Funnel Out), respectively. Typical voltages on the einzel lens are 10/-15/10 V and -10/18/-10 V for positive and negative ions, respectively, and need to be adjusted according to the flatpole bias in a specific experiment to achieve the best focusing. We note that the resonance frequency of the bent flatpole ion guide was reduced to 1.17 MHz to improve the transmission of high- m/z ions.⁶¹ Typical voltages on the einzel lens are 23/2/23 V and -17/3/-17 V for positive and negative ions, respectively. IonCCD profiles were obtained using 50 ms integration time.⁶²

Figure 3.1 (a) A cross-section view of the RWMA from SIMION simulations showing the equipotential lines (red) at $\theta = 0^\circ$ and $\theta = 30^\circ$. The black arrows indicate the direction of the electric field. The equipotential lines inside the RWMA are evenly spaced indicating that a homogeneous rotating field is constructed in the central region of the RWMA. (b) A schematic drawing of the ion soft landing instrument composed of a high-transmission ESI interface, an einzel lens, the RWMA and an IonCCD/surface. The left bottom corner shows the schematic drawing of the RWMA fabricated in our lab, and a diagram showing the phases of the sinusoidal rf waveforms applied to the eight electrodes. This panel is adopted from ref. [51] and presented here for clarity. (c) Cross-sectional view of the electrode geometry used in SIMION simulations including a conductance limit plate, einzel lens, RWMA, and IonCCD/surface. The red, green, and blue traces indicate the ion trajectories of 12000 ions of $m/z=253.2$, $m/z=329.2$, $m/z=470.3$, respectively, at a kinetic energy of 20 eV.



Fitting of the ion beam profiles was carried out in Excel using a sum of Lorentzian distributions. The peak positions were first defined, and the peak intensities and widths were optimized by minimizing the sum of squares of deviations between the experimental and simulated data points to obtain the best-fit curves. For the determination of the FWHM of the peaks, three

replicates of ion beam profiles were collected in the experiments to obtain statistically significant results.

Ion trajectories were simulated using SIMION 8.0.4 software package (Scientific Instrument Services, Ringoes, NJ). We used the Lua macro to generate the geometry of the electrodes and the time-dependent electric field in the potential array. The size of the grid unit in the potential array was defined as 0.3175 mm to enhance the smoothness of the electrode surfaces. Two electrode geometries were considered. In the first electrode geometry, ion beam was generated at the conductance limit, focused by the einzel lens, dispersed by the RWMA and deposited on an IonCCD/surface (Figure 3.1(c)). This geometry represents the experimental setup used on our study. In the second electrode geometry used to study the intrinsic properties of the device, an isolated RMWA was constructed, with two mesh grids positioned at the entrance and the exit of the RWMA to terminate the rotating field (Figure 3.1(d)). For each m/z , a group of 12000 ions was produced with a birth step of 0.01 μs between each ion. The product of the birth step and the number of replicate ions should be equal or greater than one rf period to create a full ring pattern on the collector plate. Ion beams with different FWHMs were created using a 2D Gaussian distribution. Kinetic energy spread of the ion beam was represented by a Gaussian kinetic energy distribution of varying width.

The kinetic energy distribution (KED) of the ions was measured using a stainless steel plate mounted 12.7 mm away from the einzel lens. The plate was connected to the picoammeter and biased, which allowed us to apply the retarding voltage to the collector plate while measuring the ion current. A stainless steel mesh (part No. 9230T51, McMaster Carr, Elmhurst, IL) kept at 0 V was mounted ~ 2 mm in front of the plate to maintain a uniform electric field close to the plate. Ion current detected on the plate was measured as a function of the retarding voltage. Each data point was acquired by averaging the ion current for 10 s. The integrated retarding potential curve was obtained by plotting the ion current as a function of the retarding voltage. KED was obtained by taking a first derivative of the retarding potential plot.

$\text{Au}_{144}(\text{SC}_4\text{H}_9)_{60}$ was synthesized by Prof. Flavio Maran's group at University of Padova, Italy, according to a known procedure.⁶³ A solution of $\text{Au}_{144}(\text{SC}_4\text{H}_9)_{60}$ used for soft landing experiments was prepared by dissolving the powder in toluene/methanol=70%/30% to reach a final

concentration of 25 μM . Polyacrylamide (PAM, $M_p=2700$, $M_w=3200$, $M_n=2500$) was kindly provided by Dr. Fan Pu and Prof. R. Graham Cooks (Department of Chemistry, Purdue University) and was used as the calibration standard. The PAM oligomer solution used for ESI was prepared by dissolving the powder in 9:1 methanol:H₂O (v/v) to a final concentration of 100 μM . Poly(dimethylsiloxane), hydride terminated (PDMS, $M_n=580$) was purchased from Sigma-Aldrich (St. Louis, MO). PDMS oligomer solution used for ESI was prepared by dissolving the PDMS in methanol/toluene=70%/30% with 10 mM ammonium acetate to a final concentration of 100 μM . Solution of ubiquitin from bovine erythrocytes ($\geq 98\%$ purity, Sigma-Aldrich) used for ESI-MS were prepared at a concentration of $\sim 0.05 \text{ mg}\cdot\text{mL}^{-1}$ in a solvent of methanol/H₂O/CH₃COOH/glycerol=49%/49%/1%/1%. Three organic dyes, 2-[4-(Dimethylamino)styryl]-1-ethylpyridinium (DASPE⁺, $m/z=253.2$), Malachite green (MG⁺, $m/z=329.2$) and Victoria blue B (VBB⁺, $m/z=470.3$) were purchased from Sigma-Aldrich. For the soft landing experiments, a solution containing all three dyes at the same concentration (45 μM each) was prepared by dissolving the dyes in methanol.

ESI-MS analyses were performed using an LTQ XL Linear Ion Trap Mass Spectrometer (Thermo Fisher Scientific GmbH, Bremen, Germany). Samples were introduced into the inlet by direct infusion through a fused silica capillary (50 μm ID, 150 μm OD) at a flow rate of $\sim 0.5 \mu\text{L}/\text{min}$. Typical mass spectrometer conditions on the LTQ for the positive and negative ionization modes were as follows: electrospray voltage: $\pm 3 \text{ kV}$, capillary temperature: 300 $^\circ\text{C}$, capillary voltage: $\pm 10 \text{ V}$, tube lens: $\pm 20 \text{ V}$. Scan range: 100-2000 m/z . High-resolution mass spectra were acquired on an Agilent 6560 IM Q-TOF (Santa Clara, CA, USA) mass spectrometer through direct infusion under the following instrument conditions: electrospray voltage: $\pm 4 \text{ kV}$, capillary temperature: 325 $^\circ\text{C}$, m/z range: 100-3200.

3.3 Results and Discussion

3.3.1 Analytical Expression for the Deposition Radius

The concept of using a rotating electric field for mass separation was first introduced by Clemmons *et al.*, who described the theory and principles of operation of the RWMA as an analytical mass spectrometer.⁵⁹ In contrast, in this contribution, we provide a detailed description of the RWMA used exclusively as a mass-dispersive device for ion soft landing experiments. In

these experiments, a continuous ion beam with well-defined beam size and kinetic energy distribution (KED) is directed into the RWMA along the instrument axis (defined by the central axis of the RWMA cylinder, Figure 3.2(a)). Ions of different m/z are radially dispersed by the rotating field. After exiting the rotating field region,

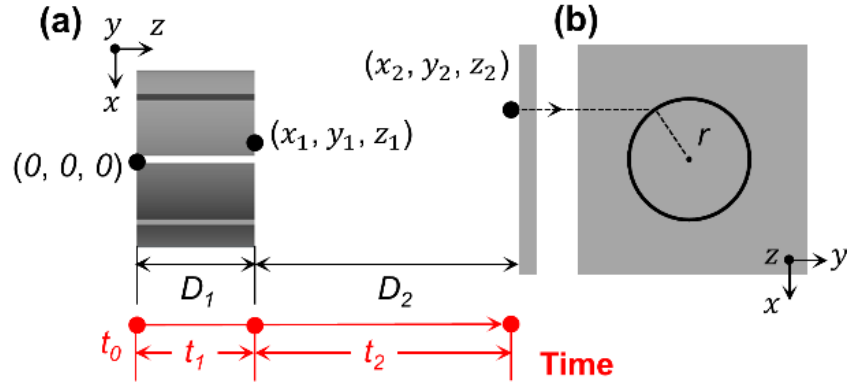


Figure 3.2 (a) A schematic diagram of the RWMA and a collector plate used to derive Eq. 1. The ion entering the RWMA at $(0,0,0)$ at time t_0 along the cylinder's central axis is radially dispersed by the rotating field and exits the RWMA at (x_1, y_1, z_1) . The length of this region and time the ion spends in this region are denoted as D_1 and t_1 , respectively. Next, the ion travels through the field-free region along its velocity vector attained at (x_1, y_1, z_1) and lands onto the collector plate at (x_2, y_2, z_2) . The length of this region and time the ion spends in this region are denoted as D_2 and t_2 , respectively. (b) A projection of the collector plate perpendicular to the central axis showing the ring deposition pattern formed by a continuous ion beam; r is the radius of the ring.

ions drift with a constant velocity in the field-free region until they hit the surface. When the collector plate is mounted at a specific distance, D_2 , behind the RWMA, ions of different m/z are collected onto distinct ring-shaped areas of different radii (Figure 3.2(b)). The radius of the ring depends on the m/z and kinetic energy of the ion, frequency and amplitude of the rotating electric field, and distance between the surface and the RWMA. Eq. 1 presents an analytical equation for predicting the radius for a specific ion:

$$R = \sqrt{x_2^2 + y_2^2} = \frac{zE}{m\omega^2} \sqrt{2(1 + \omega^2 t_1 t_2 + \omega^2 t_2^2)(1 - \cos \omega t_1) + \omega t_1(\omega t_1 - 2\sin \omega t_1)}$$

(Equation 3.1)

where

$$f = \frac{\omega}{2\pi} \quad t_1 = D_1 \sqrt{\frac{m}{2E_k}} \quad t_2 = D_2 \sqrt{\frac{m}{2E_k}}$$

where m , z , E_K are the mass, charge state, and kinetic energy of the ion, E and f are the amplitude and frequency the rotating field, and D_1 and D_2 are the lengths of the rotating field and field-free region, respectively. A similar expression in polar coordinates was presented by Clemmons *et al.*⁵⁹

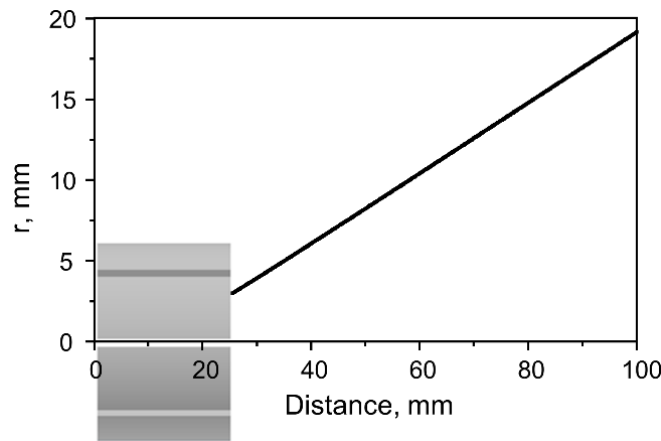


Figure 3.3 Deposition radius as a function of distance from the RWMA entrance for an ion of $m/z=253.2$, $E_k=35$ eV/charge with RWMA operating at $f=70$ kHz, $10 V_{p-p}$.

It is evident from Eq. 3.1 that the radius of the ring is proportional to the amplitude of the rotating field, E . Furthermore, we found that the radius increases linearly with the length of the field-free region, D_2 (Figure 3.3). It is also clear that there is a strong dependence of the radius on m/z , E_K and f . In order to better understand this dependence, we show in Figure 3.4 the calculated value of the deposition radius as a function of m/z assuming the same kinetic energy per charge (35 eV/charge) and the same charge state (± 1) for all the m/z . This represents the scenario of spreading singly-charged ions generated from oligomer mixtures onto a surface. We observe that at 70 kHz and 90 kHz, the radius decreases gradually with increase in m/z in the presented m/z range. In contrast, the curves at higher frequencies start to “fold” at higher m/z meaning that, beginning from some m/z referred to as the turning point, the radius increases with increase in m/z . The turning point is seen to shift towards lower m/z with increase in the frequency of the rotating field. Folding of the curve results in an overlap in the radii of different m/z ions and failure of ion

separation in the folded m/z range. The calculated radii of $m/z = 200, 400, 600,$ and 800 are extracted from the plots in Figure 3.4(a) and reconstructed as simulated mass spectra at different frequencies in Figure 3.4(b). We observe that at 70-110 kHz (black, red, and blue spectra), the four peaks are properly ordered as the radii decrease with m/z . Furthermore, we find that the peaks of the same series of ions are farther separated at 90 kHz than at 70 kHz. This is consistent with the larger slope of the r vs. m/z curve at higher frequencies (Figure 3.4(a)), which indicates the resolution for separation of ions in a specific m/z range can be improved by adjusting the frequency to an optimal value. However, at frequencies above 110 kHz, the order of the rings changes with m/z 800 observed at a larger radius than m/z 600 at 130 kHz (green spectrum) and at a larger radius than both m/z 600 and m/z 400 at 150 kHz (purple spectrum). Clearly, for this m/z range, the RWMA must be operated at a frequency of the rotating field below 110 kHz.

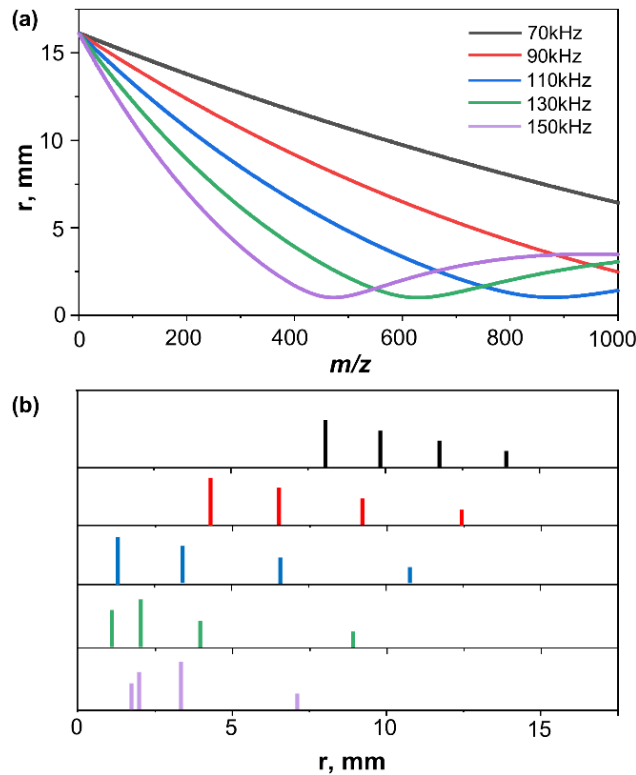


Figure 3.4 (a) Plots of the deposition radius as a function of m/z for singly-charged ions of the same E_k (35 eV) and at several frequencies of the rotating field shown in different colors. (b) Simulated RWMA mass spectra containing four signals ($m/z = 200, 400, 600,$ and 800) extracted from the plots shown in panel (a) at different frequencies shown using the same color coding as in panel (a). The heights of the bars in the simulated spectra indicate the m/z .

We provide a qualitative explanation for the observed trend. The extent of radial dispersion depends on the time the ion spends in the rotating field, which is determined by ion's m/z and kinetic energy. At lower rotating field frequencies, ions in the presented m/z range are ejected from the rotating field region within the first rf period. In this case, each m/z is dispersed into a ring with a distinct radius, which is inversely proportional to m/z . In contrast, at higher frequencies, higher m/z ions that spend longer time in the field are subjected to an additional radial dispersion from the second rf period. As a result, some of the radii correspond to more than one m/z , which is detrimental to the mass-dispersive ion separation. Similar effect may be achieved by decreasing the kinetic energy of the ions. To avoid this folding, for a particular kinetic energy of the ion beam, the frequency of the rotating field is selected such that the m/z range of interest leaves the RWMA within one rf period.

3.3.2 Calibration

Eq. 3.1 is derived assuming that the rotating field is confined within the physical dimensions of the RWMA. However, the field strength along the instrument axis extracted from SIMION simulations shown in Figure 2.5 displays a penetration of the rotating field into the field-free region. This indicates that ions exiting the RWMA are still being influenced by the field. As a result, the experimentally observed deposition radius deviates from the radius calculated using Eq. 3.1. To correct for this deviation, we established a calibration procedure using a series of polyacrylamide (PAM) oligomers as the calibrants. Negative-mode ESI of PAM ($M_n = 1500$) produces deprotonated oligomer anions spaced by $m/z = 71$ (Figure 3.6 and Table 3.1).⁶⁴ The m/z values of the PAM oligomers used for the calibration are listed in Table 3.1. In a typical calibration procedure, IonCCD is mounted at a desired distance from the RWMA, and the radii of the PAM calibrant ions are extracted from the IonCCD profile with the RWMA operating at a desired frequency and amplitude. The experimentally determined radii of the oligomers are compared with the values predicted by the analytical equation. The initial rotating electric field strength is calculated using Eq. 3.1 assuming that the field is confined to the physical dimensions of the RWMA (i.e. the field length, D_f , equals 25.4 mm). The sum of squares of deviations between the calculated and experimentally determined radii is subsequently minimized using the GRG Nonlinear algorithm provided by Excel's Solver with the strength and length of the rotating field

being the only adjustable parameters. This calibration procedure is similar to the “Simplex Optimization” in time-of-flight mass spectrometry.⁶⁵ During the optimization, the total distance

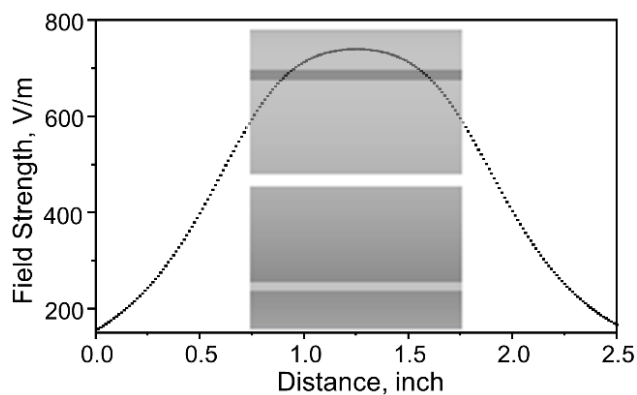


Figure 3.5 The rotating electric field strength along the main axis of the RWMA. The location of the RWMA relative to the plot is shown in the figure.

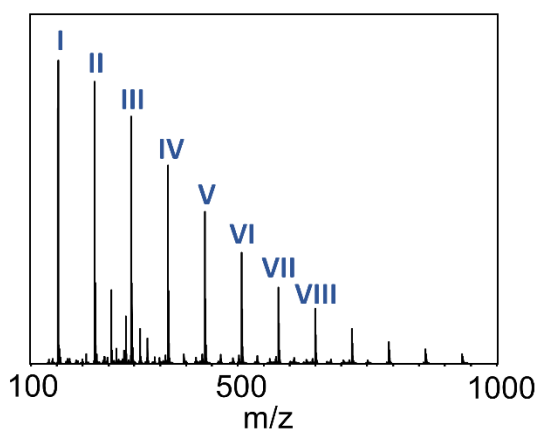


Figure 3.6 Negative ESI-MS spectrum of PAM ($M_n=1500$); m/z of the major oligomers observed in the spectrum (I to VIII) are listed in Table 2.1.

Table 3.1 m/z of the major oligomers observed in the spectrum (I to VIII) in Figure 2.6.

Peaks	m/z
I	152.0035
II	223.0401
III	294.0779
IV	365.1155
V	436.1527
VI	507.1901
VII	578.2271
VIII	649.2636

$(D_1 + D_2)$ is kept constant. In the calibration carried out with $f=70$ kHz, $V_{0-p}=10$ V, and IonCCD at a distance of 50.8 mm from the RWMA, with the PAM anions travelling through the RWMA at a kinetic energy of 35 eV/charge, the optimal length of the field was found to be $D_1=44.1$ mm, which is longer than the length of the RWMA. In addition, the optimized field strength of $E=705$ V/m is lower than the maximum field strength of 740 V/m extracted from the SIMION simulation (Figure 3.5). These findings are in agreement with our hypothesis that the penetration of the rotating field outside of the RWMA causes the observed deviation between the predicted and experimental radii and that the effective field length and field strength must be calibrated to obtain accurate peak assignments based on the experimentally-measured radii.

Next, we generated a calibration curve using Eq. 3.1 and the optimized parameters obtained from the calibration procedure. Figure 3.7 shows the calibration curves of the deposition radii, r , as a function of m/z at $f=70$ kHz (solid) and $f=50$ kHz (dashed) at an ion kinetic energy of 35 eV/charge. The curves were obtained using the calibrated rotating field strength ($E=705$ V/m) and length ($D_1=44.1$ mm). The radii of the PAM calibrant ions used for the calibration are labeled as filled circles in Figure 3.7. The performance of the calibration was examined using different types of charged analytes with the same instrument configuration. Specifically, we measured ion beam profiles for two multicomponent mixtures using the RWMA with the IonCCD positioned 50.8 mm away from the analyzer. The first mixture is composed of organic dyes generating singly-charged ions and the second mixture generates singly charged ammonium adducts of PDMS oligomers.⁶⁶ The kinetic energy of the ions was 35 eV. The rotating field frequencies employed for dispersion of the dyes and the PDMS oligomers were 70 kHz and 50 kHz, respectively. The experimentally determined radii are shown in Figure 3.7 and Table 3.2. We observe a ~2% relative error of the calculated radii from the experimental values for the PDMS oligomers (Table 3.2). This demonstrate that the same calibration parameters can be used for different frequencies of the rotating field and for ions of both polarities.

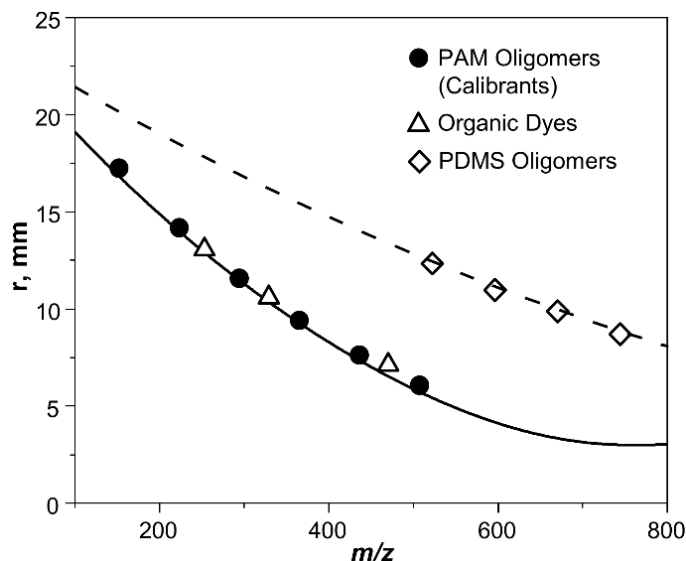


Figure 3.7 Plots of the calibrated deposition radii vs m/z at $f=70$ kHz (solid) and $f=50$ kHz (dashed). The experimental data points are shown for PAM calibrants (filled circles), organic dyes (open triangles), and PDMS oligomers (open diamonds). The r values were calculated using Eq. 1 using the effective rotating field strength (E) and length of the field (D_1) obtained from the calibration.

Table 3.2 m/z of the major oligomers observed in the spectrum (I to VIII) in Figure 2.7.

	m/z	r , experiment (mm)	r , calibration (mm)	Relative Error
I	253.17	13.1±0.1	12.9	1.5%
II	329.20	10.6±0.0	10.4	1.9%
III	470.26	7.0±0.2	6.5	7.1%
IV	522.19	12.3±0.1	12.4	0.8%
V	596.20	11.0±0.1	11.3	2.7%
VI	670.22	9.9±0.1	10.0	1.0%
VII	744.24	8.7±0.0	8.9	2.3%

In the field of mass spectrometry, mass calibration is commonly conducted using a polynomial curve fitting, in which calibrant ions are selected to cover the m/z range of interest. Mass calibration of high m/z species typically requires a series of high m/z calibrant ions. In contrast, we find that mass calibration of the RWMA conducted using the low m/z PAM oligomers can be used for a much broader m/z range of interest independent of the charge state and kinetic energy of the ions. In this experiment, we generated multiply-charged ubiquitin (8.6 kDa) ions using ESI of an acidified solution. Figure 3.8(a) shows an LTQ mass spectrum of a 5 μ M ubiquitin in 49:49:1:1 methanol/H₂O/CH₃COOH/glycerol (v/v/v/v). We observe a distribution of charge states ranging from 7+ to 13+, with 9+ showing the highest abundance.⁶⁷ The same solution was

used to generate an ion beam in the soft landing instrument for the RWMA separation. [We note that the ESI interfaces of the LTQ and our custom-designed soft-landing instrument are quite different. As a result, the abundances of the individual charge states are likely different on the two instruments.] The resulting IonCCD beam profile acquired with the rotating field of $f=40$ kHz at a distance of 50.8 mm from the exit of the RWMA and the kinetic energy of 30 eV/charge is shown in Figure 3.8(b). We observe several pairs of peaks symmetrically located around the center of the x axis ($x=0$) corresponding to different charge states of ubiquitin. In particular, four pairs of peaks with decreasing radii were assigned to +11, +10, +9, +8 charge states. The experimentally obtained radii were subsequently compared with the predicted values using the calibrated parameters listed in Table 2.3. We find a good match between the predicted and experimental radii indicating the robustness of the calibration procedure and accurate charge state assignments. The relative errors of the calibration are $\sim 0.7\%$.

Table 3.3 Experimentally-determined radii of the ubiquitin ions and the values predicted using calibrated Equation 3.1 along with the corresponding relative errors.

Charge State	m/z	r, experiment (mm)	r, calibration (mm)	Relative Error
8+	1070.61	9.3 \pm 0.0	9.4	1.1%
9+	951.65	10.8 \pm 0.1	10.9	0.9%
10+	856.48	12.2 \pm 0.1	12.2	0.0%
11+	778.62	13.4 \pm 0.0	13.3	0.7%

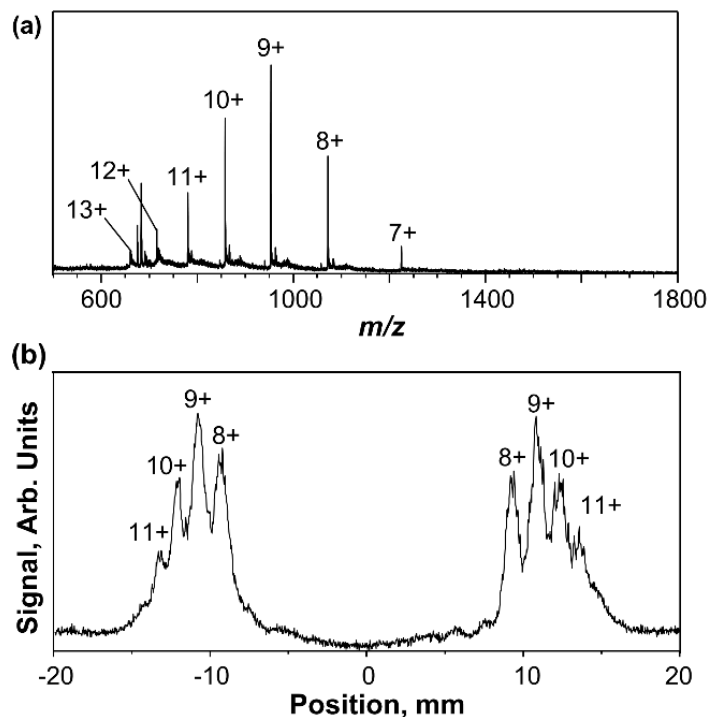


Figure 3.8 (a) An ESI mass spectrum of 5 μM ubiquitin in 49:49:1:1 methanol/ H_2O / CH_3COOH /glycerol (v/v/v/v) showing a distribution of charge states ranging from 7+ to 13+. (b) An IonCCD profile of ubiquitin ions separated by the RWMA operated at a frequency of $f=40$ kHz. The charge state assignment of each peak is labeled in the profile.

Based on these results, it is reasonable to conclude that the same calibration parameters obtained using PAM oligomers can be readily adapted to other ion mixtures independent of the polarity, charge state, kinetic energy of the ions, and the frequency of the rotating field. In addition, because the effective field strength and length are independent of m/z , it is reasonable to assume that the calibration parameters obtained using low- m/z PAM can be used to predict the radii of high m/z ions. Our previously reported results for 33.7 kDa $\text{Au}_{144}(\text{SC}_4\text{H}_9)_{60}$ ions are consistent with this assertion.⁶⁰

3.3.3 Mass Resolution

In mass spectrometry, mass resolution is defined as the ratio of m/z and full-width-at-half-maximum (FWHM) of the peak in a mass spectrum. Similarly, mass resolution of the RWMA is determined by the spatial separation of the individual components and is calculated by taking the ratio of the deposition radius (r) to the width of the ring (Δr). We estimate mass resolution of this device based on the ion beam profile obtained from the IonCCD, in which the ring is detected as

a pair of peaks separated by a distance corresponding to the diameter of the ring. The radius of the ring is determined from the measured separation distance between the two peaks and the width of the ring corresponds to the FWHM of the individual peak.

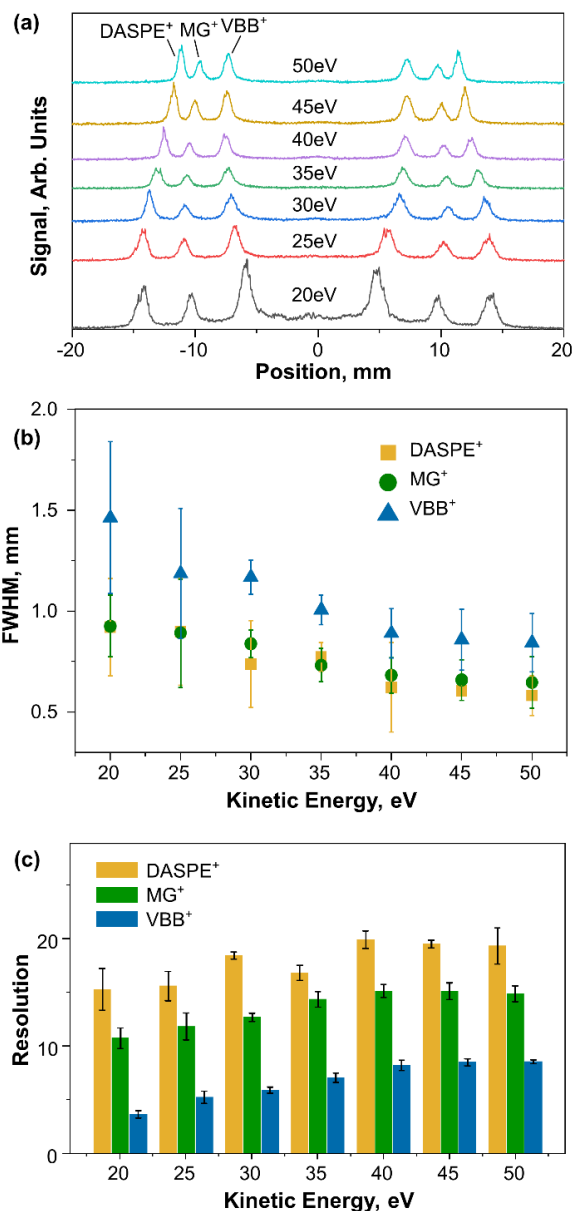


Figure 3.9 (a) IonCCD profile of a mixture of the three dyes acquired using RWMA operated at $f=70$ kHz, $10 V_{0-p}$ at different kinetic energies. (b) The FWHMs of the peaks in the profiles shown in (a) and the corresponding values of mass resolution (c).

Mass resolution of the RWMA in its current configuration was experimentally determined using a standard mixture containing three organic dyes. Specifically, a beam containing positively-

charged DASPE⁺ (m/z 253.2), MG⁺ (m/z 329.2) and VBB⁺ (m/z 470.3) was separated using the RWMA operated at $f=70$ kHz, $10 V_{0-p}$, with the IonCCD positioned at a distance of 2'' from the device. Typical ion beam profiles acquired at kinetic energies ranging from 20 eV to 50 eV are shown in Figure 3.9(a). Three pairs of peaks symmetrically located around the center of each profile are assigned to the three singly-charged dyes, with lower m/z corresponding to peaks at larger radii. The profiles were subsequently fitted with sums of Lorentzian distributions, from which the FWHM values were extracted (Figure 3.10). Figure 3.9(b) and (c) shows the FWHM and mass resolution of the peaks of the dyes obtained by averaging the values of FWHM from three repeated measurements and from both the left and right side of the profiles. From this experiment, we conclude that the upper limit of mass resolution ($m/\Delta m$) of ~ 20 is achievable for the RWMA in its current configuration, which is comparable to the mass resolution of mass analyzers typically used in nanocluster research ($m/\Delta m=20-50$).⁶⁸

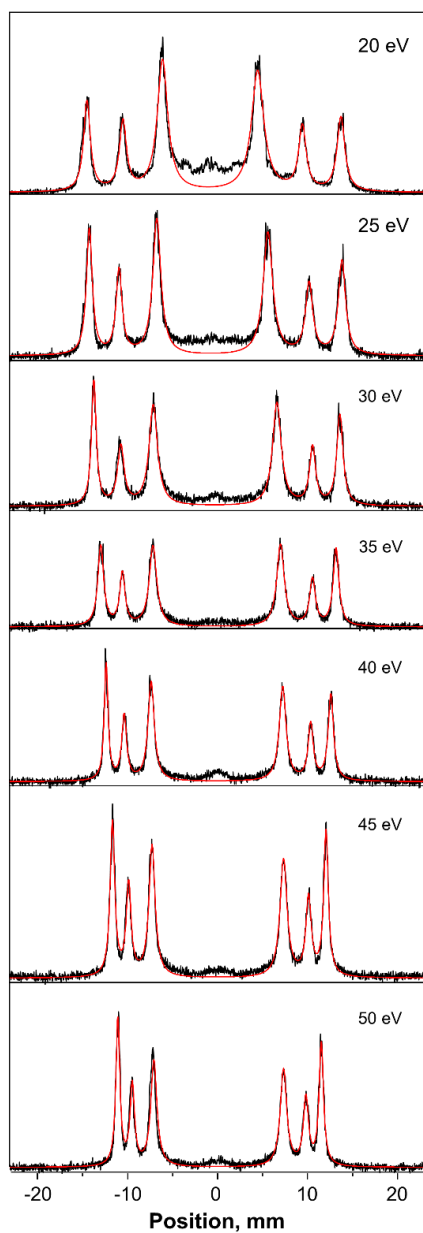


Figure 3.10 Experimental IonCCD profiles (black) and simulated profiles (red) using sums of best-fit Lorentzian distributions of the beam of the dye mixture at different kinetic energies.

In addition, we observe that, for all the ions, peak width decreases with an increase in kinetic energy. In fact, a similar trend in the beam width was obtained when the rotating field was switched off, with a higher energy ion beam showing a narrower profile (data not shown). This is attributed to the known difficulty in focusing of lower-energy ion beams. Furthermore, the VBB^+ peak is slightly broader than peaks of MG^+ and $DASPE^+$ at all kinetic energies, while the peak widths of MG^+ and $DASPE^+$ are similar.

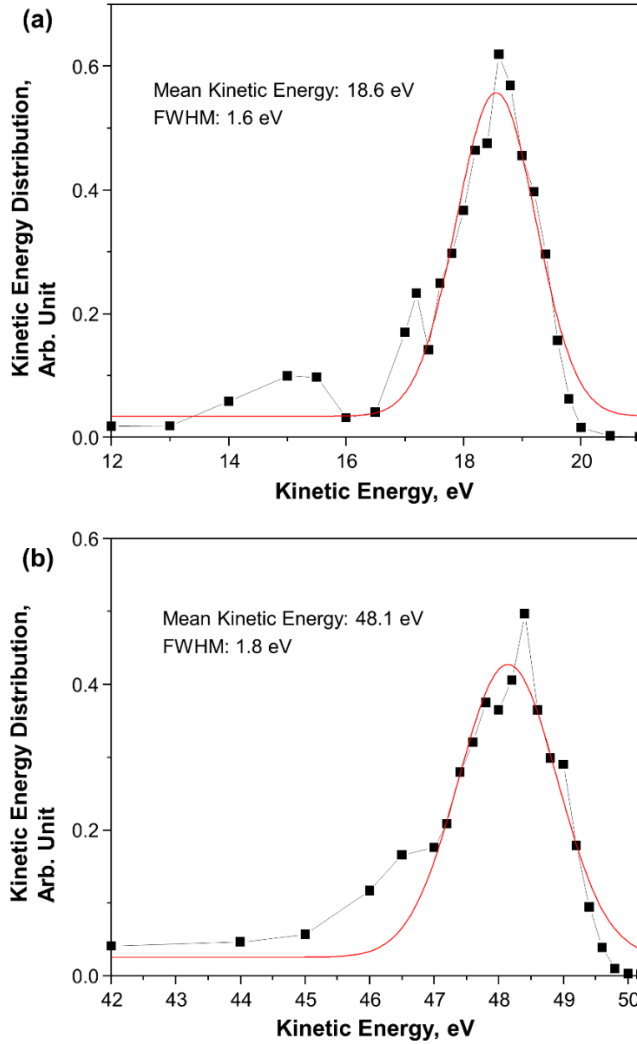


Figure 3.11 Kinetic energy distributions of the dyes at 20 eV (a) and 50 eV (b). The black and red traces represent the experimental first derivative of the retarding voltage plot and the Gaussian-fitted curve, respectively.

In the following, we carried out a set of SIMION simulations to reproduce the realistic experimental conditions. In the electrode geometry, we implemented a conductance limit plate and einzel lens in front of the RWMA (Figure 3.1(c)). In each simulation scenario, ion beam containing the three dyes was produced at the conductance limit plate and sent through the einzel lens and RWMA to the collector plate. The locations of the individual ion splats on the collector plate positioned 2” away from the RWMA were recorded for 12,000 ions of each m/z . The distances between the ion landing locations and the center of the surface were subsequently extracted and used to construct histograms (bin width=0.01 mm) of the deposition ring radii. The histograms were fitted with Gaussian distributions, and the FWHMs were extracted as the simulated FWHMs

of the deposition rings. Due to the physical restrictions of the instrument, we cannot measure the width of the beam at the conductance limit. However, the kinetic energy distribution (KED) of the beam can be measured using a retarding potential method described in detail in the Experimental section. In particular, we measured the KED of the ion beam at a distance of 12.7 mm out of the einzel lens where the RWMA is typically positioned. The mean KED and FWHM measured experimentally are 18.6 eV and 1.6 eV, respectively, for the flatpole bias of 20 V and 48.1 eV and 1.8 eV, respectively, for the flatpole bias of 50 V (Figure 3.11). These values were used as the initial beam conditions in SIMION simulations. Due to the unknown initial width of the beam at the conductance limit, we performed a series of simulations with different initial beam widths ranging from 0.5 mm to 2 mm (filled circle distribution) to cover a broad range of possible scenarios. For each beam width, we systematically adjusted the voltage on the second element of the einzel lens to achieve the best focusing on the surface. Figure 2.12 shows the optimal simulated distributions of the deposition radii for beam kinetic energies of 20 eV and 50 eV. The experimental ion beam profiles and the corresponding Lorentzian curve fitting results are shown for comparison. The best matches between the simulated and experimental beam profiles were obtained using the initial beam width of 1 mm and 0.7 mm for beam kinetic energies of 20 eV and 50 eV, respectively. The einzel lens voltages providing best focusing in the simulations were 1.2 V/-50 V/1.2 V and 25.5 V/-25 V/25.5 V for 20 and 50 eV ion beams, which are in close agreement with the experimentally obtained voltages of 1.2 V/-40.1 V/1.2 V and 25.5 V/-22.6 V/25.5 V for 20 and 50 eV ion beams, respectively. At both kinetic energies, the simulated widths of the deposition rings are similar for all the m/z .

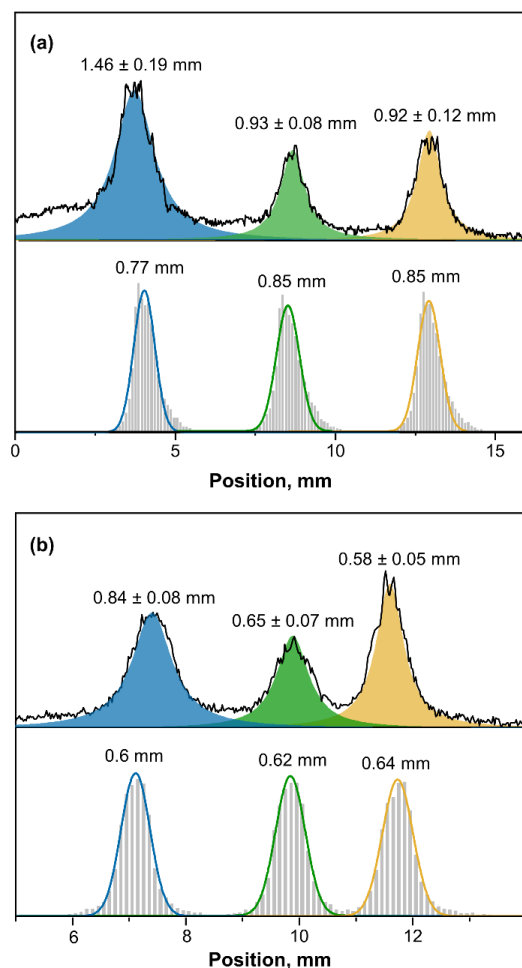


Figure 3.12 Experimental beam profiles (top black trace) and the corresponding profiles generated using SIMION simulations (light grey bars) of the three dyes at kinetic energies of 20 eV (a) and 50 eV (b). Yellow, green, and blue areas/curves on the top/bottom of each panel represent Lorentzian profiles obtained from the best fit of the underlying peaks of DASPE⁺ (m/z 253.2), MG⁺ (m/z 329.2) and VBB⁺ (m/z 470.3), respectively.

Based on the simulation results discussed above, we conclude that the focusing conditions of the einzel lens have a pronounced effect on the mass resolution of the RWMA. However, it is not clear from these simulations how the mass resolution is affected by the two important intrinsic parameters of the ion beam, the FWHM and KED. In the following, we describe a series of SIMION simulations with an isolated RWMA configuration shown in Figure 3.1(d) to understand how the rotating field affects the width of the deposition ring. In particular, we generated ion beams of DASPE⁺ (m/z 253.2) of different widths in the source (FWHM of 0.5 mm, 1 mm, 1.5 mm, and 2 mm along with 0 mm corresponding to a point source) with the KED of FWHM of 0.2 eV, 1 eV and 2 eV centered at 20 eV/charge. The results of the simulations are summarized in Figure 3.13.

We observe that the width of the deposition ring decreases with decrease in both the beam width and FWHM of the KED. However, the observed trend is strongly dependent on the width of the KED. In particular, for a relatively narrow KED (FWHM of 0.2 eV and 1 eV), the width of the deposition ring shows a near proportional decrease with decrease in the initial beam width. In contrast, for a broader KED (FWHM of 2 eV), the extent of decrease in the width of the deposition ring is not as pronounced especially when the initial beam is very narrow. These results indicate a substantial deterioration of the device performance with an increase in the KED spread. It follows that an improvement in mass resolution of the RWMA may be achieved only by narrowing both the beam width and KED simultaneously.

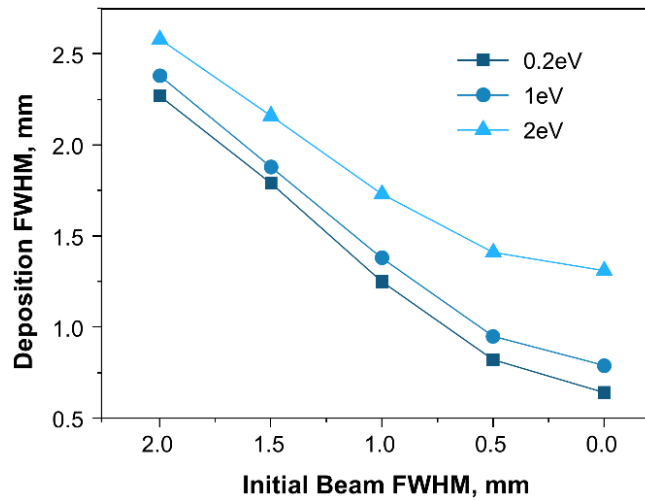


Figure 3.13 Simulated FWHM of the deposition ring of DASPE⁺ (m/z 253.2) with Gaussian-shaped KEDs of 0.2 eV, 1 eV and 2 eV FWHM centered at 20 eV/charge and various initial beam widths (0 mm, 0.5 mm, 1 mm, 1.5 mm and 2 mm).

Based on the SIMION simulations, we conclude that both the initial width and KED of the ion beam have a pronounced effect on mass resolution of the RWMA. Higher mass resolution can be obtained using a narrow parallel ion beam with a narrow KED. A narrow ion beam can be generated using either two einzel lenses or a collisional multipole with a small conductance limit aperture. Meanwhile, the narrow KED can be obtained by minimizing the acceleration gradient at the exit of the collisional flatpole in our existing instrument. In addition, it has been demonstrated that an ion beam with a narrow KED of ~ 0.2 eV can be generated by extending the collisional

multipole into the high vacuum region⁶⁹ or by employing an exponential lens^{70,71} to eliminate the kinetic energy spread of the ion beam.

3.3.4 Deposition of High- m/z Nanoclusters

The ability of RWMA to separate high-mass ions using low rf amplitudes is demonstrated using an atomically-precise Au₁₄₄(SC₄H₉)₆₀ cluster (33.7 kDa) as a model system.⁷² Owing to its distinct electrochemical,⁷² optical,⁷³⁻⁷⁵ biological,⁷⁶ and catalytic properties,^{77,78} Au₁₄₄(SR)₆₀ (Figure 3.14) is one of the most widely studied thiolated gold clusters. Previous studies employed ESI-MS to determine the composition of atomically-precise Au₁₄₄(SR)₆₀ clusters;^{63,79} structural characterization was performed using scanning transmission electron microscopy (STEM),⁸⁰ nuclear magnetic resonance,⁶³ single-crystal X-ray diffraction⁸¹ along with theoretical calculations.^{63,80,82} In this experiment, we do not attempt to separate this cluster from a mixture but rather demonstrate that a specific charge state of the Au₁₄₄(SR)₆₀ cluster may be deposited onto a surface for subsequent structure determination. Furthermore, the high-flux deposition of cluster ions reported in this study provides a direct path for the preparation of cluster-based multilayered assemblies.

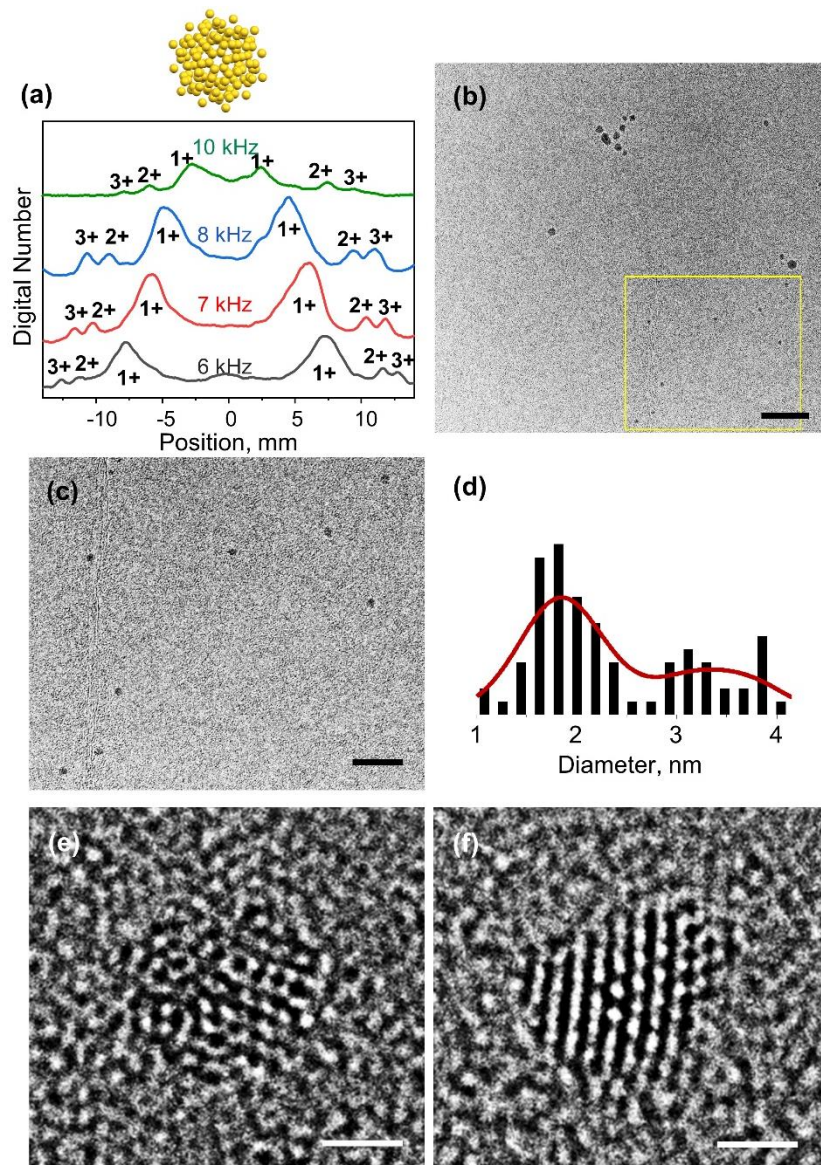


Figure 3.14 a) Gold atom arrangement in an atomic structure of $\text{Au}_{144}(\text{SCH}_2\text{Ph})_{60}$ ⁸¹ and the IonCCD beam profile showing $\text{Au}_{144}(\text{SC}_4\text{H}_9)_{60}^{n+}$ ($n=1,2,3$) separated by RWMA at $f=6/7/8/10$ kHz, $10 V_{0-p}$ when the IonCCD was positioned $1''$ after RWMA. The charge states of $\text{Au}_{144}(\text{SC}_4\text{H}_9)_{60}$ are labelled on top of the peaks. b) TEM images of $\text{Au}_{144}(\text{SC}_4\text{H}_9)_{60}^+$ deposited onto graphene-coated Cu grid acquired at 300 kV acceleration voltage, scale bar: 20 nm. c) An expanded view of an area of the TEM image highlighted with the yellow-squared area in panel b) containing monodisperse $\text{Au}_{144}(\text{SC}_4\text{H}_9)_{60}^+$ clusters, scale bar: 10 nm. d) A cluster size distribution extracted from the TEM image in b). e) A representative HRTEM image of an individual $\text{Au}_{144}(\text{SC}_4\text{H}_9)_{60}^+$ cluster acquired at 300 kV acceleration voltage. f) HRTEM image of the cluster shown in E) after electron beam irradiation. Scale bar=1 nm.

In these experiments, cationic $\text{Au}_{144}(\text{SC}_4\text{H}_9)_{60}$ clusters produced by ESI were separated using the RWMA operating at $f=7$ kHz and $V_{0-p}=10$ V. We obtained almost 1 nA of ion current for $\text{Au}_{144}(\text{SC}_4\text{H}_9)_{60}$ cluster on a surface positioned after the RWMA. The kinetic energy of the ions

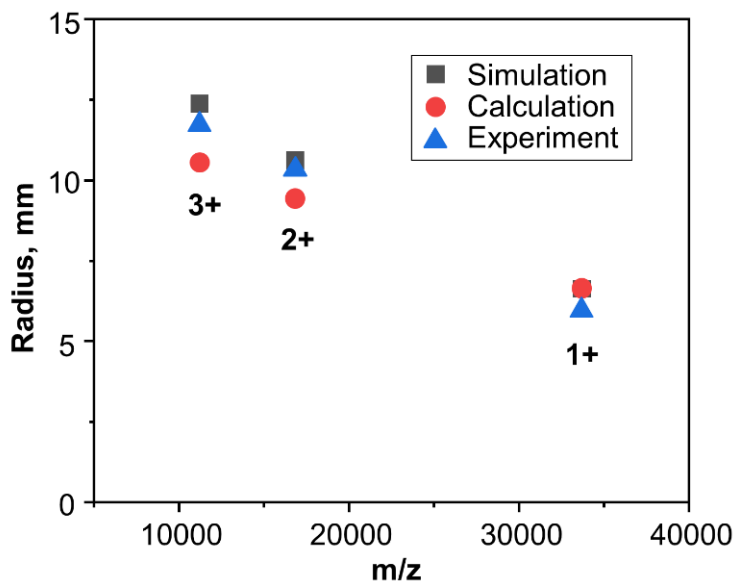


Figure 3.15 Deposition radius of $\text{Au}_{144}(\text{SC}_4\text{H}_9)_{60}^{n+}$ ($n=1,2,3$) from SIMION simulations, analytical expression (equation 10), and experiments at $f=70$ kHz, $V_{0-p}=10$ V with the IonCCD positioned 1'' away from RWMA.

entering the RWMA was 35 eV/charge. IonCCD mounted 1'' away from the RWMA showed two major peaks corresponding to singly-charged $\text{Au}_{144}(\text{SC}_4\text{H}_9)_{60}^+$ ions ($m/z=33.7\text{k}$) (Figure 3.14(a)). In addition, we observed minor signals of $\text{Au}_{144}(\text{SC}_4\text{H}_9)_{60}^{2+}$ ($m/z=16.9\text{k}$) and $\text{Au}_{144}(\text{SC}_4\text{H}_9)_{60}^{3+}$ ($m/z=11.2\text{k}$) at larger radii, which agrees with previously reported charge state distribution of $\text{Au}_{144}(\text{SR})_{60}$ in ESI-MS.^{63,79} The results obtained at different frequencies of the rotating field are shown in Figure 3.14(a) as well. The experimentally observed radii of $\text{Au}_{144}(\text{SC}_4\text{H}_9)_{60}$ cations are consistent with the simulated values (Figure 3.15). Furthermore, we show in Figure 3.16 the ability to separate the charge state distribution of Apoferritin (480 kDa), a cage-like protein complex extensively studied by cryogenic electron microscopy¹⁶ and native MS.⁸³

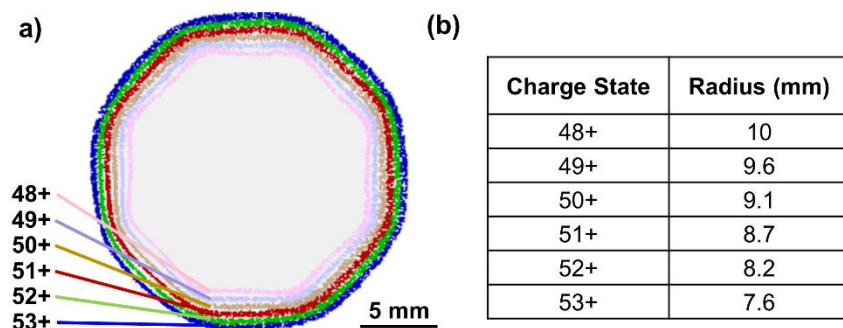


Figure 3.16 a) SIMION simulations of the native charge state distribution of Apoferritin (480 kDa)⁸³ separated by RWMA operating at $f=10$ kHz, $V_{0-p}=10$ V. The collecting plate is positioned 3'' away from the RWMA. The kinetic energy of the ions is 5 eV/charge. The scale bar in the picture is 5 mm. b) Deposition radius of different charge states of Apoferritin extracted from SIMION simulations presented in (a).

We used the same conditions to deposit singly-charged $\text{Au}_{144}(\text{SC}_4\text{H}_9)_{60}^+$ clusters onto a graphene-coated TEM copper grid. A specially-designed TEM grid holder was used to position the grid within the ring-shaped $\text{Au}_{144}(\text{SC}_4\text{H}_9)_{60}^+$ ion beam (Figure 3.17). To ensure gentle

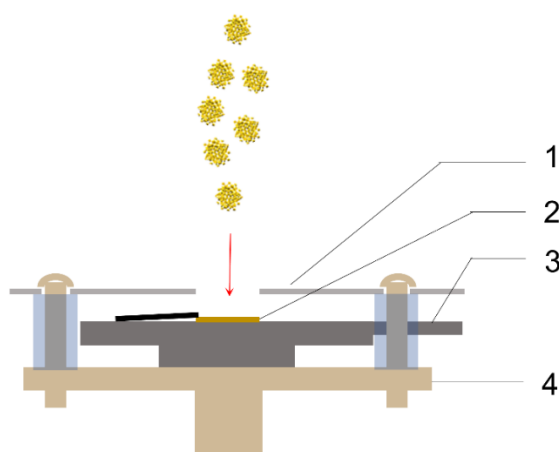


Figure 3.17 Schematic diagram of the TEM grid holder used for $\text{Au}_{144}(\text{SC}_4\text{H}_9)_{60}$ cluster deposition. 1: grounded mask with a 3 mm diameter aperture in the center; 2: TEM grid; 3: current collector; 4: PEEK adapter connected to a XYZ positioner.

deposition, the kinetic energy of the cluster was reduced to ~ 3 eV by biasing the grid. Both TEM (Figure 3.14(b) and 6.14(c)) and STEM (Figure 3.18) images confirm that a substantial fraction of $\text{Au}_{144}(\text{SC}_4\text{H}_9)_{60}$ clusters are deposited uniformly as dimensionally intact species with the expected diameter of ~ 1.8 nm.⁸¹ The bimodal cluster size distribution (Figure 3.14(d)) indicates that some

of the clusters aggregate on the TEM grid as also seen in Figure 3.14(b). The aggregation is likely driven by the mobility of the $\text{Au}_{144}(\text{SC}_4\text{H}_9)_{60}$ clusters on the TEM grid at room temperature and could be either induced by the electron beam or thermal processes on the surface.⁸⁰ Similar bimodal size distribution has been previously reported for $\text{Au}_{25}(\text{S}(\text{CH}_2)_2\text{Ph})_{18}$ clusters drop casted onto TEM grids.⁸⁴

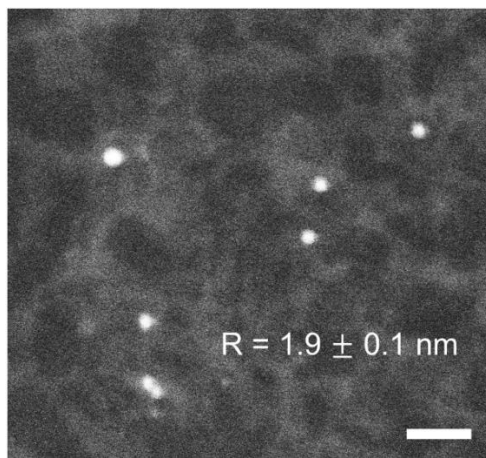


Figure 3.18 STEM image of deposited $\text{Au}_{144}(\text{SC}_4\text{H}_9)_{60}^+$ on graphene-coated Cu grid. The average cluster diameter is labeled. Scale bar: 10 nm.

A representative high-resolution TEM (HRTEM) image of an individual $\text{Au}_{144}(\text{SC}_4\text{H}_9)_{60}$ cluster is shown in Figure 3.14(e). The observed cluster core is consistent with the known icosahedral structure of $\text{Au}_{144}(\text{SR})_{60}$.⁸¹ However, we cannot rule out possible beam-induced rearrangement of the cluster. Indeed, a substantially different face-centered cubic- (*fcc*-) like gold core arrangement was observed for the same cluster after several frame shots (Figure 3.14(f)). Additional HRTEM images are shown in Figure 3.19. The observed rearrangement is attributed to the acceleration voltage used in the study. It has been shown that radiation damage of $\text{Au}_{144}(\text{SC}_2\text{H}_4\text{Ph})_{60}$ clusters may be minimized using a lower acceleration voltage of 80 kV.^[23] Regardless, the apparent low level of background noise in the sample prepared by ion soft landing results in the enhanced image contrast observed in HRTEM experiments. The use of RWMA substantially expands the range of ion soft landing applications in nanocluster research bringing it to the boundary between nanoclusters and nanocrystals. The uniform deposition of $\text{Au}_{144}(\text{SC}_4\text{H}_9)_{60}$ clusters onto TEM grids enabled by this technique is particularly advantageous for their structure

determination using low electron-dose HRTEM single-particle reconstruction⁸⁵ and STEM nanobeam electron diffraction.^{80,86}

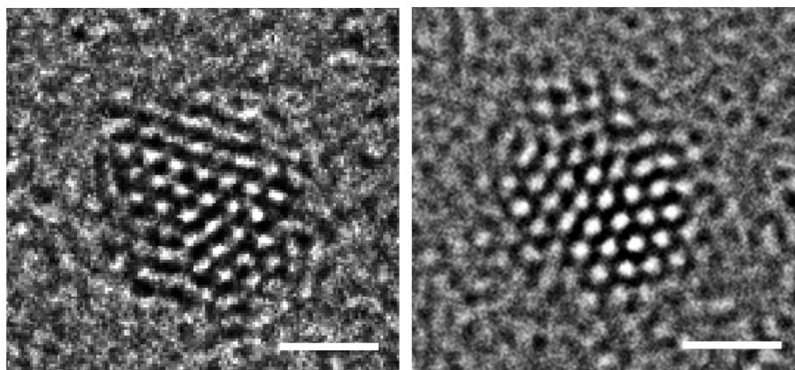


Figure 3.19 Representative HRTEM images of individual $\text{Au}_{144}(\text{SC}_4\text{H}_9)_{60}^+$ on graphene-coated Cu grid showing fcc-like Au core arrangement. Scale bar=1 nm.

3.3.5 High-Throughput Deposition of Multicomponent Mixtures

Separation and simultaneous deposition of ions with different m/z by spreading them onto a surface based on their m/z is another important attribute of RWMA. This capability facilitates high-throughput deposition of species present in multicomponent mixtures, which is of interest to the rapid screening of their mass- or size-dependent properties. We note that when mass filtering is employed in preparative mass spectrometry experiments focused on separating and screening components of mixtures, the experimental throughput is determined by the complexity of the mixture. In contrast, mass-dispersive devices such as RWMA enable simultaneous deposition of all the components onto distinct locations on a surface determined by their m/z . In addition, mass-dispersive soft landing of mixtures may be used to prepare physical and chemical gradients on surfaces.^{87,88}

Polymer surfaces with a wettability gradient have been used in biomedical research for protein adsorption and cell adhesion.⁸⁹ In this study, we prepared a wettability gradient by spreading hydrophilic polyacrylamide (PAM) oligomers onto a hydrophobic fluorinated self-assembled monolayer (FSAM) surface. In this experiment, different oligomers are deposited onto different rings on the surface. We expect that the hydrophilicity of the surface manifested by a decrease in the contact angle will increase with the length of the hydrophilic oligomer.

Traditionally, contact angle measurement between a surface and a water droplet is used to evaluate the hydrophilicity or hydrophobicity of a surface. Hydrophilic surfaces are characterized by contact angles $<90^\circ$ and hydrophobic surfaces display contact angles $>90^\circ$. A negative-mode ESI-MS spectrum of PAM ($M_n=1500$) shown in Figure 3.6 contains deprotonated oligomer anions spaced by $71 m/z$.⁹⁰ A mixture of PAM oligomers was separated using RWMA operated at $f=70$ kHz and $V_{0-p}=10$ V. IonCCD positioned at a distance of 2'' from the RWMA showed an eagle-wing-like beam profile composed of multiple rings corresponding to the oligomer series (Figure 3.20(a)). The prepared surface was analyzed by spatially-resolved nanospray desorption electrospray ionization (nano-DESI) MS.⁹¹ In this experiment described in detail elsewhere,⁶² line scans were acquired across the deposition area providing information on the spatial localization of individual oligomers. The resulting profile of the spatial distribution of the oligomers is shown in Figure 3.20(b). The total oligomer signal (black trace in Figure 3.20(b)) is consistent with the IonCCD profile (Figure 3.20(a)) confirming the spatial separation of oligomeric species on the surface based on their m/z . As expected, the diameter of the ring decreases with an increase in m/z of the oligomer. The mass resolution of the RWMA was determined by taking the ratio of the deposition radius of an individual component and the FWHM of the peak observed in the nano-DESI profile.

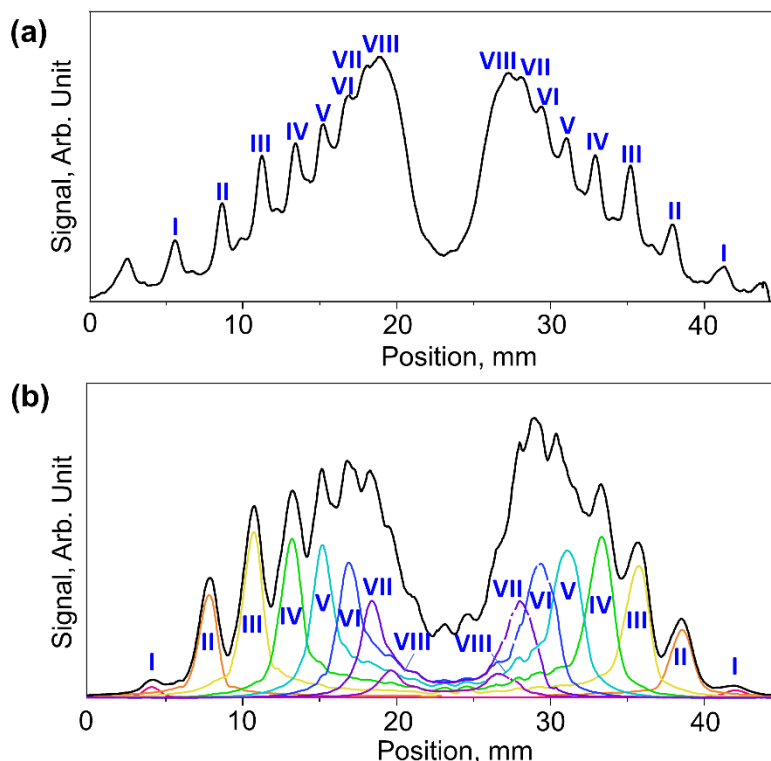


Figure 3.20 (a) IonCCD beam profile of the PAM oligomers with RWMA operating at $f=70$ kHz, $V_{0-p}=10$ V with the IonCCD positioned 2'' after RWMA; peaks corresponding to different oligomers are marked in the figure. (b) Nano-DESI line scan along the deposition region showing extracted ion signals for different oligomers (colored lines) and total ion signal (black line).

The presence of the wettability gradient on the surface containing the PAM oligomers was confirmed using contact angle measurements (Figure 3.21(a)). Small water droplets ($1 \mu\text{L}$) were placed on the surface from the edge to the center where PAM oligomers of increased length were deposited. We observe that the contact angle of the surface decreases with an increase in the oligomer size indicating a gradual increase in the hydrophilicity of the surface. Further evidence of the wettability gradient was inferred from nano-DESI experiments. Specifically, we observed that the peak width of the nano-DESI profiles of individual oligomers increases with oligomer size (Figure 3.22). This broadening of the individual profiles is attributed to an increase in the size of the liquid bridge when it is brought in contact with the more hydrophilic part of the surface containing larger oligomers. This observation is consistent with the contact angle measurements.

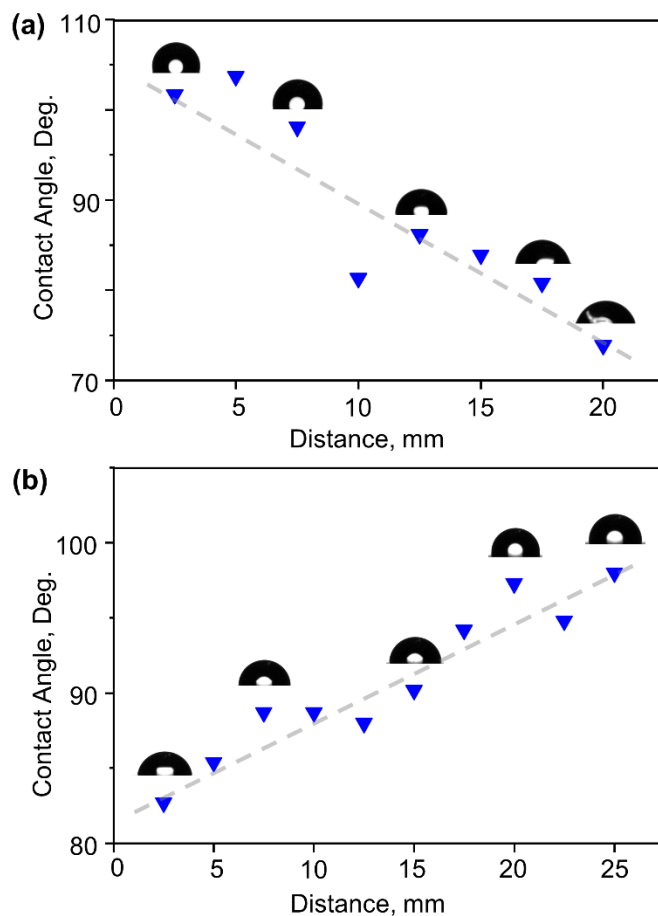


Figure 3.21 Contact angles of the (a) hydrophobic FSAM surface covered with hydrophilic PAM oligomers and (b) hydrophilic gold surface covered with hydrophobic PDMS oligomers. The x coordinate of the plot corresponds to the distance between the point of measurement and the edge of the surface. The grey dashed lines are shown to guide the eye.

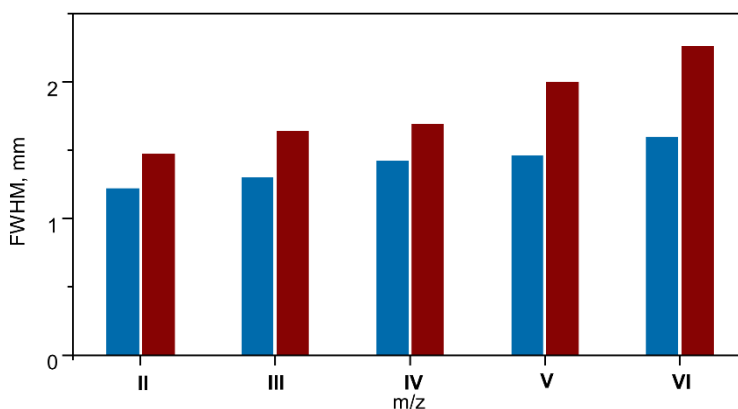


Figure 3.22 Full-width-at-half-maximum (FWHM) of the nano-DESI profiles of PAM oligomers II through VI on the left side (blue bars) and right side (red bars) of the line scan in Figure 2.20.

In another experiment, we generated a different wettability gradient by depositing hydrophobic polydimethylsiloxane (PDMS) oligomers onto a hydrophilic bare gold surface. We anticipate an increase in hydrophobicity from the edge to the center of the surface where longer PDMS oligomers were deposited. Positive-mode ESI-MS spectrum of PDMS ($M_n \sim 580$) contains ammonium adducts of PDMS oligomers separated by 74 m/z (Figure 3.23). Figure 2.24 shows the IonCCD beam profile of the mixture of PDMS oligomers separated using RWMA operated at frequency of $f=50 \text{ kHz}$ and amplitude of $V_{0-p}=10 \text{ V}$. Figure 3.21(b) shows the contact angles of the prepared surface from the edge to the center where longer-chain PDMS oligomers were deposited. As expected, deposition of PDMS oligomers of longer chain length results in increased hydrophobicity of the surface.

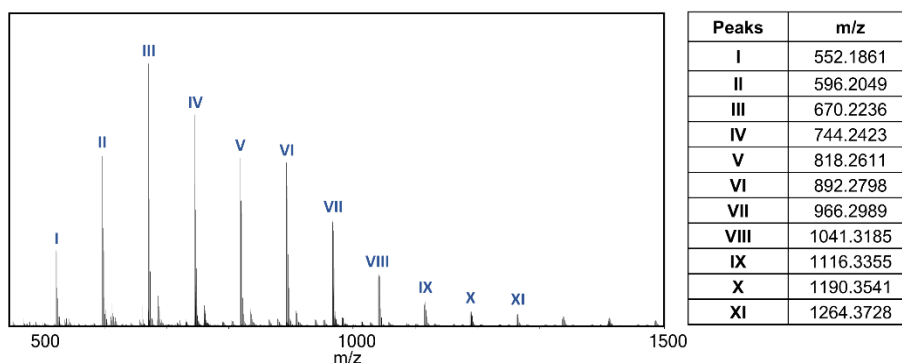


Figure 3.23 A positive mode ESI-MS spectrum of PDMS ($M_n \sim 580$); m/z of the major oligomers observed in the spectrum (I to XI) are listed in the table.

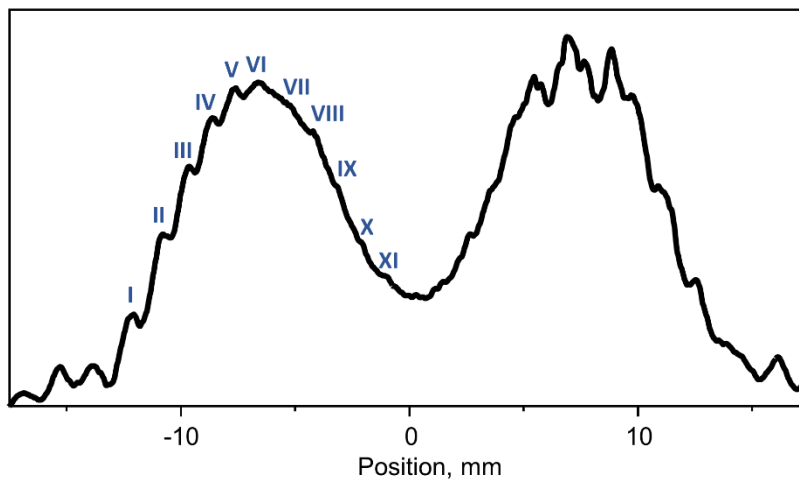


Figure 3.24 IonCCD beam profile of the PDMS oligomers with RWMA operating at $f=50 \text{ kHz}$, $V_{0-p}=10 \text{ V}$; peaks corresponding to different oligomers are marked in the figure.

3.4 Conclusions

In conclusion, we present the performance of a mass-dispersive device, RWMA, for ion soft landing research. Ions of different m/z travelling through the device are separated onto distinct rings of different radii on a surface. We present an analytical expression for predicting the deposition radius of ions. The separation performance for ions in different range of m/z and kinetic energy can be optimized by adjusting the frequency of the rotating electric field. In addition, we describe a universal calibration of the device using a series of polyacrylamide ions to obtain a reliable prediction of the deposition radii for unknown analytes. Moreover, ion trajectory simulations and experiments demonstrate that mass resolution of the device can be improved by minimizing the width and kinetic energy spread of the ion beam. The use of RWMA greatly reduces the complexity and cost of preparative mass spectrometry instrumentation due to the moderate vacuum requirement ($<10^{-3}$ Torr) and simple electronics. These characteristics of the RWMA make it a promising candidate for the development of inexpensive and transportable preparative mass spectrometers.⁹² Such affordable ion deposition systems would facilitate the use of preparative mass spectrometry in applications in photonics, memory storage, molecular electronics, catalysis, and biology.

3.5 References

- (1) Palmer, R. E.; Cai, R.; Vernieres, J. Synthesis without solvents: The cluster (nanoparticle) beam route to catalysts and sensors. *Acc. Chem. Res.* **2018**, *51*, 2296-2304.
- (2) Laskin, J.; Johnson, G. E.; Warneke, J.; Prabhakaran, V. From Isolated Ions to Multilayer Functional Materials Using Ion Soft Landing. *Angew. Chem. Int. Ed.* **2018**, *57*, 16270-16284.
- (3) Vernieres, J.; Steinhauer, S.; Zhao, J.; Grammatikopoulos, P.; Ferrando, R.; Nordlund, K.; Djurabekova, F.; Sowwan, M. Site-Specific Wetting of Iron Nanocubes by Gold Atoms in Gas-Phase Synthesis. *Adv. Sci.* **2019**, 1900447.
- (4) Kaposi, T.; Joshi, S.; Hoh, T.; Wiengarten, A.; Seufert, K.; Paszkiewicz, M.; Klappenberger, F.; Ecija, D.; Đorđević, L.; Marangoni, T. Supramolecular spangling, crocheting, and knitting of functionalized pyrene molecules on a silver surface. *ACS nano* **2016**, *10*, 7665-7674.
- (5) Verbeck, G.; Hoffmann, W.; Walton, B. Soft-landing preparative mass spectrometry. *Analyst* **2012**, *137*, 4393-4407.

- (6) Rauschenbach, S.; Ternes, M.; Harnau, L.; Kern, K. Mass spectrometry as a preparative tool for the surface science of large molecules. *Ann. Rev. Anal. Chem.* **2016**, *9*, 473-498.
- (7) Johnson, G. E.; Hu, Q.; Laskin, J. Soft landing of complex molecules on surfaces. *Ann. Rev. Anal. Chem.* **2011**, *4*, 83-104.
- (8) Johnson, G. E.; Gunaratne, D.; Laskin, J. Soft-and reactive landing of ions onto surfaces: Concepts and applications. *Mass Spectrom. Rev.* **2016**, *35*, 439-479.
- (9) Cyriac, J.; Pradeep, T.; Kang, H.; Souda, R.; Cooks, R. Low-energy ionic collisions at molecular solids. *Chem. Rev.* **2012**, *112*, 5356-5411.
- (10) Grill, V.; Shen, J.; Evans, C.; Cooks, R. G. Collisions of ions with surfaces at chemically relevant energies: instrumentation and phenomena. *Rev. Sci. Instrum.* **2001**, *72*, 3149-3179.
- (11) Gologan, B.; Takáts, Z.; Alvarez, J.; Wiseman, J. M.; Talaty, N.; Ouyang, Z.; Cooks, R. G. Ion soft-landing into liquids: Protein identification, separation, and purification with retention of biological activity. *J. Am. Soc. Mass. Spectrom.* **2004**, *15*, 1874-1884.
- (12) Mazzei, F.; Favero, G.; Frasconi, M.; Tata, A.; Tuccitto, N.; Licciardello, A.; Pepi, F. Soft-Landed Protein Voltammetry: A Tool for Redox Protein Characterization. *Anal. Chem.* **2008**, *80*, 5937-5944.
- (13) Gunaratne, K. D. D.; Prabhakaran, V.; Andersen, A.; Johnson, G. E.; Laskin, J. Charge retention of soft-landed phosphotungstate Keggin anions on self-assembled monolayers. *PCCP* **2016**, *18*, 9021-9028.
- (14) Su, P.; Hu, H.; Warneke, J.; Belov, M. E.; Anderson, G. A.; Laskin, J. Design and Performance of a Dual-Polarity Instrument for Ion Soft Landing. *Anal. Chem.* **2019**, *91*, 5904-5912.
- (15) Longchamp, J.-N.; Rauschenbach, S.; Abb, S.; Escher, C.; Lатычевскаиа, T.; Kern, K.; Fink, H.-W. Imaging proteins at the single-molecule level. *Proc. Natl. Acad. Sci.* **2017**, *114*, 1474-1479.
- (16) Mikhailov, V. A.; Mize, T. H.; Benesch, J. L.; Robinson, C. V. Mass-selective soft-landing of protein assemblies with controlled landing energies. *Anal. Chem.* **2014**, *86*, 8321-8328.
- (17) Thontasen, N.; Levita, G.; Malinowski, N.; Deng, Z.; Rauschenbach, S.; Kern, K. Grafting Crown Ether Alkali Host– Guest Complexes at Surfaces by Electrospray Ion Beam Deposition. *J. Phys. Chem. C* **2010**, *114*, 17768-17772.
- (18) Prabhakaran, V.; Mehdi, B. L.; Ditto, J. J.; Engelhard, M. H.; Wang, B.; Gunaratne, K. D. D.; Johnson, D. C.; Browning, N. D.; Johnson, G. E.; Laskin, J. Rational design of efficient electrode–electrolyte interfaces for solid-state energy storage using ion soft landing. *Nature communications* **2016**, *7*, 11399.

- (19) Dubey, G.; Urcuyo, R.; Abb, S.; Rinke, G.; Burghard, M.; Rauschenbach, S.; Kern, K. Chemical modification of graphene via hyperthermal molecular reaction. *J. Am. Chem. Soc.* **2014**, *136*, 13482-13485.
- (20) Li, A.; Zi, Y.; Guo, H.; Wang, Z. L.; Fernández, F. M. Triboelectric nanogenerators for sensitive nano-coulomb molecular mass spectrometry. *Nat. Nanotechnol.* **2017**, *12*, 481.
- (21) Ouyang, Z.; Takáts, Z.; Blake, T. A.; Gologan, B.; Guymon, A. J.; Wiseman, J. M.; Oliver, J. C.; Davisson, V. J.; Cooks, R. G. Preparing protein microarrays by soft-landing of mass-selected ions. *Science* **2003**, *301*, 1351-1354.
- (22) Wang, P.; Laskin, J. Helical peptide arrays on self-assembled monolayer surfaces through soft and reactive landing of mass-selected ions. *Angew. Chem. Int. Ed.* **2008**, *47*, 6678-6680.
- (23) Wang, P.; Hadjar, O.; Laskin, J. Covalent Immobilization of Peptides on Self-Assembled Monolayer Surfaces Using Soft-Landing of Mass-Selected Ions. *J. Am. Chem. Soc.* **2007**, *129*, 8682-8683.
- (24) Halder, A.; Curtiss, L. A.; Fortunelli, A.; Vajda, S. Perspective: Size selected clusters for catalysis and electrochemistry. *J. Chem. Phys.* **2018**, *148*, 110901.
- (25) Ustarroz, J.; Ornelas, I. M.; Zhang, G.; Perry, D.; Kang, M.; Bentley, C. L.; Walker, M.; Unwin, P. R. Mobility and Poisoning of Mass-Selected Platinum Nanoclusters during the Oxygen Reduction Reaction. *ACS Catal.* **2018**, *8*, 6775-6790.
- (26) Cuddy, M. J.; Arkill, K. P.; Wang, Z. W.; Komsa, H.-P.; Krashennnikov, A. V.; Palmer, R. E. Fabrication and atomic structure of size-selected, layered MoS₂ clusters for catalysis. *Nanoscale* **2014**, *6*, 12463-12469.
- (27) Zhao, Y. X.; Wang, M. M.; Zhang, Y.; Ding, X. L.; He, S. G. Activity of Atomically Precise Titania Nanoparticles in CO Oxidation. *Angew. Chem. Int. Ed.* **2019**, *58*, 8002-8006.
- (28) Vajda, S.; White, M. G. Catalysis applications of size-selected cluster deposition. *ACS Catal.* **2015**, *5*, 7152-7176.
- (29) Tyo, E. C.; Vajda, S. Catalysis by clusters with precise numbers of atoms. *Nat. Nanotechnol.* **2015**, *10*, 577.
- (30) Ha, M.-A.; Baxter, E. T.; Cass, A. C.; Anderson, S. L.; Alexandrova, A. N. Boron switch for selectivity of catalytic dehydrogenation on size-selected Pt clusters on Al₂O₃. *J. Am. Chem. Soc.* **2017**, *139*, 11568-11575.
- (31) Prabhakaran, V.; Johnson, G. E.; Wang, B.; Laskin, J. In situ solid-state electrochemistry of mass-selected ions at well-defined electrode–electrolyte interfaces. *Proc. Natl. Acad. Sci.* **2016**, *113*, 13324-13329.

- (32) Su, P.; Prabhakaran, V.; Johnson, G. E.; Laskin, J. In Situ Infrared Spectroelectrochemistry for Understanding Structural Transformations of Precisely Defined Ions at Electrochemical Interfaces. *Anal. Chem.* **2018**, *90*, 10935-10942.
- (33) Warneke, J.; McBriarty, M. E.; Riechers, S. L.; China, S.; Engelhard, M. H.; Aprà, E.; Young, R. P.; Washton, N. M.; Jenne, C.; Johnson, G. E. Self-organizing layers from complex molecular anions. *Nature communications* **2018**, *9*, 1889.
- (34) Deng, Z.; Thontasen, N.; Malinowski, N.; Rinke, G.; Harnau, L.; Rauschenbach, S.; Kern, K. A Close Look at Proteins: Submolecular Resolution of Two- and Three-Dimensionally Folded Cytochrome c at Surfaces. *Nano Lett.* **2012**, *12*, 2452-2458.
- (35) Rinke, G.; Rauschenbach, S.; Schrettl, S.; Hoheisel, T. N.; Blohm, J.; Gutzler, R.; Rosei, F.; Frauenrath, H.; Kern, K. Soft-landing electrospray ion beam deposition of sensitive oligoynes on surfaces in vacuum. *Int. J. Mass spectrom.* **2015**, *377*, 228-234.
- (36) Abb, S.; Tarrat, N.; Cortés, J.; Andriyevsky, B.; Harnau, L.; Schön, J. C.; Rauschenbach, S.; Kern, K. Carbohydrate self-assembly at surfaces: STM imaging of sucrose conformation and ordering on Cu (100). *Angew. Chem.* **2019**, *131*, 8424-8428.
- (37) Lünskens, T.; Heister, P.; Thämer, M.; Walenta, C. A.; Kartouzian, A.; Heiz, U. Plasmons in supported size-selected silver nanoclusters. *PCCP* **2015**, *17*, 17541-17544.
- (38) Rauschenbach, S.; Vogelgesang, R.; Malinowski, N.; Gerlach, J. W.; Benyoucef, M.; Costantini, G.; Deng, Z.; Thontasen, N.; Kern, K. Electrospray ion beam deposition: soft-landing and fragmentation of functional molecules at solid surfaces. *ACS nano* **2009**, *3*, 2901-2910.
- (39) Erler, P.; Schmitt, P.; Barth, N.; Irmeler, A.; Bouvron, S.; Huhn, T.; Groth, U.; Pauly, F.; Gragnaniello, L.; Fonin, M. Highly Ordered Surface Self-Assembly of Fe₄ Single Molecule Magnets. *Nano Lett.* **2015**, *15*, 4546-4552.
- (40) Paschke, F.; Erler, P.; Enenkel, V.; Gragnaniello, L.; Fonin, M. Bulk-Like Magnetic Signature of Individual Fe₄H Molecular Magnets on Graphene. *ACS Nano* **2019**, *13*, 780-785.
- (41) Kahle, S.; Deng, Z.; Malinowski, N.; Tonnoir, C. n.; Forment-Aliaga, A.; Thontasen, N.; Rinke, G.; Le, D.; Turkowski, V.; Rahman, T. S. The quantum magnetism of individual manganese-12-acetate molecular magnets anchored at surfaces. *Nano Lett.* **2011**, *12*, 518-521.
- (42) Baker, S.; Thornton, S.; Keen, A.; Preston, T.; Norris, C.; Edmonds, K.; Binns, C. The construction of a gas aggregation source for the preparation of mass-selected ultrasmall metal particles. *Rev. Sci. Instrum.* **1997**, *68*, 1853-1857.
- (43) Rauschenbach, S.; Stadler, F. L.; Lunedei, E.; Malinowski, N.; Koltsov, S.; Costantini, G.; Kern, K. Electrospray ion beam deposition of clusters and biomolecules. *small* **2006**, *2*, 540-547.
- (44) Zhang, C.; Tsunoyama, H.; Akatsuka, H.; Sekiya, H.; Nagase, T.; Nakajima, A. Advanced nanocluster ion source based on high-power impulse magnetron sputtering and time-resolved measurements of nanocluster formation. *J. Phys. Chem. A* **2013**, *117*, 10211-10217.

- (45) Gunaratne, K. D. D.; Prabhakaran, V.; Ibrahim, Y. M.; Norheim, R. V.; Johnson, G. E.; Laskin, J. Design and performance of a high-flux electrospray ionization source for ion soft landing. *Analyst* **2015**, *140*, 2957-2963.
- (46) Majumdar, A.; Köpp, D.; Ganeva, M.; Datta, D.; Bhattacharyya, S.; Hippler, R. Development of metal nanocluster ion source based on dc magnetron plasma sputtering at room temperature. *Rev. Sci. Instrum.* **2009**, *80*, 095103.
- (47) Von Issendorff, B.; Palmer, R. A new high transmission infinite range mass selector for cluster and nanoparticle beams. *Rev. Sci. Instrum.* **1999**, *70*, 4497-4501.
- (48) Roy, C.; Sebok, B.; Scott, S.; Fiordaliso, E.; Sørensen, J.; Bodin, A.; Trimarco, D.; Damsgaard, C.; Vesborg, P.; Hansen, O. Impact of nanoparticle size and lattice oxygen on water oxidation on NiFeO_x H_y. *Nat. Catal.* **2018**, *1*, 820.
- (49) Peng, W.-P.; Goodwin, M. P.; Nie, Z.; Volný, M.; Ouyang, Z.; Cooks, R. G. Ion soft landing using a rectilinear ion trap mass spectrometer. *Anal. Chem.* **2008**, *80*, 6640-6649.
- (50) Mayer, P. S.; Tureček, F.; Lee, H.-N.; Scheidemann, A. A.; Olney, T. N.; Schumacher, F.; Štrop, P.; Smrčina, M.; Pátek, M.; Schirlin, D. Preparative separation of mixtures by mass spectrometry. *Anal. Chem.* **2005**, *77*, 4378-4384.
- (51) Palmer, R.; Cao, L.; Yin, F. Note: Proof of principle of a new type of cluster beam source with potential for scale-up. *Rev. Sci. Instrum.* **2016**, *87*, 046103.
- (52) Röttgen, M. A.; Judai, K.; Antonietti, J.-M.; Heiz, U.; Rauschenbach, S.; Kern, K. Conical octopole ion guide: Design, focusing, and its application to the deposition of low energetic clusters. *Rev. Sci. Instrum.* **2006**, *77*, 013302.
- (53) Hartmann, H.; Popok, V.; Barke, I.; von Oeynhausen, V.; Meiwes-Broer, K.-H. Design and capabilities of an experimental setup based on magnetron sputtering for formation and deposition of size-selected metal clusters on ultra-clean surfaces. *Rev. Sci. Instrum.* **2012**, *83*, 073304.
- (54) Badu-Tawiah, A. K.; Wu, C.; Cooks, R. G. Ambient ion soft landing. *Anal. Chem.* **2011**, *83*, 2648-2654.
- (55) Hou, J.; Zheng, Q.; Badu-Tawiah, A. K.; Xiong, C.; Guan, C.; Chen, S.; Nie, Z.; Wang, D.; Wan, L. Electrospray soft-landing for the construction of non-covalent molecular nanostructures using charged droplets under ambient conditions. *Chem. Commun.* **2016**, *52*, 13660-13663.
- (56) Johnson, G. E.; Prabhakaran, V.; Browning, N. D.; Mehdi, B. L.; Laskin, J.; Kottke, P. A.; Fedorov, A. G. DRILL Interface Makes Ion Soft Landing Broadly Accessible for Energy Science and Applications. *Batteries & Supercaps* **2018**, *1*, 97-101.
- (57) Clemmons, J.; Herrero, F. Mass spectroscopy using a rotating electric field. *Rev. Sci. Instrum.* **1998**, *69*, 2285-2291.

- (58) Nojima, M.; Anai, Y.; Hotta, M.; Kurumi, S.; Suzuki, K.; Adachi, T.; Kusanagi, T.; Moritani, K. Development of a mass spectrometer using two rotating electric fields. *J. Vac. Sci. Technol. B Nanotechnol. Microelectron.* **2016**, *34*, 03H132.
- (59) Clemmons, J. H.; Herrero, F. A. Mass spectroscopy using a rotating electric field. *Rev. Sci. Instrum.* **1998**, *69*, 2285-2291.
- (60) Su, P.; Hu, H.; Unsihuay, D.; Zhang, D.; Dainese, T.; Diaz, R. E.; Lee, J.; Gunaratne, D. K.; Wang, H.; Maran, F.; Mei, J.; Laskin, J. Preparative Mass Spectrometry Using a Rotating-Wall Mass Analyzer. *Angew. Chem. Int. Ed.* **2020**, *n/a*, DOI: Angew. Chem. Int. Ed. 10.1002/anie.202000065.
- (61) Fort, K. L.; Van de Waterbeemd, M.; Boll, D.; Reinhardt-Szyba, M.; Belov, M. E.; Sasaki, E.; Zschoche, R.; Hilvert, D.; Makarov, A. A.; Heck, A. J. Expanding the structural analysis capabilities on an Orbitrap-based mass spectrometer for large macromolecular complexes. *Analyst* **2018**, *143*, 100-105.
- (62) Hadjar, O.; Johnson, G.; Laskin, J.; Kibelka, G.; Shill, S.; Kuhn, K.; Cameron, C.; Kassan, S. IonCCD™ for Direct Position-Sensitive Charged-Particle Detection: from Electrons and keV Ions to Hyperthermal Biomolecular Ions. *J. Am. Soc. Mass. Spectrom.* **2011**, *22*, 612-623.
- (63) Dainese, T.; Agrachev, M.; Antonello, S.; Badocco, D.; Black, D. M.; Fortunelli, A.; Gascón, J. A.; Stener, M.; Venzo, A.; Whetten, R. L. Atomically precise Au 144 (SR) 60 nanoclusters (R= Et, Pr) are capped by 12 distinct ligand types of 5-fold equivalence and display gigantic diastereotopic effects. *Chem. Sci.* **2018**, *9*, 8796-8805.
- (64) Nefliu, M.; Venter, A.; Cooks, R. G. Desorption electrospray ionization and electrosonic spray ionization for solid- and solution-phase analysis of industrial polymers. *Chem. Commun.* **2006**, 888-890.
- (65) Christian, N. P.; Arnold, R. J.; Reilly, J. P. Improved Calibration of Time-of-Flight Mass Spectra by Simplex Optimization of Electrostatic Ion Calculations. *Anal. Chem.* **2000**, *72*, 3327-3337.
- (66) Chen, X.; Raab, S. A.; Poe, T.; Clemmer, D. E.; Larriba-Andaluz, C. Determination of Gas-Phase Ion Structures of Locally Polar Homopolymers Through High-Resolution Ion Mobility Spectrometry–Mass Spectrometry. *J. Am. Soc. Mass. Spectrom.* **2019**, *30*, 905-918.
- (67) Hu, Q.; Laskin, J. Secondary Structures of Ubiquitin Ions Soft-Landed onto Self-Assembled Monolayer Surfaces. *J. Phys. Chem. B* **2016**, *120*, 4927-4936.
- (68) Issendorff, B. v.; Palmer, R. E. A new high transmission infinite range mass selector for cluster and nanoparticle beams. *Rev. Sci. Instrum.* **1999**, *70*, 4497-4501.
- (69) Moision, R. M.; Armentrout, P. B. An electrospray ionization source for thermochemical investigation with the guided ion beam mass spectrometer. *J. Am. Soc. Mass. Spectrom.* **2007**, *18*, 1124-1134.
- (70) Vestal, M. L.; Blakley, C. R.; Ryan, P. W.; Futrell, J. H. New crossed-beam apparatus for the study of ion–molecule collision processes. *Rev. Sci. Instrum.* **1976**, *47*, 15-26.

- (71) O'Connor, P. J.; Leroi, G. E.; Allison, J. Understanding ion deceleration lenses: what are the simplicity/performance trade-offs? *J. Am. Soc. Mass. Spectrom.* **1991**, *2*, 322-335.
- (72) Murray, R. W. Nanoelectrochemistry: Metal Nanoparticles, Nanoelectrodes, and Nanopores. *Chem. Rev.* **2008**, *108*, 2688-2720.
- (73) Hesari, M.; Ding, Z. A Grand Avenue to Au Nanocluster Electrochemiluminescence. *Acc. Chem. Res.* **2017**, *50*, 218-230.
- (74) Zhou, M.; Zeng, C.; Chen, Y.; Zhao, S.; Sfeir, M. Y.; Zhu, M.; Jin, R. Evolution from the plasmon to exciton state in ligand-protected atomically precise gold nanoparticles. *Nat. Commun.* **2016**, *7*, 13240.
- (75) Guryanov, I.; Polo, F.; Ubyvovk, E. V.; Korzhikova-Vlakh, E.; Tennikova, T.; Rad, A. T.; Nieh, M.-P.; Maran, F. Polylysine-grafted Au 144 nanoclusters: birth and growth of a healthy surface-plasmon-resonance-like band. *Chem. Sci.* **2017**, *8*, 3228-3238.
- (76) Becucci, L.; Guidelli, R.; Polo, F.; Maran, F. Interaction of Mixed-Ligand Monolayer-Protected Au₁₄₄ Clusters with Biomimetic Membranes as a Function of the Transmembrane Potential. *Langmuir* **2014**, *30*, 8141-8151.
- (77) Li, W.; Ge, Q.; Ma, X.; Chen, Y.; Zhu, M.; Xu, H.; Jin, R. Mild activation of CeO₂-supported gold nanoclusters and insight into the catalytic behavior in CO oxidation. *Nanoscale* **2016**, *8*, 2378-2385.
- (78) Das, S.; Goswami, A.; Hesari, M.; Al-Sharab, J. F.; Mikmeková, E.; Maran, F.; Asefa, T. Reductive deprotection of monolayer protected nanoclusters: An efficient route to supported ultrasmall Au nanocatalysts for selective oxidation. *Small* **2014**, *10*, 1473-1478.
- (79) Qian, H.; Jin, R. Controlling nanoparticles with atomic precision: the case of Au₁₄₄ (SCH₂CH₂Ph) 60. *Nano letters* **2009**, *9*, 4083-4087.
- (80) Bahena, D.; Bhattarai, N.; Santiago, U.; Tlahuice, A.; Ponce, A.; Bach, S. B.; Yoon, B.; Whetten, R. L.; Landman, U.; Jose-Yacamán, M. STEM electron diffraction and high-resolution images used in the determination of the crystal structure of the Au₁₄₄ (SR) 60 cluster. *The journal of physical chemistry letters* **2013**, *4*, 975-981.
- (81) Yan, N.; Xia, N.; Liao, L.; Zhu, M.; Jin, F.; Jin, R.; Wu, Z. Unraveling the long-pursued Au₁₄₄ structure by x-ray crystallography. *Sci. Adv.* **2018**, *4*, eaat7259.
- (82) Lopez-Acevedo, O.; Akola, J.; Whetten, R. L.; Gronbeck, H.; Häkkinen, H. Structure and bonding in the ubiquitous icosahedral metallic gold cluster Au₁₄₄ (SR) 60. *J. Phys. Chem. C* **2009**, *113*, 5035-5038.
- (83) Leney, A. C.; Heck, A. J. Native mass spectrometry: what is in the name? *Journal of The American Society for Mass Spectrometry* **2017**, *28*, 5-13.

- (84) Venzo, A.; Antonello, S.; Gascón, J. A.; Guryanov, I.; Leapman, R. D.; Perera, N. V.; Sousa, A.; Zamuner, M.; Zanella, A.; Maran, F. Effect of the charge state ($z = -1, 0, +1$) on the nuclear magnetic resonance of monodisperse Au₂₅[S(CH₂)₂Ph]_{18z} clusters. *Anal. Chem.* **2011**, *83*, 6355-6362.
- (85) Azubel, M.; Koivisto, J.; Malola, S.; Bushnell, D.; Hura, G. L.; Koh, A. L.; Tsunoyama, H.; Tsukuda, T.; Pettersson, M.; Häkkinen, H. Electron microscopy of gold nanoparticles at atomic resolution. *Science* **2014**, *345*, 909-912.
- (86) Liu, J.; Jian, N.; Ornelas, I.; Pattison, A. J.; Lahtinen, T.; Salorinne, K.; Häkkinen, H.; Palmer, R. E. Exploring the atomic structure of 1.8 nm monolayer-protected gold clusters with aberration-corrected STEM. *Ultramicroscopy* **2017**, *176*, 146-150.
- (87) Genzer, J.; Bhat, R. R. Surface-Bound Soft Matter Gradients. *Langmuir* **2008**, *24*, 2294-2317.
- (88) Wijesundara, M. B.; Fuoco, E.; Hanley, L. Preparation of chemical gradient surfaces by hyperthermal polyatomic ion deposition: a new method for combinatorial materials science. *Langmuir* **2001**, *17*, 5721-5726.
- (89) Kim, M. S.; Khang, G.; Lee, H. B. Gradient polymer surfaces for biomedical applications. *Progress in Polymer Science* **2008**, *33*, 138-164.
- (90) Nefliu, M.; Venter, A.; Cooks, R. G. Desorption electrospray ionization and electrosonic spray ionization for solid-and solution-phase analysis of industrial polymers. *Chem. Commun.* **2006**, 888-890.
- (91) Roach, P. J.; Laskin, J.; Laskin, A. Nanospray desorption electrospray ionization: an ambient method for liquid-extraction surface sampling in mass spectrometry. *Analyst* **2010**, *135*, 2233-2236.
- (92) Ouyang, Z.; Cooks, R. G. Miniature Mass Spectrometers. *Ann. Rev. Anal. Chem.* **2009**, *2*, 187-214.

CHAPTER 4. IN SITU SPECTROELECTROCHEMISTRY FOR UNDERSTANDING STRUCTURAL TRANSFORMATIONS OF PRECISELY DEFINED IONS AT ELECTROCHEMICAL INTERFACES

4.1 Introduction

Electrode-electrolyte interfaces (EEl)s play a central role in electrochemical processes and energy technology.¹ The performance of electrochemical systems is strongly affected by the kinetics and mechanisms of electron transfer as well as degradation processes occurring at EEl)s. Understanding the structural changes of electroactive species during electrochemical processes is critically important to the development of tailored EEl)s with desired properties.² Several *in situ* and *operando* characterization approaches have been developed to obtain a better understanding of the complex processes occurring at operating EEl)s. Nuclear magnetic resonance (NMR) spectroscopy,³ second harmonic generation (SHG),⁴ vibrational spectroscopy,⁵ and X-ray photoelectron spectroscopy (XPS),^{6,7} have traditionally been used for *in situ* characterization of EEl)s. Infrared (IR) spectroelectrochemistry has been developed for *in situ* probing of processes at solid-liquid interfaces.^{8,9} This approach enables structural characterization of electroactive species during electrochemical cycling. In particular, infrared reflection absorption spectroscopy (IRRAS) has been widely used in spectroelectrochemistry experiments to study redox active organic pigments, ionic liquids, and transition metal clusters.¹⁰⁻¹³ Most of the *in situ* approaches to studying solid-liquid EEl)s rely on specially-fabricated liquid electrochemical cells.^{14,15} Despite substantial progress in this field, *in situ* characterization of solid state EEl)s remains challenging.

In a recent publication, we reported the development of a new *in situ* thin-film electrochemical cell for characterizing the activity of electroactive species at solid-state EEl)s both under vacuum conditions and controlled partial pressures of reactive gases.¹⁶ The electrochemical cell was fabricated on a screen-printed electrode (SPE) using carefully-designed nanoporous ionic liquid (IL) membranes (Figure 4.1). This cell mimics many state-of-the-art solid-state electrochemical devices used for energy conversion and storage.¹⁷ The electroactive species were deposited onto the cell using ion soft-landing,¹⁸⁻²⁵ which enables precise control over the composition and charge state of the ions along with their kinetic energy and coverage. In this study, we expand this approach to enable *in situ* structural characterization of well-defined electroactive

species at solid-state EEIs using IRRAS during electrochemical cycling. Soft-landing has been used previously for preparation of electrode surfaces with superior specific capacitance and electrochemical stability.²⁶ The ability to prepare interfaces containing well-defined electroactive species makes ion soft-landing a powerful approach for obtaining a fundamental understanding of interfacial processes and characterization of the intrinsic properties of ions at EEIs.

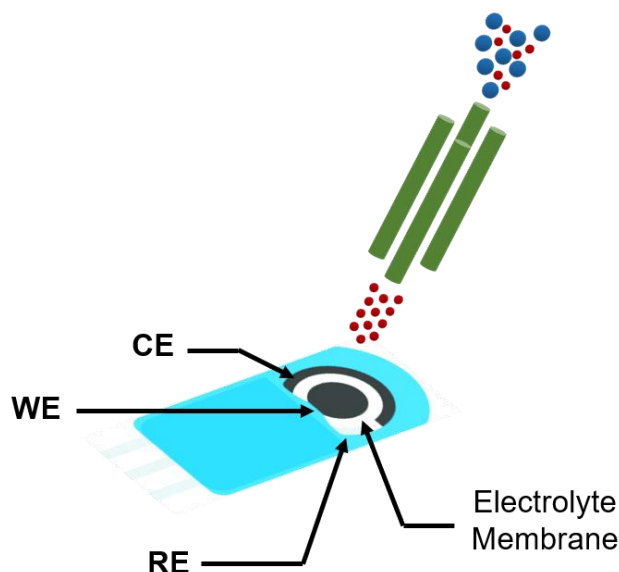


Figure 4.1 in situ vacuum-compatible electrochemical cell using a nanoporous ionic liquid membrane. WE=working electrode, CE=counter electrode, RE=reference electrode.

Proof-of-principle experiments were performed using well-characterized stable Keggin polyoxometalate (POM) anions with unique multielectron redox activity as a model system.²⁷ Their ability to accommodate 24 excess electrons (e^-) each with retention of structural integrity was reported previously for $\text{PMo}_{12}\text{O}_{40}^{3-}$, making these anions promising candidates for use in rechargeable batteries,²⁸ water electrolyzers,²⁹ electrocatalysts,³⁰ and molecular supercapacitors.³¹ In this study, we selected tungsten POM (WPOM) anions ($\text{PW}_{12}\text{O}_{40}^{3-}$) as a model system due to their established structural stability³² and well-defined IRRAS bands.³³ The stability and rigidity of WPOM makes it resilient towards structural transformations during redox processes.^{34,35} Our previous work employed IRRAS to understand charge retention by WPOM anions soft-landed onto self-assembled monolayer (SAM) surfaces.³³ We demonstrated that the position of the terminal $\text{W}=\text{O}_t$ band shifts systematically with the charge state of the anion.³³ Herein, we examined for the first time, structures of WPOM anions at operating EEIs. We observed that the WPOM

cage undergoes reversible structural changes during redox cycling. Although during the reduction process the WPOM cage preserves its structural integrity without substantial expansion, the W=O_t band shows a systematic shift to lower wavenumbers. This shift facilitates the identification of different charge states of WPOM that are present at the interface at different stages of the oxidation/reduction cycle. These results establish a powerful methodology of using an *in situ* spectroelectrochemical cell combined with ion soft-landing for studying structural transformations of well-defined electroactive ions at operating solid-state EEIs.

4.2 Experimental Section

Sodium phosphotungstate tribasic hydrate (Na₃[PW₁₂O₄₀]·xH₂O), 1-ethyl-3-methylimidazolium tetrafluoroborate (EMIMBF₄), poly(vinylidene fluoride-co-hexafluoropropylene) (PVDF-HFP) and anhydrous N,N-dimethylformamide (DMF) were all purchased from Sigma-Aldrich (St. Louis, MO) and used as received. The 10 × 10 mm gold coated silicon wafers (100 nm Au layer and 5 nm Ti adhesion layer) were purchased from Platypus Technologies (Madison, WI).

The three-electrode IR spectroelectrochemical cell shown in Figure 4.2 was fabricated using the following procedure: A gold substrate was used as the working electrode (WE). The gold-coated substrate was ultrasonically washed in methanol, placed in an ultraviolet cleaner (Boekel Scientific, Feasterville, PA) for 20 min, transferred onto a specially-designed polyether ether ketone (PEEK) cell holder with a 11 × 11 mm² recessed square groove, and affixed to the holder using two stainless steel clamps. A Pt counter electrode (CE) and Ag pseudo-reference electrode (RE) were wired around the edges of the WE (Figure 3.2). The Pt and Ag wires were purchased from Alfa Aesar (Tewksbury, MA).

An aprotic electrolyte cell membrane containing EMIMBF₄ ionic liquid (IL) and PVDF-HFP copolymer was prepared using the following steps: 2 g of PVDF-HFP was dissolved in 13 mL of anhydrous DMF and stirred overnight at room temperature to make a homogeneous solution. 2 mL of EMIMBF₄ was subsequently added to the solution and the mixture was continuously stirred for 4 hours and stored in a N₂-purged glove box. The cell membrane was prepared by carefully and evenly casting approximately 20 μL of the solution onto the entire three-electrode

assembly and slowly drying the resulting liquid layer in a vacuum oven (Sheldon Manufacturing, Cornelius, OR) at room temperature for 24 hours to remove DMF and trace amounts of water.

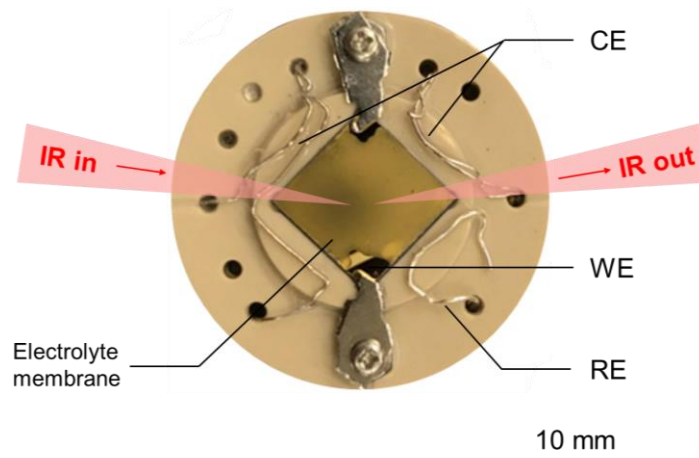


Figure 4.2 A photographic image of the three-electrode cell assembly and schematic drawing of the IR light beam used for IRRAS measurements. WE = working electrode, CE = counter electrode, RE = reference electrode. The electrolyte membrane covers all three electrodes.

Soft-landing experiments were performed using a specially-designed high-flux ion deposition instrument described in detail elsewhere.³⁶ The *in situ* spectroelectrochemical cell was mounted on a linear translator and introduced into the vacuum system. The cell holder was equipped with a three-pin connector wired to an electrical vacuum feedthrough providing electrical connections from the WE, CE, and RE to a potentiostat (Versastat 3, Princeton Applied Research). Ions were produced by negative mode electrospray ionization (ESI) of a 150 μM solution of $\text{Na}_3[\text{PW}_{12}\text{O}_{40}] \cdot x\text{H}_2\text{O}$ in methanol. Solvent droplets containing WPOM were produced by applying a -2.5 kV potential to the ESI emitter and introduced into the vacuum system through a heated (150 $^\circ\text{C}$) stainless-steel inlet to promote desolvation. Ions were subsequently transferred into vacuum by a dual ion funnel system,³⁶ mass-selected using a quadrupole mass filter (Extrel Pittsburgh, PA), and deposited onto the WE area of the electrochemical cell at a kinetic energy of 30-35 eV per charge. The ion current was measured at the WE by the potentiostat in zero-resistance ammeter mode. A typical ion current of -6.5 nA was achieved for mass-selected deposition of $\text{PW}_{12}\text{O}_{40}^{3-}$ ions onto the electrochemical cell. The total number of deposited ions was calculated by integrating the ion current over time.

Prior to soft landing of WPOM, electrochemical impedance spectroscopy (EIS) measurements were conducted to examine the different interfacial regions of the electrochemical cell maintained in vacuum. EIS was performed by applying a sinusoidal perturbation with an amplitude of 10 mV and frequency in the range of 100 KHz to 10 Hz. Cyclic voltammetry (CV) measurements were carried out before and after soft-landing of WPOM using the potentiostat. The CVs were acquired at scan rates of 0.5 mV s⁻¹ in the range of 0.3 mV to -2.1 mV in triplicates after 3 × 10¹⁵ PW₁₂O₄₀³⁻ (WPOM) ions were soft-landed onto the cell.

The spectroscopic performance of the cell was optimized for IRRAS experiments by adjusting the position of the cell to maximize the signal amplitude. Grazing-incidence IRRAS experiments were performed using a Bruker Vertex 70 FTIR spectrometer (Bruker Optics, Billerica, MA) equipped with a liquid nitrogen cooled mercury-cadmium-telluride (MCT) detector. The experimental details have been explained elsewhere.³⁷ IRRAS spectra were acquired at different potentials applied to the WE at a spectral resolution of 4 cm⁻¹ using p-polarized light. Each spectrum was collected by averaging 5000 scans corresponding to a 20-minute acquisition time. Fitting of the IRRAS spectra was carried out in Excel using a sum of several Lorentzian distributions with peak positions in the range between 1000 cm⁻¹ and 800 cm⁻¹. The experimental IRRAS plots were baseline-corrected in an interactive mode. The peak positions were first defined, and all the peak widths were constrained at a value of 12 cm⁻¹. The peak intensities and widths were optimized by minimizing the sum of squares of deviations between the experimental and simulated data points to obtain the best-fit curves.

4.3 Results and Discussion

In this study, we developed a solid-state thin-film electrochemical cell that enables *in situ* IRRAS characterization of energized electrochemical interfaces prepared using soft-landing of mass- and charge-selected electroactive ions. A photographic image of the cell and a schematic drawing of the IR light beam are shown in Figure 4.2. The three-electrode assembly is mounted on a specially-designed PEEK holder. We evaluated several cell designs to explore the effect of the electrode configuration and membrane preparation on cell performance. A bare gold surface (10 × 10 mm) was used as a working electrode (WE). Gold is a suitable substrate for spectroelectrochemical measurements since it forms a nearly ideal electrical double layer and has

a high conductivity and optical reflectivity.³⁸ The WE was mounted in the middle of the PEEK holder. The counter and reference electrodes (CE and RE) were wired as close to the WE as possible without direct electrical contact. A Pt wire used as the CE was coiled in loops close to three edges of the gold substrate to maximize the area of the CE. A silver wire used as a pseudo RE was positioned next to the fourth edge of the gold surface. To accommodate the small incidence angle of the incoming IR beam while keeping the three electrodes at a similar height, a shallow square groove was machined in the PEEK holder for the WE. A nanoporous electrolyte membrane was prepared by casting a solution composed of a conductive copolymer and EMIMBF₄ IL on top of the three-electrode assembly and allowing it to dry under vacuum. We have previously shown that such electrolyte membranes are stable both in vacuum and under controlled partial pressures of gases.¹⁶ In order to improve the IRRAS sensitivity, the electrolyte membrane thickness was minimized by using the least amount possible (20 μ L) of the IL cast solution. The solution composition was optimized to enable the fabrication of the IL membrane that covered all of the electrode surfaces with physical continuity. The thickness of the membrane is estimated to be around 10 μ m based on the volume of the copolymer and IL. The uniformity of the membrane on the WE helps improve the spectroscopic response by eliminating multiple reflections of the IR beam from the membrane surface. Preparation of the optimized membrane involved casting of the solution in the center of the WE and allowing it to expand and stabilize by itself. This process is largely determined by the viscosity of the solution. Casting of lower-viscosity solutions containing a higher molar ratio of IL resulted in rapid expansion of the droplet on the surface and formation of a non-uniform membrane. Slow spreading of viscous solutions prepared using higher molar ratios of copolymer made it difficult to prepare a thin membrane. In addition, the wettability of the surface by the IL solution may affect the quality of the membrane. For example, the IL solution used in this study could not form a good-quality film on a hydrophobic surface.

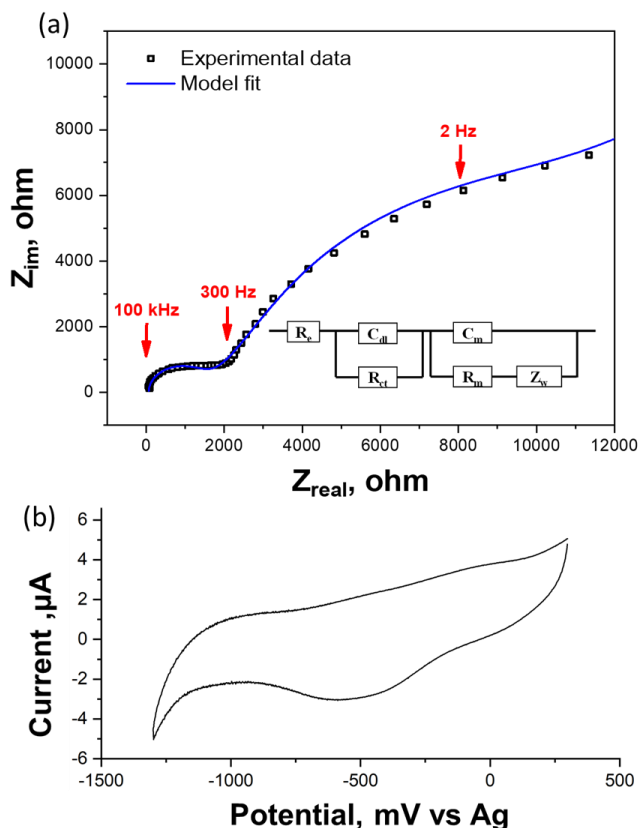


Figure 4.3 (a) Nyquist plot obtained from the potentiostatic EIS of the *in situ* spectroelectrochemical cell (Frequency range: 100 kHz to 1 Hz, amplitude: 10 mV). Inset: the equivalent circuit model used to fit the EIS data, R_e - electrolyte resistance, R_{ct} - charge transfer resistance, C_{dl} - double layer capacitance, R_m - porous membrane resistance, C_m - double layer capacitance derived at porous membrane, and Z_w - Warburg impedance). (b) CV of the blank spectroelectrochemical cell before soft landing experiments acquired at scan rate of 50 mV s^{-1} .

Prior to voltammetry characterization, the different interfacial regions of the cell were evaluated using electrochemical impedance spectroscopy (EIS) measurements in vacuum. The experimental EIS data were fitted using the EIS spectrum Analyzer software and the equivalent circuit model presented in Figure 4.3.³⁹ In this model, the impedance of the Au/IL interface and the pores in the IL membrane are considered as separate elements. The experimental Nyquist plot and the best fit obtained using the equivalent circuit are shown in Figure 4.3(a). The presence of a semicircle in the high-frequency range (100 kHz – 300 Hz) is attributed to the charge transfer kinetics due to polarization of the WE and indicates the formation of a well-defined double layer at the Au/IL interface. The EIS model shows that the impedance of this range of frequencies is a combination of the electrolyte resistance ($R_e = 64 \text{ } \Omega$), charge transfer resistance ($R_{ct} = 5000 \text{ } \Omega$)

and double layer capacitance ($C_{dl} = 5.8 \times 10^{-6}$ F). The frequency range between 300 Hz and 2 Hz is attributed to the diffusion controlled polarization through the IL layers on the WE. The impedance of this region consists of the resistance of the porous membrane ($R_m = 1430 \Omega$), double layer capacitance at the porous membrane ($C_m = 3.7 \times 10^{-8}$ F), and Warburg impedance ($Z_w = 2 \times 10^4 \Omega \cdot s^{-0.5}$), which arises from the limited adsorption of ionic species at the WE. Overall, the EIS analysis showed that the presence of a characteristic diffusion controlled region in the cell corresponds to compact double-layer structure. This type of interface is representative of technologically-relevant solid-state EEIs, in which the limited diffusion of ions in the porous electrolyte results in additional diffusional resistance.⁴⁰⁻⁴² Following the EIS experiments, CV measurements were performed for several cycles prior to ion deposition (Figure 4.3(b)) and showed the interface to be very stable.

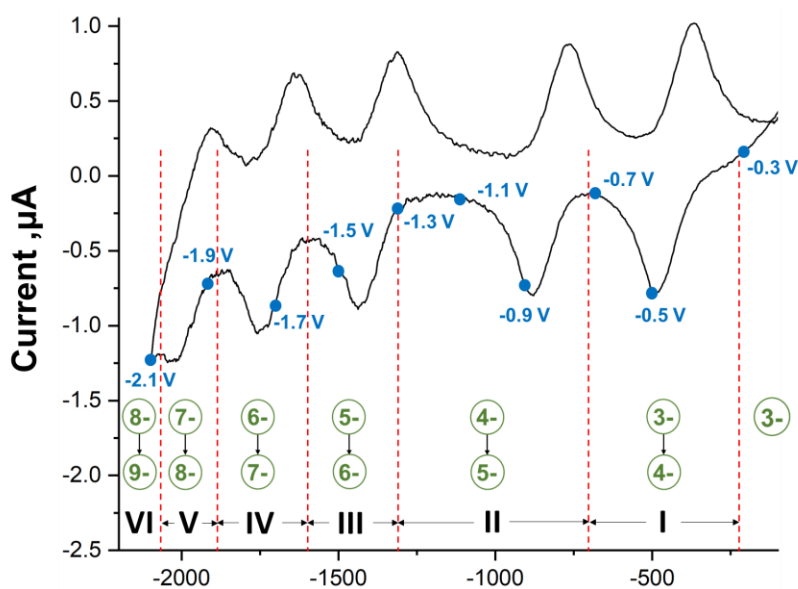


Figure 4.4 *In situ* CV of soft-landed $PW_{12}O_{40}^{3-}$ anions in the potential range between -2100 and -100 mV. CV measurements were performed after 3×10^{15} ions were deposited onto the cell. Scan rate: 0.5 mV s^{-1} . The reduction portion of the CV curve showing potential regions outlined with red dashed lines and labeled with numbers on top along with key electron transfer processes examined spectroelectrochemically. The potentials used in the IRRAS measurements are marked with blue dots on the CV curve.

Table 4.1 Calculated electrochemical parameters in the CV studies of WPOM anions at a scan rate of 0.5 mV s⁻¹. The E_{p, red} and E_{p, ox} refer to reduction and re-oxidation peak potentials; E_{1/2, red} and E_{1/2, ox} refer to reduction and re-oxidation half-wave peak potentials.

Peak #	Reduction			Re-oxidation			Number of electron transferred, n
	E _{p, red} , mV	E _{1/2, red} , mV	Δ (E _{1/2, red} - E _{p, red}), mV	E _{p, ox} , mV	E _{1/2, ox} , mV	Δ (E _{1/2, ox} - E _{p, ox}), mV	
1	-478	-417	61	-373	-439	66	1
2	-875	-814	61	-770	-835	65	1
3	-1430	-1369	61	-1318	-1377	59	1
4	-1744	-1687	57	-1640	-1696	56	1
5	-2028	-1988	40	-1913	-1964	51	1

An *in situ* CV study of the soft-landed WPOM was performed in vacuum after deposition of 3×10^{15} ions onto the WE of the cell. A typical CV plot obtained for the soft-landed PW₁₂O₄₀³⁻ anions at a scan rate of 0.5 mV s⁻¹ is shown in Figure 4.4. Consistent with previous studies,^{35,43} five pairs of oxidation/reduction peaks corresponding to multielectron transfer processes were observed in the potential range between -2100 and -100 mV. The reduction and re-oxidation peak potentials (E_{p, red} and E_{p, ox}) and the number of electrons transferred in each process (n) are listed in Table 4.1. We observe quasi-reversible behavior of the WPOM anions in terms of electrochemical performance, which is attributed to the relatively slow diffusion of the ions in the electrolyte membrane. All of the redox peaks show one electron transfer behavior. Thus, the major electrochemical reactions taking place at EEIs in the different potential regions may be attributed to a stepwise conversion of WPOM anions from one charge state to the next as shown in Figure 4.4. To facilitate the discussion, we split the reduction potential range into six regions (I–VI) each containing a single reduction peak (Figure 4.4). In each of the potential regions, reduced WPOM species are produced through conversion of the lower charge state of WPOM present at EEI.

Previous electrochemical and spectroscopic studies have demonstrated the exceptional “electron sponge-like” behavior of Keggin POM anions.^{27,28,31} According to density functional theory (DFT) calculations, PMO₁₂O₄₀³⁻ can accommodate up to 24 excess electrons to produce a super-reduced PMO₁₂O₄₀²⁷⁻ anion.³¹ DFT calculations also indicate that similar molecular and electronic structural changes to PMO₁₂O₄₀³⁻ can be expected for PW₁₂O₄₀³⁻ in the reduction

process.³¹ The structural evolution of reduced POM anions was observed previously using *operando* Mo K-edge extended X-ray absorption fine structure (XAFS) analysis of a MoPOM molecular cluster battery.²⁷ During the reduction process, the terminal Mo=O bonds are converted into single Mo-O bonds. Meanwhile, the size of the anion does not change to a large extent until the Mo-Mo bonds start to form following the transfer of more than 13 electrons. The WPOM anions examined in this study are structurally more rigid than MoPOM anions.³⁴ Gas-phase studies also indicate that WPOM anions undergo dissociation at higher internal energies than MoPOM.³² Thus, changes in different types of W-O bond lengths are expected to be less pronounced in WPOM compared with MoPOM. However, WPOM anions produce better-quality IRRAS spectra in comparison to MoPOM with narrower and more intense absorption bands corresponding to P-O and W-O bonds.⁴⁴ Furthermore, we have previously shown similar trends in the positions of terminal Mo=O_t and W=O_t bands as a function of the charge state of the POM anion.³³ Herein, we used IRRAS for *in situ* characterization of structural transitions in WPOM anions during reduction/oxidation processes at different potentials applied to the WE.

In situ IRRAS spectra acquired at different ion coverages during the WPOM deposition are shown in Figure 4.5. These spectra were obtained using the cell without WPOM as a background. Several bands in the range between 3000 and 1200 cm⁻¹, which increase in intensity during the deposition process, are observed at wavenumbers corresponding to EMIMBF₄ vibrational bands reported in the literature³⁸ and attributed to structural changes in the electrolyte membrane resulting from ion soft-landing (Figure 4.5) and electrochemical cycling (Figure 4.6 and Figure 4.7).^{38,45} Detailed assignment of these bands is outside of the scope of this chapter. In addition, WPOM bands in the range between 1100 and 800 cm⁻¹ are clearly visible at higher ion coverages, which confirms that the soft-landed WPOM anions are successfully deposited onto the WE.

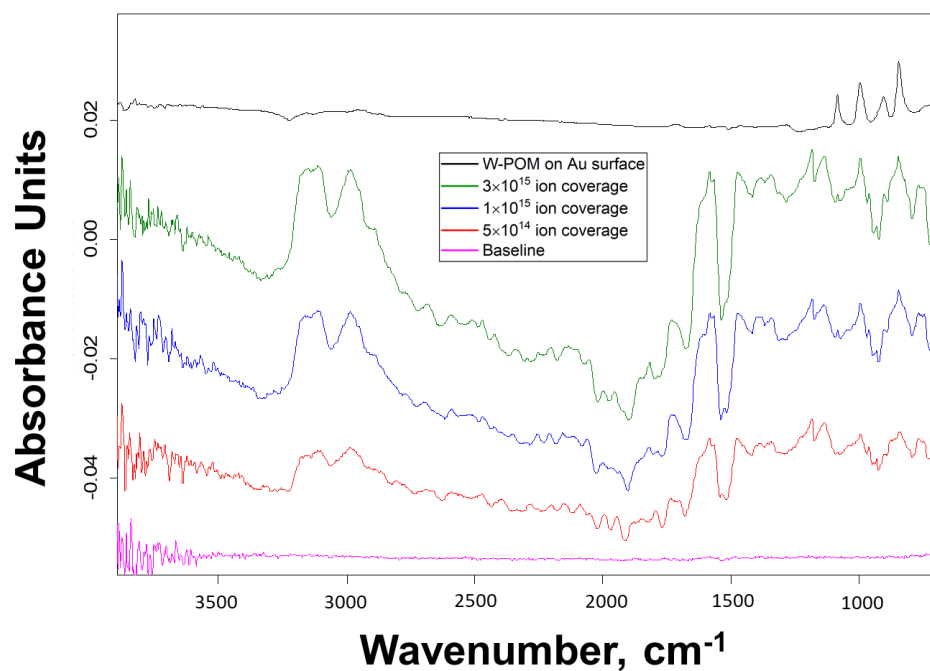


Figure 4.5 *In situ* IR spectra of the electrochemical cell obtained at different ion coverages. The IR spectrum of the initial blank cell is used as the baseline. The top spectrum represents the WPOM soft-landed on a bare Au surface for comparison.

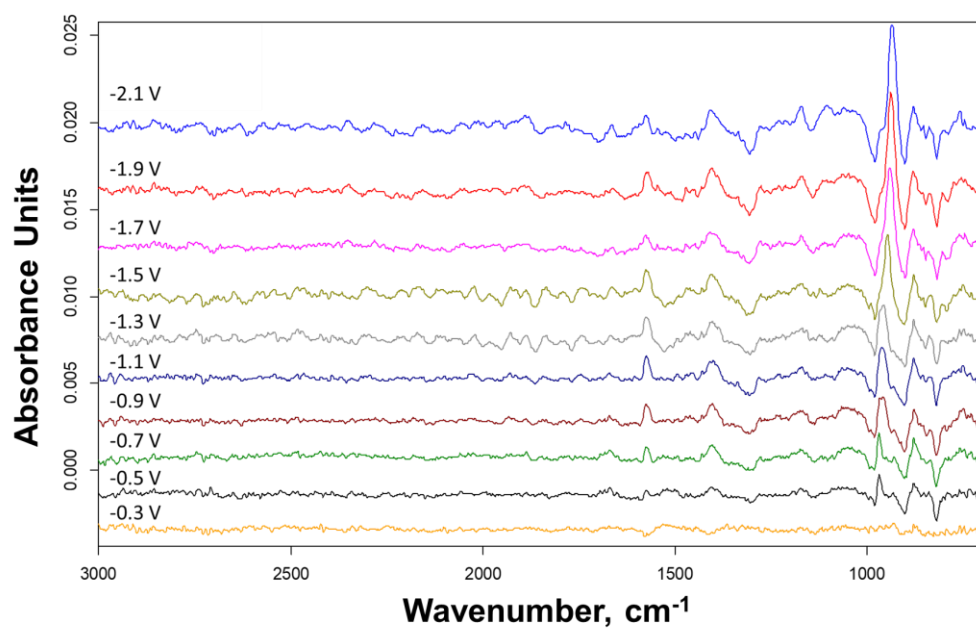


Figure 4.6 IRRAS spectra of *in situ* spectroelectrochemical cell obtained at different potentials during reduction processes indicated on the left side in the range of 3000-700 cm⁻¹.

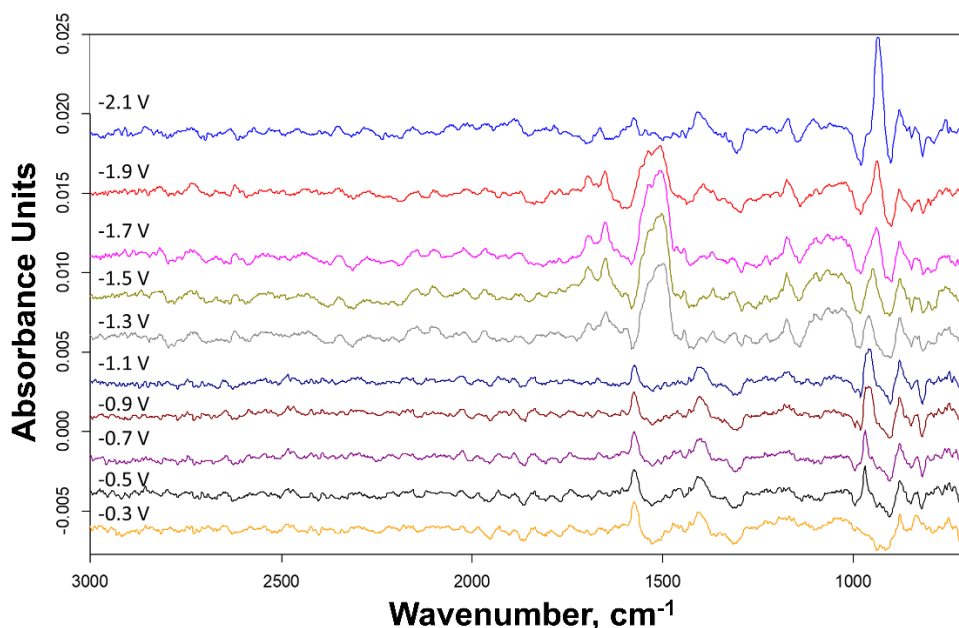


Figure 4.7 IRRAS spectra of *in situ* spectroelectrochemical cell obtained at different potentials during re-oxidation processes indicated on the left side in the range of 3000-700 cm^{-1} .

Another background IRRAS spectrum was acquired at the end of the ion deposition and prior to the *in situ* IR spectroelectrochemical experiments. The IRRAS baseline was collected with 0.3 V applied to the WE because no electron transfer process was observed at this potential indicating that $\text{PW}_{12}\text{O}_{40}^{3-}$ ions are the dominant electroactive species at the EEI. Using this background spectrum, IR bands affected by the potentials applied to the WE of the *in situ* cell were observed with high sensitivity and without substantial interference from other bands. To examine structural changes of WPOM anions during the oxidation/reduction reactions at EEI, *in situ* IRRAS spectra were acquired at different potentials marked with blue dots in Figure 4.4. In these experiments, the cell was held at different potentials that were varied stepwise from -0.3 V to -2.1 V in intervals of 0.2 V. At each WE potential, the cell was allowed to equilibrate for 10 min and the cell current was observed to stabilize at its minimum value (Figure 4.8) which ensures the equilibrium state of the EEI during the IRRAS measurements at each potential.

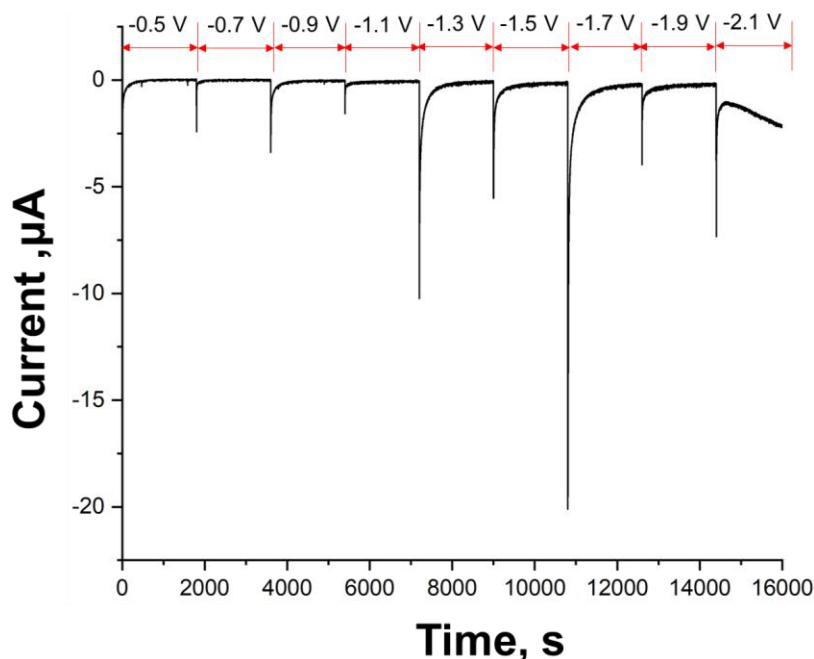


Figure 4.8 Chronoamperometry during the spectroelectrochemistry experiments. The measurements are shown in consecutive 1800-sec segments (including 600 sec equilibration and 1200 sec IRRAS measurement time).

IRRAS spectra acquired at different potentials during the reduction and oxidation processes are presented in Figures 4.9(c) and 4.9(d), respectively. Full-range IRRAS spectra obtained during the reduction process are shown in Figures 4.6 and 4.7. A spectrum of soft-landed $\text{PW}_{12}\text{O}_{40}^{3-}$ on a bare gold surface is shown in Figures 4.9(a) for comparison. A spectrum acquired at -2.1 V is shown separately in Figures 4.9(b) to illustrate the IR features discussed in detail in the following paragraphs. Specifically, band A corresponds to a broad negative feature at 980 cm^{-1} ; band B refers to the positive feature at 969 cm^{-1} . The negative bands at 904 cm^{-1} , the positive band at 880 cm^{-1} and the negative band at 820 cm^{-1} are referred to as band C, D and E, respectively. During the reduction process, no obvious changes in the IRRAS spectra were detected at potentials more positive than -0.3 V applied to the WE. As a result, the spectrum obtained at -0.3 V is indistinguishable from the background spectrum. However, several positive and negative bands appeared at -0.5 V and their positions and intensities continued to evolve at more negative potentials. Specifically, band A appeared at -0.5 V and continued growing in intensity at more negative potentials. Band B appeared at -0.5 V, became broader and shifted towards lower wavenumbers in region II and continued growing in abundance and shifting towards lower wavenumbers in regions III through VI. Bands C, D and E appeared at -0.5 V and showed only a

slight change in abundance over the entire range of potentials. The observed trend is reversible as indicated by the intensities and positions of the bands observed during the oxidation process, in which the WE potential was increased from -2.1 to -0.3 V.

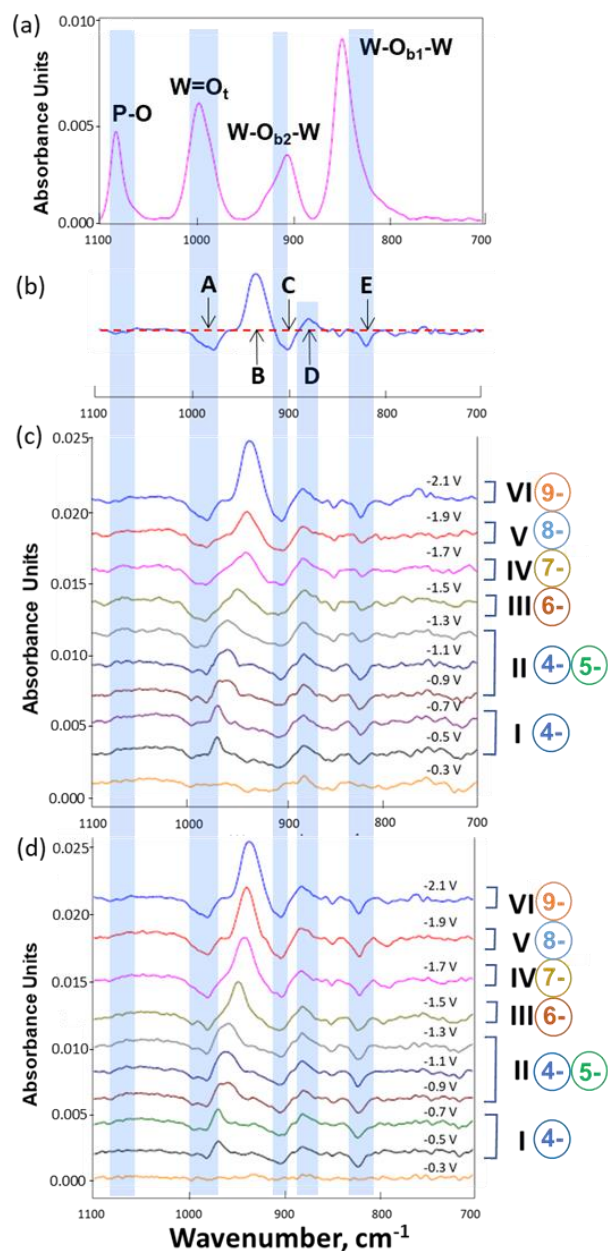


Figure 4.9 (a) *In situ* IRRAS spectrum of WPOM anions soft-landed on a bare gold surface. (b) Representative IRRAS spectrum acquired at -2.1 V shown to illustrate new features that appear during the spectroelectrochemical measurements. The red dashed line indicates the IR baseline. *In situ* IRRAS spectra obtained at different potentials during the (c) reduction and (d) oxidation processes of WPOM. The potential regions I-VI and the corresponding charge states of the reduced WPOM species are marked on the right.

Comparison of the IRRAS spectra obtained at different potentials with the spectrum of $\text{PW}_{12}\text{O}_{40}^{3-}$ on neutral gold indicates that the observed bands may be attributed to structural changes occurring in WPOM anions at the energized EEIs. The positive peaks in the IR spectra in Figures 4.9(c) and 4.9(d) can be interpreted as emerging features of the reduced WPOM anions, while the negative peaks correspond to absorption bands of $\text{PW}_{12}\text{O}_{40}^{3-}$, which was originally present at the EEI and becomes depleted with reduction. These bands disappear as the 3- anions are reduced and are observed as negative signals relative to the $\text{PW}_{12}\text{O}_{40}^{3-}$ background.

IR bands of WPOM were assigned based on our previous study of soft-landed $\text{PW}_{12}\text{O}_{40}^{3-}$ anions¹ and are compared with both the experimental IR spectrum of phosphotungstic acid² and the calculated vibrational bands of isolated $\text{PW}_{12}\text{O}_{40}^{3-}$ in the gas phase.^{1,3} Specifically, the bands at 990 and 1083 cm^{-1} are assigned to the terminal $\text{W}=\text{O}_t$ stretching vibration and asymmetric coupling of P-O and $\text{W}=\text{O}_t$ stretching modes (shown as P-O in Figure 4.9(a)), respectively. Meanwhile the two bands at 900 and 835 cm^{-1} are assigned to the vibrational stretching of two types of bridging oxygen atoms, $\text{W}-\text{O}_{b2}-\text{W}$ and $\text{W}-\text{O}_{b1}-\text{W}$, respectively. The P-O and $\text{W}=\text{O}_t$ symmetric coupling motion appears to be a shoulder on the $\text{W}=\text{O}_t$ stretching band at lower wavenumbers (961 cm^{-1}). We note that band positions may be shifted in the spectroelectrochemistry experiments described in this study in comparison with gas-phase literature values due to interactions of WPOM anions with electrolyte ions (IL ions) at the interface.

IRRAS spectra obtained using soft-landed $\text{PW}_{12}\text{O}_{40}^{3-}$ as a background (Figures 4.9(c) and 4.9(d)) do not contain a peak around 1083 cm^{-1} indicating that the P-O band is not affected by the redox processes. Bands A (negative) and B (positive) may be attributed to changes in the $\text{W}=\text{O}_t$ vibration. Changes in the position and intensity of these bands will be discussed in detail later. Bands C, D and E may be attributed to the evolution of the $\text{W}-\text{O}_{b2}-\text{W}$ and $\text{W}-\text{O}_{b1}-\text{W}$ bridging bands at different potentials. Specifically, bands C and E may be attributed to either the disappearance or shift in position of the $\text{W}-\text{O}_{b2}-\text{W}$ and $\text{W}-\text{O}_{b1}-\text{W}$ bands, respectively. Although an intense $\text{W}-\text{O}_{b1}-\text{W}$ bridging band at 835 cm^{-1} is present in the IRRAS spectrum of WPOM soft-landed onto a bare gold surface (Figures 4.9(a)), the abundance of band E is low indicating that the $\text{W}-\text{O}_{b1}-\text{W}$ bridging mode does not undergo substantial changes during the reduction process. In contrast, similar intensities of bands C (positive) and D (negative) may be ascribed to the same vibrational mode, which is shifted towards lower wavenumbers (from 904 cm^{-1} to 880 cm^{-1}) during the redox

process. We propose that the observed change may be attributed to an elongation of the W-O_{b2}-W bridging band with WPOM reduction, which is consistent with the literature XAFS studies described earlier.⁴ Both bridging band peaks appear after the first reduction step and their positions do not change substantially over the entire potential range. This observation indicates that after the initial structural change at -0.5 V, the bridging bands do not change substantially when WPOM accepts additional electrons. This is in agreement with the slight elongation of the bridging bands and relatively small change in reduced POM cage size indicated by previous XAFS and DFT studies.^{4,5}

In contrast to the bridging bands, the intensity and position of the W=O_t band is strongly affected by the redox processes. Band A that appears at -0.5 V and increases in intensity at more negative potentials is assigned as W=O_t vibrations of the soft-landed PW₁₂O₄₀³⁻ anions. The gradual increase in the intensity of band A over the entire reduction potential range indicates an incomplete initial conversion of the soft-landed WPOM³⁻ resulting in the observed reduction of this ion at more negative potentials. The number of WPOM reduced at the surface is limited by the migration of ions in the diffuse layer. The soft-landed PW₁₂O₄₀³⁻ are distributed throughout the bulk of the electrolyte membrane, which limits the rate of their transport to the electrode surface. Reduction of the remaining PW₁₂O₄₀³⁻ anions is most likely driven by the increased potential-controlled migration of ions at more negative overpotentials and contributes to the observed gradual increase in band A.

In addition, we observed pronounced and reversible changes in both peak positions and intensities of band B in the wavenumber range between 969 and 935 cm⁻¹ during the reduction/oxidation process. According to the XAFS experiments cited earlier,⁴ as the cluster is reduced to more negative charge states, the terminal W=O_t bond gradually loses its double bond character and is converted into a single bond. The observed shift in the position of the W=O_t band toward lower wavenumbers in our IRRAS spectra is consistent with this previous assertion. We hypothesized that the formation of different charge states of WPOM at different potentials applied to the WE is responsible for the observed change in both the position and intensity of the W=O_t peak in the wavenumber range between 969 and 935 cm⁻¹.

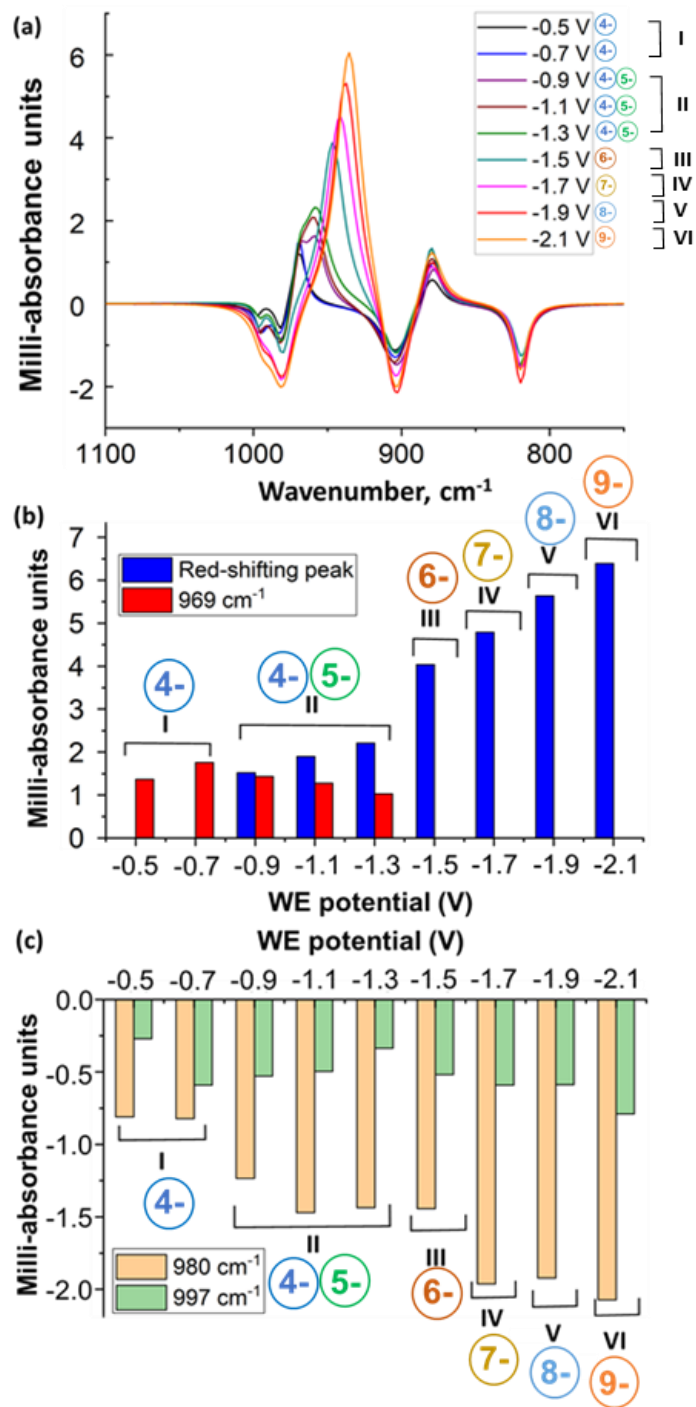


Figure 4.10 (a) Fitted IR spectra obtained during the reduction process in the wavenumber range between 1000 to 800 cm^{-1} . Bar graphs showing the intensities of the positive (b) and negative (c) bands in the $\text{W}=\text{O}_i$ region obtained from curve fitting as a function of the potential applied to the WE. The potential regions (I-VI) and charge states of the reduced WPOM at each potential are marked to facilitate understanding.

To test this hypothesis, we fitted the IR spectra obtained at potentials ranging from -0.5 to -2.1 V in the reduction process. The spectra were simulated using a sum of several Lorentzian distributions with peak positions in the range between 1000 and 800 cm^{-1} , as described in detail in the experimental section. Spectra obtained from the best fit of the IRRAS data during the reduction process are shown in Figures 4.10(a). A comparison of the experimental and simulated IRRAS spectra at each reduction potential is shown in Figures 4.11. We observed moderate changes in the intensities of the bridging bands, indicating that they do not undergo substantial evolution during the reduction process. In addition, curve fitting provides insights into changes in the $\text{W}=\text{O}_t$ band in the different potential regions observed experimentally. The shape of the $\text{W}=\text{O}_t$ band was adequately reproduced using a sum of two negative peaks at 997 and 980 cm^{-1} and two positive bands: one at 969 cm^{-1} has a fixed position over the entire potential range, while another one shifts towards lower wavenumbers (red shifts) from 958 to 935 cm^{-1} with increasing WPOM reduction. The intensities of the two positive and negative bands as a function of the applied potential obtained from curve fitting are shown in Figures 4.10(a) and 4.10(b). In region I, we observe one positive growing feature at 969 cm^{-1} . Because the spectra were acquired with $\text{PW}_{12}\text{O}_{40}^{3-}$ as a background, we propose that this peak corresponds to the $\text{W}=\text{O}_t$ band of $\text{PW}_{12}\text{O}_{40}^{4-}$. This peak gradually decreases in region II and disappears at more negative potentials. We attribute the presence of this band in region II to the incomplete conversion of $\text{PW}_{12}\text{O}_{40}^{4-}$ into $\text{PW}_{12}\text{O}_{40}^{5-}$. Another peak appears in region II at 958 cm^{-1} , which subsequently grows in intensity and shifts to 947 cm^{-1} (region III), 942 cm^{-1} (region IV), 938 cm^{-1} (region V), and 935 cm^{-1} (region VI). We propose that this red-shifting peak corresponds to $\text{PW}_{12}\text{O}_{40}^{5-}$, $\text{PW}_{12}\text{O}_{40}^{6-}$, $\text{PW}_{12}\text{O}_{40}^{7-}$, $\text{PW}_{12}\text{O}_{40}^{8-}$ and $\text{PW}_{12}\text{O}_{40}^{9-}$ in regions II, III, IV, V, and VI, respectively (summarized in Table 4.2). The shift in the position of this peak is attributed to elongation of the $\text{W}=\text{O}_t$ bond as it converts from a double bond to a more single-like bond with increasing reduction of WPOM. The negative peak at 980 cm^{-1} grows in intensity in regions I through IV while the negative peak at 997 cm^{-1} does not show a clear trend with the increase in the applied potential. The origin of the 997 cm^{-1} band cannot be determined based on our current results. However, the evolution of the 980 cm^{-1} feature is consistent with our assignment of this band to the $\text{PW}_{12}\text{O}_{40}^{3-}$ species. As discussed earlier, the increase in abundance of the peak at 980 cm^{-1} during the reduction process is attributed to the incomplete conversion of $\text{PW}_{12}\text{O}_{40}^{3-}$.

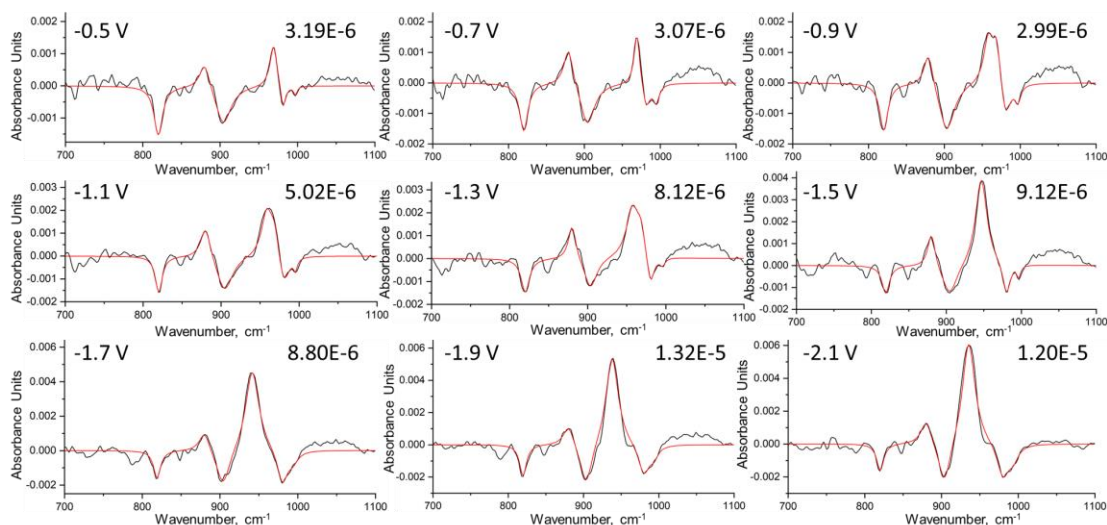


Figure 4.11 Experimental and curve-fitted IRRAS spectra at different potentials in the reduction process marked on the top left side of each plot. In each plot, experimental spectrum is shown in black and the best fit curve is shown in red. The sum of squares in each curve fitting is indicated on the top right.

Table 4.2 IR band assignments to different charge states of reduced WPOM from the spectroelectrochemistry experiments in the range of 1000-800 cm^{-1} .

IR band (cm^{-1})	A	B	C	D	E
Species					
$\text{PW}_{12}\text{O}_{40}^{4-}$	997	980	969	904	880 820
$\text{PW}_{12}\text{O}_{40}^{5-}$	997	980	958	904	880 820
$\text{PW}_{12}\text{O}_{40}^{6-}$	997	980	947	904	880 820
$\text{PW}_{12}\text{O}_{40}^{7-}$	997	980	942	904	880 820
$\text{PW}_{12}\text{O}_{40}^{8-}$	997	980	938	904	880 820
$\text{PW}_{12}\text{O}_{40}^{9-}$	997	980	935	904	880 820

4.4 Conclusions

In summary, the observed changes in the IRRAS spectra of WPOM during the redox process may be attributed to the presence of the different charge states at the interface. We observed an incomplete conversion of WPOM anions in the first two reduction steps. At more negative potentials, the conversion efficiency is challenging to estimate because of the substantial increase in the abundance of the $\text{W}=\text{O}_t$ band that obscures the lower charge states potentially

present at the interface. The incomplete conversion is attributed to potential-controlled migration of ions at more negative overpotentials. These results demonstrate that minor structural changes in the reduced WPOM anions may be observed using the spectroelectrochemical approach developed in this study in combination with precise control of the electroactive species prepared by soft-landing of mass- and charge-selected ion onto a specially-designed electrochemical cell.

4.5 References

- (1) Bard, A. J.; Abruna, H. D.; Chidsey, C. E.; Faulkner, L. R.; Feldberg, S. W.; Itaya, K.; Majda, M.; Melroy, O.; Murray, R. W. The electrode/electrolyte interface—a status report. *J. Phys. Chem.* **1993**, *97*, 7147-7173.
- (2) Hamnett, A. The electrode–electrolyte interface. *Handbook of Fuel Cells* **2010**.
- (3) Ilott, A. J.; Trease, N. M.; Grey, C. P.; Jerschow, A. Multinuclear in situ magnetic resonance imaging of electrochemical double-layer capacitors. *Nat. Commun.* **2014**, *5*, 4536.
- (4) Pozniak, B.; Scherson, D. A. Dynamics of a surface phase transition as monitored by in situ second harmonic generation. *J. Am. Chem. Soc.* **2003**, *125*, 7488-7489.
- (5) Le Rille, A.; Tadjeddine, A.; Zheng, W.; Peremans, A. Vibrational spectroscopy of a Au (hkl)-electrolyte interface by in situ visible-infrared difference frequency generation. *Chem. Phys. Lett.* **1997**, *271*, 95-100.
- (6) Itkis, D. M.; Velasco-Velez, J. J.; Knop-Gericke, A.; Vyalikh, A.; Avdeev, M. V.; Yashina, L. V. Probing operating electrochemical interfaces by photons and neutrons. *ChemElectroChem* **2015**, *2*, 1427-1445.
- (7) Salmeron, M.; Schlögl, R. Ambient pressure photoelectron spectroscopy: A new tool for surface science and nanotechnology. *Surf. Sci. Rep.* **2008**, *63*, 169-199.
- (8) Ashley, K.; Pons, S. Infrared spectroelectrochemistry. *Chem. Rev.* **1988**, *88*, 673-695.
- (9) Jebaraj, A. J. J.; Kumsa, D.; Scherson, D. A. Oxidation of hydroxylamine on gold electrodes in aqueous electrolytes: Rotating ring-disk and in situ infrared reflection absorption spectroscopy studies. *J. Phys. Chem. C* **2012**, *116*, 6932-6942.
- (10) Alkire, R. C.: *Diffraction and spectroscopic methods in electrochemistry*; John Wiley & Sons, 2006; Vol. 9.
- (11) Roth, J. D.; Lewis, G. J.; Safford, L. K.; Jiang, X.; Dahl, L. F.; Weaver, M. J. Exploration of the ionizable metal cluster-electrode surface analogy: infrared spectroelectrochemistry of [Pt₂₄(CO)₃₀] N, [Pt₂₆(CO)₃₂] N, and [Pt₃₈(CO)₄₄] N (n= 0 to-10) and comparisons with potential-dependent spectra of carbon monoxide adlayers on platinum surfaces. *J. Am. Chem. Soc.* **1992**, *114*, 6159-6169.

- (12) Mäntele, W.; Wollenweber, A.; Nabedryk, E.; Breton, J. Infrared spectroelectrochemistry of bacteriochlorophylls and bacteriopheophytins: Implications for the binding of the pigments in the reaction center from photosynthetic bacteria. *Proc. Natl. Acad. Sci.* **1988**, *85*, 8468-8472.
- (13) Richey, F. W.; Dyatkin, B.; Gogotsi, Y.; Elabd, Y. A. Ion dynamics in porous carbon electrodes in supercapacitors using in situ infrared spectroelectrochemistry. *J. Am. Chem. Soc.* **2013**, *135*, 12818-12826.
- (14) Seki, H.; Kunitatsu, K.; Golden, W. A thin-layer electrochemical cell for infrared spectroscopic measurements of the electrode/electrolyte interface. *Appl. Spectrosc.* **1985**, *39*, 437-443.
- (15) Iwasita, T.; Nart, F. In situ infrared spectroscopy at electrochemical interfaces. *Prog. Surf. Sci.* **1997**, *55*, 271-340.
- (16) Prabhakaran, V.; Johnson, G. E.; Wang, B.; Laskin, J. In situ solid-state electrochemistry of mass-selected ions at well-defined electrode–electrolyte interfaces. *Proc. Natl. Acad. Sci.* **2016**, *113*, 13324-13329.
- (17) MacFarlane, D. R.; Forsyth, M.; Howlett, P. C.; Kar, M.; Passerini, S.; Pringle, J. M.; Ohno, H.; Watanabe, M.; Yan, F.; Zheng, W. Ionic liquids and their solid-state analogues as materials for energy generation and storage. *Nat. Rev. Mater.* **2016**, *1*, 15005.
- (18) Grill, V.; Shen, J.; Evans, C.; Cooks, R. G. Collisions of ions with surfaces at chemically relevant energies: instrumentation and phenomena. *Rev. Sci. Instrum.* **2001**, *72*, 3149-3179.
- (19) Rauschenbach, S.; Stadler, F. L.; Lunedei, E.; Malinowski, N.; Koltsov, S.; Costantini, G.; Kern, K. Electrospray ion beam deposition of clusters and biomolecules. *small* **2006**, *2*, 540-547.
- (20) Johnson, G. E.; Hu, Q.; Laskin, J. Soft landing of complex molecules on surfaces. *Ann. Rev. Anal. Chem.* **2011**, *4*, 83-104.
- (21) Cyriac, J.; Pradeep, T.; Kang, H.; Souda, R.; Cooks, R. Low-energy ionic collisions at molecular solids. *Chem. Rev.* **2012**, *112*, 5356-5411.
- (22) Verbeck, G.; Hoffmann, W.; Walton, B. Soft-landing preparative mass spectrometry. *Analyst* **2012**, *137*, 4393-4407.
- (23) Johnson, G. E.; Gunaratne, D.; Laskin, J. Soft-and reactive landing of ions onto surfaces: Concepts and applications. *Mass Spectrom. Rev.* **2016**, *35*, 439-479.
- (24) Laskin, J.; Johnson, G. E.; Prabhakaran, V. Soft Landing of Complex Ions for Studies in Catalysis and Energy Storage. *J. Phys. Chem. C* **2016**, *120*, 23305-23322.
- (25) Laskin, J.; Johnson, G. E.; Warneke, J.; Prabhakaran, V. From Isolated Ions to Multilayer Functional Materials Using Ion Soft-Landing. *Angew. Chem. Int. Ed.* **2018**.

- (26) Prabhakaran, V.; Mehdi, B. L.; Ditto, J. J.; Engelhard, M. H.; Wang, B.; Gunaratne, K. D. D.; Johnson, D. C.; Browning, N. D.; Johnson, G. E.; Laskin, J. Rational design of efficient electrode–electrolyte interfaces for solid-state energy storage using ion soft landing. *Nat. Commun.* **2016**, *7*, 11399.
- (27) Wang, H.; Hamanaka, S.; Nishimoto, Y.; Irle, S.; Yokoyama, T.; Yoshikawa, H.; Awaga, K. In operando X-ray absorption fine structure studies of polyoxometalate molecular cluster batteries: polyoxometalates as electron sponges. *J. Am. Chem. Soc.* **2012**, *134*, 4918-4924.
- (28) Kawasaki, N.; Wang, H.; Nakanishi, R.; Hamanaka, S.; Kitaura, R.; Shinohara, H.; Yokoyama, T.; Yoshikawa, H.; Awaga, K. Nanohybridization of polyoxometalate clusters and single-wall carbon nanotubes: applications in molecular cluster batteries. *Angew. Chem.* **2011**, *123*, 3533-3536.
- (29) Symes, M. D.; Cronin, L. Decoupling hydrogen and oxygen evolution during electrolytic water splitting using an electron-coupled-proton buffer. *Nat. Chem.* **2013**, *5*, 403.
- (30) Sadakane, M.; Steckhan, E. Electrochemical properties of polyoxometalates as electrocatalysts. *Chem. Rev.* **1998**, *98*, 219-238.
- (31) Nishimoto, Y.; Yokogawa, D.; Yoshikawa, H.; Awaga, K.; Irle, S. Super-reduced polyoxometalates: excellent molecular cluster battery components and semipermeable molecular capacitors. *J. Am. Chem. Soc.* **2014**, *136*, 9042-9052.
- (32) Gunaratne, K. D. D.; Prabhakaran, V.; Johnson, G. E.; Laskin, J. Gas-Phase Fragmentation Pathways of Mixed Addenda Keggin Anions: $\text{PMo}_{12-n}\text{W}_n\text{O}_{403}$ ($n = 0-12$). *J. Am. Soc. Mass. Spectrom.* **2015**, *26*, 1027-1035.
- (33) Gunaratne, K. D. D.; Prabhakaran, V.; Andersen, A.; Johnson, G. E.; Laskin, J. Charge retention of soft-landed phosphotungstate Keggin anions on self-assembled monolayers. *PCCP* **2016**, *18*, 9021-9028.
- (34) Thouvenot, R.; Fournier, M.; Franck, R.; Rocchiccioli-Deltcheff, C. Vibrational investigations of polyoxometalates. 3. Isomerism in molybdenum (VI) and tungsten (VI) compounds related to the Keggin structure. *Inorg. Chem.* **1984**, *23*, 598-605.
- (35) Zhang, J.; Bond, A. M.; MacFarlane, D. R.; Forsyth, S. A.; Pringle, J. M.; Mariotti, A. W.; Glowinski, A. F.; Wedd, A. G. Voltammetric studies on the reduction of polyoxometalate anions in ionic liquids. *Inorg. Chem.* **2005**, *44*, 5123-5132.
- (36) Gunaratne, K. D. D.; Prabhakaran, V.; Ibrahim, Y. M.; Norheim, R. V.; Johnson, G. E.; Laskin, J. Design and performance of a high-flux electrospray ionization source for ion soft landing. *Analyst* **2015**, *140*, 2957-2963.
- (37) Hu, Q.; Wang, P.; Gassman, P. L.; Laskin, J. In situ studies of soft-and reactive landing of mass-selected ions using infrared reflection absorption spectroscopy. *Anal. Chem.* **2009**, *81*, 7302-7308.

- (38) Nanbu, N.; Sasaki, Y.; Kitamura, F. In situ FT-IR spectroscopic observation of a room-temperature molten salt| gold electrode interphase. *Electrochem. Commun.* **2003**, *5*, 383-387.
- (39) Bondarenko, A. S.; Ragoisha, G. A.: *Inverse problem in potentiodynamic electrochemical impedance*; Nova Science Publishers: New York, 2005.
- (40) Lou, F.; Zhou, H.; Huang, F.; Vullum-Bruer, F.; Tran, T. D.; Chen, D. Facile synthesis of manganese oxide/aligned carbon nanotubes over aluminium foil as 3D binder free cathodes for lithium ion batteries. *J. Mater. Chem. A* **2013**, *1*, 3757-3767.
- (41) Song, J. Y.; Lee, H. H.; Wang, Y. Y.; Wan, C. C. Two- and three-electrode impedance spectroscopy of lithium-ion batteries. *Journal of Power Sources* **2002**, *111*, 255-267.
- (42) Lasia, A.: *Electrochemical impedance spectroscopy and its applications*; Springer, 2017.
- (43) Eda, K.; Osakai, T. How can multielectron transfer be realized? A case study with Keggin-type polyoxometalates in acetonitrile. *Inorg. Chem.* **2015**, *54*, 2793-2801.
- (44) Gunaratne, K. D. D.; Johnson, G. E.; Andersen, A.; Du, D.; Zhang, W.; Prabhakaran, V.; Lin, Y.; Laskin, J. Controlling the charge state and redox properties of supported polyoxometalates via soft landing of mass-selected ions. *J. Phys. Chem. C* **2014**, *118*, 27611-27622.
- (45) Sandoval, A. P.; Suárez-Herrera, M. F.; Feliu, J. M. IR and electrochemical synthesis and characterization of thin films of PEDOT grown on platinum single crystal electrodes in [EMMIM] Tf₂N ionic liquid. *Beilstein J. Org. Chem.* **2015**, *11*, 348.

CHAPTER 5. GAS PHASE FRAGMENTATION OF HOST-GUEST COMPLEXES OF CYCLODEXTRINS AND POLYOXOMETALATES

5.1 Introduction

Host-guest supramolecular chemistry refers to the encapsulation of a guest molecule by the cavity of a macrocyclic host molecule via non-covalent interactions¹⁻³. It has been widely employed for the design and construction of supramolecular assemblies for applications in catalysis^{4,5}, materials sciences^{6,7}, and drug delivery^{8,9}. The hydrophobic effect was originally proposed to be a major driving force for the formation of host-guest complexes in the solution phase^{10,11}. The incorporation of a hydrophobic guest into the apolar cavity of a host molecule is a thermodynamically favorable process¹².

Recent studies have demonstrated an unexpected formation of strongly bound complexes, in which a chaotropic anion is embedded in a hydrophobic cavity of a macrocyclic host molecule. Chaotropic anions are often described as hydrophilic species with a delocalized charge, which form complexes with host molecules mainly because of a strong binding of the anion to the host molecule¹³. The formation and stability of these host-guest complexes have been discussed in the context of a chaotropic effect as an alternative driving force for supramolecular assembly in an aqueous solution^{12,14}. The chaotropic effect is explained as follows: encapsulation of a chaotropic ion into the binding pocket of a host molecule allows for the recovery of the water structure initially disrupted by the ion¹⁵. Despite the entropic penalty resulting from the reorganization of water molecules, this process is thermodynamically favorable due to a large negative enthalpy of complexation¹⁶. The chaotropic effect becomes particularly pronounced for halogenated dodecaborates ($B_{12}X_{12}^{2-}$, X = F, Cl, Br, I) and small polyoxometalates (POMs) referred to as superchaotropic anions that lie far beyond the classical Hofmeister series^{17,18}. The strong binding between $B_{12}X_{12}^{2-}$ anions and several host molecules have been observed in the gas phase free of solvent environment¹⁹.

Superchaotropic POM anions^{20,21} also have been explored as guest species in host-guest supramolecular complexes with macrocyclic host molecules such as pseudorotaxanes²², cucurbit[n]uril²³⁻²⁵, and calix[4]arene derivatives^{26,27}. The unique redox properties of POMs make

their host-guest complexes particularly attractive building blocks for the design of functional supramolecular assemblies²⁸⁻³⁰. In particular, host-guest complexes of POMs and cyclodextrins (CDs) have been extensively studied. CDs are a class of cyclic oligosaccharides composed of 6, 7, and 8 D-glucopyranosyl residues (α -, β -, and γ -CD, respectively) linked by α -1,4 glycosidic bonds³¹. The shape-persistent hydrophobic cavity of a well-defined size enables the wide application of CDs as exceptional synthetic receptors in nanotechnology^{32,33}, catalysis^{34,35}, and pharmaceutical science^{36,37}.

The first example of CD-POM host-guest complexes was described by Stoddart and co-workers³⁸. Several novel CD-POM host-guest supramolecular hybrid materials have been successfully prepared through solution-phase approaches, and the non-covalent interactions of the host-guest assemblies have been systematically characterized³⁹⁻⁴³. Nuclear magnetic resonance (NMR) and single-crystal X-ray diffraction (XRD) analyses have confirmed that hydrogen-bonding between POM and CD contributes to a majority of supramolecular interactions both in solution and in the solid state³⁸⁻⁴⁰. Meanwhile, the intrinsic non-covalent interactions between POMs and CDs free of solvent effects are still largely unexplored.

Mass spectrometry (MS) enables the investigation of structures and stabilities of host-guest complexes as isolated species in the gas phase⁴⁴⁻⁴⁷. Several studies have examined gas-phase fragmentation of CD complexes with amino acids⁴⁸, peptides⁴⁹, nucleobases⁵⁰, and organometallic compounds^{51,52}. Of particular interest to this work are gas phase fragmentation studies of CD-POM complexes using collision-induced dissociation (CID), which provide insights into the intrinsic interactions of POMs and CDs^{53,54}. Herein, we explore the effect of the cavity diameter of the host CD molecule and properties of the guest POM anion on the gas phase fragmentation of CD-POM complexes. In particular, we examine CD-POM host-guest complexes of two archetypal POM structures, Keggin ($\text{PW}_{12}\text{O}_{40}^{3-}$, $\text{W}_{12}\text{POM}^{3-}$) and Lindqvist ($\text{M}_6\text{O}_{19}^{2-}$, $\text{M}_6\text{POM}^{2-}$, where $\text{M} = \text{Mo}$ or W) anions with three types of CDs with different cavity diameters, α -, β -, and γ -CD. Aside from proton transfer and direct dissociation pathways, which are characteristic of CID of non-covalent complexes, we observe simultaneous loss of multiple water molecules from the complex. We attribute this unusual fragmentation pathway to covalent bond formation between the CD host and POM fragments induced by proton transfer upon collisional activation. Covalent coupling of non-covalent complexes in CID has been previously

reported for complexes of crown ethers with amines⁵⁵⁻⁵⁷. Furthermore, unusual reactivity in the gas phase has been observed when the host cavity of cucurbiturils was used as a molecular reaction container⁵⁸. However, to the best of our knowledge the reactivity observed in this study has not been previously reported. The results presented herein open up intriguing opportunities for studying proton-induced chemistry of guest anions inside host cavities and covalent modification of macrocyclic host molecules.

5.2 Experimental Sections

5.2.1 Chemicals

Sodium phosphotungstate tribasic hydrate ($\text{Na}_3[\text{PW}_{12}\text{O}_{40}] \cdot x\text{H}_2\text{O}$), sodium molybdate (Na_2MoO_4), sodium tungstate dihydrate ($\text{Na}_2\text{WO}_4 \cdot 2\text{H}_2\text{O}$), tetrabutylammonium bromide (TBA) ($\text{C}_{16}\text{H}_{36}\text{BrN}$), α -cyclodextrin ($\text{C}_{36}\text{H}_{60}\text{O}_{30}$), β -cyclodextrin ($\text{C}_{42}\text{H}_{70}\text{O}_{35}$), γ -cyclodextrin ($\text{C}_{48}\text{H}_{80}\text{O}_{40}$), methanol- d_4 (CD_3OD , 99.8 atom % D), deuterium oxide (D_2O , 99 atom % D), and water- ^{18}O (H_2^{18}O , 97 atom % ^{18}O) were all purchased from Sigma-Aldrich (St. Louis, MO, USA). Hydrochloric acid (HCl, 25 wt %) was purchased from Honeywell (Mexico City, Mexico). Ethyl ether ($(\text{C}_2\text{H}_5)_2\text{O}$, anhydrous), water (H_2O , HPLC grade), and methanol (CH_3OH) were purchased from Fisher Scientific (Fair Lawn, NJ, USA).

5.2.2 Synthesis

1. Preparation of Keggin [$\text{CD} + \text{W}_{12}\text{POM}$] $^{3-}$ Host-Guest Complex Solutions: A 1 mM stock solution of $\text{W}_{12}\text{POM}^{3-}$ was prepared by dissolving $\text{Na}_3[\text{PW}_{12}\text{O}_{40}]$ in methanol. 1 mM stock solutions of α -, β -, and γ -CD were prepared by dissolving CD in 90:10 (v/v) methanol/water solution. We found it to be necessary to include water to better solubilize the CDs. The final solution for ESI-MS was prepared by combining the Keggin POM and CD stock solutions in a 1:1 ratio and diluting the mixture with methanol to a final concentration of 10 μM .

2. One-Pot Synthesis of Lindqvist [$\text{CD} + \text{M}_6\text{POM}$] $^{2-}$ Host-Guest Complexes: $\text{Na}_2[\text{X-CD} + \text{M}_6\text{O}_{19}]$ (where $\text{M} = \text{W}$ or Mo , and $\text{X} = \alpha$, β , or γ) was synthesized using a one-pot method adapted from Cadot, et al⁵⁹. Typical synthetic procedure is described here using $[\text{Na}^+]_2[\gamma\text{-CD} + \text{W}_6\text{O}_{19}]^{2-}$ as an example: 0.1 g (0.3 mmol) $\text{Na}_2\text{WO}_4 \cdot 2\text{H}_2\text{O}$ was dissolved in 4 mL of water, followed by addition of 0.072 g (0.05 mmol) of γ -CD under stirring. The same 6:1 molar ratio of

Na₂MoO₄ and CD was used for the one-pot synthesis with both α - and β -CD. A total of six of these syntheses were performed in order to get a sample of each combination of [X-CD + M₆O₁₉]²⁻. These solutions were diluted with methanol to a concentration of 10 μ M for MS analysis. We also verified that the same Lindqvist CD-POM complex can be made by mixing [(n-C₄H₉)₄N]₂[W₆O₁₉] and γ -CD directly in methanol in the case of [γ -CD + W₆POM]²⁻. Synthesis of [(n-C₄H₉)₄N]₂[W₆O₁₉] was done by a procedure adapted from Klemperer et al ⁶⁰.

5.2.3 MS Experiments

1. Low-energy CID and HCD Conditions: ESI-MS analyses of the CD-POM complexes were performed using LTQ XL Linear Ion Trap Mass Spectrometer and Q-Exactive HF-X Hybrid Quadrupole-Orbitrap Mass Spectrometer (Thermo Fisher Scientific GmbH, Bremen, Germany). Samples were introduced into the MS inlet by direct infusion from a capillary (50 μ m ID, 150 μ m OD) at a flow rate of \sim 0.5 μ L/min. Typical mass spectrometer conditions on LTQ were as follows: electrospray voltage: -3 kV, capillary temperature: 200 $^{\circ}$ C, capillary voltage: -10 V, tube lens: -20 V. Scan range: 100-2000 m/z . In the low-energy CID experiments, negatively-charged host-guest complexes were isolated in the linear ion trap and subjected to collisions with helium buffer gas. Typical isolation width was 1 m/z . The q value was set at 0.25, and the typical activation time was 30 ms. Typical mass spectrometer conditions on Q-Exactive were as follows: electrospray voltage: -3 kV, capillary temperature: 250 $^{\circ}$ C, RF funnel level: 100. Mass spectra were acquired over 150-2000 m/z at 240000 resolution (m/z 400). In Higher-Energy Collisional Dissociation (HCD) experiments, ions were mass-selected in quadrupole mass filter and subjected to collisions with the background gas in the HCD cell. The isolation width for all of the complexes was 0.4 m/z . Collision energies (CE) are reported in the manufacturer-specified arbitrary units.

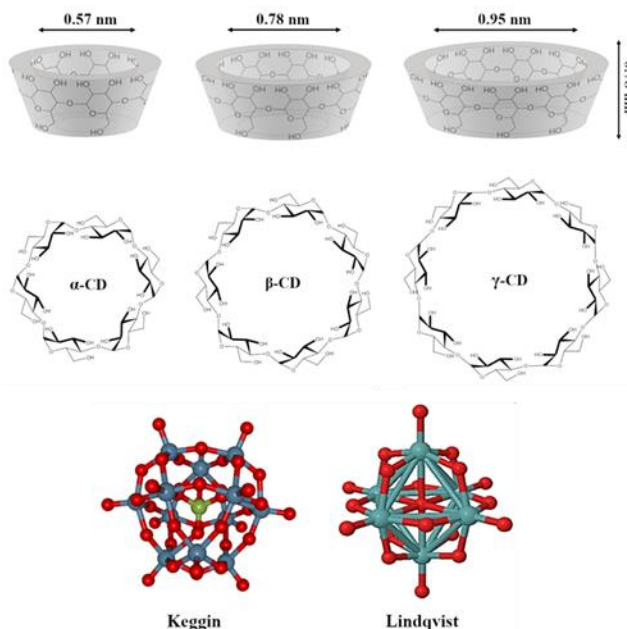
2. Hydrogen/Deuterium Exchange (HDX) Experiments: The HDX experiments were conducted by diluting the solution containing [γ -CD + W₆POM]²⁻ with 50:50 (v/v) CD₃OD/D₂O solvent to a final concentration of \sim 10 μ M. The solution was allowed to rest for three hours. All ESI-MS and low-energy CID conditions were consistent with those described above.

3. ¹⁸O Exchange Experiments: The ¹⁸O-enriched complex, [γ -CD + W₆POM]²⁻, was generated using the one-pot synthesis procedure described in the previous section with H₂¹⁸O as a

solvent. ESI-MS analysis was performed by diluting the solution containing $[\gamma\text{-CD} + \text{W}_6\text{POM}]^{2-}$ in 50:50 (v/v) acetonitrile: $^{18}\text{H}_2\text{O}$ to a final concentration of $\sim 10\ \mu\text{M}$. ESI-MS and low-energy CID experiments were performed using the experimental conditions described earlier.

5.3 Results and Discussion

The CD-POM host-guest complexes examined in this study are composed of three types of CD (α , β , and γ) and two types of POM (Keggin and Lindqvist, structures are shown in Scheme 5.1). They were used to generate six different host-guest complexes ($[\alpha\text{-CD} + \text{W}_{12}\text{POM}]^{3-}$, $[\beta\text{-CD} + \text{W}_{12}\text{POM}]^{3-}$, $[\gamma\text{-CD} + \text{W}_{12}\text{POM}]^{3-}$, $[\alpha\text{-CD} + \text{W}_6\text{POM}]^{2-}$, $[\beta\text{-CD} + \text{W}_6\text{POM}]^{2-}$, and $[\gamma\text{-CD} + \text{W}_6\text{POM}]^{2-}$). Although this study is mainly focused on W-containing POM anions ($\text{W}_{12}\text{POM}^{3-}$, $\text{W}_6\text{POM}^{2-}$), several experiments were performed using $\text{Mo}_6\text{POM}^{2-}$ anion for comparison. Each of the anionic complexes was found to be an abundant species in the ESI-MS spectrum (Figure 5.1). Although complexes with more than one CD molecule are often produced by ESI-MS^{53,54,59}, only host-guest complexes of 1:1 stoichiometry were examined in this study.



Scheme 5.1 Cyclodextrins (α , β , and γ -CD) and POM anions (Keggin $\text{W}_{12}\text{POM}^{3-}$, Lindqvist $\text{W}_6\text{POM}^{2-}$) used in this study.

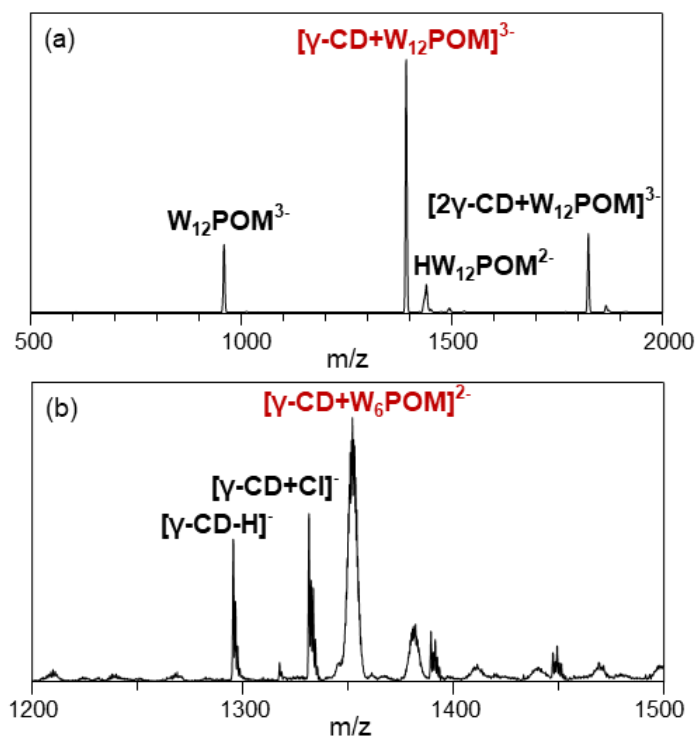


Figure 5.1 ESI-MS spectra of solutions containing (a) $[\gamma-CD + W_{12}POM]^{3-}$ and (b) $[\gamma-CD + W_6POM]^{2-}$.

5.3.1 ESI-MS of tungsten CD-POM complexes

Figure 5.1(a) shows a typical ESI-MS spectrum of a solution containing γ -CD and $W_{12}POM^{3-}$. Consistent with the results reported by Cao et al.⁵⁴, we observe $[\gamma-CD + W_{12}POM]^{3-}$ and $[2\gamma-CD + W_{12}POM]^{3-}$ as the major species in the m/z range below 2000 (Figure 5.1(a)). In addition to host-guest complexes, the spectrum contains peaks corresponding to $W_{12}POM^{3-}$ and $HW_{12}POM^{2-}$ anions. Similar ESI-MS spectra were obtained for complexes of $W_{12}POM^{3-}$ with α - and β -CD (Figure 5.2). In this study, we examine for the first time fragmentation of $[\alpha-CD + W_{12}POM]^{3-}$ and $[\beta-CD + W_{12}POM]^{3-}$ anions.

CD- W_6POM and CD- Mo_6POM complexes were generated using the one-pot synthetic procedure reported by Cadot et al.⁵⁹. In that study, single-crystal X-ray diffraction (XRD) analysis was used to confirm that $W_6O_{19}^{2-}$ residing inside the γ -CD cavity has the Lindqvist-type structure⁵⁹. A portion of the ESI-MS spectrum of the resulting solution is shown in Figure 5.1(b). Aside from the $[\gamma-CD + W_6POM]^{2-}$ anion, the spectrum contains peaks corresponding to the Cl^- adduct

of $[\gamma\text{-CD} + \text{Cl}]^-$ due to the presence of hydrochloric acid in solution, and deprotonated CD, $[\gamma\text{-CD} - \text{H}]^-$.

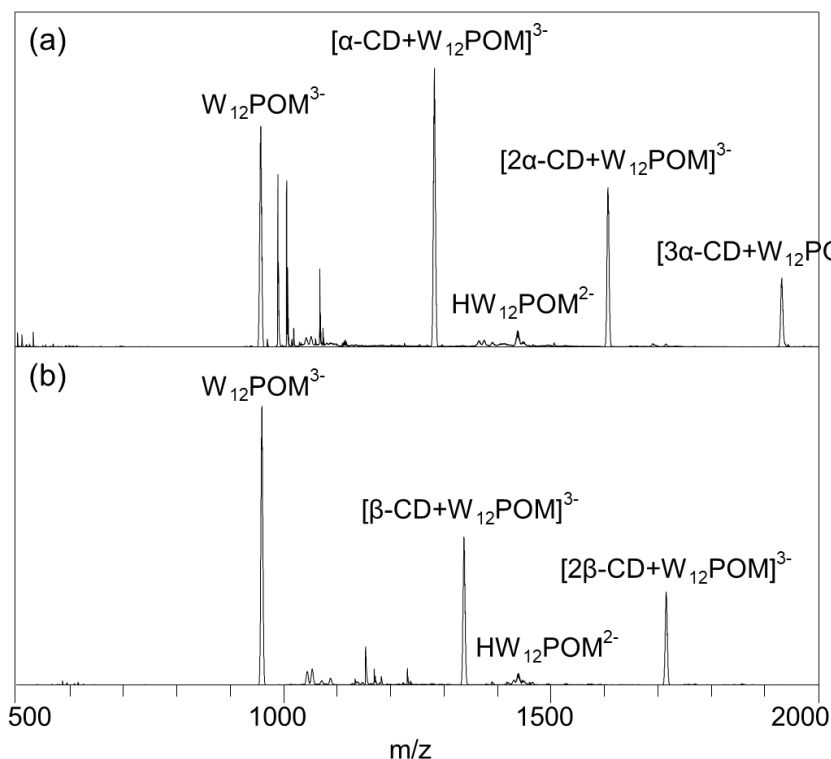
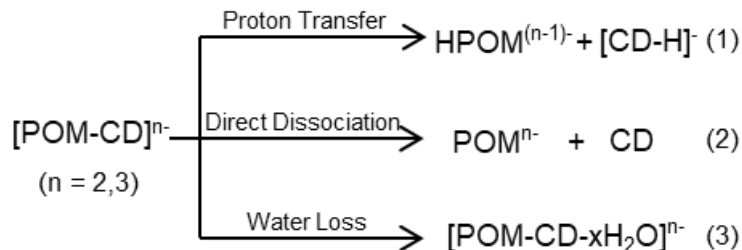


Figure 5.2 ESI-MS spectra of solutions containing (a) $[\alpha\text{-CD} + \text{W}_{12}\text{POM}]^{3-}$ and (b) $[\beta\text{-CD} + \text{W}_{12}\text{POM}]^{2-}$.

5.3.2 Gas Phase fragmentation Pathways

We systematically investigated the gas phase fragmentation pathways of anionic CD-WPOM host-guest complexes using both higher-energy collisional dissociation (HCD) on a QE-Orbitrap and low-energy CID on an ion trap. For both CD- W_{12}POM and CD- W_6POM complexes, we observe three major pathways shown in Scheme 5.2: (1) proton transfer from CD to POM, which generates peaks corresponding to protonated POM and deprotonated CD in the spectrum; (2) direct dissociation of the complex, which generates the original POM anion and undetectable neutral CD species; (3) a series of multiple water losses from the complex. The distinctly different fragmentation patterns of the CD-POM complexes observed in HCD and low-energy CID provide insights into the kinetics of the competing fragmentation pathways, which will be discussed in detail in the following sections.



Scheme 5.2 Major fragmentation pathways observed for the CD-POM host-guest complexes in the gas phase.

5.3.2.1 MS/MS of W_{12} POM-CD complexes. Fragmentation spectra of CD- W_{12} POM complexes obtained under both HCD and low-energy CID conditions are shown in Figure 5.3. We observe similar fragmentation patterns for all three types of CDs under the same activation conditions and distinctly different fragmentation patterns in HCD and low-energy CID. Specifically, HCD spectra of CD- W_{12} POM complexes (Figure 5.3(a)) contain abundant peaks corresponding to products of both the proton transfer (pathway 1 in Scheme 5.2) and direct dissociation (pathway 2 in Scheme 5.2) pathways. In contrast, pathway 1 generating $HW_{12}POM^{2-}$ and $[CD - H]^-$ is dominant in low-energy CID spectra (Figure 5.3(b)). We note that the relatively low abundance of the $[CD - H]^-$ fragment ion in comparison with $HW_{12}POM^{2-}$ fragment is attributed both to the lower charge state and to subsequent fragmentation of $[CD - H]^-$ (Figure 5.4), which reduce the observed signal intensity. Water loss (pathway 3 in Scheme 5.2) appears to be a minor process for CD- W_{12} POM complexes in both HCD and low-energy CID experiments.

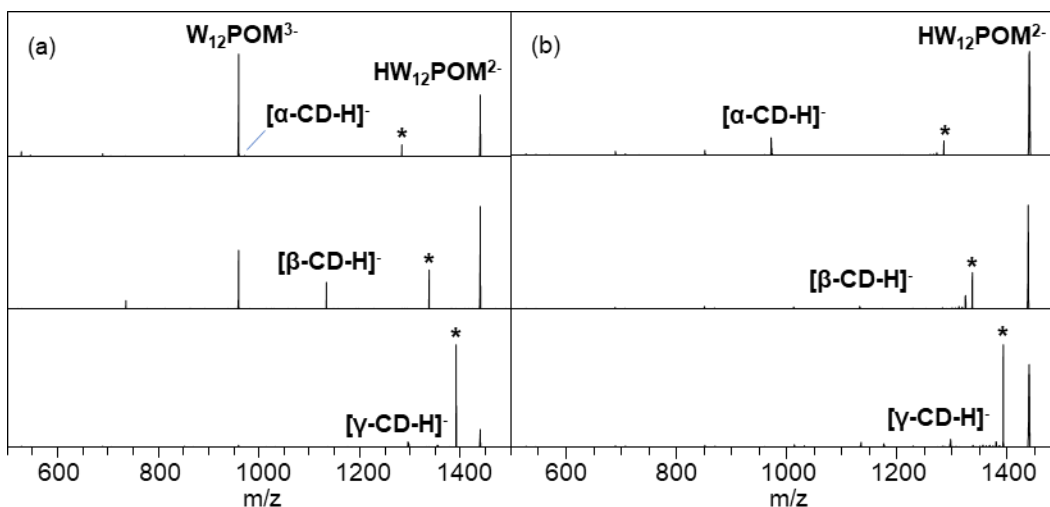


Figure 5.3 (a) HCD (CE = 45) and (b) low-energy CID (CE = 17) spectra of Keggin CD- W_{12} POM complexes under same conditions. The precursor ion signal in each spectrum is marked with an asterisk.

It is well established that slow collisional excitation in the ion trap favors low-energy dissociation pathways, while HCD experiments provide access to entropically favorable higher-energy dissociation pathways under high-energy conditions⁶¹⁻⁶³. The observed dominance of direct dissociation in HCD spectra and the absence of this pathway in low-energy CID indicate that it efficiently competes with proton transfer at higher internal excitations. This observation suggests that proton transfer, which is dominant in the low-energy CID spectrum is a low-energy channel while direct dissociation of the complex is an entropically favorable process with a higher threshold energy than proton transfer.

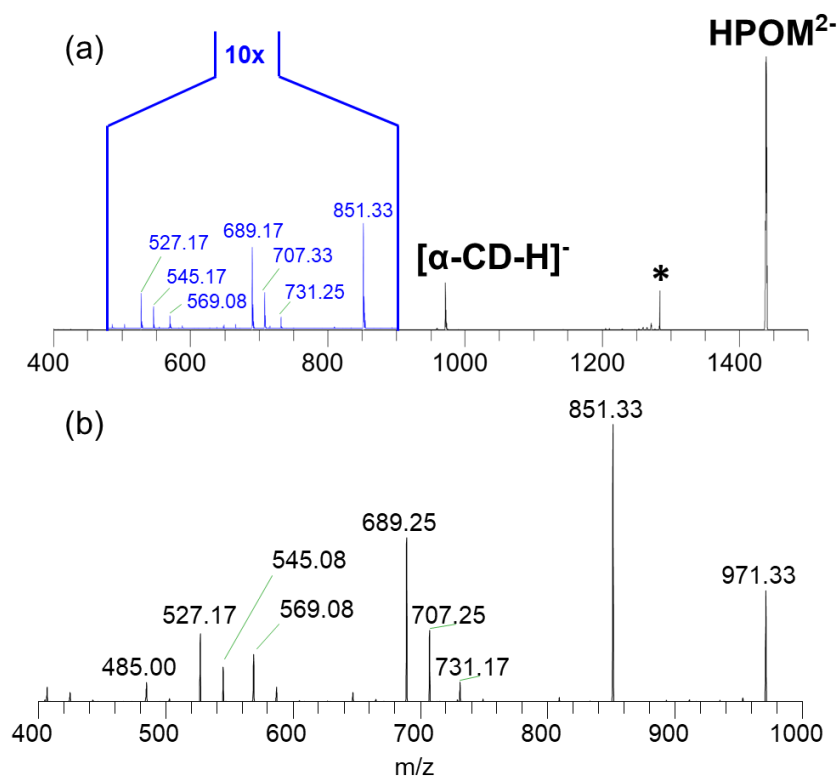


Figure 5.4 (a) CID spectrum of $[\alpha\text{-CD} + \text{W}_{12}\text{POM}]^{3-}$ complex with 10 \times magnified lower m/z region. The fragments observed in the low m/z region is confirmed as the subsequent fragments of $[\text{CD} - \text{H}]^-$ by CID spectrum of $[\text{CD} - \text{H}]^-$ (b).

Figure 5.3 also indicates that the extent of fragmentation of the complex decreases with increase in the size of the CD with the $[\gamma\text{-CD} + \text{W}_{12}\text{POM}]^{3-}$ anion showing the smallest extent of fragmentation both in HCD and low-energy CID spectra. This may be attributed to an increase in the strength of host-guest interactions between $\text{W}_{12}\text{POM}^{3-}$ and CD with increase in the cavity diameter. Crystal structure of the related $[\gamma\text{-CD} + \text{Mo}_{12}\text{POM}]^{3-}$ complex indicates that $\text{Mo}_{12}\text{POM}^{3-}$ fits deep inside the larger cavity of $\gamma\text{-CD}$ (9.5 Å) and the complex is stabilized by multiple hydrogen-bonding interactions with CD³⁸. Similar sizes of $\text{Mo}_{12}\text{POM}^{3-}$ and $\text{W}_{12}\text{POM}^{3-}$ suggest that $\text{W}_{12}\text{POM}^{3-}$ also fits well into the $\gamma\text{-CD}$ cavity. The cavity diameter of $\alpha\text{-}$ and $\beta\text{-CD}$ are 5.7 Å and 7.8 Å, respectively, which are smaller in comparison with $\gamma\text{-CD}$ ³¹. It is reasonable to assume that fewer hydrogen-bonding interactions and weaker dispersion forces between POM and smaller CDs make the corresponding complexes less stable than the complex of Keggin POM and $\gamma\text{-CD}$. Another possible explanation for the decrease in the extent of fragmentation of the complex with increase in the size of CD is that the larger $\gamma\text{-CD-POM}$ complex has a larger number of vibrational

degrees of freedom, which results in a decrease in the unimolecular dissociation rate and thereby reduces the extent of fragmentation ⁶⁴.

The prevalence of proton transfer over other dissociation channels observed in Figure 5.3(b) may be attributed to the strong hydrogen bonding interactions between $W_{12}POM^{3-}$ and CD in the complex, which facilitate proton transfer from CD to POM. A crystal structure of CD- $Mo_{12}POM$ complex indicates the presence of multiple hydrogen bonds between hydroxyl groups of CD and oxygen atoms of the POM anion as a major type of non-covalent interactions between POM and CD ³⁸. Although the energetics of proton transfer within the complex is not known, it is reasonable to assume that proton transfer from CD to $W_{12}POM^{3-}$ is energetically favorable based on the substantial difference in the gas-phase basicity of the isolated $W_{12}POM^{3-}$ (374 – 385 kcal/mol) ⁶⁵ and the Brønsted acidity of CD (325 – 327 kcal/mol) ⁶⁶. We propose that upon collisional excitation, a proton is abstracted from the proton donor (CD) by the most basic oxygen site of the proton acceptor ($W_{12}POM^{3-}$). It also is reasonable to assume that proton abstraction is inhibited in CID of CD-POM complexes containing less basic POM anions, such as Lindqvist anion discussed in the next section. Indeed, no proton transfer was observed in CID of a host-guest complex of β -CD with another superchaotropic anion, $B_{12}F_{12}^{2-}$, with lower gas-phase basicity (322 kcal/mol) ⁶⁷. Instead, the $[\beta\text{-CD} + B_{12}F_{12}]^{2-}$ complex exhibited loss of a sugar unit, which was attributed to the strong binding between β -CD and $B_{12}F_{12}^{2-}$ in the absence of solvent ¹⁹.

5.3.2.2 MS/MS of CD- W_6POM complexes. Gas phase fragmentation pathways of Lindqvist CD- W_6POM complexes under HCD and low-energy CID conditions are shown in Figure 5.5(a) and 8.5(b), respectively. Similar to Keggin CD- $W_{12}POM$ complexes, we observe comparable fragmentation patterns for CD- W_6POM complexes containing different CDs under the same collisional activation conditions. However, distinctly different fragmentation patterns are observed in HCD and low-energy CID experiments. In contrast with low-energy CID of CD- $W_{12}POM$ complexes described earlier, proton transfer from CD to W_6POM^{2-} (pathway 1 in Scheme 5.2) is a minor process in CID spectra of CD- W_6POM complexes. Instead, HCD spectra of CD- W_6POM complexes contain abundant $W_6O_{19}^{2-}$ peaks corresponding to direct dissociation (pathway 2 in Scheme 5.2). The observed decrease in the extent of dissociation for different types of CDs is similar to that of CD- $W_{12}POM$ complexes, which has been discussed in detail in the previous section. The presence of an abundant W_6POM^{2-} fragment produced by direct dissociation of $[\alpha$ -

$[\alpha\text{-CD} + \text{W}_6\text{POM}]^{2-}$ in the low-energy CID spectrum is consistent with the relatively weak binding between the smaller $\alpha\text{-CD}$ cavity and $\text{W}_6\text{POM}^{2-}$ anion.

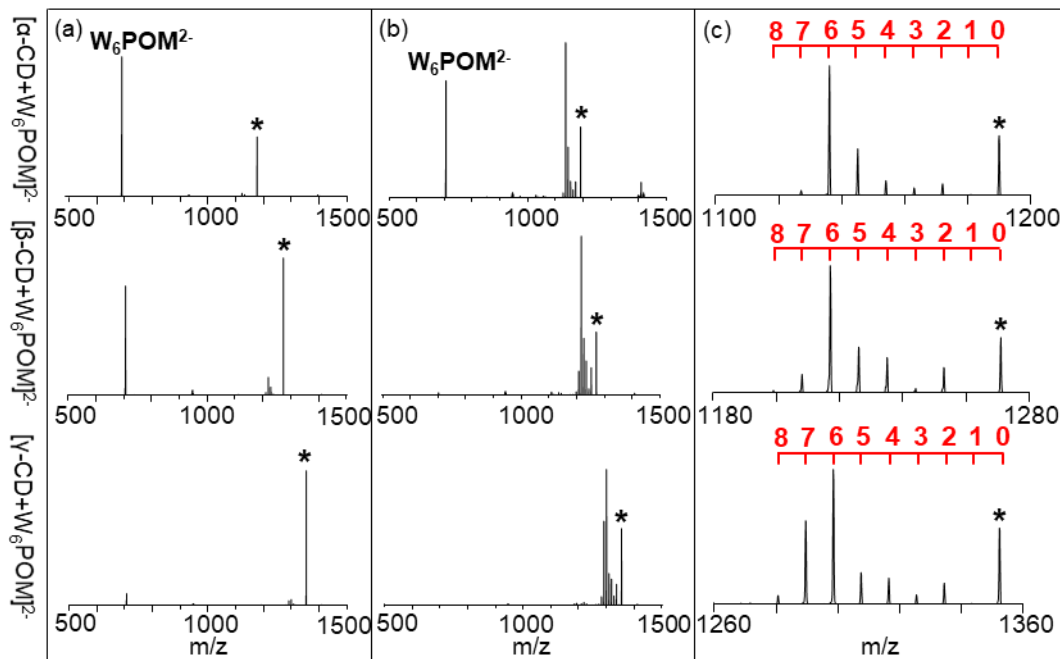


Figure 5.5 (a) CID spectrum of $[\alpha\text{-CD} + \text{W}_{12}\text{POM}]^{3-}$ complex with 10 \times magnified lower m/z region. The fragments observed in the low m/z region is confirmed as the subsequent fragments of $[\text{CD} - \text{H}]^-$ by CID spectrum of $[\text{CD} - \text{H}]^-$ (b).

Direct dissociation of $[\alpha\text{-CD} + \text{W}_6\text{POM}]^{2-}$ is observed in competition with losses of multiple water molecules from the complex (pathway 3 in Scheme 5.2), which is the only pathway in low-energy CID spectra of $[\beta\text{-CD} + \text{W}_6\text{POM}]^{2-}$ and $[\gamma\text{-CD} + \text{W}_6\text{POM}]^{2-}$ anions (Figure 5.5(b)). Water losses also are observed as lower-abundance peaks in HCD spectra of CD- W_6POM complexes. Figure 5.5(c) shows regions of the low-energy CID spectra of CD- W_6POM complexes containing the water loss pattern observed as a distribution of peaks spaced by 9 m/z units ($z = 2$). For all three complexes, the most abundant fragment, $[\text{CD} + \text{W}_6\text{POM} - 6\text{H}_2\text{O}]^{2-}$, corresponds to the loss of six water molecules. Interestingly, very low signal was obtained for a fragment ion corresponding to a single water loss and loss of three water molecules. Similar fragmentation patterns were observed in low-energy CID spectra acquired at different excitation voltages (Figure 5.6) indicating that the observed losses of multiple water molecules are not sequential but rather

occur in parallel. Loss of seven water molecules becomes more abundant for the $[\gamma\text{-CD} + \text{W}_6\text{POM}]^{2-}$ complex.

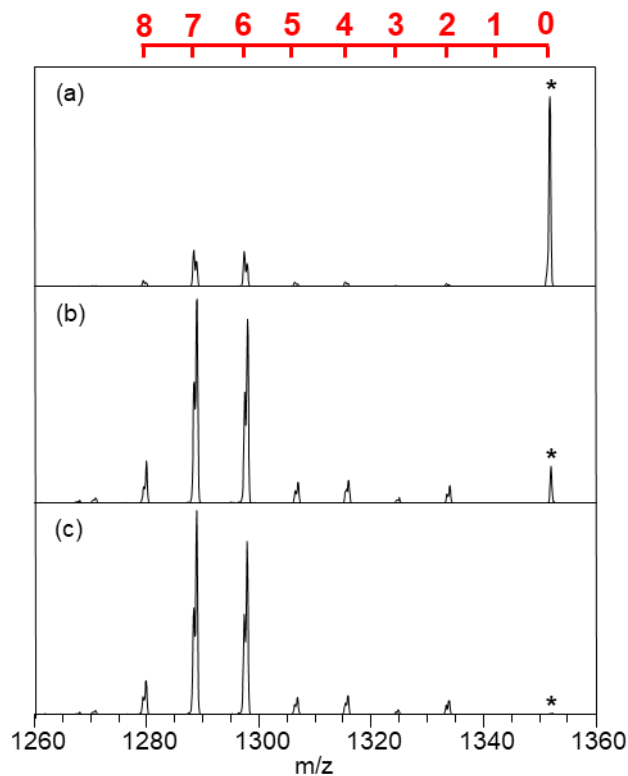


Figure 5.6 A region of low-energy CID spectra of $[\gamma\text{-CD} + \text{W}_6\text{POM}]^{2-}$ showing multiple water losses at (a) CE = 16, (b) CE = 19, and (c) CE = 22. The precursor ion signal in each spectrum is marked with an asterisk. The red ruler on top of the panel shows the corresponding number of water losses.

Further excitation of the fragment ions produced via loss of either single or multiple water molecules from $[\gamma\text{-CD} + \text{W}_6\text{POM}]^{2-}$ in an MS^3 experiment (Figure 5.7) results in additional losses of water molecules. The preference for the overall loss of 6 water molecules is clearly observed in the MS^3 experiments. MS^3 of $[\gamma\text{-CD} + \text{W}_6\text{O}_{19} - 6\text{H}_2\text{O}]^{2-}$ shows abundant losses of one and two water molecules and a minor peak corresponding to three water losses. Despite the preference for the loss of six water molecules in the MS^2 experiment, an overall loss of up to ten water molecules was observed in the MS^3 spectra.

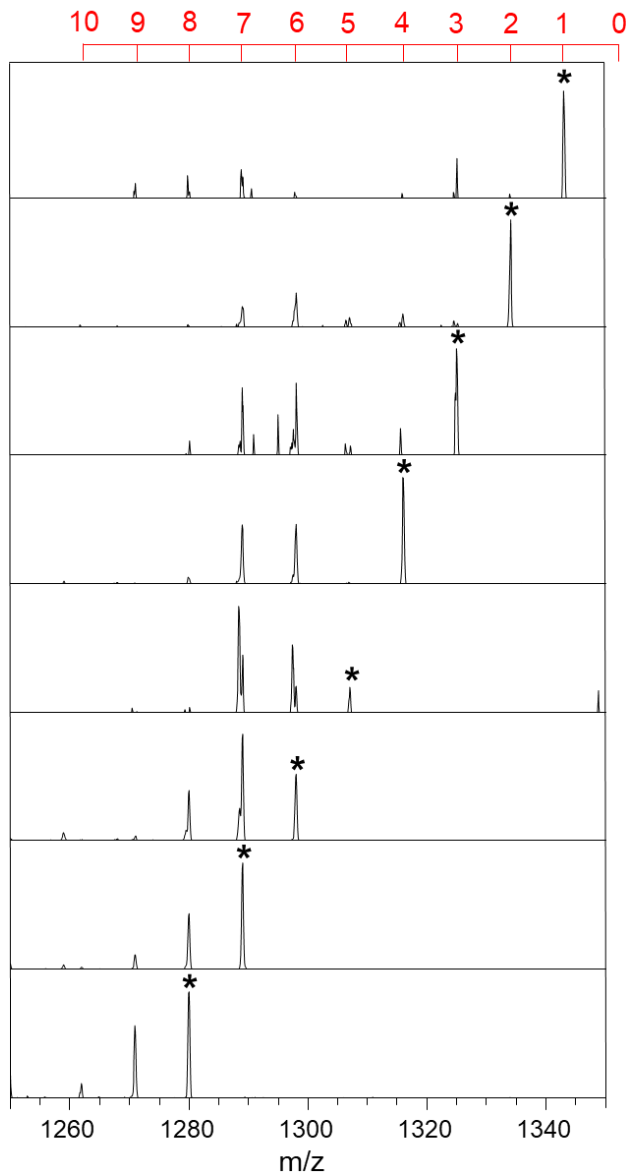


Figure 5.7 Expanded m/z range of the MS^3 spectra showing further multiple water loss peaks from the $[\gamma\text{-CD} + \text{W}_6\text{POM}]^{2-}$ complex ($CE = 17$ eV). The parent peak in each of the MS^3 spectrum isolated from the MS^2 of $[\gamma\text{-CD} + \text{W}_6\text{POM}]^{2-}$ is marked with an asterisk. The red ruler on top of the panel shows the corresponding number of water losses from the original complex.

The observed loss of multiple water molecules is not limited to $\text{W}_6\text{POM}^{2-}$. Low-energy CID spectra of CD- Mo_6POM complexes shown in Figure 5.8 contain similar multiple water loss patterns. However, in contrast with CD- W_6POM , CD- Mo_6POM complexes predominantly lose five water molecules, with a single water loss almost absent in the spectra. In addition, we observed an abundant pair of fragments, $\text{HMo}_4\text{O}_{13}^-$ and $[\text{CD} + \text{Mo}_2\text{O}_6 - \text{H} - \text{H}_2\text{O}]^-$, as confirmed by high-resolution MS experiments. The latter is most likely produced via a loss of one water molecule

from the $[\text{CD} + \text{Mo}_2\text{O}_6 - \text{H}]^-$ anion. Similarly, $\text{HW}_4\text{O}_{13}^-$ fragment ion is present as a minor peak in the spectrum of CD- W_6POM . However, the complementary anion undergoes more substantial dehydration forming a distribution of $[\text{CD} + \text{W}_2\text{O}_6 - \text{H} - x\text{H}_2\text{O}]^-$ ($x = 1, 2, 3$) fragments with two and three water losses as the dominant species (Figure 5.9). This observation is consistent with the greater extent of water loss from the CD- W_6POM as compared to CD- Mo_6POM .

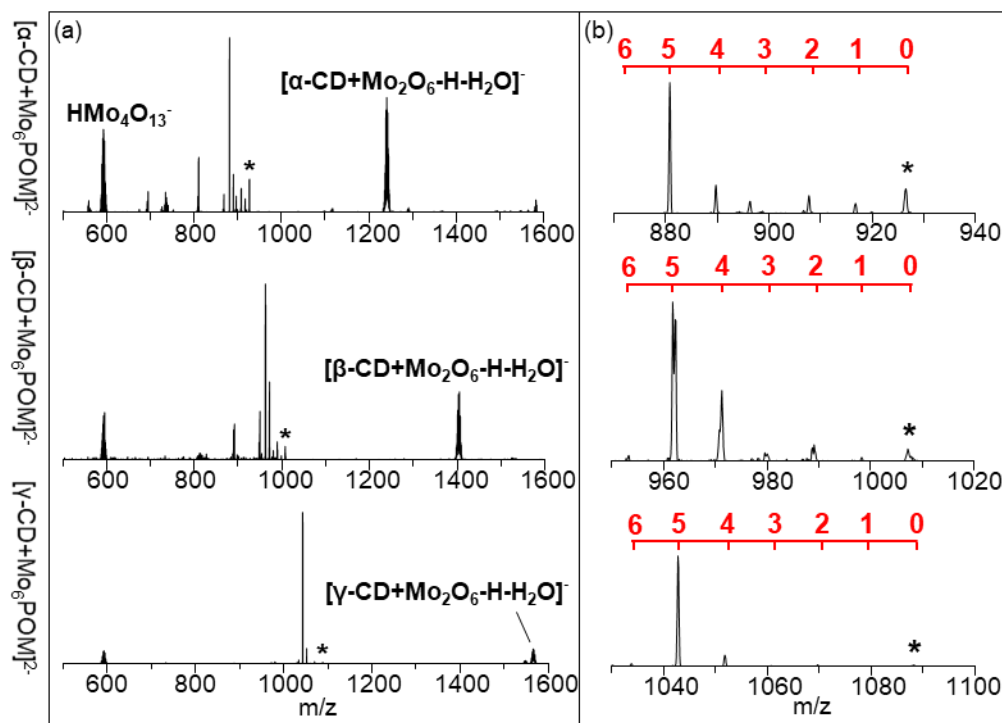


Figure 5.8 (a) Low-energy CID spectra of Lindqvist CD- Mo_6POM complexes at $\text{CE} = 17$. The precursor ion signal in each spectrum is marked with an asterisk. (b) Expanded m/z range of the spectra showing multiple water loss peaks. The red ruler on top of each spectrum shows the corresponding number of water losses.

Simultaneous loss of multiple water molecules is an unusual pathway in low-energy CID. We propose that this pathway is initiated by a proton transfer from the CD to the $\text{W}_6\text{POM}^{2-}$ anion. Proton transfer is a dominant pathway in dissociation of Keggin CD- W_{12}POM discussed earlier. However, for the Keggin CD- W_{12}POM complex, proton transfer is followed by the separation of $[\text{CD} - \text{H}]^-$ and $\text{HW}_{12}\text{POM}^{2-}$. Comparison of the gas phase basicities of $\text{W}_{12}\text{POM}^{3-}$ (374 – 385 kcal/mol)⁶⁵ and $\text{W}_6\text{POM}^{2-}$ (335 – 347 kcal/mol)⁶⁸ indicates that proton transfer from CD (Brønsted acidity: 325 – 327 kcal/mol)⁶⁶ to $\text{W}_{12}\text{POM}^{3-}$ is more exothermic than to $\text{W}_6\text{POM}^{2-}$, which could promote the separation of fragments formed through pathway 1. The absence of the

$\text{HW}_6\text{O}_{19}^-$ fragment in the CID spectra of CD- W_6POM complexes could be explained by assuming that the separation of $[\text{CD} - \text{H}]^-$ and $\text{HW}_6\text{O}_{19}^-$ does not efficiently compete with other dissociation pathways.

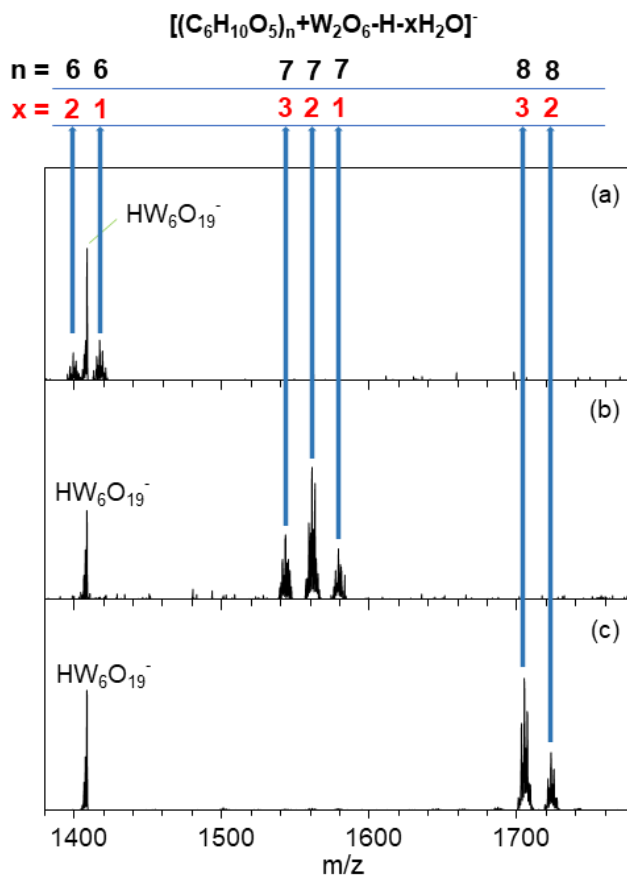


Figure 5.9 Expanded m/z range of the spectra showing the $[\text{CD} + \text{W}_2\text{O}_6 - \text{H} - x\text{H}_2\text{O}]^-$ fragments produced from low-energy CID experiments of $[\alpha\text{-CD} + \text{W}_6\text{POM}]^{2-}$ (a), $[\beta\text{-CD} + \text{W}_6\text{POM}]^{2-}$ (b), and $[\gamma\text{-CD} + \text{W}_6\text{POM}]^{2-}$ (c).

In order to rationalize simultaneous losses of multiple water molecules from the complex, we assume that $\text{HW}_6\text{O}_{19}^-$ or $\text{HM}_6\text{O}_{19}^-$ formed through the proton transfer step decompose into several smaller fragments. We propose that POM fragments formed in this initial step subsequently attack the CD cage thereby forming covalent bonds to the host molecule and eliminating multiple water molecules. The anionic product of this dissociation pathway is a derivatized CD. MS^n experiments (data not shown) demonstrate that this species undergoes subsequent loss of several water molecules followed by losses of hydrocarbon fragments. However, no losses of W-

containing neutral molecules were observed in these experiments. These results confirm that POM fragments form strong covalent bonds with CD thereby yielding an unusual CD derivative.

The observed distribution of water losses from the complex may be attributed to the presence of multiple pathways for the covalent attachment of metal oxide fragments to the CD. Meanwhile, the difference between the preferred number of water losses from the CD-W₆POM and CD-Mo₆POM likely indicates the differences in either the type or reactivity of the fragments of HMo₆POM⁻ in comparison with HW₆POM⁻.

The formation of the HMo₄O₁₃⁻ and [CD + Mo₂O₆ - H - H₂O]⁻ pair of fragments could be rationalized using the same mechanism. However, in this case only one covalent bond is formed between the CD and Mo₂O₆ fragment releasing one water molecule. In contrast, up to three water molecules are released by covalent bond formation between CD and W₂O₆ fragment, which indicates that W₂O₆ is more reactive than Mo₂O₆. This finding is in agreement with the more efficient water loss from CD-W₆POM as compared to CD-Mo₆POM. However, this pathway is only observed as a minor dissociation channel for CD-W₆POM, which is consistent with the higher exothermicity of the proton transfer from the CD (Brønsted acidity: 325 – 327 kcal/mol)⁶⁶ to Mo₆POM²⁻ (gas-phase basicity in the range of 342 – 355 kcal/mol)⁶⁸ as compared to W₆POM²⁻ (gas-phase basicity in the range of 335 – 347 kcal/mol)⁶⁸.

5.3.3 Isotopic Labeling Experiments and Statistical Modeling

5.3.3.1 Hydrogen/Deuterium Exchange. It is reasonable to assume that a majority of water losses involve hydroxyl groups of the CD host molecule. In order to obtain additional insights into the types of hydrogen and oxygen atoms involved in the process, we carried out H/D exchange (HDX) and ¹⁸O exchange experiments using [γ-CD + W₆POM]²⁻ as a representative species. Experimental CID spectra of the complexes were rationalized using statistical simulations.

HDX experiments were performed by diluting the stock solution of [γ-CD + W₆POM]²⁻ complex in a deuterated solvent. The extent of HDX was controlled by varying the solvent composition. Specifically, a very limited extent of HDX of the hydroxyl groups of γ-CD was observed using CD₃OD as a solvent. In contrast, more extensive HDX was observed in a CD₃OD/D₂O mixture. γ-CD has 24 labile hydrogens of the hydroxyl groups available for HDX⁶⁹.

Each of the (α -1,4)-linked α -D-glucopyranose units on the CD structure contains one primary and two secondary hydroxyl groups on the outer rim and inner cavity of CD, respectively. The primary hydroxyl groups are flexible and often involved in intermolecular hydrogen bonding. Meanwhile, the 16 secondary hydroxyl groups on the inner CD surface are connected by intramolecular hydrogen bonds, which determine the rigidity of the CD cavity in the condensed phase ⁶⁹. More than sixteen exchanges were previously observed in gas-phase HDX experiments of γ -CD indicating that the exchange is not limited to the primary hydroxyl groups ⁷⁰. The remaining hydrogen atoms in γ -CD on the C-H sites of the glucopyranose units are not exchangeable due to their lower acidity.

In the condensed phase, W_6POM^{2-} is deeply embedded into the CD cavity with the eight primary hydroxyl groups pointing away from the complex thereby optimizing the interactions with solvent molecules in solution or with other complexes in the crystalline phase ⁵⁹. However, little is known about the structure of the $[\gamma\text{-CD} + W_6POM]^{2-}$ complex in the gas phase. The HDX experiments described herein were designed to probe whether only the secondary or all of the hydroxyl groups are involved in the observed water losses.

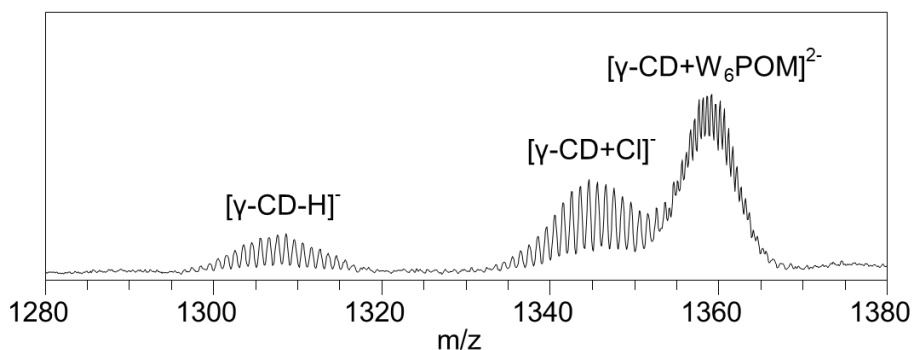


Figure 5.10 ESI-MS spectrum of a solution of $[\gamma\text{-CD} + W_6POM]^{2-}$ in 50:50 (v/v) CD_3OD/D_2O solvent showing the isotopic envelopes of $[\gamma\text{-CD-H}]^-$, $[\gamma\text{-CD} + Cl]^-$, and $[\gamma\text{-CD} + W_6POM]^{2-}$ after three hours of H/D exchange.

An ESI-MS spectrum of a solution of $[\gamma\text{-CD} + W_6POM]^{2-}$ in 50:50 (v/v) CD_3OD/D_2O solvent analyzed three hours after mixing is shown in Figure 5.10. We observe a series of peaks ranging from $m/z = 1296$ to $m/z = 1320$ arising from the isotopomers of $[\gamma\text{-CD} - H]^-$ produced by HDX. The distribution is centered at $m/z = 1312$ corresponding to 16 exchanged hydrogens (Figure 5.10). In addition, an isotopic envelope of $[\gamma\text{-CD} + W_6POM]^{2-}$ is observed in a range of $m/z = 1351$

- 1365. The center of the isotopic envelope of $[\gamma\text{-CD} + \text{W}_6\text{POM}]^{2-}$ after HDX is shifted to $m/z = 1360$ from $m/z = 1352$ for the original complex corresponding to an average exchange of 16 hydrogens.

We systematically examined MS^2 of the isotopic peaks of $[\gamma\text{-CD} + \text{W}_6\text{POM}]^{2-}$ from this distribution using an isolation window of 1 m/z . The m/z range corresponding to multiple water losses in the low-energy CID spectrum of $m/z = 1365$ from the high m/z side of the isotopic distribution is shown in Figure 5.11(a). Each of the features in this region contains a distribution of isotopic peaks originating from a combined loss of H_2O , HDO , and D_2O due to the partial exchange of hydrogens with deuterium atoms.

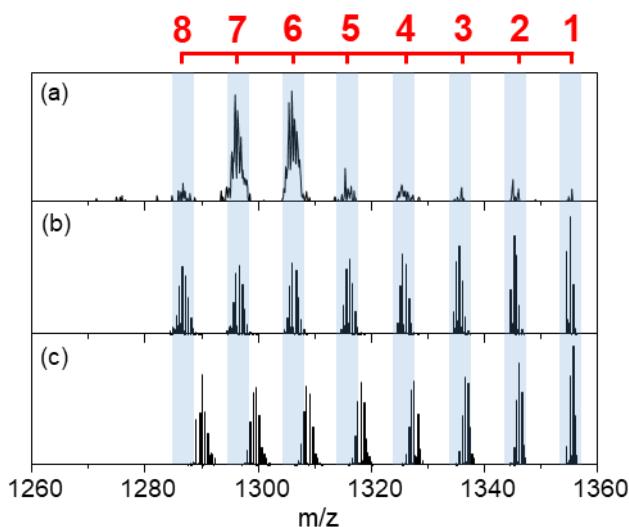


Figure 5.11 Experimental (a) and simulated (b and c) distributions of water losses from $m/z = 1365$ isolated from the isotopic pattern of deuterium-exchanged $[\gamma\text{-CD} + \text{W}_6\text{POM}]^{2-}$. Panel (b) shows a simulated spectrum obtained assuming that all of the 24 -OH groups are available for the water loss channel; panel (c) shows a simulated spectrum obtained assuming that only 16 -OH groups participate in the water loss channel. The red ruler shows the corresponding number of water losses.

The observed isotopic distributions of water losses from partially exchanged $[\gamma\text{-CD} + \text{W}_6\text{POM}]^{2-}$ complexes may be rationalized using the following model. We assume that 1) the complex has a similar distribution of hydrogen and deuterium atoms as the $[\gamma\text{-CD} - \text{H}]^-$ detected in the ESI-MS spectrum; 2) loss of a single or multiple water molecules is a random single-step process. The latter assumption is supported by the non-sequential loss of multiple water molecules

discussed earlier. First, we calculate the distribution of deuterium atoms in a selected isotopic peak of the complex. Next, we use a hypergeometric distribution to predict the number of deuterium atoms incorporated into the water molecules eliminated from this isotopic peak of the complex in CID. Finally, we compare the simulated distribution with the experimental CID data.

In the first step, we calculate all possible combinations of the isotopes of the partially exchanged γ -CD and W_6POM^{2-} that have an m/z in the $\pm 0.5 m/z$ window selected in the CID experiment. This generates a predicted distribution of hydrogen and deuterium atoms in the isolated precursor ion.

In the second step, we calculate the probability of deuterium incorporation into the products using a hypergeometric distribution by considering two scenarios: 1) when all of the 24 hydroxyl groups participate in the reaction; and 2) only 16 randomly selected hydrogen or deuterium atoms can be incorporated into the products. The second scenario represents a situation when only the secondary hydroxyl groups participate in the reaction. Knowing the total number of hydrogen and deuterium atoms in the pool (N), we calculate the probability of incorporating k deuterium atoms into n water losses (n is in the range of 1 - 8). This probability is given by the hypergeometric distribution in Eq. 8.1:

$$C(p, k) = \frac{\frac{p!}{k!(p-k)!} \cdot \frac{(N-p)!}{(2n-k)!(N-p-2n+k)!}}{\frac{(N)!}{(2n)!(N-2n)!}}$$

(Equation 5.1)

where p represents the total number of available deuterium atoms in the pool. We note that Eq. 8.1 is also used to calculate the initial distribution of deuterium atoms in the second scenario described earlier, in which we limited the number of available hydrogen or deuterium atoms to 16. The calculated distributions of possible neutral losses from $m/z = 1365$ when either 24 or 16 hydroxyl groups participate in the reaction are shown in Figures 8.11(b) and 8.11(c), respectively. We observe a similar bell-shaped isotopic pattern for each of the multiple water loss features in both of the simulated spectra. However, the simulated distribution in Figure 6c demonstrates a distinct shift in the center of m/z in each of the multiple water loss features with respect to the experimental

isotopic distribution. The deviation of the center of m/z obtained from the simulation and the experimental value increases gradually with an increase in the number of water losses. In contrast, the experimental results are in a good agreement with the simulation, in which all of the 24 hydroxyl groups are assumed to be involved in the water loss channel (Figure 5.11(b)). We conclude that all of the 24 hydroxyl groups are involved in the observed water losses. It is unlikely that W_6POM^{2-} interacts with all the 24 hydroxyl groups prior to collisional excitation. The lack of selectivity towards specific types of hydroxyl groups in CD participating in the water loss indicates that the initial gas phase structure of the complex may not be the determining factor in the mechanism of this fragmentation pathway.

5.3.3.2 ^{18}O Exchange. A similar approach was used to examine fragmentation of ^{18}O -exchanged $[\gamma\text{-CD} + W_6POM]^{2-}$ anions. In these experiments, the complex was generated using the one-pot synthesis of in $H_2^{18}O$. The incorporation of ^{18}O atoms into W_6POM^{2-} was confirmed using ESI-MS (Figure 5.12). We observe that the isotopic pattern of CD remains the same in $H_2^{16}O$ and $H_2^{18}O$ indicating that oxygen atoms of γ -CD do not participate in the ^{18}O exchange. Meanwhile, the center of the isotopic distribution of W_6POM^{2-} shifts from $m/z = 704$ to $m/z = 722$ corresponding to the incorporation of eighteen ^{18}O atoms into W_6POM^{2-} . Similarly, the center of the isotopic distribution of $[\gamma\text{-CD} + W_6POM]^{2-}$ complex is shifted from $m/z = 1352$ to $m/z = 1370$ confirming the same extent of ^{18}O exchange in the complex.

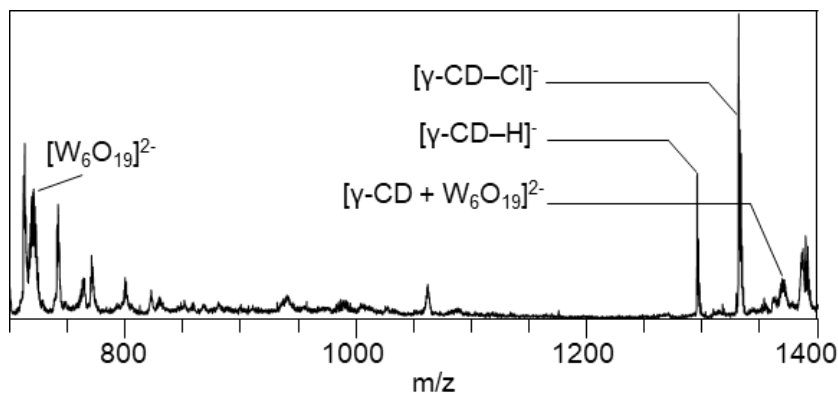


Figure 5.12 ESI-MS spectrum of a solution of ^{18}O -exchanged $[\gamma\text{-CD} + W_6POM]^{2-}$ in 50:50 (v/v) acetonitrile/ $H_2^{18}O$ solvent showing W_6POM^{2-} and $[\gamma\text{-CD} + W_6POM]^{2-}$.

MS^2 spectra of the isotopic peaks of $[\gamma\text{-CD} + W_6POM]^{2-}$ from this distribution were acquired using an isolation window of 0.5 m/z . Figure 5.13 shows the low-energy CID spectrum

of $m/z = 1369.5$ in the m/z range containing water loss fragments. The most abundant isotopic signal in each of the water loss features corresponds to losses of H_2^{18}O molecules, which indicates that oxygen atoms of $\text{W}_6\text{POM}^{2-}$ participate in this reaction.

We rationalize the observed isotopic distribution of multiple water losses from ^{18}O -exchanged $[\gamma\text{-CD} + \text{W}_6\text{POM}]^{2-}$ using the same statistical modeling described earlier. Three scenarios are considered in these simulations: 1) only 19 oxygen atoms of $\text{W}_6\text{POM}^{2-}$ participate in the reaction; and 2) 35 oxygen atoms of both $\text{W}_6\text{POM}^{2-}$ and 16 primary hydroxyl groups of $\gamma\text{-CD}$ can be incorporated into the reaction product; 3) 43 oxygen atoms of both $\text{W}_6\text{POM}^{2-}$ and all 24 hydroxyl groups of $\gamma\text{-CD}$ are involved in the process.

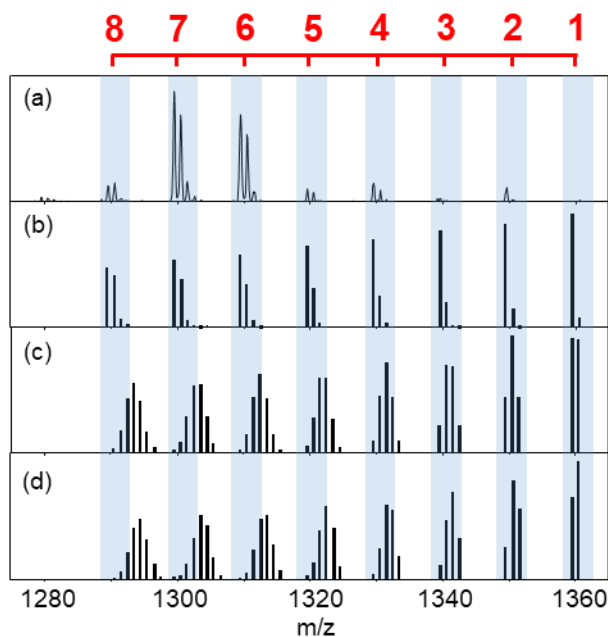


Figure 5.13 Experimental (a) and simulated (b, c and d) distributions of water losses from $m/z = 1369.5$ isolated from the isotopic pattern of ^{18}O -exchanged $[\gamma\text{-CD} + \text{W}_6\text{POM}]^{2-}$. (b-d) Simulated spectra obtained assuming that different number of oxygen atoms participate in the water loss channel: (b) only the oxygen atoms of $\text{W}_6\text{POM}^{2-}$; (c) a total of 35 oxygen atoms of both $\text{W}_6\text{POM}^{2-}$ and 16 secondary hydroxyl groups of $\gamma\text{-CD}$; (d) a total of 43 oxygen atoms of $\text{W}_6\text{POM}^{2-}$ and all 24 hydroxyl groups of $\gamma\text{-CD}$. The red ruler shows the corresponding number of water losses.

The calculated distributions of possible water losses from $m/z = 1369.5$ in the above described scenarios are shown in Figure 5.13(b), 8.13(c) and 8.13(d), respectively. The simulated

water loss spectrum shown in Figure 5.13(b) is in good agreement with the experimental result, showing substantial incorporation of ^{18}O into the neutral products. In contrast, simulated water loss spectra (Figure 5.13(c) and 8.13(d)) deviate from the experimental spectrum in both the center of m/z and shape of the isotopic distribution. These results indicate that oxygen atoms of $\text{W}_6\text{POM}^{2-}$ are predominantly incorporated into the water molecules produced in this reaction.

Based on the results of HDX and O^{18} exchange experiments, we conclude that the multiple water losses in the low-energy CID spectra of CD- M_6POM ($\text{M} = \text{Mo}, \text{W}$) complexes are composed of H atoms from the hydroxyl groups of CD and O atoms of $\text{M}_6\text{POM}^{2-}$. The observed fragmentation pathway may be rationalized assuming that the initial proton transfer from CD to $\text{M}_6\text{POM}^{2-}$ results in dissociation of HM_6POM^- producing reactive metal oxide species. These species subsequently undergo multiple condensation reactions with the hydroxyl groups of CD eliminating water molecules. Dehydration reactions between alcohols and multinuclear transition metal oxides in the gas phase resulting in a loss of one water molecule have been previously reported⁷¹⁻⁷³. The reaction mechanism involves deprotonation of an alcohol by a metal oxide followed by alkoxo ligand substitution resulting in elimination of a water molecule⁷⁴. Isotopic labeling experiments have confirmed that the oxygen atom in the resulting alkylated metal oxide product originates from the alcohol, which is consistent with our results⁷¹. It has been demonstrated that W-containing metal oxides are more reactive towards alcohol dehydration than their Mo-containing analogs⁷¹. The enhanced reactivity of W-containing metal oxides may be used to rationalize the more efficient water loss from CD- W_6POM as compared to CD- Mo_6POM observed in this study⁷⁵.

5.4 Conclusions

We report a systematic investigation of the gas phase fragmentation pathways of host-guest complexes of CDs (α -, β -, and γ -CD) and small POMs (Keggin $\text{W}_{12}\text{POM}^{3-}$, Lindqvist $\text{W}_6\text{POM}^{2-}$ and $\text{Mo}_6\text{POM}^{2-}$). We observe three major fragmentation pathways under high-energy and low-energy CID conditions: proton transfer from CD to POM, direct dissociation, and a series of multiple water losses from the complex. The major dissociation channel is determined by the cavity diameter of the CD, the size of the complex, and gas-phase basicity and structural stability of the POM anion. In particular, proton transfer from CD to POM followed by the separation of

[CD - H]⁺ and HW₁₂POM²⁻ in CD-W₁₂POM complexes is a major channel observed in the low-energy CID spectra and attributed to the higher gas-phase basicity and stability of the W₁₂POM³⁻ anion. In contrast, direct dissociation is more pronounced in HCD indicating that this is an entropically favorable pathway associated with a higher threshold energy than the proton transfer channel. An unusual fragmentation pathway observed in low-energy CID experiments of CD-W₆POM and CD-Mo₆POM complexes corresponds to multiple water losses from the complex. These water losses are found to occur in parallel as competing channels and are attributed to covalent coupling of the fragments of Lindqvist POM to CD accompanied by elimination of multiple water molecules upon collisional excitation. This covalent bond formation efficiently competes with other dissociation channels of the CD-W₆POM and CD-Mo₆POM host-guest complexes in the gas phase. The results presented in this study demonstrate the unique proton-mediated reactivity of transition metal oxide clusters for covalent modification of the macrocyclic host molecule via supramolecular gas-phase ion chemistry. Future experiments will examine the properties of the derivatized CD produced in the gas phase by depositing them onto surfaces for preparing unconventional condensed-phase materials⁷⁶⁻⁷⁸.

5.5 References

- (1) Lehn, J. M. Supramolecular chemistry—scope and perspectives molecules, supermolecules, and molecular devices (Nobel Lecture). *Angew. Chem. Int. Ed. Engl.* **1988**, *27*, 89-112.
- (2) Steed, J. W.; Turner, D. R.; Wallace, K.: *Core Concepts in Supramolecular Chemistry and Nanochemistry*; John Wiley & Sons, 2007.
- (3) Vögtle, F.; Weber, E.: *Host Guest Complex Chemistry Macrocycles: Synthesis, Structures, Applications*; Springer Science & Business Media, 2012.
- (4) Brown, C. J.; Toste, F. D.; Bergman, R. G.; Raymond, K. N. Supramolecular catalysis in metal–ligand cluster hosts. *Chem. Rev.* **2015**, *115*, 3012-3035.
- (5) Jiao, Y.; Tang, B.; Zhang, Y.; Xu, J. F.; Wang, Z.; Zhang, X. Highly efficient supramolecular catalysis by endowing the reaction intermediate with adaptive reactivity. *Angew. Chem.* **2018**, *130*, 6185-6189.
- (6) Zhang, D. S.; Gao, Q.; Chang, Z.; Liu, X. T.; Zhao, B.; Xuan, Z. H.; Hu, T. L.; Zhang, Y. H.; Zhu, J.; Bu, X. H. Rational Construction of Highly Tunable Donor–Acceptor Materials Based on a Crystalline Host–Guest Platform. *Adv. Mater.* **2018**, *30*, 1804715.

- (7) Qu, D.-H.; Wang, Q.-C.; Zhang, Q.-W.; Ma, X.; Tian, H. Photoresponsive host–guest functional systems. *Chem. Rev.* **2015**, *115*, 7543-7588.
- (8) Mao, D.; Liang, Y.; Liu, Y.; Zhou, X.; Ma, J.; Jiang, B.; Liu, J.; Ma, D. Acid-Labile Acyclic Cucurbit [n] uril Molecular Containers for Controlled Release. *Angew. Chem. Int. Ed.* **2017**, *56*, 12614-12618.
- (9) Ma, X.; Zhao, Y. Biomedical applications of supramolecular systems based on host–guest interactions. *Chem. Rev.* **2014**, *115*, 7794-7839.
- (10) Chandler, D. Interfaces and the driving force of hydrophobic assembly. *Nature* **2005**, *437*, 640.
- (11) Schneider, H. J. Binding mechanisms in supramolecular complexes. *Angew. Chem. Int. Ed.* **2009**, *48*, 3924-3977.
- (12) Assaf, K. I.; Nau, W. M. The chaotropic effect as an assembly motif in chemistry. *Angew. Chem. Int. Ed.* **2018**, *57*, 13968-13981.
- (13) Kaabel, S.; Adamson, J.; Topić, F.; Kiesilä, A.; Kalenius, E.; Öeren, M.; Reimund, M.; Prigorchenko, E.; Lõokene, A.; Reich, H. J. Chiral hemicucurbit [8] uril as an anion receptor: selectivity to size, shape and charge distribution. *Chemical science* **2017**, *8*, 2184-2190.
- (14) Gibb, C. L.; Gibb, B. C. Anion binding to hydrophobic concavity is central to the salting-in effects of Hofmeister chaotropes. *J. Am. Chem. Soc.* **2011**, *133*, 7344-7347.
- (15) Assaf, K. I.; Ural, M. S.; Pan, F.; Georgiev, T.; Simova, S.; Rissanen, K.; Gabel, D.; Nau, W. M. Water Structure Recovery in Chaotropic Anion Recognition: High-Affinity Binding of Dodecaborate Clusters to γ -Cyclodextrin. *Angew. Chem. Int. Ed.* **2015**, *54*, 6852-6856.
- (16) Sullivan, M. R.; Yao, W.; Tang, D.; Ashbaugh, H. S.; Gibb, B. C. The Thermodynamics of Anion Complexation to Nonpolar Pockets. *J. Phys. Chem. B* **2018**, *122*, 1702-1713.
- (17) Assaf, K. I.; Gabel, D.; Zimmermann, W.; Nau, W. M. High-affinity host–guest chemistry of large-ring cyclodextrins. *Organic & biomolecular chemistry* **2016**, *14*, 7702-7706.
- (18) Assaf, K. I.; Hennig, A.; Peng, S.; Guo, D.-S.; Gabel, D.; Nau, W. M. Hierarchical host–guest assemblies formed on dodecaborate-coated gold nanoparticles. *Chem. Commun.* **2017**, *53*, 4616-4619.
- (19) Warneke, J.; Jenne, C.; Bernarding, J.; Azov, V. A.; Plaumann, M. Evidence for an intrinsic binding force between dodecaborate dianions and receptors with hydrophobic binding pockets. *Chem. Commun.* **2016**, *52*, 6300-6303.
- (20) Buchecker, T.; Schmid, P.; Renaudineau, S.; Diat, O.; Proust, A.; Pfitzner, A.; Bauduin, P. Polyoxometalates in the Hofmeister series. *Chem. Commun.* **2018**, *54*, 1833-1836.

- (21) Naskar, B.; Diat, O.; Nardello-Rataj, V. r.; Bauduin, P. Nanometer-size polyoxometalate anions adsorb strongly on neutral soft surfaces. *J. Phys. Chem. C* **2015**, *119*, 20985-20992.
- (22) Pang, H.-j.; Peng, J.; Zhang, C.-j.; Li, Y.-g.; Zhang, P.-p.; Ma, H.-y.; Su, Z.-m. A polyoxometalate-encapsulated 3D porous metal–organic pseudo-rotaxane framework. *Chem. Commun.* **2010**, *46*, 5097-5099.
- (23) Cao, H.-L.; Cai, F.-Y.; Huang, H.-B.; Karadeniz, B.; Lü, J. Polyoxometalate-cucurbituril molecular solid as photocatalyst for dye degradation under visible light. *Inorg. Chem. Commun.* **2017**, *84*, 164-167.
- (24) Fang, X.; Kögerler, P.; Isaacs, L.; Uchida, S.; Mizuno, N. Cucurbit [n] uril– polyoxoanion hybrids. *J. Am. Chem. Soc.* **2008**, *131*, 432-433.
- (25) Goel, T.; Barooah, N.; Mallia, M. B.; Bhasikuttan, A. C.; Mohanty, J. Recognition-mediated cucurbit [7] uril-heptamolybdate hybrid material: A facile supramolecular strategy for 99m Tc separation. *Chem. Commun.* **2016**, *52*, 7306-7309.
- (26) Ishii, Y.; Takenaka, Y.; Konishi, K. Porous Organic–Inorganic Assemblies Constructed from Keggin Polyoxometalate Anions and Calix [4] arene–Na⁺ Complexes: Structures and Guest-Sorption Profiles. *Angew. Chem.* **2004**, *116*, 2756-2759.
- (27) Tian, A.; Lin, X.; Ying, J.; Zhang, J.; Lin, H.; Liu, G.; Zhao, D.; Li, N.; Wang, X. Self-assembly of a molecular crown as a structural analogue of calix [4] arene to modify Keggin anions. *Dalton Transactions* **2013**, *42*, 9809-9812.
- (28) Su, P.; Prabhakaran, V.; Johnson, G. E.; Laskin, J. In Situ Infrared Spectroelectrochemistry for Understanding Structural Transformations of Precisely Defined Ions at Electrochemical Interfaces. *Anal. Chem.* **2018**, *90*, 10935-10942.
- (29) Prabhakaran, V.; Lang, Z.; Clotet, A.; Poblet, J. M.; Johnson, G. E.; Laskin, J. Controlling the Activity and Stability of Electrochemical Interfaces Using Atom-by-Atom Metal Substitution of Redox Species. *ACS nano* **2018**, *13*, 458-466.
- (30) Martin-Sabi, M.; Soriano-López, J.; Winter, R. S.; Chen, J.-J.; Vilà-Nadal, L.; Long, D.-L.; Galán-Mascarós, J. R.; Cronin, L. Redox tuning the Weakley-type polyoxometalate archetype for the oxygen evolution reaction. *Nature catalysis* **2018**, *1*, 208.
- (31) Szejtli, J. Introduction and general overview of cyclodextrin chemistry. *Chem. Rev.* **1998**, *98*, 1743-1754.
- (32) Montes-García, V.; Pérez-Juste, J.; Pastoriza-Santos, I.; Liz-Marzán, L. M. Metal nanoparticles and supramolecular macrocycles: a tale of synergy. *Chem. Eur. J.* **2014**, *20*, 10874-10883.
- (33) Engel, S.; Möller, N.; Ravoo, B. J. Stimulus-Responsive Assembly of Nanoparticles using Host–Guest Interactions of Cyclodextrins. *Chem. Eur. J.* **2018**, *24*, 4741-4748.

- (34) Zhang, P.; Mejjide Suárez, J.; Driant, T.; Derat, E.; Zhang, Y.; Ménand, M.; Roland, S.; Sollogoub, M. Cyclodextrin Cavity-Induced Mechanistic Switch in Copper-Catalyzed Hydroboration. *Angew. Chem.* **2017**, *129*, 10961-10965.
- (35) Li, H.; Meng, B.; Chai, S.-H.; Liu, H.; Dai, S. Hyper-crosslinked β -cyclodextrin porous polymer: an adsorption-facilitated molecular catalyst support for transformation of water-soluble aromatic molecules. *Chemical science* **2016**, *7*, 905-909.
- (36) Jing, J.; Szarpak-Jankowska, A.; Guillot, R.; Pignot-Paintrand, I.; Picart, C.; Auzély-Velty, R. Cyclodextrin/paclitaxel complex in biodegradable capsules for breast cancer treatment. *Chem. Mater.* **2013**, *25*, 3867-3873.
- (37) Zhou, J.; Yu, G.; Huang, F. Supramolecular chemotherapy based on host-guest molecular recognition: a novel strategy in the battle against cancer with a bright future. *Chem. Soc. Rev.* **2017**, *46*, 7021-7053.
- (38) Wu, Y.; Shi, R.; Wu, Y.-L.; Holcroft, J. M.; Liu, Z.; Frascioni, M.; Wasielewski, M. R.; Li, H.; Stoddart, J. F. Complexation of polyoxometalates with cyclodextrins. *J. Am. Chem. Soc.* **2015**, *137*, 4111-4118.
- (39) Moussawi, M. A.; Leclerc-Laronze, N.; Floquet, S.; Abramov, P. A.; Sokolov, M. N.; Cordier, S.; Ponchel, A.; Monflier, E.; Bricout, H.; Landy, D. Polyoxometalate, cationic cluster, and γ -cyclodextrin: from primary interactions to supramolecular hybrid materials. *J. Am. Chem. Soc.* **2017**, *139*, 12793-12803.
- (40) Moussawi, M. A.; Haouas, M.; Floquet, S.; Shepard, W. E.; Abramov, P. A.; Sokolov, M. N.; Fedin, V. P.; Cordier, S.; Ponchel, A.; Monflier, E. Nonconventional Three-Component Hierarchical Host-Guest Assembly Based on Mo-Blue Ring-Shaped Giant Anion, γ -Cyclodextrin, and Dawson-type Polyoxometalate. *J. Am. Chem. Soc.* **2017**, *139*, 14376-14379.
- (41) Zhang, B.; Guan, W.; Yin, F.; Wang, J.; Li, B.; Wu, L. Induced chirality and reversal of phosphomolybdate cluster via modulating its interaction with cyclodextrins. *Dalton Transactions* **2018**, *47*, 1388-1392.
- (42) Yang, P.; Zhao, W.; Shkurenko, A.; Belmabkhout, Y.; Eddaoudi, M.; Dong, X.; Alshareef, H. N.; Khashab, N. M. Polyoxometalate-Cyclodextrin Metal-Organic Frameworks: From Tunable Intrinsic Microporosity to Customized Storage Functionality. *J. Am. Chem. Soc.* **2019**.
- (43) Stuckart, M.; Izarova, N. V.; van Leusen, J.; Smekhova, A.; Schmitz-Antoniak, C.; Bamberger, H.; van Slageren, J.; Santiago-Schübel, B.; Kögerler, P. Host-Guest-Induced Environment Tuning of 3d Ions in a Polyoxopalladate Matrix. *Chem. Eur. J.* **2018**, *24*, 17767-17778.
- (44) Gabelica, V.; Galic, N.; De Pauw, E. On the specificity of cyclodextrin complexes detected by electrospray mass spectrometry. *J. Am. Soc. Mass. Spectrom.* **2002**, *13*, 946-953.

- (45) Schalley, C. A. Supramolecular chemistry goes gas phase: the mass spectrometric examination of noncovalent interactions in host–guest chemistry and molecular recognition. *Int. J. Mass spectrom.* **2000**, *194*, 11-39.
- (46) Weimann, D. P.; Schalley, C. A. Host–guest chemistry of self-assembling supramolecular capsules in the gas phase. *Supramol. Chem.* **2008**, *20*, 117-128.
- (47) Qi, Z.; Heinrich, T.; Moorthy, S.; Schalley, C. A. Gas-phase chemistry of molecular containers. *Chem. Soc. Rev.* **2015**, *44*, 515-531.
- (48) Lebrilla, C. B. The gas-phase chemistry of cyclodextrin inclusion complexes. *Acc. Chem. Res.* **2001**, *34*, 653-661.
- (49) Penn, S. G.; He, F.; Lebrilla, C. B. Peptides complexed to cyclodextrin fragment rather than dissociate when subjected to blackbody infrared radiation. *J. Phys. Chem. B* **1998**, *102*, 9119-9126.
- (50) Vrkic, A. K.; O'Hair, R. A.; Lebrilla, C. B. Unusual covalent bond-breaking reactions of β -cyclodextrin inclusion complexes of nucleobases/nucleosides and related guest molecules. *Eur. J. Mass Spectrom.* **2003**, *9*, 563-577.
- (51) Ma, X.; Wei, Z.; Xiong, X.; Jiang, Y.; He, J.; Zhang, S.; Fang, X.; Zhang, X. Gas-phase fragmentation of host–guest complexes between β -cyclodextrin and small molecules. *Talanta* **2012**, *93*, 252-256.
- (52) Bakhtiar, R.; Kaifer, A. Mass spectrometry studies on the complexation of several organometallic complexes by α - and β -cyclodextrins. *Rapid Commun. Mass Spectrom.* **1998**, *12*, 111-114.
- (53) Fan, Y.; Lu, S.; Cao, J. A novel inorganic-organic hybrid complex between polyoxometalate and cyclodextrin: Synthesis, structure and catalytic activity. *Int. J. Mass spectrom.* **2019**, *435*, 163-167.
- (54) Fan, Y.; Zhang, Y.; Jia, Q.; Cao, J.; Wu, W. The Stabilizing Role of Cyclodextrins on Keggin Phosphotungstic Acid by Complexation Unveiled by Electrospray Mass Spectrometry. *Mass Spectrometry Letters* **2015**, *6*, 13-16.
- (55) Julian, R. R.; May, J. A.; Stoltz, B. M.; Beauchamp, J. Molecular Mousetraps: Gas-Phase Studies of the Covalent Coupling of Noncovalent Complexes Initiated by Reactive Carbenes Formed by Controlled Activation of Diazo Precursors. *Angew. Chem. Int. Ed.* **2003**, *42*, 1012-1015.
- (56) Julian, R. R.; May, J. A.; Stoltz, B. M.; Beauchamp, J. Biomimetic approaches to gas phase peptide chemistry: combining selective binding motifs with reactive carbene precursors to form molecular mousetraps. *Int. J. Mass spectrom.* **2003**, *228*, 851-864.

- (57) Schaefer, M. Supramolecular crown ether adducts in the gas phase: from molecular recognition of amines to the covalent coupling of host/guest molecules. *Angew. Chem. Int. Ed.* **2003**, *42*, 1896-1899.
- (58) Lee, T.-C.; Kalenius, E.; Lazar, A. I.; Assaf, K. I.; Kuhnert, N.; Grün, C. H.; Jänis, J.; Scherman, O. A.; Nau, W. M. Chemistry inside molecular containers in the gas phase. *Nat. Chem.* **2013**, *5*, 376.
- (59) Falaise, C.; Moussawi, M. A.; Floquet, S.; Abramov, P. A.; Sokolov, M. N.; Haouas, M.; Cadot, E. Probing Dynamic Library of Metal-Oxo Building Blocks with γ -Cyclodextrin. *J. Am. Chem. Soc.* **2018**, *140*, 11198-11201.
- (60) Klemperer, W. G. Tetrabutylammonium isopolyoxometalates. *Inorg. Synth.* **1990**, *27*, 74-85.
- (61) Fetterolf, D.; Yost, R.-A. Energy-resolved collision-induced dissociation in tandem mass spectrometry. *Int. J. Mass Spectrom. Ion Phys.* **1982**, *44*, 37-50.
- (62) Wells, J. M.; McLuckey, S. A. Collision-induced dissociation (CID) of peptides and proteins. *Methods Enzymol.* **2005**, *402*, 148-185.
- (63) Bayat, P.; Gatineau, D.; Lesage, D.; Marhabaie, S.; Martinez, A.; Cole, R. B. Investigation of activation energies for dissociation of host-guest complexes in the gas phase using low-energy collision induced dissociation. *J. Mass Spectrom.* **2019**.
- (64) Vinokur, N.; Ryzhov, V. Using collision-induced dissociation with corrections for the ion number of degrees of freedom for quick comparisons of relative bonding strength. *J. Mass Spectrom.* **2004**, *39*, 1268-1274.
- (65) Ganapathy, S.; Fournier, M.; Paul, J.; Delevoye, L.; Guelton, M.; Amoureux, J. Location of protons in anhydrous Keggin heteropolyacids $H_3PMO_{12}O_{40}$ and $H_3PW_{12}O_{40}$ by $^1H \{^31P\} / ^{31}P \{^1H\}$ REDOR NMR and DFT quantum chemical calculations. *J. Am. Chem. Soc.* **2002**, *124*, 7821-7828.
- (66) Li, Z.; Couzijn, E. P.; Zhang, X. Intrinsic properties of α -cyclodextrin complexes with benzoate derivatives in the gas phase: an experimental and theoretical study. *J. Phys. Chem. B* **2012**, *116*, 943-950.
- (67) Jenne, C.; Keßler, M.; Warneke, J. Protic Anions $[H(B_{12}X_{12})]^-$ (X= F, Cl, Br, I) That Act as Brønsted Acids in the Gas Phase. *Chem. Eur. J.* **2015**, *21*, 5887-5891.
- (68) Li, S.; Dixon, D. A. Molecular and electronic structures, Brønsted basicities, and Lewis acidities of group VIB transition metal oxide clusters. *J. Phys. Chem. A* **2006**, *110*, 6231-6244.
- (69) Price, N. P. Oligosaccharide structures studied by hydrogen– deuterium exchange and MALDI-TOF mass spectrometry. *Anal. Chem.* **2006**, *78*, 5302-5308.

- (70) Kellersberger, K. A.; Dejsupa, C.; Liang, Y.; Pope, R. M.; Dearden, D. V. Gas phase studies of ammonium–cyclodextrin compounds using Fourier transform ion cyclotron resonance. *Int. J. Mass spectrom.* **1999**, *193*, 181-195.
- (71) Waters, T.; O'Hair, R. A.; Wedd, A. G. Catalytic gas phase oxidation of methanol to formaldehyde. *J. Am. Chem. Soc.* **2003**, *125*, 3384-3396.
- (72) Llusar, R.; Sorribes, I.; Vicent, C. Electrospray ionization based methods for the generation of polynuclear oxo-and hydroxo group 6 anions in the gas-phase. *J. Cluster Sci.* **2009**, *20*, 177-192.
- (73) Harris, B. L.; Waters, T.; Khairallah, G. N.; O'Hair, R. A. Gas-phase reactions of $[\text{VO}_2(\text{OH})_2]^-$ and $[\text{V}_2\text{O}_5(\text{OH})]^-$ with methanol: experiment and theory. *J. Phys. Chem. A* **2012**, *117*, 1124-1135.
- (74) Jackson, P.; Fisher, K. J.; Willett, G. D. The catalytic activation of primary alcohols on niobium oxide surfaces unraveled: the gas phase reactions of Nb_xO_y^- clusters with methanol and ethanol. *Chem. Phys.* **2000**, *262*, 179-187.
- (75) Waters, T.; O'Hair, R. A.; Wedd, A. G. Gas-Phase Reactivity of Heterobinuclear Oxometalate Anions $[\text{CrMoO}_6(\text{OR})]^-$, $[\text{CrWO}_6(\text{OR})]^-$, and $[\text{MoWO}_6(\text{OR})]^-$ (R= H, ⁿBu). *Inorg. Chem.* **2005**, *44*, 3356-3366.
- (76) Laskin, J.; Johnson, G. E.; Warneke, J.; Prabhakaran, V. From Isolated Ions to Multilayer Functional Materials Using Ion Soft-Landing. *Angew. Chem. Int. Ed.* **2018**, *57*, 16270-16284.
- (77) Warneke, J.; McBriarty, M. E.; Riechers, S. L.; China, S.; Engelhard, M. H.; Apra, E.; Young, R. P.; Washton, N. M.; Jenne, C.; Johnson, G. E.; Laskin, J. Self-organizing layers from complex molecular anions. *Nat. Commun.* **2018**, *9*, 1889.
- (78) Su, P.; Hu, H.; Warneke, J.; Belov, M. E.; Anderson, G. A.; Laskin, J. Design and Performance of a Dual-Polarity Instrument for Ion Soft Landing. *Anal. Chem.* **2019**, *91*, 5904-5912.

CHAPTER 6. GAS PHASE REACTIVITY OF $[\text{Mo}_6\text{X}_{14}]^{2-}$ ($\text{X}=\text{CL}, \text{BR}, \text{I}$) DIANIONS

6.1 Introduction

The $[\text{Mo}_6\text{X}_{14}]^{2-}$ ($\text{X} = \text{halogen}$) dianions consist of an octahedral Mo_6 metal core surrounded by eight face-bridging (X^i) and six axial (X^a) halides (Figure 1). Previous studies have shown that these clusters exhibit high chemical stability, have long-lived excited electronic states, and can undergo facile ground and excited state electron transfer reactions.¹⁻³ Such properties have been explored to develop luminescence materials, oxygen sensors, and singlet oxygen sensitizers.⁴⁻⁷ For example, being highly emissive in the red-NIR region with high photoluminescence quantum yields and long emission lifetimes, $[\text{Mo}_6\text{X}_{14}]^{2-}$ are potentially interesting molecular units applied in devices for solar energy conversion and photodynamic therapy.^{8,9} Additionally, these metal clusters have been used as building blocks for the construction of various functional supramolecular structures such as nanomaterials and multidimensional molecular assemblies.¹⁰⁻¹²

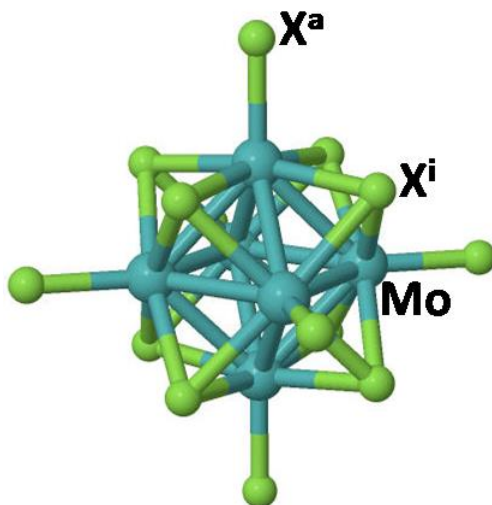


Figure 6.1 Geometry of octahedral hexanuclear molybdenum $[\text{Mo}_6\text{X}_8\text{X}_6]^{2-}$ ($\text{X} = \text{F}, \text{Cl}, \text{Br}, \text{I}$) cluster anions.

Investigation of the structural and electronic properties of the octahedral¹³ metal clusters has a long standing history and is of ongoing interest.¹⁴⁻²³ Brosset first determined the structure of the $[\text{Mo}_6\text{Cl}_8]^{4+}$ core on the basis of his study of $[\text{Mo}_6\text{Cl}_8](\text{OH})_4 \cdot 14\text{H}_2\text{O}$ and $[\text{Mo}_6\text{Cl}_8](\text{Cl}_4 \cdot 2\text{H}_2\text{O}) \cdot 6\text{H}_2\text{O}$

crystals using X-ray diffraction,^{24,25} followed by structure determination of other molybdenum halide complexes, including their bond lengths and vibrational modes.²⁶⁻³² The photochemical and electrochemical properties of $[\text{Mo}_6\text{X}_{14}]^{2-}$ were studied using absorption spectroscopy, emission spectroscopy, and electrochemical measurements in solution or solid state.^{2,3,33} In addition, ground and excited electronic states of $[\text{Mo}_6\text{X}_{14}]^{2-}$ have been also investigated using computational chemistry methods.³⁴⁻³⁷ Molecular orbital calculations showed that the highest occupied molecular orbital (HOMO) was formed by the 4d atomic orbitals of the core Mo_6 atoms^{38,39} and emission occurred via decay of a triplet state.^{1,40,41}

The current study aims to enhance the knowledge about the fundamental molecular properties of $[\text{Mo}_6\text{X}_{14}]^{2-}$ dianions. To the best of our knowledge, a gas phase reactivity study of these compounds without influence of environmental factors has not been reported. In this work, we discuss the gas phase ion chemistry of these clusters initiated by low-energy collision-induced dissociation (CID). All of these results are discussed in comparison with the *closo*-dodecaborate $[\text{B}_{12}\text{X}_{12}]^{2-}$ (X=Cl, Br, I) dianions, which were recently studied using the same experimental and theoretical methods.⁴² *Closo*-dodecaborates are highly symmetric dianions with the negative charge delocalized in the extended molecular framework similar to $[\text{Mo}_6\text{X}_{14}]^{2-}$ which is our focus in this study.

6.2 Experimental Section

In-source CID and ion trap CID experiments of $[\text{Mo}_6\text{X}_{14}]^{2-}$ (X=Cl, Br, I) were performed on a Thermo LTQ XL ion trap mass spectrometer (Thermo Fisher Scientific GmbH, Bremen, Germany). Specifically, TBA salt of $[\text{Mo}_6\text{X}_{14}]^{2-}$ (X=Cl, Br, I) was dissolved in acetonitrile at a concentration of $\sim 10^{-5}$ mol/L for MS analyses. Samples were loaded into a gas-tight syringe (Hamilton, Reno, NV, USA), and injected into the MS inlet from a capillary (50 μm ID, 150 μm OD) through direct infusion using a syringe pump (KD Scientific, Holliston, MA, USA) at a typical flow rate of 0.5 $\mu\text{L}/\text{min}$. For acquisition of spectra without fragmentation of ions, typical settings were as follows: electrospray voltage: -3 kV, capillary temperature: 250 $^\circ\text{C}$, capillary voltage: -10 V, tube lens: -20 V, scan range: m/z 100-2000.

In-source CID experiments were performed by applying an accelerating voltage gradient in the intermediate pressure region of the ion trap. DC voltages of the inlet capillary and tube lens

were adjusted to -140 V and -240 V, respectively, to generate sufficient amount of in-source fragments of $[\text{Mo}_6\text{X}_{14}]^{2-}$. The pressure in the tube lens region was ~ 2 Torr.⁴³ In the ion-trap CID experiments, the fragment ions generated in-source were isolated in the linear ion trap and were subjected to collisions with helium buffer gas. An isolation window of one m/z unit was used throughout the measurements. A typical activation time of 2000 ms was used to investigate reactions of the isolated ions with background gases in the ion trap.

6.3 Results and Discussion

Gas phase fragmentation pathways of $[\text{Mo}_6\text{X}_{14}]^{2-}$ ($\text{X}=\text{Cl}$, Br and I) anions and the reactivities of the corresponding fragment ions towards background gases were systematically investigated by collision-induced dissociation (CID) experiments using in-source CID and ion-trap CID methods. It is well established that in-source fragmentation of ions in the intermediate pressure region provides access to higher excitation energies.⁴⁴ Therefore, it allows the generation of smaller fragments, which cannot be formed in lower-energy ion-trap CID.^{45,46} Instead, ion-trap CID experiments enables the isolation and fragmentation of ions of a particular m/z value, which allows to determine fragmentation pathways. The composition of the background gases in the ion source region and in the ion trap are different, so that different adducts with background gases may be observed.

The ESI-MS spectrum of the TBA salt of $[\text{Mo}_6\text{X}_{14}]^{2-}$ in acetonitrile solution contains doubly-charged $[\text{Mo}_6\text{X}_{14}]^{2-}$ as the predominant species in negative mode (Figure 6.2). Excitation of these ions resulted in the detection of a large variety of different singly charged ions.

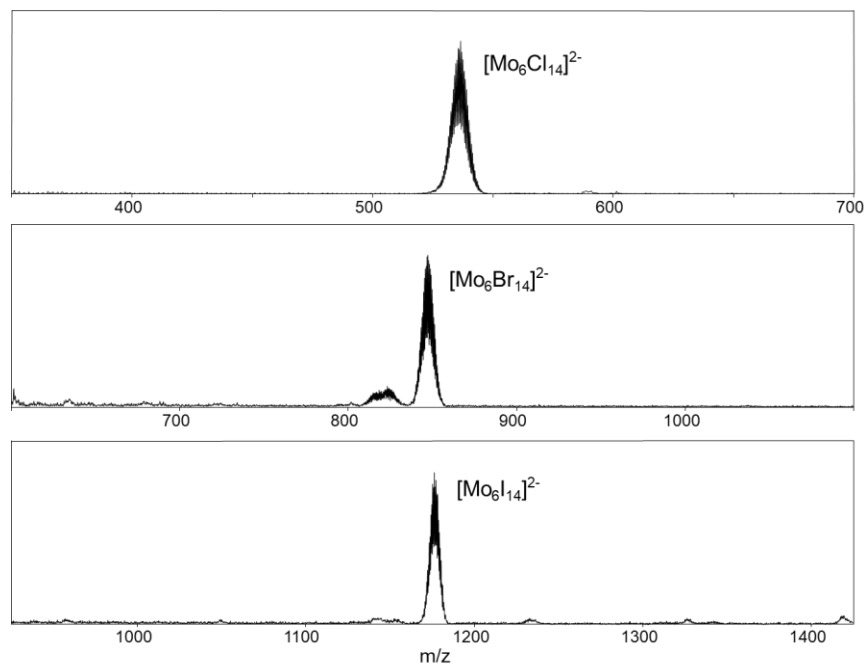


Figure 6.2 ESI-MS spectra of TBA salt of $[\text{Mo}_6\text{X}_{14}]^{2-}$ ($\text{X}=\text{Cl}$ (a), Br (b) and I (c)) in acetonitrile, showing the doubly-charged $[\text{Mo}_6\text{X}_{14}]^{2-}$ as the predominant species.

6.3.1 In-Source Collision-Induced Dissociation

Figure 6.3 show the in-source CID spectra for all the three $[\text{Mo}_6\text{X}_{14}]^{2-}$ ions under optimized conditions (see experimental section). We label these fragments in the following simplified manner by using the number of Mo atoms and halogen atoms in brackets separated by a comma. We have observed exclusively single-charged fragments. However, distinctively different fragment species and reaction products with background gases were detected for $\text{X}=\text{Cl}$ in comparison with $\text{X}=\text{Br}$ and I . In particular, the in-source CID spectrum of $[\text{Mo}_6\text{Cl}_{14}]^{2-}$ shows fragment ions with one to six Mo atoms. Most of the fragments with less than six Mo atoms show adduct formation with a single H_2O molecule (Figure 6.3(a)). In contrast, in-source CID reaction products for $\text{X}=\text{Br}$ and I showed the general formula $[\text{Mo}_6\text{X}_n(\text{O}_2)_y]^-$. In Figure 6.3(b) and 9.3(c) all ions with $y=0$ are denoted as $[6,n]$ and arrows connect the signals of these ions with corresponding $y>0$ ions. Specifically, ions containing one O_2 were found for fragments with more halogen ligands ($n=10, 11, 12$ for $\text{X}=\text{Br}$ and $n=9, 10, 11$ for $\text{X}=\text{I}$). Addition of up to two O_2 molecules was observed for fragments containing less than seven halogen ligands, while three O_2 molecules can attach to smaller fragments for both $\text{X}=\text{Br}$ and $\text{X}=\text{I}$ series. Four O_2 units were only observed to be bound to

the fragments $[\text{Mo}_6\text{Br}_2]^-$ ([6,2]) and $[\text{Mo}_6\text{Br}_3]^-$ ([6,3]). It may be assumed that ions with one and multiple O_2 are formed from sequential addition of O_2 molecules to the corresponding [6,n] ions.

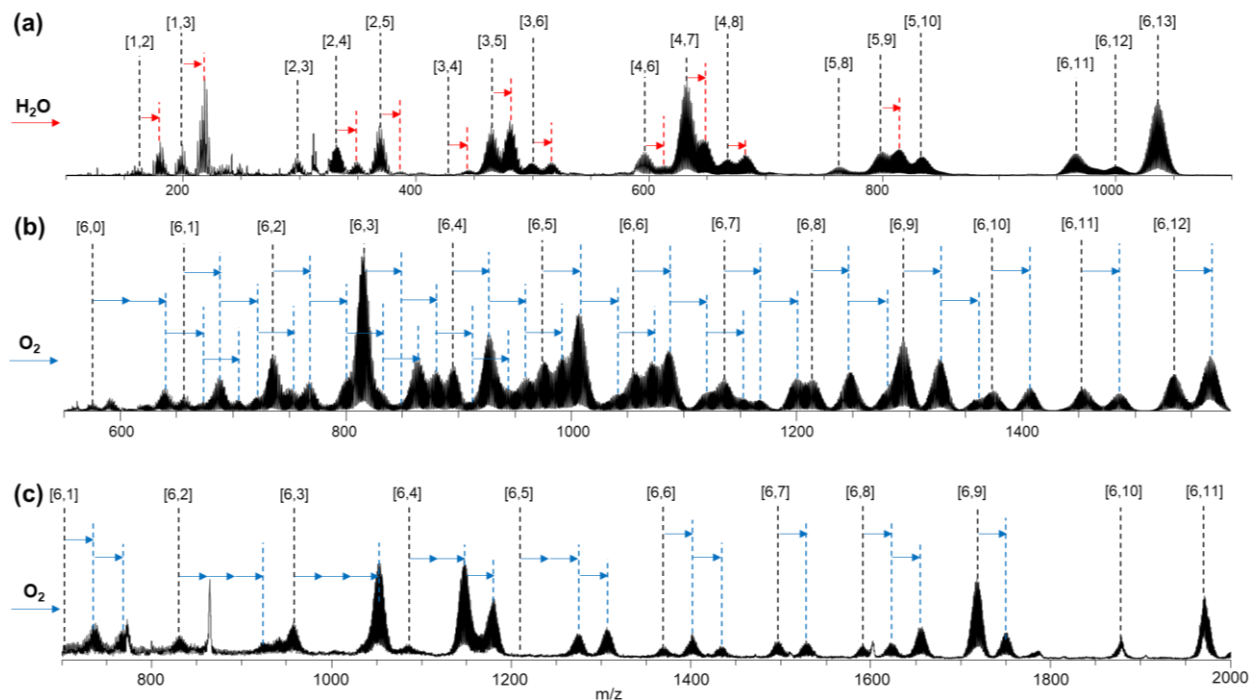
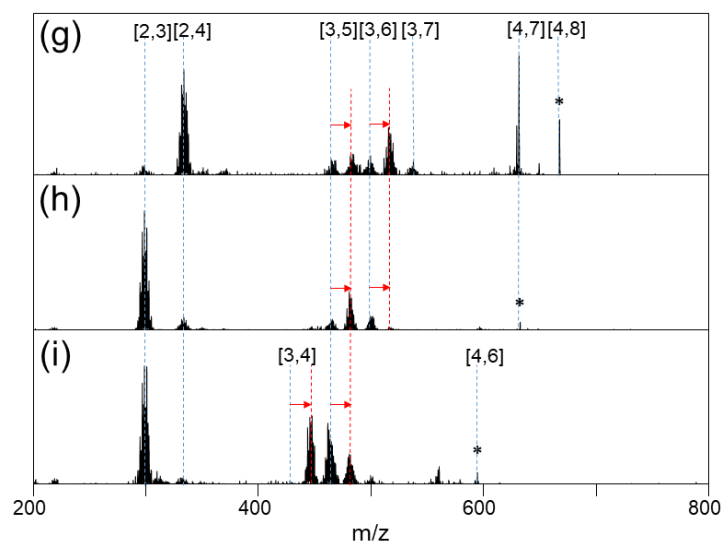
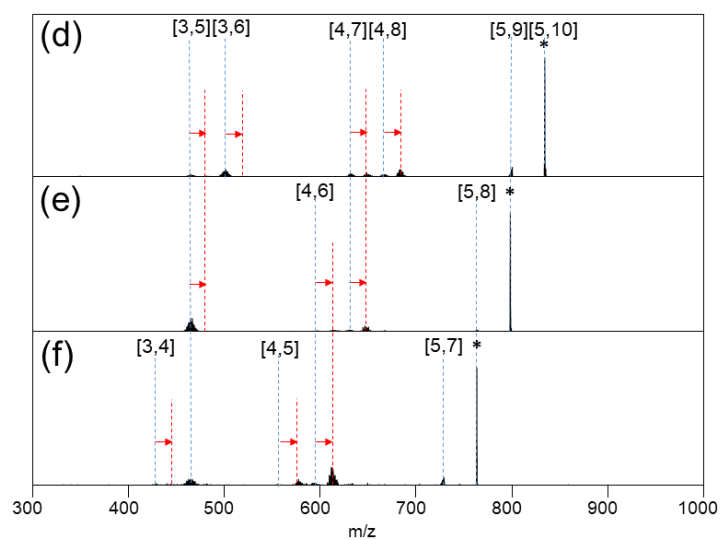
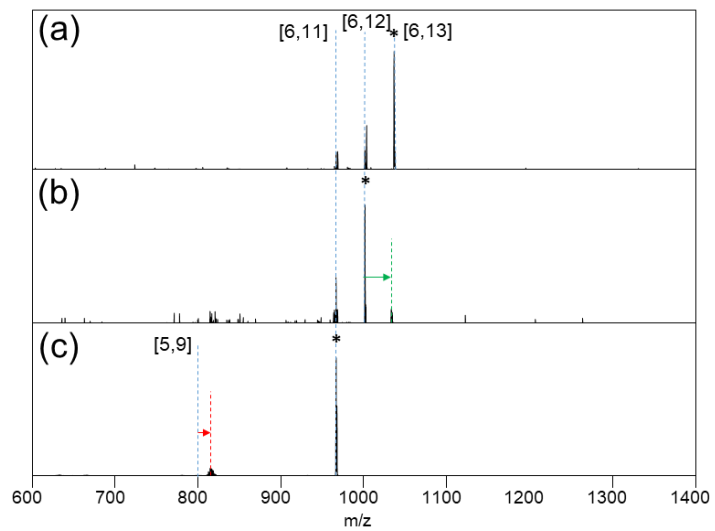


Figure 6.3 In-source CID spectra, showing an overview of molecular fragment ions and their reaction products with background gases for a) $[\text{Mo}_6\text{Cl}_{14}]^{2-}$, b) $[\text{Mo}_6\text{Br}_{14}]^{2-}$ and c) $[\text{Mo}_6\text{I}_{14}]^{2-}$. All observed fragments are singly charged. Adducts with H_2O and O_2 are marked with red and blue arrows, respectively. Multiple arrows in (b) and (c) indicate the number of O_2 added. Fragment ions which have not reacted with background gas molecules are marked with a black dotted line and their molecular formula is abbreviated by [Number of Mo atoms, Number of halogen atoms].

6.3.2 Reaction Pathways Probed by Ion-Trap CID

To obtain more insights into the nature of fragmentation reactions, we systematically investigated the reaction pathways of $[\text{Mo}_m\text{X}_n]^-$ fragment ions by their sequential isolation and fragmentation in the ion trap. Spectra are shown in Figures 6.4, 6.5, and 6.6. We discuss first the fragmentation pathways and then the reactions with residual gases.

Figure 6.4 Ion-trap CID mass spectra of $[\text{Mo}_x\text{Cl}_y]^-$ clusters: (a) $[\text{Mo}_6\text{Cl}_{13}]^-$ (b) $[\text{Mo}_6\text{Cl}_{12}]^-$ (c) $[\text{Mo}_6\text{Cl}_{11}]^-$ (d) $[\text{Mo}_5\text{Cl}_{10}]^-$ (e) $[\text{Mo}_5\text{Cl}_9]^-$ (f) $[\text{Mo}_5\text{Cl}_8]^-$ (g) $[\text{Mo}_4\text{Cl}_8]^-$ (h) $[\text{Mo}_4\text{Cl}_7]^-$ (i) $[\text{Mo}_4\text{Cl}_6]^-$ (j) $[\text{Mo}_3\text{Cl}_6]^-$ (k) $[\text{Mo}_3\text{Cl}_5]^-$ (l) $[\text{Mo}_2\text{Cl}_5]^-$ (m) $[\text{Mo}_2\text{Cl}_4]^-$ (n) $[\text{Mo}_2\text{Cl}_3]^-$. Parent ions, generated via in-source CID, are marked by *. Fragment ions which have not reacted with background gas molecules are marked with a blue, dotted line and their molecular formula is abbreviated by [Number Mo atoms, Number halogen atoms]. The red arrow indicates the reaction with water and green arrow indicates the reaction with O_2 , while dotted line indicates the corresponding adducts.



(Figure 6.4 continued)

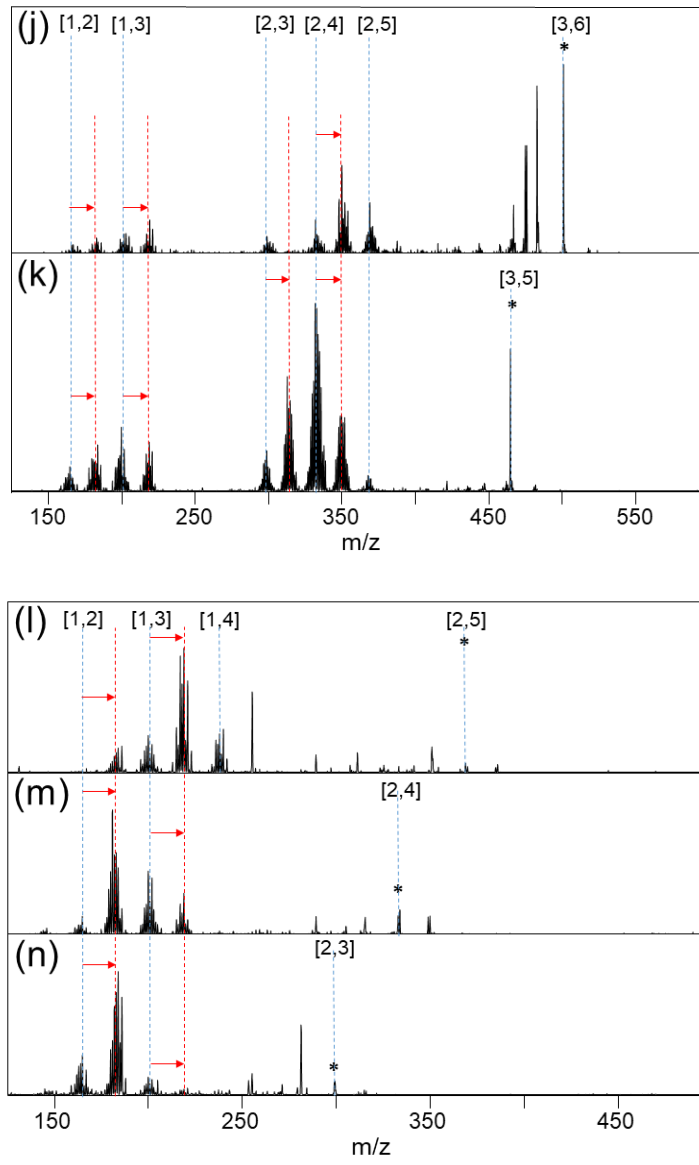
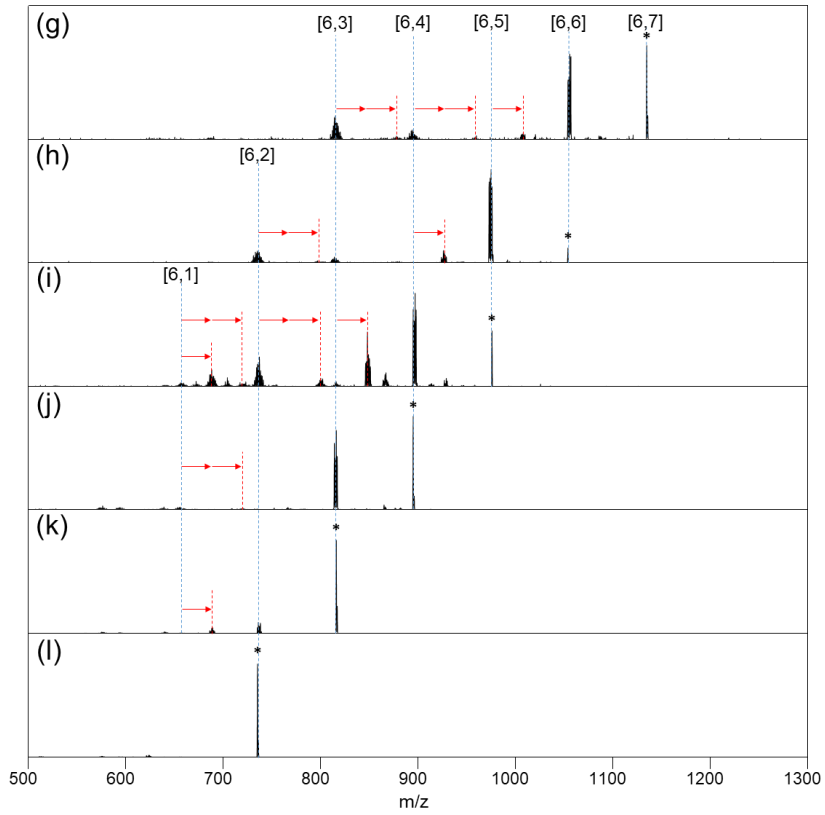
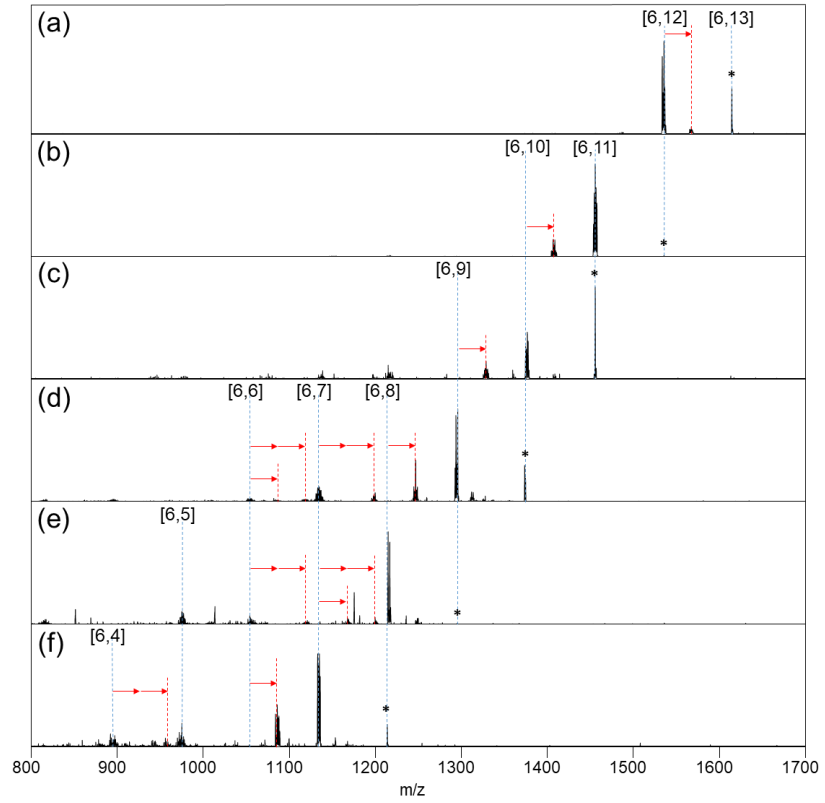


Figure 6.5 Ion-trap CID mass spectra of $[\text{Mo}_x\text{Br}_y]^-$ clusters: (a) $[\text{Mo}_6\text{Br}_{13}]^-$ (b) $[\text{Mo}_6\text{Br}_{12}]^-$ (c) $[\text{Mo}_6\text{Br}_{11}]^-$ (d) $[\text{Mo}_6\text{Br}_{10}]^-$ (e) $[\text{Mo}_6\text{Br}_9]^-$ (f) $[\text{Mo}_6\text{Br}_8]^-$ (g) $[\text{Mo}_6\text{Br}_7]^-$ (h) $[\text{Mo}_6\text{Br}_6]^-$ (i) $[\text{Mo}_6\text{Br}_5]^-$ (j) $[\text{Mo}_6\text{Br}_4]^-$ (k) $[\text{Mo}_6\text{Br}_3]^-$ (l) $[\text{Mo}_6\text{Br}_2]^-$. Parent ions, generated via in-source CID, are marked by *. Fragment ions which have not reacted with background gas molecules are marked with a blue, dotted line and their molecular formula is abbreviated by [Number Mo atoms, Number halogen atoms]. The red arrow indicates the reaction with dioxygen, while dotted line indicates the corresponding adducts. Multiple arrows indicate the number of O_2 added.



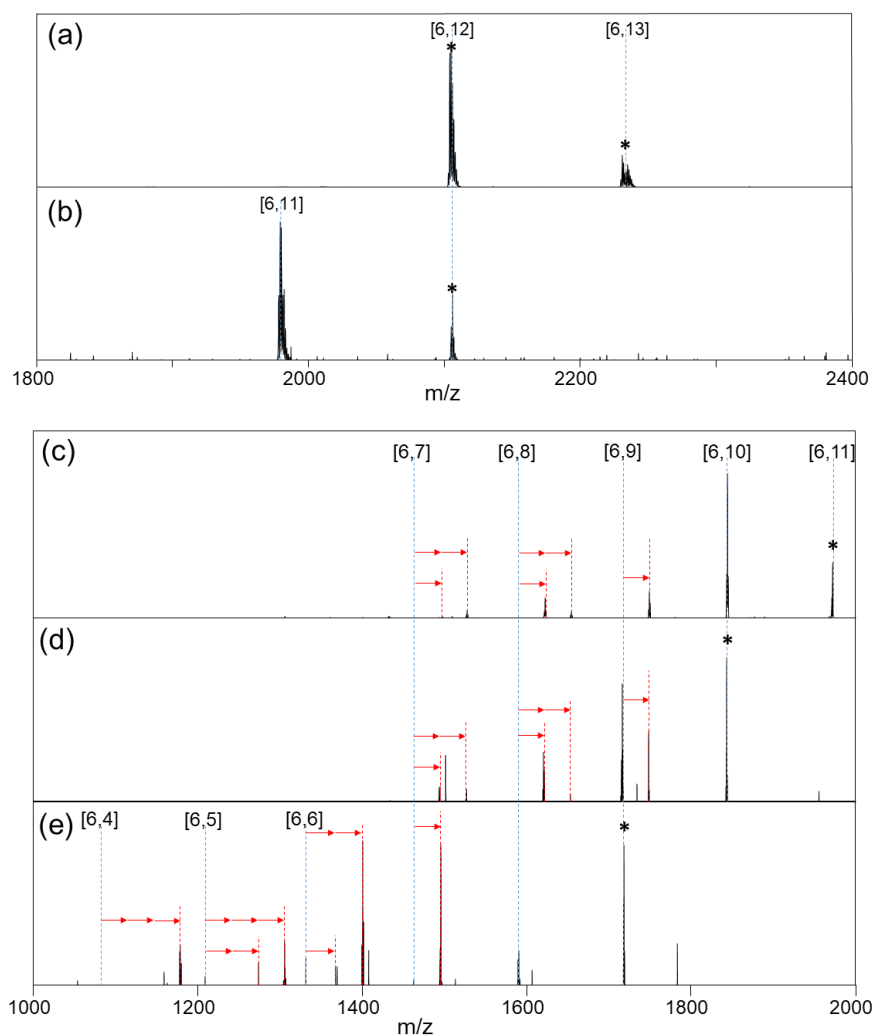
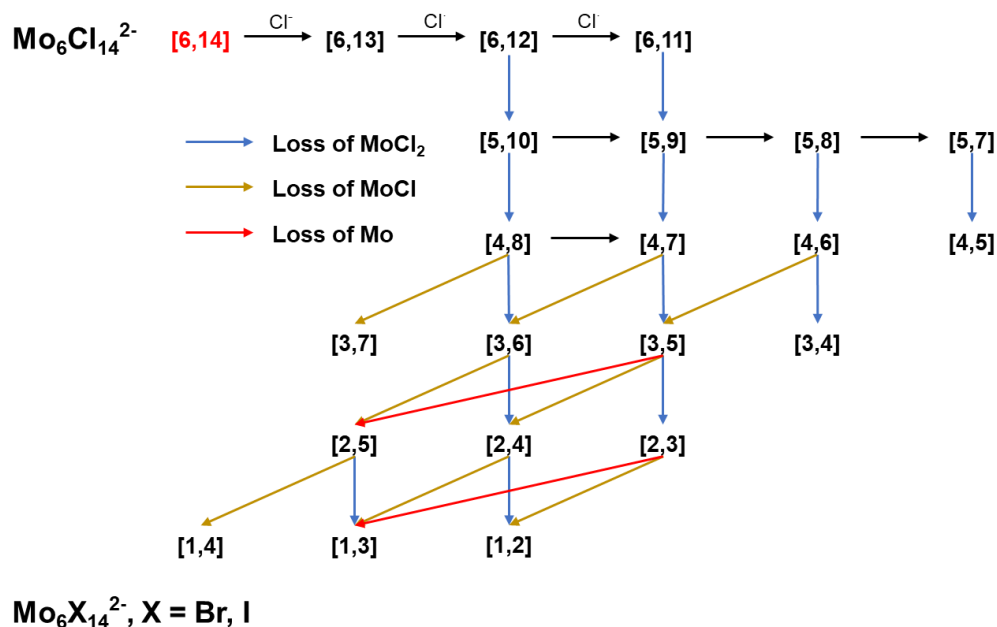


Figure 6.6 Ion-trap CID mass spectra of $[\text{Mo}_x\text{I}_y]^-$ clusters: (a) $[\text{Mo}_6\text{I}_{13}]^-$ (b) $[\text{Mo}_6\text{I}_{12}]^-$ (c) $[\text{Mo}_6\text{I}_{11}]^-$ (d) $[\text{Mo}_6\text{I}_{10}]^-$ (e) $[\text{Mo}_6\text{I}_9]^-$. Parent ions, generated via in-source CID, are marked by *. Fragment ions which have not reacted with background gas molecules are marked with a blue, dotted line and their molecular formula is abbreviated by [Number Mo atoms, Number halogen atoms]. The red arrow indicates the reaction with dioxygen, while dotted line indicates the corresponding adducts. Multiple arrows indicate the number of O_2 added. We note that (a) and (b) are acquired under extended mass range on the LTQ-XL instrument.

6.3.2.1. Fragmentation Pathways. The corresponding fragmentation pathways are summarized in Scheme 6.1. Note that Scheme 1 covers only fragmentation and does not include product ions which result from reactions with residual gases (H_2O and O_2). Fragmentation pathways leading to the formation of the ions observed in in-source CID are well retraced.



Scheme 6.1 Gas-phase fragmentation pathways of $[\text{Mo}_6\text{X}_{14}]^{2-}$ (X=Cl, Br and I) ions by ion-trap CID experiments. Molecular formulae of the ions are abbreviated by [Number Mo atoms, Number halogen atoms]. Singly charged ions are written black, doubly charged ions red. Arrows mark the fragmentation pathways evidenced by ion-trap CID.

Independent of the halogen, isolation and excitation of $[\text{Mo}_6\text{X}_{14}]^{2-}$ in the ion trap resulted in the loss of a X^\cdot and the formation of $[\text{Mo}_6\text{X}_{13}]^\cdot$ anions, labeled as [6,13] (Figure 6.7). Further isolation and excitation of [6,13] ions result in loss of X^\cdot radicals and formation of singly charged [6,12] and [6,11] ions. However, further dissociation was found to be strongly dependent on the type of halogen ligand X. For X=Cl, neutral MoCl_2 loss were observed for [6,12] and [6,11] (Figures 6.4(a) and 6.4(b)). MoCl_2 loss is the only fragmentation channel observed in considerable abundance for all [5,n] ions (Figure 6.4, d-f) of the $[\text{Mo}_6\text{Cl}_{14}]^{2-}$ series. Meanwhile, a competing channel of MoCl neutral loss started to be observed in the dissociation of [4,n] fragments (Figure 6.4, g-i), and becomes the dominant dissociation channel for [3,n] and [2,n] fragments (Figure 6.4, j-n). In addition, an atomic Mo loss was observed in low abundance in the CID of [3,5] and [2,3] fragments (Figures 6.4(k) and 6.4(n)). Cl^\cdot radical loss is a minor dissociation channel observed in very low abundance in the ion trap CID spectra of many of the aforementioned fragments. In contrast, for X=Br and I, excitation of every [6,n] fragment ion results in X^\cdot radical loss (Figures

6.5 and 6.6). In the case of X=Br, a bare $[\text{Mo}_6]^-$ cluster (full bromine loss) is observed in low abundance.

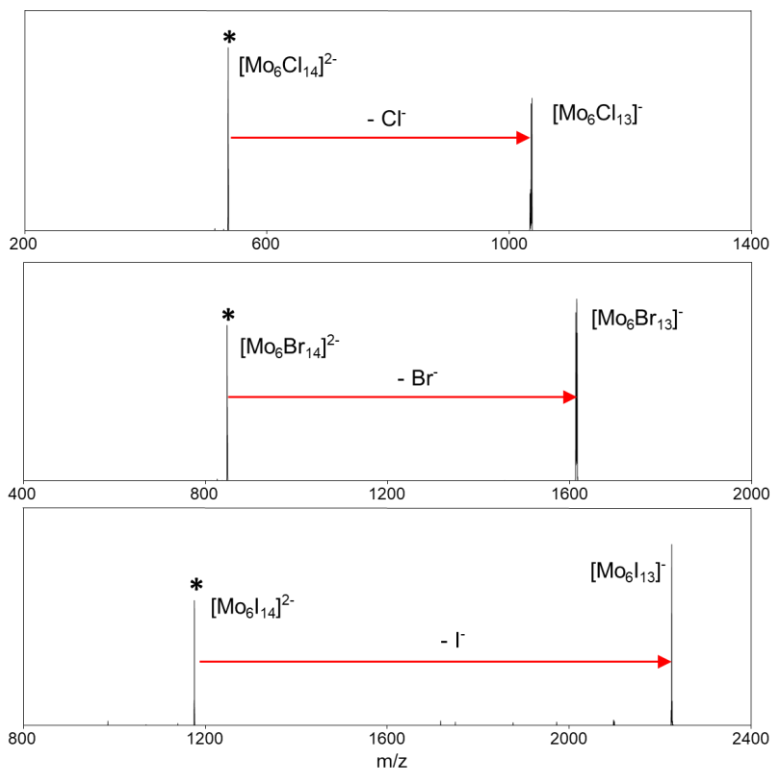


Figure 6.7 Ion-trap CID mass spectra of $[\text{Mo}_6\text{X}_{14}]^{2-}$ clusters: (a) $[\text{Mo}_6\text{Cl}_{14}]^{2-}$ (b) $[\text{Mo}_6\text{Br}_{14}]^{2-}$ (c) $[\text{Mo}_6\text{I}_{14}]^{2-}$. Parent ions are marked by *. The red arrows indicate the loss of X^- .

The observed fragmentation behavior shows some parallels with the one of $[\text{B}_{12}\text{X}_{12}]^{2-}$ clusters. For X=I successive loss of halogen radicals⁴⁶⁻⁴⁸ was found down to $[\text{B}_{12}\text{I}]^-$, similar to $[\text{Mo}_6\text{I}_{14}]^{2-}$. For X=Cl, a decomposition of the boron unit by loss of BCl_3 and BCl units was found, similar to the observed MoCl_2 and MoCl losses of $[\text{Mo}_6\text{Cl}_{14}]^{2-}$.⁴⁶ While $[\text{B}_{12}\text{Br}_{12}]^{2-}$ was showing an intermediate position (loss of Br radicals as well as BBr_3 and BBr in significant abundance), $[\text{Mo}_6\text{Br}_{14}]^{2-}$ behaves similar to its iodinated neighbor and loses only Br radicals.

6.3.2.2. Reactivity of Fragment Ions in the Ion Trap. As expected, isolation of some smaller fragments of $[\text{Mo}_6\text{Cl}_{14}]^{2-}$ resulted in the addition of water to these ions. Surprisingly, no spontaneous O_2 addition could be observed by isolation of any $[\text{6},n]$ fragment of $[\text{Mo}_6\text{Br}_{14}]^{2-}$ and $[\text{Mo}_6\text{I}_{14}]^{2-}$, although corresponding ions containing O_2 were observed in high intensity using in-source CID. It is known that O_2 is present in the ion trap and was shown to add to radical ions

generated in the same instrument.¹ Strikingly, if collisional activation condition in the ion trap is applied, O₂ addition to the resulting fragments was observed. We demonstrate this on a concrete example: Isolation of [Mo₆I₁₀]⁻ did not result in any O₂ addition, but ion trap CID led to the formation of [Mo₆I₉]⁻ and [Mo₆I₉(O₂)]⁻ (Figure 6.6(d)). However, isolation of [Mo₆I₉]⁻ formed by in-source CID did not result in any O₂ addition (Figure 6.6(e)).

Spontaneous binding of the diradical O₂ is usually associated with a localized radical site within the ion¹⁻⁴. Therefore, we hypothesize that localized radical sites are present in the fragments produced in-source, which react with O₂. Collisional cooling in the ion trap during the isolation process may result in structural rearrangement or relaxation into lower electronic states, which deactivates the reactive sites. The formation of fragments with multiple O₂ molecules attached is not necessarily the result of multiple oxygen additions to one particular [6,n] ion. Also, sequential X[·] loss followed by O₂ additions from ions with larger n can explain the experimental observations. Isolation and fragmentation of an O₂ containing ion results indeed in the loss of X[·] and not O₂, confirming this hypothesis (Figure 6.8).

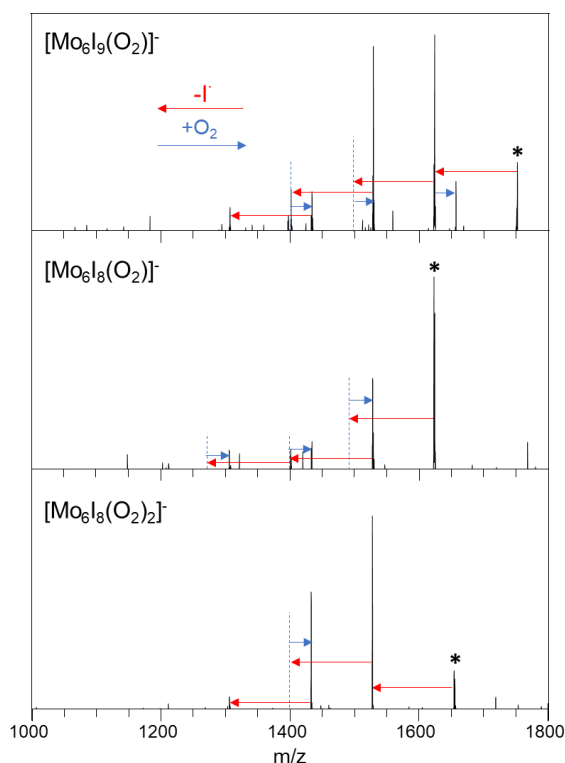


Figure 6.8 Examples of isolation of $[\text{Mo}_6\text{In}(\text{O}_2)_y]^-$ adducts in the ion trap: (a) $[\text{Mo}_6\text{I}_9(\text{O}_2)]^-$, (b) $[\text{Mo}_6\text{I}_8(\text{O}_2)]^-$, (c) $[\text{Mo}_6\text{I}_8(\text{O}_2)_2]^-$. Parent ions are marked by *. The red and blue arrows indicate the mass difference between two peaks corresponding to I^\cdot loss and O_2 addition, respectively.

Distinct differences are notably when we compare the reactivity of $[\text{Mo}_6\text{X}_{14}]^{2-}$ fragment ions with the reactivity of $[\text{B}_{12}\text{X}_{12}]^{2-}$ fragments. While $[\text{B}_{12}\text{X}_{11}]^-$ ions, formed by loss of one negative substituent, exhibit superelectrophilic reactivity and binds H_2O , N_2 and even noble gases within the mass spectrometer,^{1,2} the corresponding $[\text{Mo}_6\text{X}_{13}]^-$ do not show any remarkable reactivity. Reactions with O_2 were so far only reported for $[\text{B}_{12}\text{I}_{11}]^{2-}$ dianions with a localized radical on the free boron binding site, which stayed active if isolated in the ion trap.³ Further fragmentation of $[\text{B}_{12}\text{I}_{11}\text{O}_2]^{2-}$ did not result in simple halogen abstraction. In contrast, $[\text{Mo}_6\text{In}(\text{O}_2)_y]^-$ can lose further I-radicals, which opens new sites for additional O_2 additions.

6.4 Conclusions

We have investigated gas phase reactivity of $[\text{Mo}_6\text{X}_{14}]^{2-}$ ions, with X= halogen. Gas phase ion chemistry of $[\text{Mo}_6\text{X}_{14}]^{2-}$ provides access to a large variety of fragment ions with interesting reactivity. For X=Cl, a decomposition of the Mo_6 unit was observed and the fragments show an

affinity to water, while for X=Br and I exclusively halogen losses were found and reaction products with multiple O₂ molecules were detected. It is interesting to note that also the “turning point” in fragmentation behavior (*loss of MoX_n for small halogens to loss of X-radicals for larger halogens*) occurs one halogen earlier along the series than for [B₁₂X₁₂]²⁻ ion, similar to the “turning point” in electronic stability. An in depth understanding of the structure, reactivity and electronic properties of these gaseous fragment ions may require fast laser spectroscopy, infrared photodissociation measurements and high-level computational investigations on excited states. Such studies may be motivated by new enhanced ion deposition methods, which may allow to utilize such gaseous ions with special properties for the generation of new condensed phase materials on surfaces⁴⁻⁶.

6.5 References

- (1) Saito, Y.; Tanaka, H. K.; Sasaki, Y.; Azumi, T. Temperature dependence of the luminescence lifetime of hexanuclear molybdenum (II) chloride cluster. Identification of lower excited triplet sublevels. *J. Phys. Chem.* **1985**, *89*, 4413-4415.
- (2) Maverick, A. W.; Najdzionek, J. S.; MacKenzie, D.; Nocera, D. G.; Gray, H. B. Spectroscopic, electrochemical, and photochemical properties of molybdenum (II) and tungsten (II) halide clusters. *J. Am. Chem. Soc.* **1983**, *105*, 1878-1882.
- (3) Maverick, A. W.; Gray, H. B. Luminescence and redox photochemistry of the molybdenum (II) cluster Mo₆C₁₁₄. *J. Am. Chem. Soc.* **1981**, *103*, 1298-1300.
- (4) Kirakci, K.; Kubát, P.; Langmaier, J.; Polívka, T.; Fuciman, M.; Fejfarová, K.; Lang, K. A comparative study of the redox and excited state properties of (n Bu 4 N)₂ [Mo 6 X 14] and (n Bu 4 N)₂ [Mo 6 X 8 (CF 3 COO) 6](X= Cl, Br, or I). *Dalton T* **2013**, *42*, 7224-7232.
- (5) Sokolov, M.; Mikhailov, M.; Virovets, A.; Brylev, K.; Bredikhin, R.; Maksimov, A.; Platonov, V.; Fedin, V. Synthesis, structure, and luminescence of the octahedral molybdenum cluster [Mo₆I₈ (SC₆F₄H) 6]²⁻. *Russ. Chem. Bull.* **2013**, *8*, 1764-1767.
- (6) Jackson, J. A.; Newsham, M. D.; Worsham, C.; Nocera, D. G. Efficient singlet oxygen generation from polymers derivatized with hexanuclear molybdenum clusters. *Chem. Mater.* **1996**, *8*, 558-564.
- (7) Jackson, J. A.; Turro, C.; Newsham, M. D.; Nocera, D. G. Oxygen quenching of electronically excited hexanuclear molybdenum and tungsten halide clusters. *J. Phys. Chem.* **1990**, *94*, 4500-4507.
- (8) Rojas-Mancilla, E.; Oyarce, A.; Verdugo, V.; Morales-Verdejo, C.; Echeverria, C.; Velásquez, F.; Chnaiderman, J.; Valiente-Echeverría, F.; Ramirez-Tagle, R. The [Mo₆C₁₁₄]²⁻ Cluster is Biologically Secure and Has Anti-Rotavirus Activity In Vitro. *Molecules* **2017**, *22*, 1108.

- (9) Gray, H. B.; Maverick, A. W. Solar chemistry of metal complexes. *Science* **1981**, *214*, 1201-1205.
- (10) Nerambourg, N.; Aubert, T.; Neaime, C.; Cordier, S.; Mortier, M.; Patriarche, G.; Grasset, F. Multifunctional hybrid silica nanoparticles based on [Mo₆Br₁₄]²⁻ phosphorescent nanosized clusters, magnetic γ -Fe₂O₃ and plasmonic gold nanoparticles. *J. Colloid Interface Sci.* **2014**, *424*, 132-140.
- (11) Cordier, S.; Dorson, F.; Grasset, F.; Molard, Y.; Fabre, B.; Haneda, H.; Sasaki, T.; Mortier, M.; Ababou-Girard, S.; Perrin, C. Novel nanomaterials based on inorganic molybdenum octahedral clusters. *J. Cluster Sci.* **2009**, *20*, 9-21.
- (12) Grasset, F.; Dorson, F.; Cordier, S.; Molard, Y.; Perrin, C.; Marie, A. M.; Sasaki, T.; Haneda, H.; Bando, Y.; Mortier, M. Water-in-Oil Microemulsion Preparation and Characterization of Cs₂ [Mo₆X₁₄]@ SiO₂ Phosphor Nanoparticles Based on Transition Metal Clusters (X= Cl, Br, and I). *Adv. Mater.* **2008**, *20*, 143-148.
- (13) Akagi, S.; Fujii, S.; Horiguchi, T.; Kitamura, N. pK_a (L) Dependences of Structural, Electrochemical, and Photophysical Properties of Octahedral Hexamolybdenum (II) Clusters:[Mo₆X₈L₆]²⁻(X= Br or I; L= carboxylate). *J. Cluster Sci.* **2017**, *28*, 757-772.
- (14) Saito, N.; Cordier, S. p.; Lemoine, P.; Ohsawa, T.; Wada, Y.; Grasset, F.; Cross, J. S.; Ohashi, N. Lattice and Valence Electronic Structures of Crystalline Octahedral Molybdenum Halide Clusters-Based Compounds, Cs₂ [Mo₆X₁₄](X= Cl, Br, I), Studied by Density Functional Theory Calculations. *Inorg. Chem.* **2017**.
- (15) Aubert, T.; Nerambourg, N.; Saito, N.; Haneda, H.; Ohashi, N.; Mortier, M.; Cordier, S.; Grasset, F. Tunable visible emission of luminescent hybrid nanoparticles incorporating two complementary luminophores: ZnO nanocrystals and [Mo₆Br₁₄]²⁻ nanosized cluster units. *Part. Part. Syst. Charact.* **2013**, *30*, 90-95.
- (16) Saito, G.; Hosoda, H.; Yoshida, Y.; Hagiwara, J.; Nishimura, K.; Yamochi, H.; Otsuka, A.; Hiramatsu, T.; Shimazaki, Y.; Kirakci, K. Synthesis and properties of charge-transfer solids with cluster units [Mo₆X₁₄]²⁻(X= Br, I). *J. Mater. Chem.* **2012**, *22*, 19774-19791.
- (17) Mocanu, A. S.; Amela-Cortes, M.; Molard, Y.; Cîrcu, V.; Cordier, S. Liquid crystal properties resulting from synergetic effects between non-mesogenic organic molecules and a one nanometre sized octahedral transition metal cluster. *Chem. Commun.* **2011**, *47*, 2056-2058.
- (18) Molard, Y.; Dorson, F.; Cîrcu, V.; Roisnel, T.; Artzner, F.; Cordier, S. Clustomesogens: Liquid Crystal Materials Containing Transition-Metal Clusters. *Angew. Chem. Int. Ed.* **2010**, *49*, 3351-3355.
- (19) Ababou-Girard, S.; Cordier, S.; Fabre, B.; Molard, Y.; Perrin, C. Assembly of hexamolybdenum metallic clusters on silicon surfaces. *ChemPhysChem* **2007**, *8*, 2086-2090.

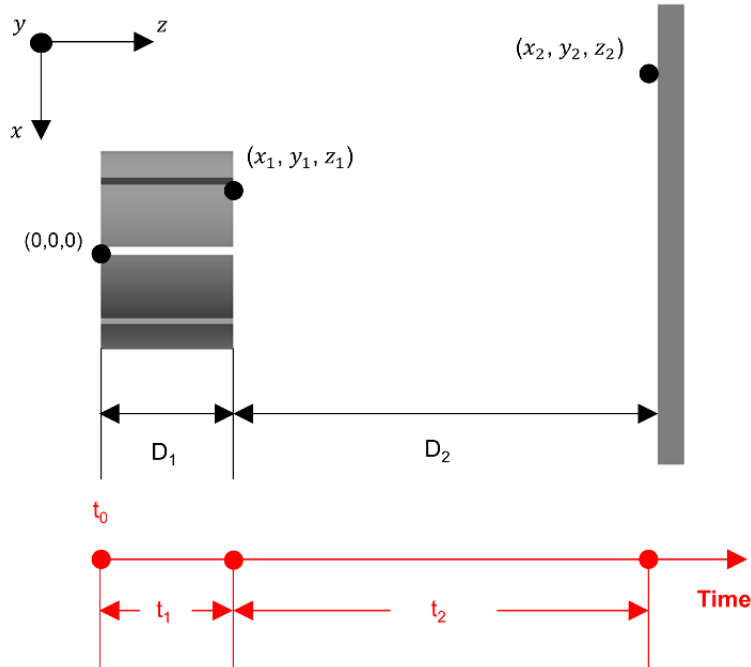
- (20) Kirakci, K.; Hosoda, H.; Cordier, S.; Perrin, C.; Saito, G. A hybrid material based on [Mo₆Br₁₄]²⁻ inorganic cluster units and [BEDO-TTF]⁺ organic monocationic radicals: Synthesis, structure and properties of (BEDO-TTF)₂Mo₆Br₁₄(PhCN)₄. *J. Solid State Chem.* **2006**, *179*, 3628-3635.
- (21) Cordier, S.; Kirakci, K.; Méry, D.; Perrin, C.; Astruc, D. Mo₆X₁₄. *Inorg. Chim. Acta* **2006**, *359*, 1705-1709.
- (22) Kirakci, K.; Cordier, S.; Perrin, C. Synthesis and Characterization of Cs₂Mo₆X₁₄ (X= Br or I) Hexamolybdenum Cluster Halides: Efficient Mo₆ Cluster Precursors for Solution Chemistry Syntheses. *Z. Anorg. Allg. Chem.* **2005**, *631*, 411-416.
- (23) Pilet, G.; Kirakci, K.; de Montigny, S. C.; Lapinte, C.; Perrin, C.; Perrin, A. Assisted Crystallization of Organometallic Cations by Interplay with Inorganic Anionic Clusters Units: Synthesis and Characterizations of the [Cp*(dppe)Fe-NCMe]₂·M₆L₁₄ Series (M₆L₁₄= Cluster Unit:[Re₆S₆Br₈]²⁻, [Mo₆Br₁₄]²⁻ and [Mo₆I₁₄]²⁻). *Eur J Inorg Chem* **2005**, *2005*, 919-928.
- (24) Brosset, C. ON THE STRUCTURE OF COMPLEX COMPOUNDS OF BIVALENT MOLYBDENUM. 2. X-RAY ANALYSIS OF [MO₆CL₈](CL₄·2H₂O)·6H₂O. *Ark. Kem.Mineral. Geol.* **1946**, *A22*, 10.
- (25) Brosset, C. Arkiv Kemi Mineral. *Ark. Kem.Mineral. Geol.* **1945**, *A20*, 16.
- (26) Brückner, P.; Preetz, W.; Pünjer, M. Darstellung, Kristallstrukturen, NMR-, Schwingungsspektren und Normalkoordinatenanalyse der Clusteranionen [(Mo₆I₈)Y₆]²⁻, Y_a= F, Cl, Br, I. *Z. Anorg. Allg. Chem.* **1997**, *623*, 8-17.
- (27) Schoonover, J. R.; Zietlow, T. C.; Clark, D. L.; Heppert, J. A.; Chisholm, M. H.; Gray, H. B.; Sattelberger, A. P.; Woodruff, W. H. Resonance Raman Spectra of [M₆X₈Y₆]²⁻ Cluster Complexes (M= Mo, W; X, Y= Cl, Br, I). *Inorg. Chem.* **1996**, *35*, 6606-6613.
- (28) Preetz, W.; Bublitz, D.; Von Schnering, H.; Sassmannshausen, J. Darstellung, Kristallstruktur und spektroskopische Eigenschaften der Clusteranionen [(Mo₆Br₈)X₆]²⁻ mit X_a= F, Cl, Br, I. *Z. Anorg. Allg. Chem.* **1994**, *620*, 234-246.
- (29) Preetz, W.; Harder, K.; von Schnering, H.; Kliche, G.; Peters, K. Synthesis, structure and properties of the cluster anions [(Mo₆Cl₈)X₆]²⁻ with X_a = F, Cl, Br, I. *J. Alloys Compd.* **1992**, *183*, 413-429.
- (30) Guggenberger, L. J.; Sleight, A. Structural and bonding characterizations of molybdenum dibromide, Mo₆Br₁₂·2H₂O. *Inorg. Chem.* **1969**, *8*, 2041-2049.
- (31) Sheldon, J. 208. Chloromolybdenum (II) compounds. *J. Chem. Soc.* **1960**, 1007-1014.
- (32) Vaughan, P. A. The Structure of the Mo₆Cl₁₄--Complex in the Crystal (NH₄)₂(Mo₆Cl₈)Cl₆·H₂O. *Proc. Natl. Acad. Sci. USA* **1950**, *36*, 461-464.

- (33) Zietlow, T. C.; Hopkins, M. D.; Gray, H. B. Electronic spectroscopy and photophysics of d4 clusters. *J. Solid State Chem.* **1985**, *57*, 112-119.
- (34) Costuas, K.; Garreau, A.; Bulou, A.; Fontaine, B.; Cuny, J.; Gautier, R.; Mortier, M.; Molard, Y.; Duvail, J.-L.; Faulques, E. Combined theoretical and time-resolved photoluminescence investigations of [Mo₆X₈L₆]²⁻ metal cluster units: evidence of dual emission. *Phys. Chem. Chem. Phys.* **2015**, *17*, 28574-28585.
- (35) Ramirez-Tagle, R.; Arratia-Pérez, R. Electronic structure and molecular properties of the [Mo₆X₈L₆]²⁻; X= Cl, Br, I; L= F, Cl, Br, I clusters. *Chem. Phys. Lett.* **2008**, *460*, 438-441.
- (36) Honda, H.; Noro, T.; Tanaka, K.; Miyoshi, E. Theoretical study on electronic excitation spectra of Mo and Re cluster complexes: [(Mo₆Cl₈)Cl₆]²⁻ and [(Re₆S₈)Cl₆]⁴⁻. *J. Chem. Phys.* **2001**, *114*, 10791-10797.
- (37) Robinson, L.; Bain, R.; Shriver, D.; Ellis, D. Effect of coordination environment on the electronic structure and properties of Mo₆-based systems: a density functional treatment. *Inorg. Chem.* **1995**, *34*, 5588-5596.
- (38) Cotton, F. A.; Stanley, G. G. Ground state electronic structures of some metal atom cluster compounds. *Chem. Phys. Lett.* **1978**, *58*, 450-453.
- (39) Cotton, F. A.; Haas, T. A molecular orbital treatment of the bonding in certain metal atom clusters. *Inorg. Chem.* **1964**, *3*, 10-17.
- (40) Azumi, T.; Saito, Y. Electronic structures of the lower triplet sublevels of hexanuclear molybdenum (II) chloride cluster. *J. Phys. Chem.* **1988**, *92*, 1715-1721.
- (41) Bursten, B. E.; Cotton, F. A.; Stanley, G. G. Bonding in Metal Atom Cluster Compounds from the d-Orbital Overlap Model to SCF-X α -SW Calculations. *Isr. J. Chem.* **1980**, *19*, 132-142.
- (42) Warneke, J.; Hou, G.-L.; Aprà, E.; Jenne, C.; Yang, Z.; Qin, Z.; Kowalski, K.; Wang, X.-B.; Xantheas, S. S. Electronic Structure and Stability of [B₁₂X₁₂]²⁻ (X= F-At): A Combined Photoelectron Spectroscopic and Theoretical Study. *J. Am. Chem. Soc.* **2017**, *139*, 14749-14756.
- (43) Zhou, X.; Ouyang, Z. Flowing gas in mass spectrometer: method for characterization and impact on ion processing. *Analyst* **2014**, *139*, 5215-5222.
- (44) Gabelica, V.; De Pauw, E. Internal energy and fragmentation of ions produced in electrospray sources. *Mass Spectrom. Rev.* **2005**, *24*, 566-587.
- (45) Gabelica, V.; De, P. E. Comparison of the collision-induced dissociation of duplex DNA at different collision regimes: evidence for a multistep dissociation mechanism. *J. Am. Soc. Mass. Spectrom.* **2002**, *13*, 91-98.
- (46) Warneke, J.; Dülcks, T.; Knapp, C.; Gabel, D. Collision-induced gas-phase reactions of perhalogenated closo-dodecaborate clusters—a comparative study. *Phys. Chem. Chem. Phys.* **2011**, *13*, 5712-5721.

- (47) Farràs, P.; Vankova, N.; Zeonjuk, L. L.; Warneke, J.; Dülcks, T.; Heine, T.; Viñas, C.; Teixidor, F.; Gabel, D. From an Icosahedron to a Plane: Flattening Dodecaiodo-dodecaborate by Successive Stripping of Iodine. *Chem. Eur. J.* **2012**, *18*, 13208-13212.
- (48) Fagiani, M. R.; Zeonjuk, L. L.; Esser, T. K.; Gabel, D.; Heine, T.; Asmis, K. R.; Warneke, J. Opening of an icosahedral boron framework: A combined infrared spectroscopic and computational study. *Chem. Phys. Lett.* **2015**, *625*, 48-52.

APPENDIX I: ANALYTICAL EXPRESSION FOR PREDICTING THE DEPOSITION RING USING ROTATING WALL MASS ANALYZER

Deriving an analytical equation for predicting the radius of the deposition ring using the rotating wall mass analyzer (RWMA):



(Schematic diagram of the setup for ion dispersion using RWMA in a Cartesian coordinate system.)

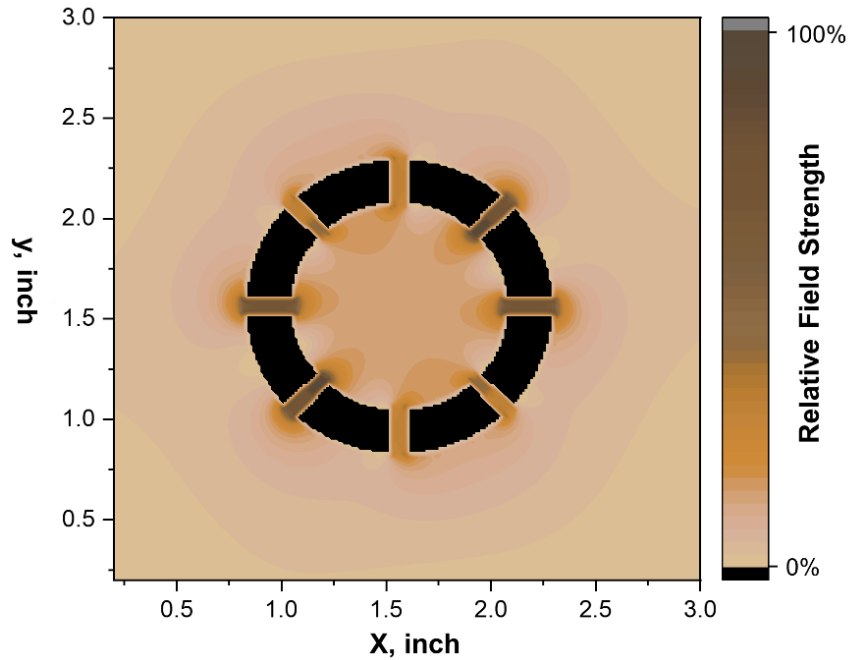
An ion of mass m , charge z , and kinetic energy per charge of E_K enters the RWMA (operating at a frequency f) at the origin denoted as $(0,0,0)$ at time t_0 and moves along the cylinder's central axis (z axis). The ion's travel time through the RWMA is denoted as t_1 . During this time, the ion beam is being radially dispersed in the x - y plane. After exiting the RWMA at a coordinate denoted as (x_1, y_1, z_1) , the ion drifts through the field-free region with the velocity vector it attains at the end of the RWMA (v_x, v_y, v_z) and lands onto a grounded target surface at a coordinate denoted as (x_2, y_2, z_2) . The travel time in the field-free region is denoted as t_2 . The final location of the ion in the x - y plane is determined by the sum of the radial displacement in the RWMA and drift motion in the field-free region (equation 1):

$$x_2 = x_1 + v_x t_2$$

$$y_2 = y_1 + v_y t_2$$

(1)

Previous studies have demonstrated that the rotating electric field is homogeneous in a large area inside the RWMA.¹ We also examined the rotating electric strength using SIMION simulations and constructed a contour plot in the x - y plane to show the spatial distribution of the field strength (Figure below):



Contour plot of the strength of the rotating electric field in the x - y plane. The black region corresponds to the cross section of the RWMA.

Therefore, it is reasonable to assume that the ion experiences the same rotating electric field strength E inside the device when it is dispersed to the off-center locations in the x - y plane. The radial velocity when the ion leaves the RWMA is given by equation 2:

$$v_x(t) = \int a_x(t)dt + c_x = \int \frac{zE}{m} \sin \omega t dt + c_x = -\frac{zE}{m\omega} \cos \omega t + c_x \quad (2)$$

Where $\omega = 2\pi f$. Assuming a parallel beam at the origin (i.e. $v_x(t = t_0) = 0$), we obtain equation 3:

$$c_x = \frac{zE}{m\omega} \cos \omega t_0 \quad (3)$$

Therefore, the velocity components of the ion beam along the x and y axes can be described using equations 4 and 5:

$$v_x(t) = \frac{zE}{m\omega} (\cos \omega t_0 - \cos \omega t) \quad (4)$$

$$v_y(t) = \frac{zE}{m\omega} (\sin \omega t - \sin \omega t_0) \quad (5)$$

The radial displacement inside the RWMA (x_1, y_1) is given by equations 6 and 7:

$$x_1 = \int v_x(t)dt + c'_x = \int \left(-\frac{zE}{m\omega} \cos \omega t + c_x\right)dt + c'_x = -\frac{zE}{m\omega^2} \sin \omega t + \frac{zE}{m\omega} t \cos \omega t_0 + c'_x$$

$$x_1 = \left(-\frac{zE}{m\omega^2} \sin \omega t + \frac{zE}{m\omega} t \cos \omega t_0 + c'_x\right) \Big|_{t_0}^{t_0+t_1} = \frac{zE}{m\omega^2} (\sin \omega t_0 - \sin(\omega t_0 + \omega t_1) + \omega t_1 \cos \omega t_0) \quad (6)$$

$$y_1 = \int v_y(t)dt + c'_y = \int \left(\frac{zE}{m\omega} \sin \omega t + c_y \right) dt + c'_y = -\frac{qE}{m\omega^2} \cos \omega t - \frac{qE}{m\omega} t \sin \omega t_0 + c'_y$$

$$y_1 = \left(-\frac{qE}{m\omega^2} \cos \omega t - \frac{qE}{m\omega} t \sin \omega t_0 + c'_y \right) \Big|_{t_0}^{t_0+t_1} = \frac{zE}{m\omega^2} (\cos \omega t_0 - \cos(\omega t_0 + \omega t_1) - \omega t_1 \sin \omega t_0)$$
(7)

The landing coordinates of the ion (x_2, y_2) are given by equations 8 and 9:

$$x_2 = x_1 + t_2 v_x$$

$$= \frac{zE}{m\omega^2} (\sin \omega t_0 - \sin(\omega t_0 + \omega t_1) + \omega t_1 \cos \omega t_0 + \omega t_2 \cos \omega t_0 - \omega t_2 \cos(\omega t_0 + \omega t_1))$$
(8)

$$y_2 = y_1 + t_2 v_y$$

$$= \frac{zE}{m\omega^2} (\cos \omega t_0 - \cos(\omega t_0 + \omega t_1) - \omega t_1 \sin \omega t_0 - \omega t_2 \sin \omega t_0 + \omega t_2 \sin(\omega t_0 + \omega t_1))$$
(9)

The distance of the landing location from the center of the surface (0, 0) is given by equation 10:

$$R = \sqrt{x_2^2 + y_2^2} = \frac{zE}{m\omega^2} \sqrt{2(1 + \omega^2 t_1 t_2 + \omega^2 t_2^2)(1 - \cos \omega t_1) + \omega t_1(\omega t_1 - 2 \sin \omega t_1)}$$
(10)

t_1 and t_2 are not affected by the rotating electric field and are only determined by the initial kinetic energy E_K , the length of the RWMA (D_1) and the drift region (D_2):

$$t_1 = D_1 \sqrt{\frac{m}{2E_K}}$$

$$t_2 = D_2 \sqrt{\frac{m}{2E_K}} \quad (11)$$

As a result, independent of t_0 , the ion is dispersed to a constant distance from the center of the surface. In other words, independent of the starting phase of the rotating electric field, a continuous ion beam of a specific m/z and E_K will be dispersed onto a ring with a radius R on the surface.

(1) Clemmons, J.; Herrero, F. Mass spectroscopy using a rotating electric field. *Rev. Sci. Instrum.* **1998**, *69*, 2285-2291.

APPENDIX II: STEP-BY-STEP FOR STATISTICAL MODELING OF MULTIPLE WATER ELIMINATION PROCESS OF ISOTOPICALLY-LABELED $[\gamma\text{-CD-W}_6\text{POM}]^{2-}$ COMPLEX

In order to clarify the statistical modeling for the HDX and ^{18}O exchange experiments, we describe herein a stepwise instruction for the simulation we described in the manuscript using CID of deuterium-exchanged $[\gamma\text{-CD-W}_6\text{POM}]^{2-}$ as an example:

Assumptions:

1. “The complex has a similar distribution of hydrogen and deuterium atoms as the $[\gamma\text{-CD} - \text{H}]^-$ detected in the ESI-MS spectrum.”

Based on the observed similar extent of shift in the isotopic envelopes of $[\gamma\text{-CD} - \text{H}]^-$ and $[\gamma\text{-CD-W}_6\text{POM}]^{2-}$, it is reasonable to make this assumption. Despite the fact that HDX is a reversible process and largely affected by the physical and chemical environment, the statistical modeling based on this assumption is adequate enough to simulate the different scenarios we consider in the multiple water loss process.

2. “Loss of a single or multiple water molecules is a random single-step process.”

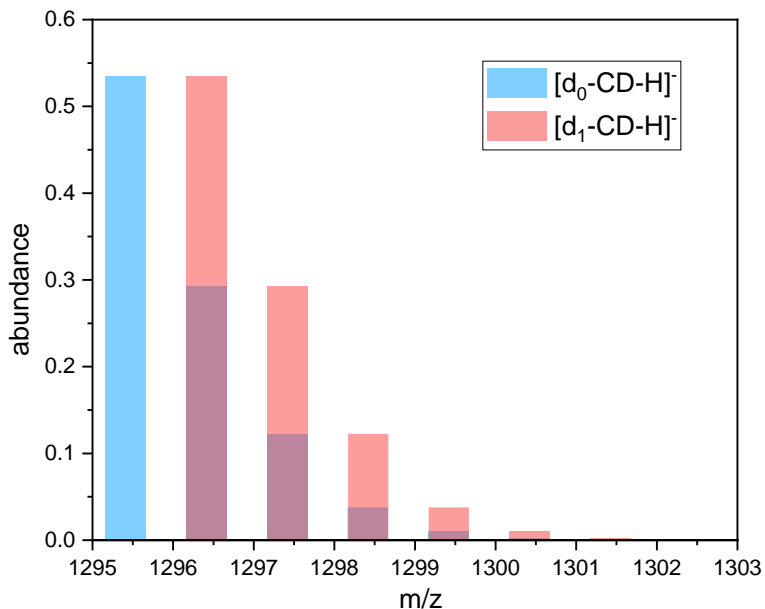
This has been discussed in the manuscript.

Procedures:

1. Determination of deuterium incorporation distribution in the complex.

A portion of the hydrogen atoms on the hydroxyl groups of $\gamma\text{-CD}$ (a total of 24) are replaced by deuterium (D) atoms in the solution. Each $[\text{CD-H}]^-$ ($\text{C}_{48}\text{H}_{79}\text{O}_{40}$) ion generated by electrospray ionization of the solution contains a total of 23 hydroxyl H/D atoms, with the possible incorporation of 0 to 23 D atoms (denoted as $[\text{d}^x\text{-CD-H}]^-$, $x = 0\text{-}23$). As a result, we observe a distribution ranging from $m/z = 1296$ to $m/z = 1320$ corresponding to a combination of all $[\text{d}^x\text{-CD-H}]^-$. $[\text{CD-H}]^-$ without D incorporation has its own isotopic distribution (modeled by “Molecular Weight Calculator” software by Matthew Monroe, Version 6.50). A replacement of one H atom by one D atom will result in $[\text{d}^1\text{-CD-H}]^-$, which demonstrates an isotopic distribution shifted by +1 m/z in comparison with $[\text{d}^0\text{-CD-H}]^-$. As a result, the first isotopic peak of $[\text{d}^1\text{-CD-H}]^-$ overlaps with

the second isotopic peak of $[d^0\text{-CD-H}]^-$ under the resolution of the ion trap (shown below), which increases the complexity of the system.



In order to determine the exact fractional abundances of each $[d^x\text{-CD-H}]^-$, we extract the relative abundances of each peak in the distribution observed in the range of $m/z = 1296$ to $m/z = 1320$ in the experimental spectrum. Each of the peak contains the contribution from several $[d^x\text{-CD-H}]^-$ isotopomers. In order to deconvolute the contribution of each $[d^x\text{-CD-H}]^-$ in the experimental distribution, we carry out a calculation by optimizing the fractional abundances of all possible $[d^x\text{-CD-H}]^-$ ($n=0-23$) until achieving the minimal square deviation from the experimental result using an evolutionary algorithm in Excel Solver. The optimized fractional abundances of $[d^x\text{-CD-H}]^-$ is considered as the deuterium incorporation distribution in $d^x\text{-CD}$ inside the host-guest complex in the following simulations.

2. Reconstruction of isotopic distributions of the complex within the isolation window.

Each of the $[\gamma\text{-CD-W}_6\text{POM}]^{2-}$ complex detected in the gas phase is composed of an $d^x\text{-CD}$ ($x = 0-23$) and an isotopomer of the POM. In the CID experiment, we select an m/z in the ± 0.5 m/z window in the isotopic envelope of the CD-POM complex. We carry out a looped filtering of possible $[d^x\text{-CD} + \text{POM}]$ combinations that fall into the selected isolation window, and store the corresponding original fractional abundance in the entire distribution (this is obtained by multiplication of fractional abundance of $d^x\text{-CD}$ and POM). The filtered combinations of $[d^x\text{-CD}$

+ POM] are thus used to reconstruct the isotopic distribution inside the selected isolation window. The fractional abundance of each [d^x-CD + POM] is obtained by normalization within the isolation window.

3. Generation of isotopic distributions of multiple water loss features by hypergeometric distribution.

In this step, we model the isotopic distributions of n water losses ($n=1-8$) from a [d^x-CD + POM] complex. The incorporation of D atoms in the multiple water loss will shift the sum of mass of water losses (denoted as M). Based on the assumption that different number of water losses are random, one-step, and independent events, it is reasonable to assume that this process behaves statistically and can be rationalized using hypergeometric distribution. We first consider scenario 1 in the HDX section described in the main text that all 24 hydroxyl groups are involved in the multiple water loss. The number of H/D atoms in the pool available for one-step drawing is 24 (N). A total of n water loss ($n = 1-8$) involves a random selection of $2n$ H/D atoms from the pool. Assuming the pool is composed of p D atoms and $(N - p)$ H atoms, the probability of getting k D atoms in a single draw of $2n$ atoms is given by:

$$C(p, k) = \frac{\frac{p!}{k!(p-k)!} \cdot \frac{(N-p)!}{(2n-k)!(N-p-2n+k)!}}{\frac{(N)!}{(2n)!(N-2n)!}} \quad (1)$$

A total of $(2n + 1)$ probabilities can be calculated to generate $(2n + 1)$ sums of mass of water loss ($M = 9n + \frac{k}{2}$). The hypergeometric distribution can also be generated using “hygepdf()” function in MATLAB. We would like to bring up an example to facilitate the understanding. In a [d³-CD + POM] complex, we have 3 D ($p = 3$) and 21 H ($N - p = 21$) available for water loss, when we consider six ($n = 6$) water losses from the complex, a total of 12 ($2n = 12$) H/D atoms will be drawn from the pool ($N = 24$), which results in 13 combinations of masses. The corresponding probabilities and sums of mass of water loss (M) are listed below in the chart:

# of D (k)	# of H ($2n - k$)	Probability	Sum of mass of water loss (M)
0	12	0.109	54
1	11	0.391	54.5
2	10	0.391	55
3	9	0.109	55.5
4	8	0	56
5	7	0	56.5
6	6	0	57
7	5	0	57.5
8	4	0	58
9	3	0	58.5
10	2	0	59
11	1	0	59.5
12	0	0	60

In each case, we calculate the m/z of the water loss signal by subtracting M from the m/z of $[d^x\text{-CD} + \text{POM}]$. The resulting fractional abundance of this water loss peak needs to be multiplied by the fractional abundance of $[d^x\text{-CD} + \text{POM}]$ calculated in step 2 in the reconstructed distribution.

In the scenario of only 16 hydroxyl groups are involved, we first consider a one-step random selection of 16 atoms from a total available number of 24 to generate a new pool. This takes into the consideration that the 16 selected atoms for water loss may be composed of different number of D atoms. This step also follows a hypergeometric distribution with a distribution of 0 to 16 D atom incorporation in the 16 atoms. In this case, 17 combinations of masses will be generated by the hypergeometric distribution (incorporation of 0-16 D atoms in a draw of 16). We stick to the example we use in the last paragraph ($[d^3\text{-CD} + \text{POM}]$ with 3 D and 21 H in the pool). Probabilities of 17 possible new pools are listed:

# of D	# of H	Probability
0	16	0.028
1	15	0.221
2	14	0.474
3	13	0.277
4	12	0
5	11	0
6	10	0
7	9	0
8	8	0
9	7	0
10	6	0
11	5	0
12	4	0
13	3	0
14	2	0
15	1	0
16	0	0

Then we repeat the modeling for n water losses ($n=1-8$) for each of the [d^x-CD + POM] complex in the isolation window using the hypergeometric distribution explained at the beginning of step 3. We note that 1) the total number of atoms in the new pool is 16 ($N = 16$); 2) the resulting probability distribution needs to be multiplied by the probability of the new pool.

4. Construction of simulated mass spectrum.

A list of m/z of the water loss signals and their corresponding fractional abundances will be generated after step 3. This is in principle a mass spectrum. This mass list can be reconstructed to simulate a mass spectrum acquired on an arbitrary mass spectrometer (of different resolutions). This can be achieved by defining different m/z bin width to combine nearby signals. We note that only the location and distribution of each water loss feature can be compared to the experimental

result. The statistical model we use herein does not consider the probability of the number of multiple water loss, since it is directly related to the reaction mechanism statistically irrelevant.

In Situ Infrared Spectroelectrochemistry for Understanding Structural Transformations of Precisely Defined Ions at Electrochemical Interfaces

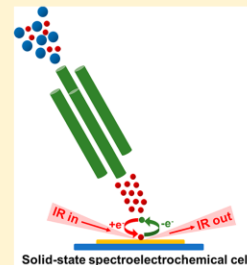
Pei Su,[†] Venkateshkumar Prabhakaran,[‡] Grant E. Johnson,[‡] and Julia Laskin^{*,†}

[†]Department of Chemistry, Purdue University, 560 Oval Drive, West Lafayette, Indiana 47907, United States

[‡]Pacific Northwest National Laboratory, P.O. Box 999, Richland, Washington 99352, United States

Supporting Information

ABSTRACT: Understanding the intrinsic properties of electroactive species at electrode–electrolyte interfaces (EEl) is essential to the rational design of high-performance solid-state energy conversion and storage systems. In situ spectroscopy combined with cyclic voltammetry (CV) provides insights into structural changes of electroactive species at functioning EEl. Ion soft landing enables precisely controlled deposition of mass- and charge-selected ions onto electrode surfaces thereby avoiding the contamination inherent with conventional electrode preparation techniques. In this contribution, we describe a new approach for the simultaneous electrochemical and spectroscopic characterization of soft-landed ions at operating solid-state EEl. The technique exploits a specially fabricated three-electrode cell that is compatible with in situ infrared reflection absorption spectroscopy (IRRAS) characterization of the soft-landed ions. Keggin polyoxometalate (POM) anions, $\text{PW}_{12}\text{O}_{40}^{3-}$, were selected as a model system for these experiments due to their multielectron redox activity, structural stability, and well-characterized IRRAS spectrum. In situ CV measurements indicated continuous multielectron transfer processes of the soft-landed $\text{PW}_{12}\text{O}_{40}^{3-}$ anions over a large potential range of -2.1 to -0.3 V. A distinct shift in the wavenumber of the terminal $\text{W}=\text{O}_t$ stretching vibration in the IRRAS spectra was observed during the multielectron reduction process. The results demonstrate the capabilities of the in situ spectroelectrochemical approach for examining structural changes of well-defined electroactive species during electron-transfer processes at operating solid-state EEl.



Electrode–electrolyte interfaces (EEl) play a central role in electrochemical processes and energy technology.¹ The performance of electrochemical systems is strongly affected by the kinetics and mechanisms of electron transfer as well as degradation processes occurring at EEl. Understanding the structural changes of electroactive species during electrochemical processes is critically important to the development of tailored EEl with desired properties.² Several in situ and operando characterization approaches have been developed to obtain a better understanding of the complex processes occurring at operating EEl. Nuclear magnetic resonance (NMR) spectroscopy,³ second-harmonic generation (SHG),⁴ vibrational spectroscopy,⁵ and X-ray photoelectron spectroscopy (XPS),^{6,7} have traditionally been used for in situ characterization of EEl. Infrared (IR) spectroelectrochemistry has been developed for in situ probing of processes at solid–liquid interfaces.^{8,9} This approach enables structural characterization of electroactive species during electrochemical cycling. In particular, infrared reflection absorption spectroscopy (IRRAS) has been widely used in spectroelectrochemistry experiments to study redox-active organic pigments, ionic liquids, and transition metal clusters.^{10–13} Most of the in situ approaches to studying solid–liquid EEl rely on specially fabricated liquid electrochemical cells.^{14,15} Despite substantial

progress in this field, in situ characterization of solid-state EEl remains challenging.

In a recent publication, we reported the development of a new in situ thin-film electrochemical cell for characterizing the activity of electroactive species at solid-state EEl both under vacuum conditions and controlled partial pressures of reactive gases.¹⁶ The electrochemical cell was fabricated on a screen-printed electrode (SPE) using carefully designed nanoporous ionic liquid (IL) membranes. This cell mimics many state-of-the-art solid-state electrochemical devices used for energy conversion and storage.¹⁷ The electroactive species were deposited onto the cell using ion soft landing,^{18–25} which enables precise control over the composition and charge state of the ions along with their kinetic energy and coverage. In this study, we expand this approach to enable in situ structural characterization of well-defined electroactive species at solid-state EEl using IRRAS during electrochemical cycling. Soft landing has been used previously for preparation of electrode surfaces with superior specific capacitance and electrochemical stability.²⁶ The ability to prepare electrochemical interfaces

Received: May 31, 2018

Accepted: August 22, 2018

Published: August 22, 2018

containing well-defined electroactive species makes ion soft landing a powerful approach for obtaining a fundamental understanding of interfacial processes and characterization of the intrinsic properties of ions at EEs.

Proof-of-principle experiments were performed using well-characterized stable Keggin polyoxometalate (POM) anions with unique multielectron redox activity as a model system.²⁷ The ability to accommodate 24 electrons (e^-) with retention of structural integrity was reported previously for $\text{PMo}_{12}\text{O}_{40}^{3-}$, making this and related POM anions promising candidates for use in rechargeable batteries,²⁸ water electrolyzers,²⁹ electrocatalysts,³⁰ and molecular supercapacitors.³¹ In this study, we selected tungsten POM (WPOM) anions ($\text{PW}_{12}\text{O}_{40}^{3-}$) as a model system due to their established structural stability³² and well-defined IRRAS bands.³³ The stability and rigidity of WPOM makes it resilient toward structural transformations during redox processes.^{34,35} Our previous work employed IRRAS to understand charge retention by WPOM anions soft-landed onto self-assembled monolayer (SAM) surfaces.³³ We demonstrated that the position of the terminal $\text{W}=\text{O}_t$ band shifts systematically with the charge state of the anion.³³ Herein, we examined, for the first time, structures of WPOM anions at operating EEs. We observed that the WPOM cage undergoes reversible structural changes during redox cycling. Although during the reduction process the WPOM cage preserves its structural integrity without substantial expansion, the $\text{W}=\text{O}_t$ band shows a systematic shift to lower wavenumbers. This shift facilitates the identification of different charge states of WPOM that are present at the interface at different stages of the oxidation/reduction cycle. These results establish a powerful methodology of using an in situ spectroelectrochemical cell combined with ion soft landing for studying structural transformations of well-defined electroactive ions at operating solid-state EEs.

EXPERIMENTAL SECTION

Sodium phosphotungstate tribasic hydrate ($\text{Na}_3[\text{PW}_{12}\text{O}_{40}] \cdot x\text{H}_2\text{O}$), 1-ethyl-3-methylimidazolium tetrafluoroborate (EMIMBF₄), poly(vinylidene fluoride-co-hexafluoropropylene) (PVDF-HFP), and anhydrous *N,N*-dimethylformamide (DMF) were all purchased from Sigma-Aldrich (St. Louis, MO) and used as received. The 10 mm \times 10 mm gold-coated silicon wafers (100 nm Au layer and 5 nm Ti adhesion layer) were purchased from Platypus Technologies (Madison, WI).

The three-electrode IR spectroelectrochemical cell shown in Figure 1 was fabricated using the following procedure: A gold substrate was used as the working electrode (WE). The gold-coated substrate was ultrasonically washed in methanol, placed in an ultraviolet cleaner (Boekel Scientific, Feasterville, PA) for 20 min, transferred onto a specially designed poly(ether ether ketone) (PEEK) cell holder with a 11 \times 11 mm² recessed square groove, and affixed to the holder using two stainless steel clamps. A Pt counter electrode (CE) and Ag pseudoreference electrode (RE) were wired around the edges of the WE (Figure 1). The Pt and Ag wires were purchased from Alfa Aesar (Tewksbury, MA).

An aprotic electrolyte cell membrane containing EMIMBF₄ ionic liquid (IL) and PVDF-HFP copolymer was prepared using the following steps: 2 g of PVDF-HFP was dissolved in 13 mL of anhydrous DMF and stirred overnight at room temperature to make a homogeneous solution. An amount of 2 mL of EMIMBF₄ was subsequently added to the solution, and the mixture was continuously stirred for 4 h and stored in a N_2 -purged glovebox. The cell membrane was prepared by carefully

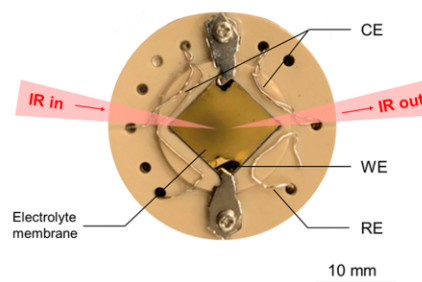


Figure 1. Photographic image of the three-electrode cell assembly and schematic drawing of the IR light beam used for IRRAS measurements. WE = working electrode, CE = counter electrode, RE = reference electrode. The electrolyte membrane covers all three electrodes.

and evenly casting approximately 20 μL of the solution onto the entire three-electrode assembly and slowly drying the resulting liquid layer in a vacuum oven (Sheldon Manufacturing, Cornelius, OR) at room temperature for 24 h to remove DMF and trace amounts of water.

Soft-landing experiments were performed using a specially designed high-flux ion deposition instrument described in detail elsewhere.³⁶ The in situ spectroelectrochemical cell was mounted on a linear translator and introduced into the vacuum system. The cell holder was equipped with a three-pin connector wired to an electrical vacuum feedthrough providing electrical connections from the WE, CE, and RE to a potentiostat (Versastat 3, Princeton Applied Research). Ions were produced by negative mode electrospray ionization (ESI) of a 150 μM solution of $\text{Na}_3[\text{PW}_{12}\text{O}_{40}] \cdot x\text{H}_2\text{O}$ in methanol. Solvent droplets containing WPOM were produced by applying a -2.5 kV potential to the ESI emitter and introduced into the vacuum system through a heated (150 $^\circ\text{C}$) stainless-steel inlet to promote desolvation. Ions were subsequently transferred into vacuum by a dual ion funnel system,³⁶ mass-selected using a quadrupole mass filter (Extrel Pittsburgh, PA), and deposited onto the WE area of the electrochemical cell at a kinetic energy of 30–35 eV per charge. The ion current was measured at the WE by the potentiostat in zero-resistance ammeter mode. A typical ion current of -6.5 nA was achieved for mass-selected deposition of $\text{PW}_{12}\text{O}_{40}^{3-}$ ions onto the electrochemical cell. The total number of deposited ions was calculated by integrating the ion current over time.

Prior to soft landing of WPOM, electrochemical impedance spectroscopy (EIS) measurements were conducted to examine the different interfacial regions of the electrochemical cell maintained in vacuum. EIS was performed by applying a sinusoidal perturbation with an amplitude of 10 mV and frequency in the range of 100 kHz to 1 Hz. Cyclic voltammetry (CV) measurements were carried out before and after soft landing of WPOM using the potentiostat. The CVs were acquired at scan rates of 0.5 mV s^{-1} in the range of 0.3 to -2.1 V in triplicates after 3×10^{15} $\text{PW}_{12}\text{O}_{40}^{3-}$ (WPOM) ions were soft-landed onto the cell.

The spectroscopic performance of the cell was optimized for IRRAS experiments by adjusting the position of the cell to maximize the signal amplitude. Grazing-incidence IRRAS experiments were performed using a Bruker Vertex 70 FT-IR spectrometer (Bruker Optics, Billerica, MA) equipped with a liquid nitrogen cooled mercury-cadmium-telluride (MCT)

detector. The experimental details have been explained elsewhere.³⁷ IRRAS spectra were acquired at different potentials applied to the WE at a spectral resolution of 4 cm^{-1} using p-polarized light. Each spectrum was collected by averaging 5000 scans corresponding to a 20 min acquisition time. Fitting of the IRRAS spectra was carried out in Excel using a sum of several Lorentzian distributions with peak positions in the range between 1000 and 800 cm^{-1} . The experimental IRRAS plots were baseline-corrected in an interactive mode. The peak positions were first defined, and all the peak widths were constrained at a value of 12 cm^{-1} . The peak intensities and widths were optimized by minimizing the sum of squares of deviations between the experimental and simulated data points to obtain the best-fit curves.

RESULTS AND DISCUSSION

In this study, we developed a solid-state thin-film electrochemical cell that enables in situ IRRAS characterization of energized electrochemical interfaces prepared using soft landing of mass- and charge-selected electroactive ions. A photographic image of the cell and a schematic drawing of the IR light beam are shown in Figure 1. The three-electrode assembly is mounted on a specially designed PEEK holder. We evaluated several cell designs to explore the effect of the electrode configuration and membrane preparation on cell performance. A bare gold surface ($10\text{ mm} \times 10\text{ mm}$) was used as a working electrode (WE). Gold is a suitable substrate for spectroelectrochemical measurements since it forms a nearly ideal electrical double layer and has a high conductivity and optical reflectivity.³⁸ The WE was mounted in the middle of the PEEK holder. The counter and reference electrodes were wired as close to the WE as possible without direct electrical contact. A Pt wire used as the CE was coiled in loops close to three edges of the gold substrate to maximize the area of the CE. A silver wire used as a pseudo RE was positioned next to the fourth edge of the gold surface. To accommodate the small incidence angle of the incoming IR beam while keeping the three electrodes at a similar height, a shallow square groove was machined in the PEEK holder for the WE. A nanoporous electrolyte membrane was prepared by casting a solution composed of a conductive copolymer and EMIMBF₄ IL on top of the three-electrode assembly and allowing it to dry under vacuum. We have previously shown that such electrolyte membranes are stable both in vacuum and under controlled partial pressures of gases.¹⁶ In order to improve the IRRAS sensitivity, the electrolyte membrane thickness was minimized by using the least amount possible ($20\text{ }\mu\text{L}$) of the IL cast solution. The solution composition was optimized to enable the fabrication of the IL membrane that covered all of the electrode surfaces with physical continuity. The thickness of the membrane is estimated to be around $10\text{ }\mu\text{m}$ based on the volume of the copolymer and IL. The uniformity of the membrane on the WE helps improve the spectroscopic response by eliminating multiple reflections of the IR beam from the membrane surface. Preparation of the optimized membrane involved casting of the solution in the center of the WE and allowing it to expand and stabilize by itself. This process is largely determined by the viscosity of the solution. Casting of lower-viscosity solutions containing a higher molar ratio of IL resulted in rapid expansion of the droplet on the surface and formation of a nonuniform membrane. Slow spreading of viscous solutions prepared using higher molar ratios of copolymer made it difficult to prepare a thin membrane. In addition, the wettability of the surface by the IL solution may

affect the quality of the membrane. For example, the IL solution used in this study could not form a good-quality film on a hydrophobic surface.

Prior to voltammetry characterization, the different interfacial regions of the cell were evaluated using EIS measurements in vacuum. The experimental EIS data were fitted using the EIS Spectrum Analyzer software and the equivalent circuit model presented in Figure 2a.³⁹ In this model, the impedance of the

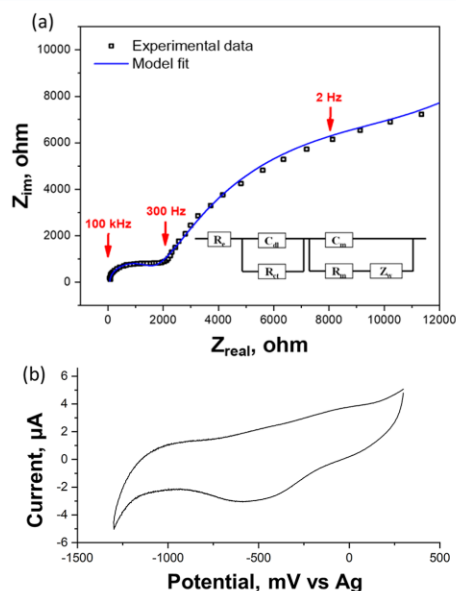


Figure 2. (a) Nyquist plot obtained from the potentiostatic EIS of the in situ spectroelectrochemical cell (frequency range, 100 kHz to 1 Hz; amplitude, 10 mV). Inset: the equivalent circuit model used to fit the EIS data: R_e , electrolyte resistance; R_{ct} , charge-transfer resistance; C_{dl} , double layer capacitance; R_m , porous membrane resistance; C_m , double layer capacitance derived at porous membrane; Z_w , Warburg impedance. (b) CV of the blank spectroelectrochemical cell before soft-landing experiments acquired at a scan rate of 50 mV s^{-1} .

Au/IL interface and the pores in the IL membrane are considered as separate elements. The experimental Nyquist plot and the best fit obtained using the equivalent circuit are shown in Figure 2a. The presence of a semicircle in the high-frequency range (100 kHz to 300 Hz) is attributed to the charge-transfer kinetics due to polarization of the WE and indicates the formation of a well-defined double layer at the Au/IL interface. The EIS model shows that the impedance of this range of frequencies is a combination of the electrolyte resistance ($R_e = 64\text{ }\Omega$), charge-transfer resistance ($R_{ct} = 5000\text{ }\Omega$), and double layer capacitance ($C_{dl} = 5.8 \times 10^{-6}\text{ F}$). The frequency range between 300 and 2 Hz is attributed to the diffusion-controlled polarization through the IL layers on the WE. The impedance of this region consists of the resistance of the porous membrane ($R_m = 1430\text{ }\Omega$), double layer capacitance at the porous membrane ($C_m = 3.7 \times 10^{-8}\text{ F}$), and Warburg impedance ($Z_w = 2 \times 10^4\text{ }\Omega\text{-s}^{-0.5}$), which arises from the limited adsorption of ionic species at the WE. Overall, the EIS analysis showed that the

presence of a characteristic diffusion-controlled region in the cell corresponds to compact double layer structure. This type of interface is representative of technologically relevant solid-state EEIs, in which the limited diffusion of ions in the porous electrolyte results in additional diffusional resistance.^{40–42} Following the EIS experiments, CV measurements were performed for several cycles prior to ion deposition (Figure 2b) and showed the interface to be very stable.

An in situ CV study of the soft-landed WPOM was performed in vacuum after deposition of 3×10^{15} ions onto the WE of the cell. A typical CV plot obtained for the soft-landed $\text{PW}_{12}\text{O}_{40}^{3-}$ anions at a scan rate of 0.5 mV s^{-1} is shown in Figure 3.

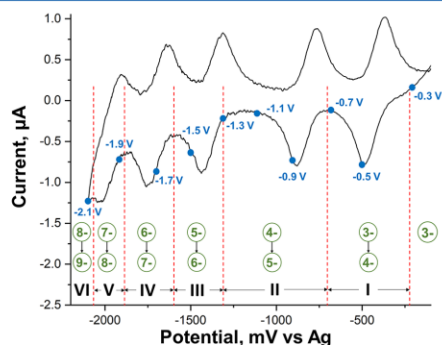


Figure 3. In situ CV of soft-landed $\text{PW}_{12}\text{O}_{40}^{3-}$ anions in the potential range between -2.1 and -0.1 V. CV measurements were performed after 3×10^{15} ions were deposited onto the cell. Scan rate: 0.5 mV s^{-1} . The reduction portion of the CV curve showing potential regions outlined with red dashed lines and labeled with numbers on top along with key electron-transfer processes examined spectroelectrochemically. The potentials used in the IRRAS measurements are marked with blue dots on the CV curve.

Consistent with previous studies,^{35,43} five pairs of oxidation/reduction peaks corresponding to multielectron transfer processes were observed in the potential range between -2100 and -100 mV. The reduction and reoxidation peak potentials ($E_{p,\text{red}}$ and $E_{p,\text{ox}}$) and the number of electrons transferred in each process (n) are listed in Table S1. We observe quasi-reversible behavior of the WPOM anions in terms of electrochemical performance, which is attributed to the relatively slow diffusion of the ions in the electrolyte membrane. All of the redox peaks show one-electron-transfer behavior. Thus, the major electrochemical reactions taking place at EEIs in the different potential regions may be attributed to a stepwise conversion of WPOM anions from one charge state to the next as shown in Figure 3. To facilitate the discussion, we split the reduction potential range into six regions (I–VI) each containing a single reduction peak (Figure 3). In each of the potential regions, reduced WPOM species are produced through conversion of the lower charge state of WPOM present at EEI.

Previous electrochemical and spectroscopic studies have demonstrated the exceptional “electron sponge”-like behavior of Keggin POM anions.^{27,28,31} According to density functional theory (DFT) calculations, $\text{PMo}_{12}\text{O}_{40}^{3-}$ can accommodate up to 24 electrons to produce a super-reduced $\text{PMo}_{12}\text{O}_{40}^{27-}$ anion.³¹ DFT calculations also indicate that similar molecular

and electronic structural changes to $\text{PMo}_{12}\text{O}_{40}^{3-}$ can be expected for $\text{PW}_{12}\text{O}_{40}^{3-}$ in the reduction process.³¹ The structural evolution of reduced POM anions was observed previously using operando Mo K edge extended X-ray absorption fine structure (XAFS) analysis of a MoPOM molecular cluster battery.²⁷ During the reduction process, the terminal Mo=O bonds are converted into single Mo–O bonds. Meanwhile, the size of the anion does not change to a large extent until the Mo–Mo bonds start to form following the transfer of more than 13 electrons. The WPOM anions examined in this study are structurally more rigid than MoPOM anions.³⁴ Gas-phase studies also indicate that WPOM anions undergo dissociation at higher internal energies than MoPOM.³² Thus, changes in different types of W–O bond lengths are expected to be less pronounced in WPOM compared with MoPOM. However, WPOM anions produce better-quality IRRAS spectra in comparison to MoPOM with narrower and more intense absorption bands corresponding to P–O and W–O bonds.⁴⁴ Furthermore, we have previously shown similar trends in the positions of terminal Mo=O_i and W=O_i bands as a function of the charge state of the POM anion.³³ Herein, we used IRRAS for in situ characterization of structural transitions in WPOM anions during reduction/oxidation processes at different potentials applied to the WE.

In situ IRRAS spectra acquired at different ion coverages during the WPOM deposition are shown in Figure S1. These spectra were obtained using the cell without WPOM as a background. Several bands in the range between 3000 and 1200 cm^{-1} , which increase in intensity during the deposition process, are observed at wavenumbers corresponding to EMIMBF₄ vibrational bands reported in the literature³⁸ and attributed to structural changes in the electrolyte membrane resulting from ion soft landing (Figure S1) and electrochemical cycling (Figure S2).^{36,45} Detailed assignment of these bands is outside of the scope of this paper. In addition, WPOM bands in the range between 1100 and 800 cm^{-1} are clearly visible at higher ion coverages, which confirms that the soft-landed WPOM anions are successfully deposited onto the WE.

Another background IRRAS spectrum was acquired at the end of the ion deposition and prior to the in situ IR spectroelectrochemical experiments. The IRRAS baseline was collected with 0.3 V applied to the WE because no electron-transfer process was observed at this potential, indicating that $\text{PW}_{12}\text{O}_{40}^{3-}$ ions are the dominant electroactive species at the EEI. Using this background spectrum, IR bands affected by the potentials applied to the WE of the in situ cell were observed with high sensitivity and without substantial interference from other bands. To examine structural changes of WPOM anions during the oxidation/reduction reactions at EEI, in situ IRRAS spectra were acquired at different potentials marked with blue dots in Figure 3. In these experiments, the cell was held at different potentials that were varied stepwise from -0.3 to -2.1 V in intervals of 0.2 V. At each WE potential, the cell was allowed to equilibrate for 10 min and the cell current was observed to stabilize at its minimum value (Figure S3), which ensures the equilibrium state of the EEI during the IRRAS measurements at each potential.

IRRAS spectra acquired at different potentials during the reduction and oxidation processes are presented in Figure 4, parts c and d, respectively. Full-range IRRAS spectra obtained during the reduction process are shown in Figure S2. A spectrum of soft-landed $\text{PW}_{12}\text{O}_{40}^{3-}$ on a bare gold surface is shown in Figure 4a for comparison. A spectrum acquired at -2.1 V is

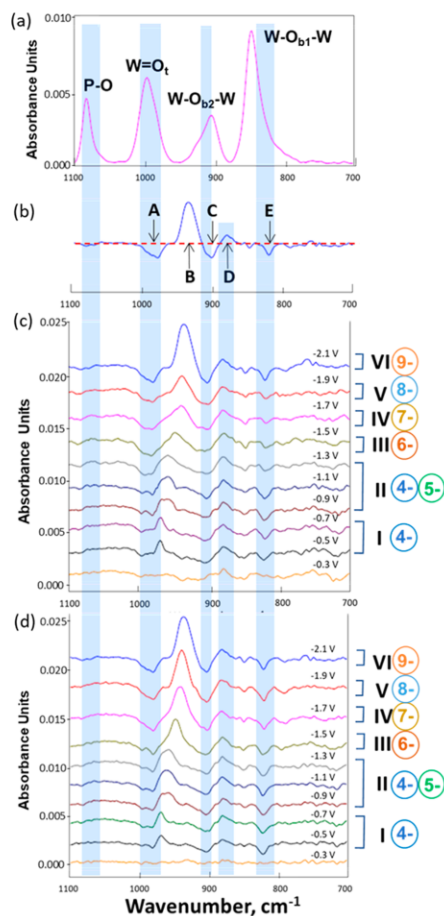


Figure 4. (a) In situ IRRAS spectrum of WPOM anions soft-landed on a bare gold surface. (b) Representative IRRAS spectrum acquired at -2.1 V shown to illustrate new features that appear during the spectroelectrochemical measurements. The red dashed line indicates the IR baseline. In situ IRRAS spectra obtained at different potentials during the (c) reduction and (d) oxidation processes of WPOM. The potential regions I–VI and the corresponding charge states of the reduced WPOM species are marked on the right.

shown separately in Figure 4b to illustrate the IR features discussed in detail in the following paragraphs. Specifically, band A corresponds to a broad negative feature at 980 cm^{-1} ; band B refers to the positive feature at 969 cm^{-1} . The negative band at 904 cm^{-1} , positive band at 880 cm^{-1} , and negative band at 820 cm^{-1} are referred to as bands C, D, and E, respectively. During the reduction process, no obvious changes in the IRRAS spectra were detected at potentials more positive than -0.3 V applied to the WE. As a result, the spectrum obtained at -0.3 V is indistinguishable from the background spectrum. However, several positive and negative bands appeared at -0.5 V, and their positions and intensities continued to evolve at more negative

potentials. Specifically, band A appeared at -0.5 V and continued growing in intensity at more negative potentials. Band B appeared at -0.5 V, became broader and shifted toward lower wavenumbers in region II, and continued growing in abundance and shifting toward lower wavenumbers in regions III–VI. Bands C, D, and E appeared at -0.5 V and showed only a slight change in abundance over the entire range of potentials. The observed trend is reversible as indicated by the intensities and positions of the bands observed during the oxidation process, in which the WE potential was increased from -2.1 to -0.3 V.

Comparison of the IRRAS spectra obtained at different potentials with the spectrum of $\text{PW}_{12}\text{O}_{40}^{3-}$ on neutral gold indicates that the observed bands may be attributed to structural changes occurring in WPOM anions at the energized EEI. The positive peaks in the IR spectra in parts c and d of Figure 4 can be interpreted as emerging features of the reduced WPOM anions, while the negative peaks correspond to absorption bands of $\text{PW}_{12}\text{O}_{40}^{3-}$, which was originally present at the EEI and becomes depleted with reduction. These bands disappear as the 3-anions are reduced and are observed as negative signals relative to the $\text{PW}_{12}\text{O}_{40}^{3-}$ background.

IR bands of WPOM were assigned based on our previous study of soft-landed $\text{PW}_{12}\text{O}_{40}^{3-}$ anions³³ and are compared with both the experimental IR spectrum of phosphotungstic acid¹⁶ and the calculated vibrational bands of isolated $\text{PW}_{12}\text{O}_{40}^{3-}$ in the gas phase.^{33,47} Specifically, the bands at 990 and 1083 cm^{-1} are assigned to the terminal $\text{W}=\text{O}_t$ stretching vibration and asymmetric coupling of P–O and $\text{W}=\text{O}_t$ stretching modes (shown as P–O in Figure 4a), respectively. Meanwhile the two bands at 900 and 835 cm^{-1} are assigned to the vibrational stretching of two types of bridging oxygen atoms, $\text{W}-\text{O}_{b2}-\text{W}$ and $\text{W}-\text{O}_{b1}-\text{W}$, respectively. The P–O and $\text{W}=\text{O}_t$ symmetric coupling motion appears to be a shoulder on the $\text{W}=\text{O}_t$ stretching band at lower wavenumbers (961 cm^{-1}). We note that band positions may be shifted in the spectroelectrochemistry experiments described in this study in comparison with gas-phase literature values due to interactions of WPOM anions with electrolyte ions (IL ions) at the interface.

IRRAS spectra obtained using soft-landed $\text{PW}_{12}\text{O}_{40}^{3-}$ as a background (Figure 4, parts c and d) do not contain a peak around 1083 cm^{-1} , indicating that the P–O band is not affected by the redox processes. Bands A (negative) and B (positive) may be attributed to changes in the $\text{W}=\text{O}_t$ vibration. Changes in the position and intensity of these bands will be discussed in detail later. Bands C, D, and E may be attributed to the evolution of the $\text{W}-\text{O}_{b2}-\text{W}$ and $\text{W}-\text{O}_{b1}-\text{W}$ bridging bands at different potentials. Specifically, bands C and E may be attributed to either the disappearance or shift in position of the $\text{W}-\text{O}_{b2}-\text{W}$ and $\text{W}-\text{O}_{b1}-\text{W}$ bands, respectively. Although an intense $\text{W}-\text{O}_{b1}-\text{W}$ bridging band at 835 cm^{-1} is present in the IRRAS spectrum of WPOM soft-landed onto a bare gold surface (Figure 4a), the abundance of band E is low, indicating that the $\text{W}-\text{O}_{b1}-\text{W}$ bridging mode does not undergo substantial changes during the reduction process. In contrast, similar intensities of bands C (positive) and D (negative) may be ascribed to the same vibrational mode, which is shifted toward lower wavenumbers (from 904 to 880 cm^{-1}) during the redox process. We propose that the observed change may be attributed to an elongation of the $\text{W}-\text{O}_{b2}-\text{W}$ bridging band with WPOM reduction, which is consistent with the literature XAFS studies described earlier.²⁷ Both bridging band peaks appear after the first reduction step, and their positions do not change

substantially over the entire potential range. This observation indicates that, after the initial structural change at -0.5 V, the bridging bands do not change substantially when WPOM accepts additional electrons. This is in agreement with the slight elongation of the bridging bands and relatively small change in reduced POM cage size indicated by previous XAFS and DFT studies.^{27,31}

In contrast to the bridging bands, the intensity and position of the $W=O_t$ band is strongly affected by the redox processes. Band A that appears at -0.5 V and increases in intensity at more negative potentials is assigned as $W=O_t$ vibrations of the soft-landed $PW_{12}O_{40}^{3-}$ anions. The gradual increase in the intensity of band A over the entire reduction potential range indicates an incomplete initial conversion of the soft-landed $WPOM^{3-}$ resulting in the observed reduction of this ion at more negative potentials. The number of WPOM reduced at the surface is limited by the migration of ions in the diffuse layer. The soft-landed $PW_{12}O_{40}^{3-}$ are distributed throughout the bulk of the electrolyte membrane, which limits the rate of their transport to the electrode surface. Reduction of the remaining $PW_{12}O_{40}^{3-}$ anions is most likely driven by the increased potential-controlled migration of ions at more negative overpotentials and contributes to the observed gradual increase in band A.

In addition, we observed pronounced and reversible changes in both peak positions and intensities of band B in the wavenumber range between 969 and 935 cm^{-1} during the reduction/oxidation process. According to the XAFS experiments cited earlier,²⁷ as the cluster is reduced to more negative charge states, the terminal $W=O_t$ bond gradually loses its double-bond character and is converted into a single bond. The observed shift in the position of the $W=O_t$ band toward lower wavenumbers in our IRRAS spectra is consistent with this previous assertion. We hypothesized that the formation of different charge states of WPOM at different potentials applied to the WE is responsible for the observed change in both the position and intensity of the $W=O_t$ peak in the wavenumber range between 969 and 935 cm^{-1} .

To test this hypothesis, we fitted the IR spectra obtained at potentials ranging from -0.5 to -2.1 V in the reduction process. The spectra were simulated using a sum of several Lorentzian distributions with peak positions in the range between 1000 and 800 cm^{-1} , as described in detail in the Experimental Section. Spectra obtained from the best fit of the IRRAS data during the reduction process are shown in Figure 5a. A comparison of the experimental and simulated IRRAS spectra at each reduction potential is shown in Figure S4. We observed moderate changes in the intensities of the bridging bands, indicating that they do not undergo substantial evolution during the reduction process. In addition, curve fitting provides insights into changes in the $W=O_t$ band in the different potential regions observed experimentally. The shape of the $W=O_t$ band was adequately reproduced using a sum of two negative peaks at 997 and 980 cm^{-1} and two positive bands: one at 969 cm^{-1} has a fixed position over the entire potential range, while another one shifts toward lower wavenumbers (red shifts) from 958 to 935 cm^{-1} with increasing WPOM reduction. The intensities of the two positive and negative bands as a function of the applied potential obtained from curve fitting are shown in Figure 5, parts b and c. In region I, we observe one positive growing feature at 969 cm^{-1} . Because the spectra were acquired with $PW_{12}O_{40}^{3-}$ as a background, we propose that this peak corresponds to the $W=O_t$ band of $PW_{12}O_{40}^{4-}$. This peak gradually decreases in region II and disappears at more negative potentials. We

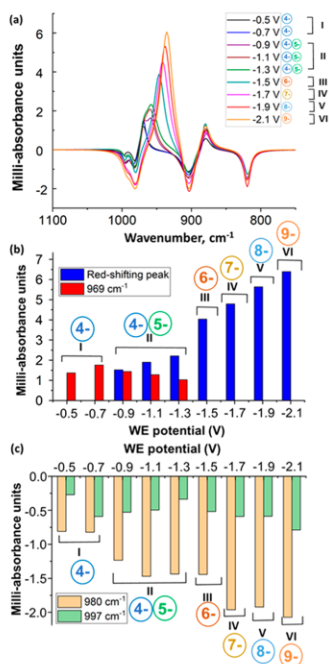


Figure 5. (a) Fitted IR spectra obtained during the reduction process in the wavenumber range between 1000 and 800 cm^{-1} . Bar graphs showing the intensities of the positive (b) and negative (c) bands in the $W=O_t$ region obtained from curve fitting as a function of the potential applied to the WE. The potential regions (I–VI) and charge states of the reduced WPOM at each potential are marked to facilitate understanding.

attribute the presence of this band in region II to the incomplete conversion of $PW_{12}O_{40}^{4-}$ into $PW_{12}O_{40}^{5-}$. Another peak appears in region II at 958 cm^{-1} , which subsequently grows in intensity and shifts to 947 cm^{-1} (region III), 942 cm^{-1} (region IV), 938 cm^{-1} (region V), and 935 cm^{-1} (region VI). We propose that this red-shifting peak corresponds to $PW_{12}O_{40}^{5-}$, $PW_{12}O_{40}^{6-}$, $PW_{12}O_{40}^{7-}$, $PW_{12}O_{40}^{8-}$, and $PW_{12}O_{40}^{9-}$ in regions II, III, IV, V, and VI, respectively (summarized in Table S2). The shift in the position of this peak is attributed to elongation of the $W=O_t$ bond as it converts from a double bond to a more single-like bond with increasing reduction of WPOM. The negative peak at 980 cm^{-1} grows in intensity in regions I–IV, while the negative peak at 997 cm^{-1} does not show a clear trend with the increase in the applied potential. The origin of the 997 cm^{-1} band cannot be determined based on our current results. However, the evolution of the 980 cm^{-1} feature is consistent with our assignment of this band to the $PW_{12}O_{40}^{3-}$ species. As discussed earlier, the increase in abundance of the peak at 980 cm^{-1} during the reduction process is attributed to the incomplete conversion of $PW_{12}O_{40}^{3-}$.

In summary, the observed changes in the IRRAS spectra of WPOM during the redox process may be attributed to the presence of the different charge states at the interface. We observed an incomplete conversion of WPOM anions in the first two reduction steps. At more negative potentials, the conversion

efficiency is challenging to estimate because of the substantial increase in the abundance of the W=O₂ band that obscures the lower charge states potentially present at the interface. The incomplete conversion is attributed to potential-controlled migration of ions at more negative overpotentials. These results demonstrate that minor structural changes in the reduced WPOM anions may be observed using the spectroelectrochemical approach developed in this study in combination with precise control of the electroactive species prepared by soft landing of mass- and charge-selected ion onto a specially designed electrochemical cell.

CONCLUSION

The in situ IR spectroelectrochemical technique developed in this study enables structural characterization of well-defined electroactive species prepared by soft landing of mass- and charge-selected ions. Proof-of-principle experiments were conducted using a structurally robust WPOM anion as a representative model system. Substantial shifts in band intensities and positions were observed by in situ IRRAS measurements at different reduction stages, indicating the utility of this approach for observing small structural changes in redox-active species at operating solid-state EEs. The thin-film solid-state electrochemical cell developed in this study is well-suited for characterizing structural transitions at technologically relevant operating EEs that are of interest to the development of robust and efficient electrochemical interfaces for functional devices. A combination of ion soft landing with the in situ IR spectroelectrochemical technique offers a unique platform to understand structural transformation during redox processes of mass-selected anions or cations and molecular fragments produced by in-source collision-induced dissociation which are difficult to synthesize and stabilize in solution-phase chemistry.^{16,32,48} In principle, the platform developed in this work can be coupled with a mass-selected nanoparticle deposition system to study the reactive electrochemistry of precisely selected nanoclusters of specific size, shape, and morphology.^{16,49,50} These capabilities will open up new opportunities for molecular-level studies of interfacial processes occurring at electrochemical interfaces used in electrocatalysis, energy conversion, and storage.

ASSOCIATED CONTENT

Supporting Information

The Supporting Information is available free of charge on the ACS Publications website at DOI: 10.1021/acs.analchem.8b02440.

Infrared spectroscopy and cyclic voltammetry studies of the soft-landed WPOM ions on the in situ spectroelectrochemistry cell, and chronoamperometry results in the spectroelectrochemical experiments (PDF)

AUTHOR INFORMATION

Corresponding Author

*Phone: 765-494-5464. E-mail: jlaskin@purdue.edu.

ORCID

Pei Su: 0000-0001-6148-0181

Venkateshkumar Prabhakaran: 0000-0001-6692-6488

Julia Laskin: 0000-0002-4533-9644

Notes

The authors declare no competing financial interest.

ACKNOWLEDGMENTS

This work was supported by the U.S. Department of Energy (DOE), Office of Science, Office of Basic Energy Sciences, Chemical Sciences, Geosciences and Biosciences Division. The research was performed using the Environmental Molecular Sciences Laboratory, a national scientific user facility sponsored by the DOE's Office of Biological and Environmental Research and located at Pacific Northwest National Laboratory (PNNL). PNNL is operated by Battelle for DOE under Contract DE-AC05-76RL01830.

REFERENCES

- (1) Bard, A. J.; Abruna, H. D.; Chidsey, C. E.; Faulkner, L. R.; Feldberg, S. W.; Itaya, K.; Majda, M.; Melroy, O.; Murray, R. W. *J. Phys. Chem.* **1993**, *97* (28), 7147–7173.
- (2) Hamnett, A. The electrode–electrolyte interface. *Handbook of Fuel Cells*; John Wiley & Sons, Ltd.: Hoboken, NJ, 2010.
- (3) Iltot, A. J.; Trease, N. M.; Grey, C. P.; Jerschow, A. *Nat. Commun.* **2014**, *5*, 4536.
- (4) Pozniak, B.; Scherson, D. A. *J. Am. Chem. Soc.* **2003**, *125* (25), 7488–7489.
- (5) Le Rille, A.; Tajeddine, A.; Zheng, W.; Peremans, A. *Chem. Phys. Lett.* **1997**, *271* (1–3), 95–100.
- (6) Itkis, D. M.; Velasco-Velez, J. J.; Knop-Gericke, A.; Vyalikh, A.; Avdeev, M. V.; Yashina, L. V. *ChemElectroChem* **2015**, *2* (10), 1427–1445.
- (7) Salmeron, M.; Schlögl, R. *Surf. Sci. Rep.* **2008**, *63* (4), 169–199.
- (8) Ashley, K.; Pons, S. *Chem. Rev.* **1988**, *88* (4), 673–695.
- (9) Jebaraj, A. J.; Kumsa, D.; Scherson, D. A. *J. Phys. Chem. C* **2012**, *116* (12), 6932–6942.
- (10) Alkire, R. C. *Diffraction and Spectroscopic Methods in Electrochemistry*; John Wiley & Sons: Hoboken, NJ, 2006; Vol. 9.
- (11) Roth, J. D.; Lewis, G. J.; Safford, L. K.; Jiang, X.; Dahl, L. F.; Weaver, M. J. *J. Am. Chem. Soc.* **1992**, *114* (15), 6159–6169.
- (12) Mäntele, W.; Wollenweber, A.; Nabedryk, E.; Breton, J. *Proc. Natl. Acad. Sci. U. S. A.* **1988**, *85* (22), 8468–8472.
- (13) Richey, F. W.; Dyatkin, B.; Gogotsi, Y.; Elabd, Y. A. *J. Am. Chem. Soc.* **2013**, *135* (34), 12818–12826.
- (14) Seki, H.; Kunimatsu, K.; Golden, W. *Appl. Spectrosc.* **1985**, *39* (3), 437–443.
- (15) Iwasita, T.; Nart, F. *Prog. Surf. Sci.* **1997**, *55* (4), 271–340.
- (16) Prabhakaran, V.; Johnson, G. E.; Wang, B.; Laskin, J. *Proc. Natl. Acad. Sci. U. S. A.* **2016**, *113* (47), 13324–13329.
- (17) MacFarlane, D. R.; Forsyth, M.; Howlett, P. C.; Kar, M.; Passerini, S.; Pringle, J. M.; Ohno, H.; Watanabe, M.; Yan, F.; Zheng, W.; Zhang, S.; Zhang, J. *Nat. Rev. Mater.* **2016**, *1* (2), 15005.
- (18) Grill, V.; Shen, J.; Evans, C.; Cooks, R. G. *Rev. Sci. Instrum.* **2001**, *72* (8), 3149–3179.
- (19) Rauschenbach, S.; Stadler, F. L.; Lunedei, E.; Malinowski, N.; Koltsov, S.; Costantini, G.; Kern, K. *Small* **2006**, *2* (4), 540–547.
- (20) Johnson, G. E.; Hu, Q.; Laskin, J. *Annu. Rev. Anal. Chem.* **2011**, *4*, 83–104.
- (21) Cyriac, J.; Pradeep, T.; Kang, H.; Souda, R.; Cooks, R. *Chem. Rev.* **2012**, *112* (10), 5356–5411.
- (22) Verbeck, G.; Hoffmann, W.; Walton, B. *Analyst* **2012**, *137* (19), 4393–4407.
- (23) Johnson, G. E.; Gunaratne, D.; Laskin, J. *Mass Spectrom. Rev.* **2016**, *35* (3), 439–479.
- (24) Laskin, J.; Johnson, G. E.; Prabhakaran, V. *J. Phys. Chem. C* **2016**, *120* (41), 23305–23322.
- (25) Laskin, J.; Johnson, G. E.; Warneke, J.; Prabhakaran, V. *Angew. Chem., Int. Ed.* **2018**, DOI: 10.1002/anie.201712296.
- (26) Prabhakaran, V.; Mehdi, B. L.; Ditto, J. J.; Engelhard, M. H.; Wang, B.; Gunaratne, K. D. D.; Johnson, D. C.; Browning, N. D.; Johnson, G. E.; Laskin, J. *Nat. Commun.* **2016**, *7*, 11399.

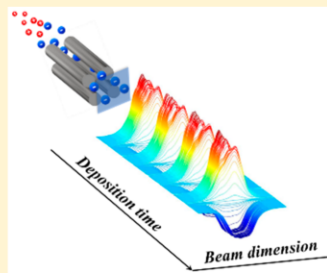
- (27) Wang, H.; Hamanaka, S.; Nishimoto, Y.; Irle, S.; Yokoyama, T.; Yoshikawa, H.; Awaga, K. *J. Am. Chem. Soc.* **2012**, *134* (10), 4918–4924.
- (28) Kawasaki, N.; Wang, H.; Nakanishi, R.; Hamanaka, S.; Kitaura, R.; Shinohara, H.; Yokoyama, T.; Yoshikawa, H.; Awaga, K. *Angew. Chem.* **2011**, *123* (15), 3533–3536.
- (29) Symes, M. D.; Cronin, L. *Nat. Chem.* **2013**, *5* (5), 403.
- (30) Sadakane, M.; Steckhan, E. *Chem. Rev.* **1998**, *98* (1), 219–238.
- (31) Nishimoto, Y.; Yokogawa, D.; Yoshikawa, H.; Awaga, K.; Irle, S. *J. Am. Chem. Soc.* **2014**, *136* (25), 9042–9052.
- (32) Gunaratne, K. D. D.; Prabhakaran, V.; Johnson, G. E.; Laskin, J. *J. Am. Soc. Mass Spectrom.* **2015**, *26* (6), 1027–1035.
- (33) Gunaratne, K. D. D.; Prabhakaran, V.; Andersen, A.; Johnson, G. E.; Laskin, J. *Phys. Chem. Chem. Phys.* **2016**, *18* (13), 9021–9028.
- (34) Thouvenot, R.; Fournier, M.; Franck, R.; Rocchiccioli-Deltcheff, C. *Inorg. Chem.* **1984**, *23* (5), 598–605.
- (35) Zhang, J.; Bond, A. M.; MacFarlane, D. R.; Forsyth, S. A.; Pringle, J. M.; Mariotti, A. W.; Glowinski, A. F.; Wedd, A. G. *Inorg. Chem.* **2005**, *44* (14), 5123–5132.
- (36) Gunaratne, K. D. D.; Prabhakaran, V.; Ibrahim, Y. M.; Norheim, R. V.; Johnson, G. E.; Laskin, J. *Analyst* **2015**, *140* (9), 2957–2963.
- (37) Hu, Q.; Wang, P.; Gassman, P. L.; Laskin, J. *Anal. Chem.* **2009**, *81* (17), 7302–7308.
- (38) Nanbu, N.; Sasaki, Y.; Kitamura, F. *Electrochem. Commun.* **2003**, *5* (5), 383–387.
- (39) Bondarenko, A. S.; Ragoisha, G. A. *Inverse Problem in Potentiodynamic Electrochemical Impedance*; Nova Science Publishers: New York, 2005.
- (40) Lou, F.; Zhou, H.; Huang, F.; Vullum-Bruer, F.; Tran, T. D.; Chen, D. *J. Mater. Chem. A* **2013**, *1* (11), 3757–3767.
- (41) Song, J. Y.; Lee, H. H.; Wang, Y. Y.; Wan, C. C. *J. Power Sources* **2002**, *111* (2), 255–267.
- (42) Lasia, A. *Electrochemical Impedance Spectroscopy and Its Applications*; Springer: New York, 2014.
- (43) Eda, K.; Osakai, T. *Inorg. Chem.* **2015**, *54* (6), 2793–2801.
- (44) Gunaratne, K. D. D.; Johnson, G. E.; Andersen, A.; Du, D.; Zhang, W.; Prabhakaran, V.; Lin, Y.; Laskin, J. *J. Phys. Chem. C* **2014**, *118* (48), 27611–27622.
- (45) Sandoval, A. P.; Suárez-Herrera, M. F.; Feliu, J. M. *Beilstein J. Org. Chem.* **2015**, *11*, 348.
- (46) Rocchiccioli-Deltcheff, C.; Fournier, M.; Franck, R.; Thouvenot, R. *Inorg. Chem.* **1983**, *22* (2), 207–216.
- (47) Bridgeman, A. J. *Chem. Phys.* **2003**, *287* (1–2), 55–69.
- (48) Johnson, G. E.; Laskin, J. *Chem. - Eur. J.* **2010**, *16* (48), 14433–14438.
- (49) Johnson, G. E.; Colby, R.; Engelhard, M.; Moon, D.; Laskin, J. *Nanoscale* **2015**, *7* (29), 12379–12391.
- (50) Johnson, G. E.; Colby, R.; Laskin, J. *Nanoscale* **2015**, *7* (8), 3491–3503.

Design and Performance of a Dual-Polarity Instrument for Ion Soft Landing

Pei Su,[†] Hang Hu,[†] Jonas Warneke,^{†,||} Mikhail E. Belov,^{‡,§} Gordon A. Anderson,[§] and Julia Laskin^{*,†,||}[†]Department of Chemistry, Purdue University, 560 Oval Drive, West Lafayette, Indiana 47907, United States[‡]Spectrograph, LLC, Kennewick, Washington 99338, United States[§]GAA Custom Engineering, LLC, POB 335, Benton City, Washington 99320, United States^{||}Wilhelm-Ostwald-Institut für Physikalische und Theoretische Chemie, Universität Leipzig, Linnestr. 2, 04103 Leipzig, Germany

Supporting Information

ABSTRACT: A new apparatus for ion soft landing research was developed and is reported in this contribution. The instrument includes a dual polarity high-flux electrospray ionization (ESI) interface, a tandem electrodynamic ion funnel system, a collisional flatpole, a quadrupole mass filter, and a focusing lens. The instrument enables production of ionic layers by soft landing of mass-selected ions onto surfaces with balanced or imbalanced charge conditions using either layer-by-layer (LBL) or fast polarity switching modes. We present the first evidence of using weakly coordinating stable anions to protect the ionizing protons of soft-landed cations on the surface. The observed proton retention is particularly efficient when fast polarity switching of anions and cations is employed to deposit small quantities of ions in short deposition segments. Furthermore, we observe more efficient charge retention and better ionic complexation in a charge-balanced layer prepared by fast polarity switching deposition. These findings open up new opportunities for the fabrication of novel ionic assemblies using well-defined gaseous ions as building blocks.



Soft landing of mass-selected ions refers to the process of depositing intact polyatomic ions onto substrates with precisely controlled composition, charge state, and kinetic energy.^{1–6} By eliminating solvent molecules, impurities, and counterions, ion soft landing provides an opportunity to explore the properties of well-defined ionic species on solid and liquid supports, which in turn facilitates molecular level understanding of the structures and reactivity of isolated ions and their assemblies in the condensed phase. The ability to control the size, shape, and position of the ion beam makes ion soft landing a promising tool for surface modification and preparation of functional materials of interest to both fundamental investigations and practical applications in chemistry, physics, materials science, and biology.^{7–10} For example, soft landing of mass-selected ions has been used to examine peptide and protein conformations^{11–14} and redox-activity¹⁵ on surfaces; prepare protein and peptide arrays,^{16,17} deposit molecular magnets,¹⁸ organometallic complexes,^{19–22} and catalytically active nanoclusters onto surfaces,^{20,23–27} and explore covalent immobilization of biomolecules^{28,29} and modification of polymer films,³⁰ self-assembled monolayers (SAMs),³¹ and carbon-based materials, such as graphene³² and carbon nanotubes.³³

Starting from the first system built by Cooks and co-workers in 1977,³⁴ the applications of ion soft landing have been tightly linked to the development of custom-designed instrumentation. In particular, ion soft landing has benefited from the

development of ionization sources and high-transmission ion optics. Electrospray ionization (ESI) is one of the most widely used approaches for continuously generating ions from solution in an ambient environment. Ion currents in the nanoampere range have been obtained by either using a funnel-shaped heated inlet³⁵ or large inner diameter inlet combined with a tandem electrodynamic ion funnel system.³⁶ Comparable ion currents of charged nanoclusters have been obtained using magnetron sputtering combined with gas aggregation.^{37,38} More recently, substantial improvement to milliamp-scale currents were achieved using a matrix assembly cluster source (MACS), which generates nanoclusters with a tunable mean diameter.^{27,39} Furthermore, the development of ambient and benchtop ion soft landing instruments has significantly advanced the scalability of this technique for applied research.^{40–43} The development of high-flux ion deposition capabilities has established ion soft landing as a promising approach for the rational design of electrical energy storage devices,⁴⁴ preparation of catalytic substrates,^{45,46} and opened up new directions for designing two-dimensional or multilayered three-dimensional ionic assemblies.⁴⁷

Received: January 17, 2019

Accepted: April 19, 2019

Published: April 19, 2019

High-coverage deposition of ions of one polarity typically examined in these studies revealed a number of interesting physical and chemical phenomena which have not been observed at low coverages.⁴⁷ Specifically, accumulation of ionic species on conductive surfaces produces charged layers balanced by the image charge on the surface.^{47,48} Although cations readily lose their charge at relatively high coverages,^{49,50} stable anions remain charged even when more than one layer is deposited on the surface.^{51,52} As a result, anion deposition generates charge-imbalanced anionic layers stabilized by strong electrostatic binding of the anions to the surface due to the presence of the induced image charge.⁴⁷ Recently, we have demonstrated that such high coverage layers are further stabilized by coadsorption of neutral molecules from the background of the vacuum system.⁴⁷ This process produces liquid-like layers which often undergo spontaneous dewetting upon exposure to laboratory air. This self-organization process is controlled by the properties of the anions, coadsorbed neutral molecules, surface, and environmental conditions. The final morphology of the resulting layer is most likely determined by the weaker interfacial forces as the image charge dissipates over time under ambient conditions. The degree of charge imbalance in the ionic layer may affect the final architecture of the ion assembly. Furthermore, charge balanced layers, which may be prepared by codepositing positive and negative ions, are promising systems for studying ion-ion interactions on surfaces and bottom-up design of novel ion-based materials.

Herein, we describe the design and performance of a first dual-polarity ion soft landing instrument, which may be used to generate both charge-balanced and charge-imbalanced layers. Employing a dual-polarity orthogonal injection high-flux ESI source, we demonstrate the utility of this instrument for either sequential layer-by-layer (LBL) deposition of ions of different polarities or almost simultaneous deposition of positive and negative ions through fast switching between polarities. Fast polarity switching has been previously employed in analytical mass spectrometry for characterizing complex mixtures,⁵³ studying ion/ion reactions,^{54,55} and ion deposition using triboelectric nanogenerators.⁵⁶ Here, we demonstrate for the first time its application to the high-flux soft landing of mass-selected ions. Our results indicate that deposition of mass-selected anions and cations on the same surface may be used to control the order, in which the ionic layer is formed; preserve their charge in the condensed phase, and tailor their interactions on surfaces. In particular, it has been demonstrated that the efficiency of charge loss by cations increases at high coverages.⁵⁰ In this study, we present the first evidence that weakly coordinating anions may be used to protect protonated molecules from losing the ionizing protons to the surface. These findings are of interest to the bottom-up assembly of functional layers using ion soft landing.

EXPERIMENTAL SECTION

The newly designed ion soft landing instrument is shown schematically in Figure 1. The instrument is equipped with a high-transmission dual polarity ESI interface (Spectrograph, LLC) composed of two orthogonal injection ESI sources (1), a tandem RF ion funnel system (2, 3), and a bent flatpole ion guide (4). The two ion funnels and the bent flatpole ion guide are housed in three differentially pumped aluminum vacuum chambers. All the electrical components are powered by a custom-designed modular intelligent power sources (MIPS)

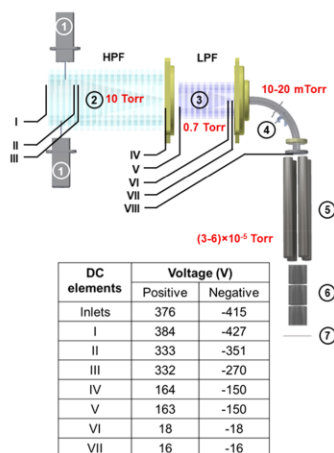


Figure 1. Schematic drawing of the dual polarity ion soft landing instrument showing the dual polarity ESI interface (1), high-pressure ion funnel (HPF, 2), low-pressure ion funnel (LPF, 3), bent flatpole ion guide (4), quadrupole mass filter (5), einzel lens (6), and surface (7). Direct current (DC) voltages on the tandem ion funnel system are shown with Roman numerals, (I) HPF repeller in, (II) HPF repeller out, (III) HPF funnel in, (IV) HPF funnel out, (V) LPF funnel in, (VI) LPF lens, (VII) LPF funnel out, and (VIII) conductance limit. The pressure in each vacuum region is marked in red. Typical DC voltages used for transmission of ions of both polarities in the tandem ion funnel region are shown in the bottom table.

system (GAA Custom Engineering, LLC). Chemicals, surface preparation, and surface characterization approaches are described in detail in the Supporting Information.

Dual Polarity ESI Interface. Ions of both polarities are produced by \pm ESI of 150 μ M solutions of selected analytes in methanol. The major ionic species generated using negative and positive ESI of the sodium phosphotungstate tribasic hydrate and tris(2,2'-bipyridyl)dichlororuthenium(II) hexahydrate solutions are $\text{PW}_{12}\text{O}_{40}^{3-}$ and $\text{Ru}(\text{bpy})_3^{2+}$, respectively. Solutions are filled into separate gastight syringes (Hamilton Robotics, Reno, NV) and introduced into the ESI source through two fused silica capillaries (Polymicro Technologies, Phoenix, AZ, 100 μ m ID, 360 μ m OD, 1' length) using two syringe pumps (Cole-Palmer, Vernon Hills, IL) at a typical flow rate of 60 μ L h^{-1} . Charged microdroplets are produced by applying a \pm 3 kV voltage to the syringe needles.

In the dual polarity ESI interface, charged droplets produced by \pm ESI are transferred into the vacuum system through two 100 mm long heated stainless steel inlet tubes (1/16" OD, 0.04" ID) mounted on the opposite sides of the first vacuum chamber. The heated inlets are mounted orthogonally to the instrument axis with one inlet positioned \sim 5 mm downstream from another one to improve gas dynamics in the chamber. Orthogonal injection of ions was shown to efficiently decouple ion transfer from gas flow dynamics and eliminate neutral molecules introduced into the vacuum system through the heated inlet.^{57,58} Two cartridge heaters (Omega Engineering, Inc., Stamford, CT) and thermocouples maintain the inlets at temperatures in the range of 25–200 $^{\circ}\text{C}$, which are independently optimized to ensure efficient desolvation of

the ESI droplets. The vacuum side of the heated capillaries protrudes into the first section of the first ion funnel by ~ 1 mm through two cutouts.

Tandem Ion Funnel System. The tandem ion funnel system composed of two printed circuit board radio frequency (RF) ion funnels is described in detail elsewhere.^{36,57,59} Briefly, a high-pressure ion funnel (HPF) is mounted in a vacuum chamber differentially pumped to 10 Torr by a dry-compression multistage Roots vacuum pump (ECODRY 65 plus, 32 cubic feet per minute (cfm), Leybold GmbH, Cologne, Germany). The HPF is composed of a stainless steel repeller plate on top and a stack of 113 ring electrodes. The first 28 electrodes have identical inner diameters (ID) of 50.8 mm (2 in), while the IDs of the following 85 electrodes decrease linearly from 50.8 to 2.5 mm (0.1 in). The last plate of the HPF acts as a conductance limit (CL) between the first and second vacuum chambers. The total length of the HPF is 5.7'. A low-pressure ion funnel (LPF) is mounted in the second vacuum chamber differentially pumped to 0.7 Torr by a second ECODRY 65 plus vacuum pump. The LPF is composed of 96 ring electrodes and has a total length of 4.3'. The first 24 ring electrodes have the same ID of 25.4 mm (1 in), while the IDs of the following 72 ring electrodes decrease linearly from 25.4 to 2.3 mm (0.09 in). An additional square-bracket-shaped electrode (denoted as lens) is inserted between the last two electrodes of the LPF.

Both ion funnels are powered by RF high-Q heads connected to the MIPS system. The resonant frequencies are ~ 740 and ~ 860 kHz, and peak-to-peak voltages are ~ 270 and ~ 135 V for the HPF and LPF, respectively. Separate direct current (DC) voltages are applied to the entrance and exit plates of each ion funnel, and axial DC potential gradients are generated using a series of 0.5 M Ω resistors connected between neighboring electrodes. The DC gradient in the HPF funnel is divided into two regions, a repeller region (the first 24 electrodes) and funnel region (the following 92 electrodes). The voltages applied to the two ESI inlets are slightly lower than the voltage applied to the HPF repeller plate, which improves ion transmission. Typical DC voltages used for the transmission of ions of both polarities are shown in Figure 1.

Bent Flatapole. The third vacuum chamber in the ion soft landing system houses a bent flatapole ion guide (4) described in detail elsewhere.^{60,61} The chamber is pumped down to 10–20 mTorr using a 90 L/sturbomolecular pump (TURBOVAC 90 I, Leybold GmbH, Cologne, Germany). The ECODRY 65 plus used for the second vacuum chamber backs the turbomolecular pump. The 90° bend of the flatapole rods effectively decouples the ion beam from the molecular beam present on the axis of the tandem ion funnel system. The flatapole is powered by a separate high-Q head connected to the MIPS system. The RF waveform applied to the flatapole rods has a frequency of ~ 1.88 MHz and peak-to-peak voltage of ~ 120 V; a typical DC bias of ± 15 – 35 V is applied to the flatapole rods for transferring positive and negative ions, respectively. Collisional cooling of ions in the flatapole RF field produces an ion beam focused to less than 2 mm at the flatapole exit.^{57,62} A stainless steel plate with a 2 mm aperture positioned at the end of the flatapole serves as a CL separating the third and fourth differentially pumped regions of the vacuum system.

Soft Landing Chamber. A soft landing chamber, in which the deposition is performed, is a modular aluminum 6 \times 6 \times 12 in. rectangular chamber (Ideal Vacuum Products,

Albuquerque, NM) that serves as the fourth differentially pumped vacuum region of the new ion soft landing instrument. The chamber houses a quadrupole mass filter, an einzel lens, and a surface. The chamber is sealed using vacuum cube plate flanges equipped with patterned openings for different types of fittings and configured with multiple 1/4"-20 threaded holes for mounting custom components inside the vacuum system. The fourth chamber is differentially pumped to 3 – 6×10^{-5} Torr by a 350 L/s turbomolecular pump (TURBOVAC 350 I, Leybold GmbH, Cologne, Germany) backed by the ECODRY 65 plus used to pump the second vacuum chamber.

A quadrupole mass filter (5) with a 9.5 mm rod diameter (Extrel CMS, Pittsburgh, PA) is mounted inside the soft landing chamber using custom-built aluminum brackets. The entrance plate is placed 2 mm away from the CL. The quadrupole mass filter has an operating frequency of 868 kHz and is powered by an RF amplifier module controlled by MIPS. MIPS provides both the RF and DC voltages necessary to operate the quadrupole in the RF/DC mode.

An einzel lens (6) is constructed using three cylindrical elements (3/4" ID, 0.75" length) and mounted after the exit plate of the quadrupole mass filter for focusing of the ion beam on the deposition surface (7). Ion beam characterization is performed using an IonCCD^{63,64} (OI Analytical, Pelham, AL) position sensitive detector mounted at a variable distance from the einzel lens. The integration times for detection of anionic and cationic beams were 20 and 5 ms, respectively. The shorter integration time for detecting negative ions was used because of the lower saturation limit of the IonCCD toward anions.⁶³ During soft landing experiments, ion current on the surface is measured using a picoammeter (RBD Instruments, Bend, OR) operated at a typical sampling rate of 300 ms.

Polarity Switching. Mass-selected ions of either the same or different polarities produced in the two ESI sources are transferred through the system and deposited onto the same substrate by switching between the RF and DC voltages independently optimized for each ion beam. Fast switching of all the RF and DC voltages, except for the \pm ESI voltages, is achieved using a custom-designed automated MIPS interface. The optimized RF and DC voltages for the best transmission of both ion beams are switched within ~ 500 ms. We note that this capability is not limited to polarity switching. Indeed, an arbitrary combination of ions generated by the two ion sources may be co-deposited onto the same surface using this approach.

Kinetic Energy Distribution (KED) Measurement. The KED of the ions exiting the flatapole was measured using a stainless steel plate mounted 5 mm away from the CL. The plate was connected to the picoammeter and biased using one of the DC voltages provided by MIPS. This configuration allowed us to apply the retarding voltage (V_r) to the collector plate while measuring the ion current. A uniform electric field close to the plate was created by mounting a stainless steel mesh (part no. 9230T51, McMaster Carr, Elmhurst, IL) ~ 2 mm in front of the plate. The mesh was kept at 0 V throughout the experiment. Ion current detected on the plate was measured as a function of V_r . Each data point was acquired by averaging the ion current for 10 s. The integrated retarding potential curve was obtained by plotting the ion current as a function of V_r . KED was obtained by taking a first derivative of the retarding potential plot.⁶⁵

RESULTS AND DISCUSSION

The new ion soft landing instrument described in this study enables either LBL or fast switching deposition of ions of both polarities, which closely mimics co-deposition. A doubly charged cation ($\text{Ru}(\text{bpy})_3^{2+}$) and a triply charged anion ($\text{PW}_{12}\text{O}_{40}^{3-}$, WPOM^{3-}) were used as representative ions to demonstrate the instrument performance. The instrument schematically shown in Figure 1 is equipped with two ESI interfaces. Each interface can generate either positive or negative ions independently. We operate the soft landing instrument in two distinct modes. In the first mode, one ESI interface is used to generate positive ions and the other interface generates negative ions. In the second mode, both interfaces are used to generate the same ions in order to improve the total ion current. We refer to these two modes of operation as ESI(\pm) and ESI \times 2, respectively. Typical mass-selected ion currents obtained on surfaces for $\text{Ru}(\text{bpy})_3^{2+}$ and WPOM^{3-} in both modes are listed in Table 1. The ESI \times 2

Table 1. Typical Ion Currents of $\text{Ru}(\text{bpy})_3^{2+}$ and WPOM^{3-} Obtained on the Surface in ESI(\pm) and ESI \times 2 Mode

mode	$\text{Ru}(\text{bpy})_3^{2+}$		WPOM^{3-}	
	ESI(\pm)	ESI \times 2	ESI(\pm)	ESI \times 2
current (nA)	+3.1	+5.3	-4.6	-8.2

mode improves the ion current by \sim 75% for both positive and negative ions. Stable ion currents obtained in this study (Figure S1) are comparable to previously published data³⁶ and can be further improved using a larger ID-heated inlet.

The position and shape of the ion beams of both polarities were characterized using a position sensitive IonCCD detector mounted 3 mm away from the einzel lens. The voltages on the einzel lens were optimized to obtain the tightest focusing and best overlap between $\text{Ru}(\text{bpy})_3^{2+}$ and WPOM^{3-} ion beams. The best voltage combinations of the einzel lens were 0 V/120 V/0 V and 0 V/−100 V/0 V for the negative and positive ion beam, respectively. The one-dimensional ion beam profiles of $\text{Ru}(\text{bpy})_3^{2+}$ and WPOM^{3-} obtained under the best focusing conditions are shown in Figure 2. The full widths at half-maximum (fwhms) are 1.5 and 2.2 mm for the positive

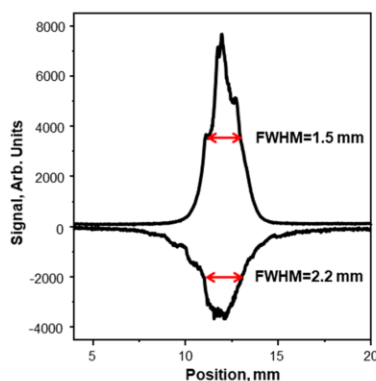


Figure 2. One-dimensional ion beam profiles of +3.1 nA $\text{Ru}(\text{bpy})_3^{2+}$ and −4.6 nA WPOM^{3-} obtained using IonCCD.

and negative ion beam, respectively. The lower signal intensity obtained for the negative ion beam is attributed to the lower anion saturation limit of the IonCCD.⁶³ The ion beam profiles shown in Figure 2 indicate good alignment and collocation of the positive and negative ion beams, which is important for both LBL and fast polarity switching experiments.

Ion KED. Precise control over the kinetic energy of the ions during deposition is an important capability of ion soft landing. Depending on their kinetic energy, ions undergo different processes upon collisions with surfaces.^{1,66,67} Preserving the structural integrity of the soft-landed ions during the deposition process is critically important to understanding their intrinsic properties on the surface. In this study, we used a retarding potential analysis to determine the KEDs of WPOM^{3-} and $\text{Ru}(\text{bpy})_3^{2+}$ ions exiting the collisional flatpole. Previous studies demonstrated that the most probable kinetic energy, KE_{mp} , of the ions in comparable soft landing systems is determined by the DC offset applied to the collisional quadrupole. This was attributed to the efficient collisional cooling of ions prior to their transfer into the high vacuum region of the instrument.

KEDs of $\text{Ru}(\text{bpy})_3^{2+}$ and WPOM^{3-} acquired at three different values of the flatpole bias are shown in Figure 3. The difference between the flatpole bias and the voltage applied to the CL was kept at +1 and −1 V for anions and cations, respectively. The narrowest KEDs for both $\text{Ru}(\text{bpy})_3^{2+}$ and WPOM^{3-} with fwhm of 1.3 and 0.8 eV, respectively, were obtained at the lowest flatpole bias of \pm 14 V. At higher flatpole bias voltages, the KEDs become slightly broader.

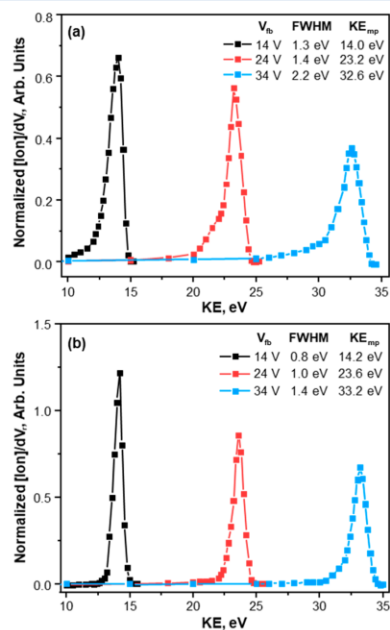


Figure 3. KEDs of $\text{Ru}(\text{bpy})_3^{2+}$ (a) and WPOM^{3-} (b) obtained at different values of the flatpole bias. The most probable KE (KE_{mp}) and fwhm are shown for each curve.

Furthermore, as shown in Figure S2, KEDs become broader with larger DC gradients between the flatpole bias and the voltage applied to the CL. The broadening of the KED may be attributed to ion–molecule collisions with the background gas during ion beam acceleration at the end of the flatpole, which become more substantial with an increase in the voltage gradient in this region. These results demonstrate that narrow KEDs may be obtained using a mild voltage gradient at the exit of the flatpole region. In the soft landing experiments described in the following sections, the kinetic energy of the ions was controlled by the flatpole bias, and the voltage difference at the end of the flatpole region was minimized to ensure good transmission and a narrow KED.

Two Modes of Ion Soft Landing Experiments. The flexible design of the dual-polarity ion soft landing instrument described in this study enables deposition of positive and negative ions on the same surface using two distinct modes of operation. In mode one, ions of each polarity are delivered to the surface in sequential long segments of deposition. Although we refer to this mode as LBL deposition, we do not imply that the resulting materials have a layered structure. Indeed, metastable layers prepared in this mode may undergo subsequent reorganization and self-assembly.⁴⁷ As a result, the initial and final architecture of the deposited layer may be different. In mode two, relatively short ion bursts of different polarities are produced using fast electronic switching between positive and negative ion beams. Mode two mimics ion co-deposition and presents a relatively simple alternative to merging two continuous ion beams of opposite polarity in the same instrument.

The fast polarity switching capability of the instrument was evaluated by depositing $\text{PMo}_{13}\text{O}_{40}^{3-}$ (MoPOM^{3-}) and $\text{Ru}(\text{bpy})_3^{2+}$ in small alternating deposition segments, which were initiated by a custom-designed automated MIPS interface. A plot of the ion current as a function of time obtained in four deposition segments of MoPOM^{3-} and $\text{Ru}(\text{bpy})_3^{2+}$ is shown in Figure 4a. The one-dimensional ion beam profiles acquired over the corresponding time period are shown as a 3D waterfall plot in Figure 4b. Each of the segments lasted for 16 s, corresponding to a deposition of $\sim 1 \times 10^{11}$ MoPOM^{3-} anions and $\sim 1.5 \times 10^{11}$ $\text{Ru}(\text{bpy})_3^{2+}$ cations, respectively. The ion current was observed to be stable for both ion beams. The length of the deposition segments can be varied independently in the range of 1 s to several days, which enables control of the number of ions delivered to the surface in each segment. This capability is important for preparing layers with different amounts of charge imbalance.

Protecting Soft-Landed Cations Using Weakly-Coordinating Anions. The first model system was designed to test the hypothesis that weakly coordinating stable anions may be used to protect the charge of cations deposited on a surface. Since its initial demonstration,⁶⁸ charge retention by soft-landed ions has attracted considerable attention and has been examined using SAM surfaces.^{49,52,69} Efficient charge retention by stable soft-landed anions has been attributed to the high energy barrier for electron detachment. In contrast, soft-landed cations more readily lose their charge on the surface. Specifically, charge loss by native cations is attributed to electron tunneling from the surface. Meanwhile, protonated molecules lose one or more of the ionizing protons to the surface. Preserving the charge of cations on surfaces is important for controlling their structures and reactivity.

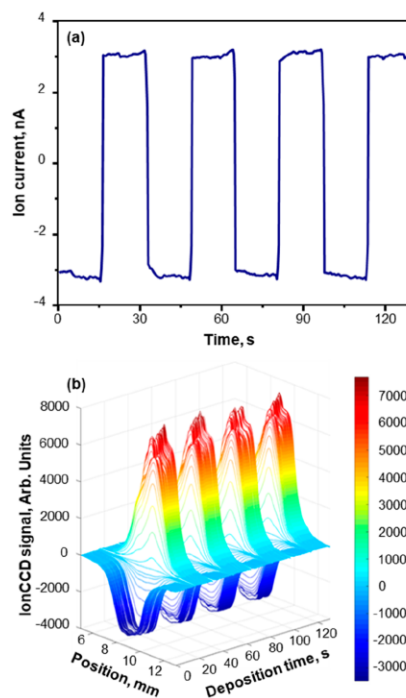


Figure 4. (a) Time-dependent ion current plot obtained during fast polarity switching deposition of MoPOM^{3-} and $\text{Ru}(\text{bpy})_3^{2+}$. In this experiment, four segments of MoPOM^{3-} and four segments of $\text{Ru}(\text{bpy})_3^{2+}$ were deposited on the surface. The ion currents were -3.2 nA for MoPOM^{3-} and $+3.2$ nA for $\text{Ru}(\text{bpy})_3^{2+}$ and the duration of each segment is 16 s. (b) 3D waterfall plot of the ion beam profiles acquired in the same time period in Figure 4a.

In this study, we used dianionic chlorinated dodecaborate ($\text{B}_{12}\text{Cl}_{12}^{2-}$) anions to protect protonated molecules on a surface. The $\text{B}_{12}\text{Cl}_{12}^{2-}$ anions were selected due to their chemical stability and extremely weak proton affinity, which is attributed to the strong diprotic acidity of the corresponding acid $\text{H}_2\text{B}_{12}\text{Cl}_{12}$.^{70,71} In this experiment, we deposited 1×10^{14} $\text{B}_{12}\text{Cl}_{12}^{2-}$ and 1×10^{14} protonated neutral red (NRH⁺) on SAMs of 1H,1H,2H,2H-perfluorodecanethiol (FSAM) using both LBL and fast polarity switching modes. This corresponds to an ~ 20 monolayer coverage for each of the deposited species. LBL was achieved by depositing a layer of 1×10^{14} $\text{B}_{12}\text{Cl}_{12}^{2-}$ followed by a layer of 1×10^{14} NRH⁺. The deposition time was 3 and 2.25 h for $\text{B}_{12}\text{Cl}_{12}^{2-}$ and NRH⁺ layers, respectively. In contrast, in the fast polarity switching experiment, the same overall coverage was achieved by alternating between the $\text{B}_{12}\text{Cl}_{12}^{2-}$ and NRH⁺ ion beams in segments of 10 and 8 s, respectively. The length of the segments was selected to deliver $\sim 1 \times 10^{11}$ ions, which corresponds to an $\sim 1\%$ monolayer coverage, over a $2 \text{ mm} \times 2 \text{ mm}$ deposition area. The total coverage corresponds to a 1:1 stoichiometry of anions and cations, producing a charge imbalanced layer. A layer of 1×10^{14} NRH⁺ on FSAM

surface also was prepared for comparison. The surfaces were characterized using visible absorption spectroscopy.

The visible spectra and optical images of the three surfaces are shown in Figure 5. The optical images demonstrate

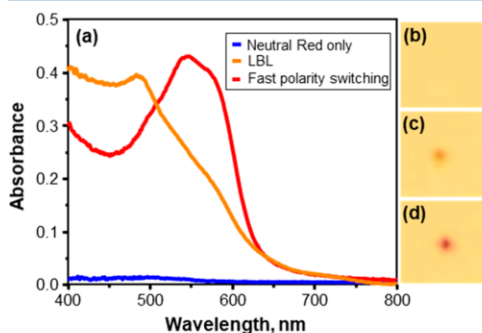


Figure 5. (a) Visible absorption spectra of $B_{12}Cl_{12}^{2-}/NRH^+$ surfaces. Optical images of the surfaces are shown on the right, (b) neutral red only, (c) LBL, and (d) fast polarity switching.

substantial differences in the visual appearance of the deposited spots. Specifically, almost no color was observed for the 1×10^{14} NRH^+ spot. Meanwhile, the LBL spot showed an orange color, and the spot obtained using fast switching appeared red. Visible spectra obtained for the three surfaces corroborate this observation. Specifically, two absorption bands observed in the visible spectrum of the LBL spot correspond to the combination of orange (major peak at ~ 480 nm) and red (minor peak at ~ 600 nm). In contrast, the major absorption peaks observed for the fast polarity switching deposition of $B_{12}Cl_{12}^{2-}/NRH^+$ appear at ~ 550 and ~ 600 nm, corresponding to the deeper red color. Finally, no substantial absorption of visible light was observed for the NRH^+ spot. These observations may be compared to the known color of neutral red in solution. In particular, neutral red shows a red color in its protonated form and turns yellow in its neutral

form (Figures S3 and S4). We infer that the deeper red color of the deposition spot prepared using fast polarity switching indicates more efficient charge retention by NRH^+ ions on the surface. Meanwhile, LBL deposition results in less efficient charge retention, and neutralization of the neutral red is observed in the absence of the protecting anions. Although the mechanism of charge retention for systems prepared using multilayer deposition are not well-understood, several factors may contribute to the reduced charge retention of the LBL deposition. For example, coadsorption of neutral molecules with $B_{12}Cl_{12}^{2-}$ anions described in our previous study⁴⁷ may alter the properties of the anionic protecting layer. Furthermore, multiple layers of NRH^+ present in the LBL spot may facilitate charge reduction. To the best of our knowledge, this is the first evidence of using weakly coordinating stable anions for protecting the ionizing protons of soft-landed cations.

Preparation of Charge-Balanced Ionic Layers. In another demonstration experiment, we explored the feasibility of the bottom-up construction of charge-balanced ionic layers using dual polarity ion soft landing. We deposited $MoPOM^{3-}$ and $Ru(bpy)_3^{2+}$ on an FSAM surface using both LBL and fast polarity switching modes. ESI-MS spectra of the extracted layer prepared using co-deposition of $MoPOM^{3-}$ and $Ru(bpy)_3^{2+}$ (Figure S5) confirm the intact deposition of the ions in these experiments. We selected $MoPOM^{3-}$ and $Ru(bpy)_3^{2+}$ as model systems for negative and positive ions due to their well-understood charge retention properties on FSAM.^{51,72} $MoPOM^{3-}$ and $Ru(bpy)_3^{2+}$ are widely used in the fabrication of hybrid electrochemiluminescent nanocomposites by solution-phase approaches.^{73,74} $MoPOM^{3-}$ shows distinct IR bands in the wavenumber region of $1100\text{--}800\text{ cm}^{-1}$, and the positions of the bands are strongly affected by the charge state of the anion and the presence of counter cations.^{51,75} Herein, we use the position of the terminal $Mo=O_t$ band of $MoPOM^{3-}$ as a reporter of the ionic interactions in different multilayered architectures prepared by dual polarity ion soft landing.

The results of these experiments are summarized in Figure 6. Two LBL assemblies of $MoPOM^{3-}$ and $Ru(bpy)_3^{2+}$ ions were prepared in our experiments. These experiments were designed

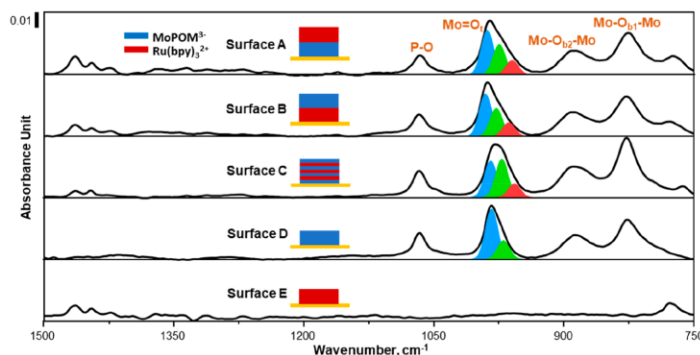


Figure 6. IRRAS spectra of the $MoPOM^{3-}/Ru(bpy)_3^{2+}$ surfaces prepared by LBL (A, B), fast polarity switching (C), $MoPOM^{3-}$ only (D), and $Ru(bpy)_3^{2+}$ only (E). The cartoon pictures of the deposition modes used to prepare surfaces A through E are shown in the corresponding figures, illustrating the surfaces that were prepared in either LBL or fast polarity switching modes. The combination of Gaussian curve fitting, are shown in each of the figures with color coding. A scale bar showing the absorbance is marked on the top left of the figure.

to obtain charge-balanced layers. Surface A was prepared using an one-segment deposition of 1×10^{14} MoPOM³⁻ anions on FSAM, followed by an one-segment deposition of 1.5×10^{14} Ru(bpy)₃²⁺. Surface B was prepared by switching the order of the deposition, i.e., first depositing 1.5×10^{14} Ru(bpy)₃²⁺ cations on FSAM, followed by 1×10^{14} MoPOM³⁻ anions. Surface C was prepared using fast polarity switching, in which ion deposition was alternated between positive and negative ions to achieve similar total coverage of the ions as that obtained for surfaces A and B by LBL. Each of the short deposition segments delivered 1×10^{11} MoPOM³⁻, followed by 1.5×10^{11} Ru(bpy)₃²⁺ to the surface. For comparison, we prepared two FSAM surfaces containing the corresponding ions of one polarity, i.e., 1×10^{14} MoPOM³⁻ (surface D) and 1.5×10^{14} Ru(bpy)₃²⁺ (surface E).

Ex situ infrared reflection absorption spectroscopy (IRRAS) of the surfaces was performed immediately after ion deposition. IRRAS spectra of surfaces A through D acquired with an FSAM surface as a background are shown in Figure 6. IR bands of MoPOM³⁻ were assigned based on our previous study.⁵¹ Specifically, the bands at 983 and 1067 cm⁻¹ are assigned to the terminal Mo=O_t stretching vibration and asymmetric coupling of P-O and Mo=O_t stretching modes (shown as P-O in Figure 6), respectively. The two bands at 887 and 827 cm⁻¹ are assigned to the vibrational stretching of the two types of bridging oxygen atoms, Mo-O_{b2}-Mo and Mo-O_{b1}-Mo, respectively. The IR bands of Ru(bpy)₃²⁺ were assigned based on the literature values.⁷⁶

We observe that the positions of the P-O, Mo-O_{b2}-Mo, and Mo-O_{b1}-Mo bands remain unchanged on all the surfaces containing MoPOM³⁻. In contrast, the terminal Mo=O_t band shows a systematic shift depending on the mode of deposition. It has been demonstrated that the terminal Mo=O_t band becomes broader and shifts toward lower wavenumbers when MoPOM³⁻ is soft landed onto an NH₃⁺-terminated SAM as compared to FSAM.⁷⁷ This is attributed to the attractive electrostatic interactions between the negatively charged MoPOM³⁻ ions and the positively charged NH₃⁺ moieties on the surface, which weaken the M=O bonds. We hypothesize that electrostatic interactions play a similar role when anions and cations are co-deposited in our soft-landing experiments. Fitting of the terminal Mo=O_t band, performed as described in our previous study,⁷⁵ provides additional insights into the observed shifts. The simulated bands are shown in Figure 6. The terminal Mo=O_t band was successfully reproduced by a combination of three Gaussian distributions referred to as the blue, green, and red band at ~987, 974, and ~960 cm⁻¹, respectively, consistent with the color coding in Figure 6.

The blue and green bands, which appear in all the spectra may be attributed to the different charge states of the MoPOM anions, as described in our previous study.⁵¹ In that work, the higher wavenumber feature (the blue band) was assigned to Mo=O_t band of MoPOM²⁻ produced by charge loss of MoPOM³⁻ in the deposited layer. The green band at lower wavenumbers was assigned to the Mo=O_t band of intact MoPOM³⁻ ions.⁵¹ This band is most abundant in the spectrum of the surface prepared by fast polarity switching deposition, which indicates better charge retention of MoPOM³⁻ on this surface. An additional feature (red band) is observed in the presence of Ru(bpy)₃²⁺ on the surface. This band may be attributed to the electrostatic interactions between MoPOM³⁻ and Ru(bpy)₃²⁺ ions, which may contribute to the observed

red-shifting of the band due to weakening of the Mo=O_t bond. The largest red shift of this band is observed for the surface prepared using fast polarity switching, which indicates stronger electrostatic interactions in this system as compared to surfaces prepared by LBL. We propose that fast polarity switching deposition of ions on the same surface results in more efficient charge retention and better ionic complexation in the layer.

CONCLUSION

In this study, we present the design and capabilities of a high-flux dual-polarity ion soft landing instrument for deposition of mass-selected cations and anions on surfaces. We describe, for the first time, the implementation of two orthogonal ESI inlets in a tandem ion funnel interface. The instrument was systematically characterized in terms of the intensity and shape of the ion beam, kinetic energy distribution of ions, and the polarity switching capabilities. We demonstrate the ability of LBL or fast polarity switching deposition of cations and anions on the same surface with precise control over the ionic composition, kinetic energy, beam shape, and total charge deposited on the surface. The independent operation of the two ESI sources and the fast electronic switching of the RF and DC voltages enable arbitrary combinations of analytes to be codeposited on the same surface. The newly developed fast polarity switching capability enables experiments, which closely approximate simultaneous codeposition of two ions beams of different polarities in a compact and relatively inexpensive instrument design. We found that fast polarity switching is the most effective approach for protecting soft-landed protonated molecules from neutralization by codepositing them with weakly coordinating anions. Furthermore, we provided spectroscopic evidence of the enhanced charge retention by native anions and better ionic complexation with cations on surfaces prepared using fast polarity switching compared to LBL. These novel capabilities of the newly designed dual polarity ion soft landing instrument open up intriguing opportunities for the rational design and fabrication of ionic assemblies with different degrees of charge imbalance, which cannot be achieved using other deposition techniques.

ASSOCIATED CONTENT

Supporting Information

The Supporting Information is available free of charge on the ACS Publications website at DOI: 10.1021/acs.analchem.9b00309.

Experimental section, ion current stability, kinetic energy distributions of ions at different DC gradients in the end of the flatpole region, visible spectra of solutions and drop casted samples of neutral red, and extraction ESI-MS spectra of the codeposited Ru(bpy)₃²⁺ and MoPOM³⁻ ions (PDF)

AUTHOR INFORMATION

Corresponding Author

*Tel: 765-494-5464; E-mail: jlaskin@purdue.edu.

ORCID

Pei Su: 0000-0001-6148-0181

Mikhail E. Belov: 0000-0002-7353-4789

Julia Laskin: 0000-0002-4533-9644

Notes

The authors declare no competing financial interest.

ACKNOWLEDGMENTS

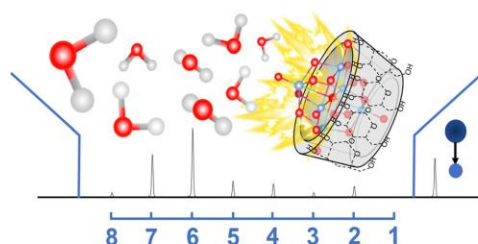
The authors thank the Jonathan Amy Facility for Chemical Instrumentation staff for technical support, Dr. Alexei Lagoutchev for help with UV-vis measurements, and Drs. Grant Johnson and Venky Prabhakaran (Pacific Northwest National Laboratory, USA) for their careful reading of the manuscript and valuable suggestions. We also thank Prof. Carsten Jenne (University of Wuppertal, Germany) for providing $B_{12}Cl_{12}^{2-}$ salts for our experiment. In addition, Jonas Warneke acknowledges support from the Feodor Lynen Fellowship from the Alexander von Humboldt Foundation.

REFERENCES

- (1) Grill, V.; Shen, J.; Evans, C.; Cooks, R. G. *Rev. Sci. Instrum.* **2001**, *72*, 3149–3179.
- (2) Johnson, G. E.; Hu, Q.; Laskin, J. *Annu. Rev. Anal. Chem.* **2011**, *4*, 83–104.
- (3) Cyriac, J.; Pradeep, T.; Kang, H.; Souda, R.; Cooks, R. *Chem. Rev.* **2012**, *112*, 5356–5411.
- (4) Verbeck, G.; Hoffmann, W.; Walton, B. *Analyst* **2012**, *137*, 4393–4407.
- (5) Johnson, G. E.; Gunaratne, D.; Laskin, J. *Mass Spectrom. Rev.* **2016**, *35*, 439–479.
- (6) Rauschenbach, S.; Ternes, M.; Harnau, L.; Kern, K. *Annu. Rev. Anal. Chem.* **2016**, *9*, 473–498.
- (7) Heiz, U.; Bullock, E. J. *Mater. Chem.* **2004**, *14*, 564–577.
- (8) Rauschenbach, S.; Stadler, F. L.; Lunedei, E.; Malinowski, N.; Koltsov, S.; Costantini, G.; Kern, K. *Small* **2006**, *2*, 540–547.
- (9) Vajda, S.; White, M. G. *ACS Catal.* **2015**, *5*, 7152–7176.
- (10) Laskin, J.; Johnson, G. E.; Prabhakaran, V. *J. Phys. Chem. C* **2016**, *120*, 23305–23322.
- (11) Wang, P.; Laskin, J. *Angew. Chem., Int. Ed.* **2008**, *47*, 6678–6680.
- (12) Hu, Q.; Laskin, J. *J. Phys. Chem. B* **2016**, *120*, 4927–4936.
- (13) Deng, Z.; Thontasen, N.; Malinowski, N.; Rinke, G.; Harnau, L.; Rauschenbach, S.; Kern, K. *Nano Lett.* **2012**, *12*, 2452–2458.
- (14) Longchamp, J.-N.; Rauschenbach, S.; Abb, S.; Escher, C.; Latschevskaia, T.; Kern, K.; Fink, H.-W. *Proc. Natl. Acad. Sci. U. S. A.* **2017**, *114*, 1474–1479.
- (15) Pepi, F.; Ricci, A.; Tata, A.; Favero, G.; Frascioni, M.; Delle Noci, S.; Mazzei, F. *Chem. Commun.* **2007**, 3494–3496.
- (16) Ouyang, Z.; Takáts, Z.; Blake, T. A.; Gologan, B.; Guymon, A. J.; Wiseman, J. M.; Oliver, J. C.; Davisson, V. J.; Cooks, R. G. *Science* **2003**, *301*, 1351–1354.
- (17) Blake, T. A.; Ouyang, Z.; Wiseman, J. M.; Takáts, Z.; Guymon, A. J.; Kothari, S.; Cooks, R. G. *Anal. Chem.* **2004**, *76*, 6293–6305.
- (18) Kahle, S.; Deng, Z.; Malinowski, N.; Tonnoir, C. n.; Forment-Aliaga, A.; Thontasen, N.; Rinke, G.; Le, D.; Turkowski, V.; Rahman, T. S.; et al. *Nano Lett.* **2012**, *12*, 518–521.
- (19) Nagaoka, S.; Matsumoto, T.; Ikemoto, K.; Mitsui, M.; Nakajima, A. *J. Am. Chem. Soc.* **2007**, *129*, 1528–1529.
- (20) Johnson, G. E.; Laskin, J. *Chem. - Eur. J.* **2010**, *16*, 14433–14438.
- (21) Peng, W.-P.; Johnson, G. E.; Fortmeyer, I. C.; Wang, P.; Hadjar, O.; Cooks, R. G.; Laskin, J. *Phys. Chem. Chem. Phys.* **2011**, *13*, 267–275.
- (22) Hauptmann, N.; Hamann, C.; Tang, H.; Berndt, R. *J. Phys. Chem. C* **2013**, *117*, 9734–9738.
- (23) Kaden, W. E.; Wu, T.; Kunkel, W. A.; Anderson, S. L. *Science* **2009**, *326*, 826–829.
- (24) Tyo, E. C.; Vajda, S. *Nat. Nanotechnol.* **2015**, *10*, 577.
- (25) Lünskens, T.; Heister, P.; Thämer, M.; Walenta, C. A.; Kartouzian, A.; Heiz, U. *Phys. Chem. Chem. Phys.* **2015**, *17*, 17541–17544.
- (26) Ha, M.-A.; Baxter, E. T.; Cass, A. C.; Anderson, S. L.; Alexandrova, A. N. *J. Am. Chem. Soc.* **2017**, *139*, 11568–11575.
- (27) Xu, J.; Murphy, S.; Xiong, D.; Cai, R.; Wei, X.; Heggen, M.; Barborini, E.; Vinati, S.; Dunin-Borkowski, R. E.; Palmer, R. E.; Liu, L. *ACS Appl. Energy Mater.* **2018**, *1*, 3013–3018.
- (28) Wang, P.; Hadjar, O.; Gassman, P. L.; Laskin, J. *Phys. Chem. Chem. Phys.* **2008**, *10*, 1512–1522.
- (29) Laskin, J.; Hu, Q. *J. Am. Soc. Mass Spectrom.* **2017**, *28*, 1304–1312.
- (30) Wijesundara, M. B.; Fuoco, E.; Hanley, L. *Langmuir* **2001**, *17*, 5721–5726.
- (31) Qin, X.; Tzvetkov, T.; Jacobs, D. C. *J. Phys. Chem. A* **2006**, *110*, 1408–1415.
- (32) Dubey, G.; Urcuyo, R.; Abb, S.; Rinke, G.; Burghard, M.; Rauschenbach, S.; Kern, K. *J. Am. Chem. Soc.* **2014**, *136*, 13482–13485.
- (33) Pepi, F.; Tata, A.; Garzoli, S.; Giacomello, P.; Ragno, R.; Patsilinos, A.; Fusco, M. D.; D'Annibale, A.; Cannistraro, S.; Baldacchini, C.; et al. *J. Phys. Chem. C* **2011**, *115*, 4863–4871.
- (34) Franchetti, V.; Solka, B.; Baitinger, W.; Amy, J.; Cooks, R. *Int. J. Mass Spectrom. Ion Phys.* **1977**, *23*, 29–35.
- (35) Pauly, M.; Sroka, M.; Reiss, J.; Rinke, G.; Albarghash, A.; Vogelgesang, R.; Hahné, H.; Kuster, B.; Sesterhenn, J.; Kern, K.; Rauschenbach, S. *Analyst* **2014**, *139*, 1856–1867.
- (36) Gunaratne, K. D. D.; Prabhakaran, V.; Ibrahim, Y. M.; Norheim, R. V.; Johnson, G. E.; Laskin, J. *Analyst* **2015**, *140*, 2957–2963.
- (37) Heiz, U.; Schneider, W.-D. *Crit. Rev. Solid State Mater. Sci.* **2001**, *26*, 251–290.
- (38) Zhang, C.; Tsunoyama, H.; Akatsuka, H.; Sekiya, H.; Nagase, T.; Nakajima, A. *J. Phys. Chem. A* **2013**, *117*, 10211–10217.
- (39) Palmer, R.; Cao, L.; Yin, F. *Rev. Sci. Instrum.* **2016**, *87*, 046103.
- (40) Badu-Tawiah, A. K.; Wu, C.; Cooks, R. G. *Anal. Chem.* **2011**, *83*, 2648–2654.
- (41) Li, A.; Baird, Z.; Bag, S.; Sarkar, D.; Prabhath, A.; Pradeep, T.; Cooks, R. G. *Angew. Chem., Int. Ed.* **2014**, *53*, 12528–12531.
- (42) Hou, J.; Zheng, Q.; Badu-Tawiah, A. K.; Xiong, C.; Guan, C.; Chen, S.; Nie, Z.; Wang, D.; Wan, L. *Chem. Commun.* **2016**, *52*, 13660–13663.
- (43) Johnson, G. E.; Prabhakaran, V.; Browning, N. D.; Mehdi, B. L.; Laskin, J.; Kottke, P. A.; Fedorov, A. G. *Batteries & Supercaps.* **2018**, *1*, 97–101.
- (44) Prabhakaran, V.; Mehdi, B. L.; Ditto, J. J.; Engelhard, M. H.; Wang, B.; Gunaratne, K. D. D.; Johnson, D. C.; Browning, N. D.; Johnson, G. E.; Laskin, J. *Nat. Commun.* **2016**, *7*, 11399.
- (45) Nesselberger, M.; Roefzaad, M.; Hamou, R. F.; Biedermann, P. U.; Schweinberger, F. F.; Kunz, S.; Schloegl, K.; Wiberg, G. K.; Ashton, S.; Heiz, U.; et al. *Nat. Mater.* **2013**, *12*, 919.
- (46) Popescu, R.; Schneider, R.; Gerthsen, D.; Böttcher, A.; Löffler, D.; Weis, P.; Kappes, M. *Surf. Sci.* **2009**, *603*, 3119–3125.
- (47) Warneke, J.; McBriarty, M. E.; Riechers, S. L.; China, S.; Engelhard, M. H.; Apra, E.; Young, R. P.; Washton, N. M.; Jenne, C.; Johnson, G. E.; Laskin, J. *Nat. Commun.* **2018**, *9*, 1889.
- (48) Laskin, J.; Johnson, G. E.; Warneke, J.; Prabhakaran, V. *Angew. Chem., Int. Ed.* **2018**, *57*, 16270–16284.
- (49) Hadjar, O.; Futrell, J. H.; Laskin, J. *J. Phys. Chem. C* **2007**, *111*, 18220–18225.
- (50) Johnson, G. E.; Priest, T.; Laskin, J. *J. Phys. Chem. C* **2012**, *116*, 24977–24986.
- (51) Gunaratne, K. D. D.; Johnson, G. E.; Andersen, A.; Du, D.; Zhang, W.; Prabhakaran, V.; Lin, Y.; Laskin, J. *J. Phys. Chem. C* **2014**, *118*, 27611–27622.
- (52) Gunaratne, K. D. D.; Prabhakaran, V.; Andersen, A.; Johnson, G. E.; Laskin, J. *Phys. Chem. Chem. Phys.* **2016**, *18*, 9021–9028.
- (53) Lamont, L.; Eijkel, G. B.; Jones, E. A.; Flinders, B.; Ellis, S. R.; Porta Siegel, T.; Heeren, R. M.; Vreeken, R. *J. Anal. Chem.* **2018**, *90*, 13229–13235.
- (54) Liang, X.; Xia, Y.; McLuckey, S. A. *Anal. Chem.* **2006**, *78*, 3208–3212.

- (55) Xia, Y.; Liang, X.; McLuckey, S. A. *J. Am. Soc. Mass Spectrom.* **2005**, *16*, 1750–1756.
- (56) Li, A.; Zi, Y.; Guo, H.; Wang, Z. L.; Fernández, F. M. *Nat. Nanotechnol.* **2017**, *12*, 481.
- (57) Belov, M. E.; Damoc, E.; Denisov, E.; Compton, P. D.; Horning, S.; Makarov, A. A.; Kelleher, N. L. *Anal. Chem.* **2013**, *85*, 11163–11173.
- (58) Chen, T.-C.; Fillmore, T. L.; Prost, S. A.; Moore, R. J.; Ibrahim, Y. M.; Smith, R. D. *Anal. Chem.* **2015**, *87*, 7326–7331.
- (59) Ibrahim, Y. M.; Baker, E. S.; Danielson, W. F.; Norheim, R. V.; Prior, D. C.; Anderson, G. A.; Belov, M. E.; Smith, R. D. *Int. J. Mass Spectrom.* **2015**, *377*, 655–662.
- (60) Rose, R. J.; Damoc, E.; Denisov, E.; Makarov, A.; Heck, A. J. *Nat. Methods* **2012**, *9*, 1084.
- (61) Peng, W.-P.; Goodwin, M. P.; Nie, Z.; Volny, M.; Ouyang, Z.; Cooks, R. G. *Anal. Chem.* **2008**, *80*, 6640–6649.
- (62) Tolmachev, A. V.; Udseth, H. R.; Smith, R. D. *Rapid Commun. Mass Spectrom.* **2000**, *14*, 1907–1913.
- (63) Hadjar, O.; Johnson, G.; Laskin, J.; Kibelka, G.; Shill, S.; Kuhn, K.; Cameron, C.; Kassan, S. *J. Am. Soc. Mass Spectrom.* **2011**, *22*, 612–623.
- (64) Johnson, G. E.; Hadjar, O.; Laskin, J. *J. Am. Soc. Mass Spectrom.* **2011**, *22*, 1388–1394.
- (65) Chantry, P.; Schulz, G. *Phys. Rev.* **1967**, *156*, 134.
- (66) Jacobs, D. C. *Annu. Rev. Phys. Chem.* **2002**, *53*, 379–407.
- (67) Laskin, J.; Wang, P.; Hadjar, O. *Phys. Chem. Chem. Phys.* **2008**, *10*, 1079–1090.
- (68) Miller, S.; Luo, H.; Pachuta, S.; Cooks, R. *Science* **1997**, *275*, 1447–1450.
- (69) Johnson, G. E.; Priest, T.; Laskin, J. *ACS Nano* **2012**, *6*, 573–582.
- (70) Jenne, C.; Kefler, M.; Warneke, J. *Chem. - Eur. J.* **2015**, *21*, 5887–5891.
- (71) Avelar, A.; Tham, F. S.; Reed, C. A. *Angew. Chem., Int. Ed.* **2009**, *48*, 3491–3493.
- (72) Laskin, J.; Wang, P. *Int. J. Mass Spectrom.* **2014**, *365*, 187–193.
- (73) Li, Y.; Yang, X.; Yang, F.; Wang, Y.; Zheng, P.; Liu, X. *Electrochim. Acta* **2012**, *66*, 188–192.
- (74) Li, Y.; Zhu, H.; Yang, X. *Talanta* **2009**, *80*, 870–874.
- (75) Su, P.; Prabhakaran, V.; Johnson, G. E.; Laskin, J. *Anal. Chem.* **2018**, *90*, 10935–10942.
- (76) Omberg, K. M.; Schoonover, J. R.; Treadway, J. A.; Leasure, R. M.; Dyer, R. B.; Meyer, T. J. *J. Am. Chem. Soc.* **1997**, *119*, 7013–7018.
- (77) Gunaratne, K. D. D.; Johnson, G. E.; Andersen, A.; Du, D.; Zhang, W.; Prabhakaran, V.; Lin, Y.; Laskin, J. *J. Phys. Chem. C* **2014**, *118*, 27611–27622.

Gas-Phase Fragmentation of Host-Guest Complexes of Cyclodextrins and Polyoxometalates

Pei Su,¹ Andrew J. Smith,¹ Jonas Warneke,^{1,2} Julia Laskin¹ ¹Department of Chemistry, Purdue University, 560 Oval Drive, West Lafayette, IN 47907, USA²Wilhelm-Ostwald-Institut für Physikalische und Theoretische Chemie, Universität Leipzig, Linnestr. 2, 04103, Leipzig, Germany

Abstract. Gas-phase fragmentation pathways of host-guest complexes of cyclodextrins (CDs) and polyoxometalates (POMs) were examined using collision-induced dissociation (CID). The host-guest complexes studied here were composed of two different classes of POMs—Keggin ($PW_{12}O_{40}^{3-}$) and Lindqvist ($M_6O_{19}^{2-}$, $M = Mo, W$)—and three types of CDs (α -, β -, and γ -CD) differing in the diameter of the inner cavity. The CD-POM complexes were generated either by

mixing methanol solutions of POM and CD or through a one-step acidic condensation of tetraoxometalates MO_4^{2-} ($M = Mo, W$) with CDs for complexes with Keggin and Lindqvist anions, respectively, and introduced into the gas phase using electrospray ionization (ESI). We observe distinct differences in fragmentation pathways of the complexes of Keggin and Lindqvist POMs under high- and low-energy CID conditions. Specifically, direct dissociation and proton transfer from CD to POM accompanied by the separation of fragments is observed in CID of Keggin CD-POM complexes. In contrast, dissociation of CD complexes with Lindqvist POMs is dominated by the simultaneous loss of multiple water molecules. This unusual fragmentation channel is attributed to dissociation of the POM cluster inside the CD cavity accompanied by covalent bond formation between the fragments and CD and elimination of multiple water molecules. The observed covalent coupling of metal oxide clusters opens up opportunities for derivatization of macrocyclic host molecules using collisional excitation of gaseous non-covalent complexes.

Keywords: Host-guest chemistry, Polyoxometalates, Cyclodextrins, Covalent coupling, Collision-induced dissociation, Mass spectrometry

Received: 5 April 2019/Revised: 11 June 2019/Accepted: 11 June 2019

Introduction

Host-guest supramolecular chemistry refers to the encapsulation of a guest molecule by the cavity of a macrocyclic host molecule via non-covalent interactions [1–3]. It has been

widely employed for the design and construction of supramolecular assemblies for applications in catalysis [4, 5], materials sciences [6, 7], and drug delivery [8, 9]. The hydrophobic effect was originally proposed to be a major driving force for the formation of host-guest complexes in the solution phase [10, 11]. The incorporation of a hydrophobic guest into the apolar cavity of a host molecule is a thermodynamically favorable process [12].

Recent studies have demonstrated an unexpected formation of strongly bound complexes, in which a chaotropic anion is embedded in a hydrophobic cavity of a macrocyclic host molecule. Chaotropic anions are often described as hydrophilic species with a delocalized charge, which form complexes with

Andrew J. Smith was an undergraduate student researcher.

Electronic supplementary material The online version of this article (<https://doi.org/10.1007/s13361-019-02266-8>) contains supplementary material, which is available to authorized users.

Correspondence to: Julia Laskin; e-mail: jlaskin@purdue.edu

Published online: 14 August 2019

host molecules mainly because of a strong binding of the anion to the host molecule [13]. The formation and stability of these host-guest complexes have been discussed in the context of a chaotropic effect as an alternative driving force for supramolecular assembly in an aqueous solution [12, 14]. The chaotropic effect is explained as follows: encapsulation of a chaotropic ion into the binding pocket of a host molecule allows for the recovery of the water structure initially disrupted by the ion [15]. Despite the entropic penalty resulting from the reorganization of water molecules, this process is thermodynamically favorable due to a large negative enthalpy of complexation [16]. The chaotropic effect becomes particularly pronounced for halogenated dodecaborates ($B_{12}X_{12}^{2-}$, $X = F, Cl, Br, I$) and small polyoxometalates (POMs) referred to as superchaotropic anions that lie far beyond the classical Hofmeister series [17, 18]. The strong binding between $B_{12}X_{12}^{2-}$ anions and several host molecules have been observed in the gas phase free of solvent environment [19].

Superchaotropic POM anions [20, 21] also have been explored as guest species in host-guest supramolecular complexes with macrocyclic host molecules such as pseudorotaxanes [22], cucurbit[n]uril [23–25], and calix[4]arene derivatives [26, 27]. The unique redox properties of POMs make their host-guest complexes particularly attractive building blocks for the design of functional supramolecular assemblies [28–30]. In particular, host-guest complexes of POMs and cyclodextrins (CDs) have been extensively studied. CDs are a class of cyclic oligosaccharides composed of 6, 7, and 8 D-glucopyranosyl residues (α -, β -, and γ -CD, respectively) linked by α -1,4 glycosidic bonds [31]. The shape-persistent hydrophobic cavity of a well-defined size enables the wide application of CDs as exceptional synthetic receptors in nanotechnology [32, 33], catalysis [34, 35], and pharmaceutical science [36, 37].

The first example of CD-POM host-guest complexes was described by Stoddart and co-workers [38]. Several novel CD-POM host-guest supramolecular hybrid materials have been successfully prepared through solution-phase approaches, and the non-covalent interactions of the host-guest assemblies have been systematically characterized [39–43]. Nuclear magnetic resonance (NMR) and single-crystal X-ray diffraction (XRD) analyses have confirmed that hydrogen bonding between POM and CD contributes to a majority of supramolecular interactions both in solution and in the solid state [38–40]. Meanwhile, the intrinsic non-covalent interactions between POMs and CDs free of solvent effects are still largely unexplored.

Mass spectrometry (MS) enables the investigation of structures and stabilities of host-guest complexes as isolated species in the gas phase [44–47]. Several studies have examined gas-phase fragmentation of CD complexes with amino acids [48], peptides [49], nucleobases [50], and organometallic compounds [51, 52]. Of particular interest to this work are gas-phase fragmentation studies of CD-POM complexes using collision-induced dissociation (CID), which provide insights into the intrinsic interactions of POMs and CDs [53, 54]. Herein, we explore the effect of the cavity diameter of the host CD molecule and properties of the guest POM anion on the gas-phase fragmentation of CD-POM

complexes. In particular, we examine CD-POM host-guest complexes of two archetypal POM structures, Keggin ($PW_{12}O_{40}^{3-}$, $W_{12}POM^{3-}$) and Lindqvist ($M_6O_{19}^{2-}$, M_6POM^{2-} , where $M = Mo$ or W) anions with three types of CDs with different cavity diameters, α -, β -, and γ -CD. Aside from proton transfer and direct dissociation pathways, which are characteristic of CID of non-covalent complexes, we observe simultaneous loss of multiple water molecules from the complex. We attribute this unusual fragmentation pathway to covalent bond formation between the CD host and POM fragments induced by proton transfer upon collisional activation. Covalent coupling of non-covalent complexes in CID has been previously reported for complexes of crown ethers with amines [55–57]. Furthermore, unusual reactivity in the gas phase has been observed when the host cavity of cucurbiturils was used as a molecular reaction container [58]. However, to the best of our knowledge the reactivity observed in this study has not been previously reported. The results presented herein open up intriguing opportunities for studying proton-induced chemistry of guest anions inside host cavities and covalent modification of macrocyclic host molecules.

Experimental Section

Chemicals

Sodium phosphotungstate tribasic hydrate ($Na_3[PW_{12}O_{40}] \cdot xH_2O$), sodium molybdate (Na_2MoO_4), sodium tungstate dihydrate ($Na_2WO_4 \cdot 2H_2O$), tetrabutylammonium bromide (TBA) ($C_{16}H_{36}BrN$), α -cyclodextrin ($C_{36}H_{60}O_{30}$), β -cyclodextrin ($C_{42}H_{70}O_{35}$), γ -cyclodextrin ($C_{48}H_{80}O_{40}$), methanol-d₄ (CD_3OD , 99.8 at.% D), deuterium oxide (D_2O , 99 at.% D), and water-¹⁸O ($H_2^{18}O$, 97 at.% ¹⁸O) were all purchased from Sigma-Aldrich (St. Louis, MO, USA). Hydrochloric acid (HCl, 25 wt%) was purchased from Honeywell (Mexico City, Mexico). Ethyl ether ($(C_2H_5)_2O$, anhydrous), water (H_2O , HPLC grade), and methanol (CH_3OH) were purchased from Fisher Scientific (Fair Lawn, NJ, USA).

Preparation of Keggin [$CD + W_{12}POM$]³⁻ Host-Guest Complex Solutions

A 1 mM stock solution of $W_{12}POM^{3-}$ was prepared by dissolving $Na_3[PW_{12}O_{40}]$ in methanol. 1 mM stock solutions of α -, β -, and γ -CD were prepared by dissolving CD in 90:10 (v/v) methanol/water solution. We found it to be necessary to include water to better solubilize the CDs. The final solution for ESI-MS was prepared by combining the Keggin POM and CD stock solutions in a 1:1 ratio and diluting the mixture with methanol to a final concentration of 10 μ M.

One-Pot Synthesis of Lindqvist [$CD + M_6POM$]²⁻ Host-Guest Complexes

$Na_2[X-CD + M_6O_{19}]$ (where $M = W$ or Mo , and $X = \alpha, \beta, \text{ or } \gamma$) was synthesized using a one-pot method adapted from Cadot et al. [59]. Typical synthetic procedure is described here using $[Na^+]_2[\gamma-CD + W_6O_{19}]^{2-}$ as an example: 0.1 g (0.3 mmol)

$\text{Na}_2\text{WO}_4 \cdot 2\text{H}_2\text{O}$ was dissolved in 4 mL of water, followed by addition of 0.072 g (0.05 mmol) of γ -CD under stirring. The same 6:1 molar ratio of Na_2WO_4 and CD was used for the one-pot synthesis with both α - and β -CD. A total of six of these syntheses were performed in order to get a sample of each combination of $[\text{X-CD} + \text{W}_6\text{O}_{19}]^{2-}$. These solutions were diluted with methanol to a concentration of 10 μM for MS analysis. We also verified that the same Lindqvist CD-POM complex can be made by mixing $[(n\text{-C}_4\text{H}_9)_4\text{N}]_2[\text{W}_6\text{O}_{19}]$ and γ -CD directly in methanol in the case of $[\gamma\text{-CD} + \text{W}_6\text{POM}]^{2-}$. Synthesis of $[(n\text{-C}_4\text{H}_9)_4\text{N}]_2[\text{W}_6\text{O}_{19}]$ was done by a procedure adapted from Klemperer et al. [60].

Low-Energy CID and HCD Conditions

ESI-MS analyses of the CD-POM complexes were performed using LTQ XL Linear Ion Trap Mass Spectrometer and Q-Exactive HF-X Hybrid Quadrupole-Orbitrap Mass Spectrometer (Thermo Fisher Scientific GmbH, Bremen, Germany). Samples were introduced into the MS inlet by direct infusion from a capillary (50 μm ID, 150 μm OD) at a flow rate of ~ 0.5 $\mu\text{L}/\text{min}$. Typical mass spectrometer conditions on LTQ were as follows: electrospray voltage, -3 kV; capillary temperature, 200 $^\circ\text{C}$; capillary voltage, -10 V; tube lens, -20 V; scan range, 100–2000 m/z . In the low-energy CID experiments, negatively charged host-guest complexes were isolated in the linear ion trap and subjected to collisions with helium buffer gas. Typical isolation width was 1 m/z . The q value was set at 0.25, and the typical activation time was 30 ms. Typical mass spectrometer conditions on Q-Exactive were as follows: electrospray voltage, -3 kV; capillary temperature, 250 $^\circ\text{C}$; RF funnel level, 100. Mass spectra were acquired over 150–2000 m/z at 140000 resolution (m/z 200). In higher-energy collisional dissociation (HCD) experiments, ions were mass-selected in a quadrupole mass filter and subjected to collisions with the background gas in the HCD cell. The isolation width for all of the complexes was 0.4 m/z . Collision energies (CE) are reported in the manufacturer-specified arbitrary units.

Hydrogen/Deuterium Exchange (HDX) Experiments

The HDX experiments were conducted by diluting the solution containing $[\gamma\text{-CD} + \text{W}_6\text{POM}]^{2-}$ with 50:50 (v/v) $\text{CD}_3\text{OD}/\text{D}_2\text{O}$ solvent to a final concentration of ~ 10 μM . The solution was allowed to rest for 3 h. All ESI-MS and low-energy CID conditions were consistent with those described above.

^{18}O Exchange Experiments

The ^{18}O -enriched complex, $[\gamma\text{-CD} + \text{W}_6\text{POM}]^{2-}$, was generated using the one-pot synthesis procedure described in the previous section with H_2^{18}O as a solvent. ESI-MS analysis was performed by diluting the solution containing $[\gamma\text{-CD} + \text{W}_6\text{POM}]^{2-}$ in 50:50 (v/v) acetonitrile: $^{18}\text{H}_2\text{O}$ to a final concentration of ~ 10 μM . ESI-MS and low-energy CID experiments were performed using the experimental conditions described earlier.

Results and Discussion

The CD-POM host-guest complexes examined in this study are composed of three types of CD (α , β , and γ) and two types of POM (Keggin and Lindqvist, structures are shown in Scheme 1). They were used to generate six different host-guest complexes ($[\alpha\text{-CD} + \text{W}_{12}\text{POM}]^{3-}$, $[\beta\text{-CD} + \text{W}_{12}\text{POM}]^{3-}$, $[\gamma\text{-CD} + \text{W}_{12}\text{POM}]^{3-}$, $[\alpha\text{-CD} + \text{W}_6\text{POM}]^{2-}$, $[\beta\text{-CD} + \text{W}_6\text{POM}]^{2-}$, and $[\gamma\text{-CD} + \text{W}_6\text{POM}]^{2-}$). Although this study is mainly focused on W-containing POM anions ($\text{W}_{12}\text{POM}^{3-}$, $\text{W}_6\text{POM}^{2-}$), several experiments were performed using $\text{Mo}_6\text{POM}^{2-}$ anion for comparison. Each of the anionic complexes was found to be an abundant species in the ESI-MS spectrum (Figure S1). Although complexes with more than one CD molecule are often produced by ESI-MS [53, 54, 59], only host-guest complexes of 1:1 stoichiometry were examined in this study.

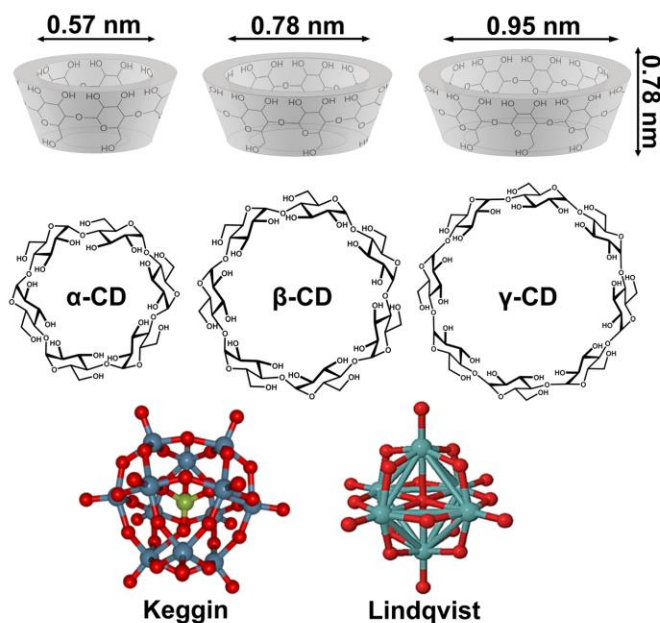
ESI-MS of Tungsten CD-POM Complexes

Figure 1a shows a typical ESI-MS spectrum of a solution containing γ -CD and $\text{W}_{12}\text{POM}^{3-}$. Consistent with the results reported by Cao et al. [54], we observe $[\gamma\text{-CD} + \text{W}_{12}\text{POM}]^{3-}$ and $[2\gamma\text{-CD} + \text{W}_{12}\text{POM}]^{3-}$ as the major species in the m/z range below 2000 (Figure 1a). In addition to host-guest complexes, the spectrum contains peaks corresponding to $\text{W}_{12}\text{POM}^{3-}$ and $\text{HW}_{12}\text{POM}^{2-}$ anions. Similar ESI-MS spectra (Figure S1) were obtained for complexes of $\text{W}_{12}\text{POM}^{3-}$ with α - and β -CD. In this study, we examine for the first time fragmentation of $[\alpha\text{-CD} + \text{W}_{12}\text{POM}]^{3-}$ and $[\beta\text{-CD} + \text{W}_{12}\text{POM}]^{3-}$ anions.

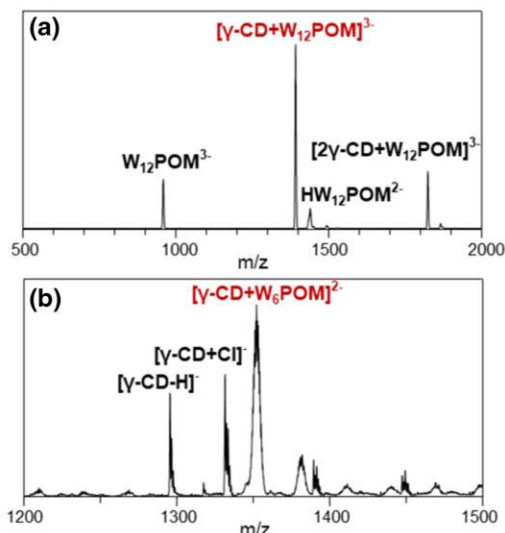
CD- W_6POM and CD- Mo_6POM complexes were generated using the one-pot synthetic procedure reported by Cadot et al. [59]. In that study, single-crystal X-ray diffraction (XRD) analysis was used to confirm that $\text{W}_6\text{O}_{19}^{2-}$ residing inside the γ -CD cavity has the Lindqvist-type structure [59]. A portion of the ESI-MS spectrum of the resulting solution is shown in Figure 1b. Aside from the $[\gamma\text{-CD} + \text{W}_6\text{POM}]^{2-}$ anion, the spectrum contains peaks corresponding to the Cl^- adduct of $[\gamma\text{-CD} + \text{Cl}]^-$ due to the presence of hydrochloric acid in solution, and deprotonated CD, $[\gamma\text{-CD} - \text{H}]^-$.

Gas-Phase Fragmentation Pathways

We systematically investigated the gas-phase fragmentation pathways of anionic CD-WPOM host-guest complexes using both high-energy collisional dissociation (HCD) on a QE-Orbitrap and low-energy CID on an ion trap. For both CD- W_{12}POM and CD- W_6POM complexes, we observe three major pathways shown in Scheme 2: (1) proton transfer from CD to POM, which generates peaks corresponding to protonated POM and deprotonated CD in the spectrum; (2) direct dissociation of the complex, which generates the original POM anion and undetectable neutral CD species; and (3) a series of multiple water losses from the complex. The distinctly different fragmentation patterns of the CD-POM complexes observed in

Scheme 1. Cyclodextrins (α , β , and γ -CD) and POM anions (Keggin $W_{12}POM^{3-}$, Lindqvist W_6POM^{2-}) used in this study

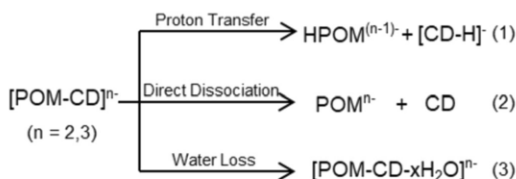
HCD and low-energy CID provide insights into the kinetics of the competing fragmentation pathways, which will be discussed in detail in the following sections.

Figure 1. ESI-MS spectra of solutions containing (a) $[\gamma\text{-CD} + W_{12}POM]^{3-}$ and (b) $[\gamma\text{-CD} + W_6POM]^{2-}$

MS/MS of $W_{12}POM$ -CD Complexes

Fragmentation spectra of CD- $W_{12}POM$ complexes obtained under both HCD and low-energy CID conditions are shown in Figure 2. We observe similar fragmentation patterns for all three types of CDs under the same activation conditions and distinctly different fragmentation patterns in HCD and low-energy CID. Specifically, HCD spectra of CD- $W_{12}POM$ complexes (Figure 2a) contain abundant peaks corresponding to products of both the proton transfer (pathway 1 in Scheme 2) and direct dissociation (pathway 2 in Scheme 2) pathways. In contrast, pathway 1 generating $HW_{12}POM^{2-}$ and $[CD - H]^-$ is dominant in low-energy CID spectra (Figure 2b). We note that the relatively low abundance of the $[CD - H]^-$ fragment ion in comparison with $HW_{12}POM^{2-}$ fragment is attributed both to the lower charge state and to subsequent fragmentation of $[CD - H]^-$ (Figure S2), which reduce the observed signal intensity. Water loss (pathway 3 in Scheme 2) appears to be a minor process for CD- $W_{12}POM$ complexes in both HCD and low-energy CID experiments.

It is well established that slow collisional excitation in the ion trap favors low-energy dissociation pathways, while HCD experiments provide access to entropically favorable higher-energy dissociation pathways under high-energy conditions [61–63]. The observed dominance of direct dissociation in HCD spectra and the absence of this pathway in low-energy CID indicate that it efficiently competes with proton transfer at higher internal excitations. This observation suggests that proton transfer, which is dominant in the low-energy CID



Scheme 2. Major fragmentation pathways observed for the CD-POM host-guest complexes in the gas phase

spectrum is a low-energy channel while direct dissociation of the complex is an entropically favorable process with a higher threshold energy than proton transfer.

Figure 2 also indicates that the extent of fragmentation of the complex decreases with increase in the size of the CD with the $[\gamma\text{-CD} + \text{W}_{12}\text{POM}]^{3-}$ anion showing the smallest extent of fragmentation both in HCD and low-energy CID spectra. This may be attributed to an increase in the strength of host-guest interactions between $\text{W}_{12}\text{POM}^{3-}$ and CD with increase in the cavity diameter. Crystal structure of the related $[\gamma\text{-CD} + \text{Mo}_{12}\text{POM}]^{3-}$ complex indicates that $\text{Mo}_{12}\text{POM}^{3-}$ fits deep inside the larger cavity of $\gamma\text{-CD}$ (9.5 Å) and the complex is stabilized by multiple hydrogen bonding interactions with CD [38]. Similar sizes of $\text{Mo}_{12}\text{POM}^{3-}$ and $\text{W}_{12}\text{POM}^{3-}$ suggest that $\text{W}_{12}\text{POM}^{3-}$ also fits well into the $\gamma\text{-CD}$ cavity. The cavity diameters of $\alpha\text{-CD}$ and $\beta\text{-CD}$ are 5.7 Å and 7.8 Å, respectively, which are smaller in comparison with $\gamma\text{-CD}$ [31]. It is reasonable to assume that fewer hydrogen bonding interactions and weaker dispersion forces between POM and smaller CDs make the corresponding complexes less stable than the complex of Keggin POM and $\gamma\text{-CD}$. Another possible explanation for the decrease in the extent of fragmentation of the complex with increase in the size of CD is that the larger $\gamma\text{-CD-POM}$ complex has a larger number of vibrational degrees of freedom, which results in a decrease in the unimolecular dissociation rate and thereby reduces the extent of fragmentation [64].

The prevalence of proton transfer over other dissociation channels observed in Figure 2b may be attributed to the strong hydrogen bonding interactions between $\text{W}_{12}\text{POM}^{3-}$ and CD in the

complex, which facilitate proton transfer from CD to POM. A crystal structure of CD- Mo_{12}POM complex indicates the presence of multiple hydrogen bonds between hydroxyl groups of CD and oxygen atoms of the POM anion as a major type of non-covalent interactions between POM and CD [38]. Although the energetics of proton transfer within the complex is not known, it is reasonable to assume that proton transfer from CD to $\text{W}_{12}\text{POM}^{3-}$ is energetically favorable based on the substantial difference in the gas-phase basicity of the isolated $\text{W}_{12}\text{POM}^{3-}$ (374–385 kcal/mol) [65] and the Brønsted acidity of CD (325–327 kcal/mol) [66]. We propose that upon collisional excitation, a proton is abstracted from the proton donor (CD) by the most basic oxygen site of the proton acceptor ($\text{W}_{12}\text{POM}^{3-}$). It also is reasonable to assume that proton abstraction is inhibited in CID of CD-POM complexes containing less basic POM anions, such as Lindqvist anion discussed in the next section. Indeed, no proton transfer was observed in CID of a host-guest complex of $\beta\text{-CD}$ with another superchaotropic anion, $\text{B}_{12}\text{F}_{12}^{2-}$, with lower gas-phase basicity (322 kcal/mol) [67]. Instead, the $[\beta\text{-CD} + \text{B}_{12}\text{F}_{12}]^{2-}$ complex exhibited loss of a sugar unit, which was attributed to the strong binding between $\beta\text{-CD}$ and $\text{B}_{12}\text{F}_{12}^{2-}$ in the absence of solvent [19].

MS/MS of CD- W_6POM Complexes

Gas-phase fragmentation pathways of Lindqvist CD- W_6POM complexes under HCD and low-energy CID conditions are shown in Figure 3a, b, respectively. Similar to Keggin CD- W_{12}POM complexes, we observe comparable fragmentation patterns for CD- W_6POM complexes containing different CDs under the same collisional activation conditions. However, distinctly different fragmentation patterns are observed in HCD and low-energy CID experiments. In contrast with low-energy CID of CD- W_{12}POM complexes described earlier, proton transfer from CD to $\text{W}_6\text{POM}^{2-}$ (pathway 1 in Scheme 2) is a minor process in CID spectra of CD- W_6POM complexes. Instead, HCD spectra of CD- W_6POM complexes contain abundant $\text{W}_6\text{O}_{19}^{2-}$ peaks corresponding to direct dissociation (pathway 2 in Scheme 2). The observed decrease in the extent of dissociation for different types of CDs is similar to

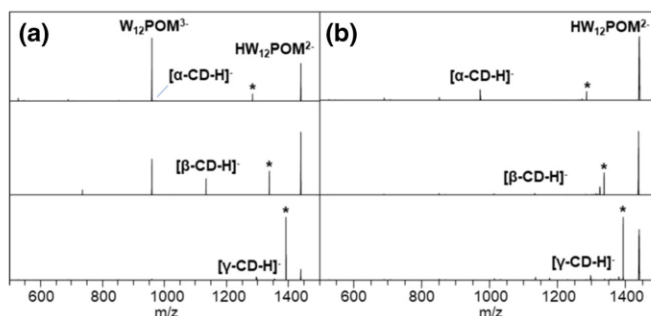


Figure 2. (a) HCD (CE = 45) and (b) low-energy CID (CE = 17) spectra of Keggin CD- W_{12}POM complexes under same conditions. The precursor ion signal in each spectrum is marked with an asterisk

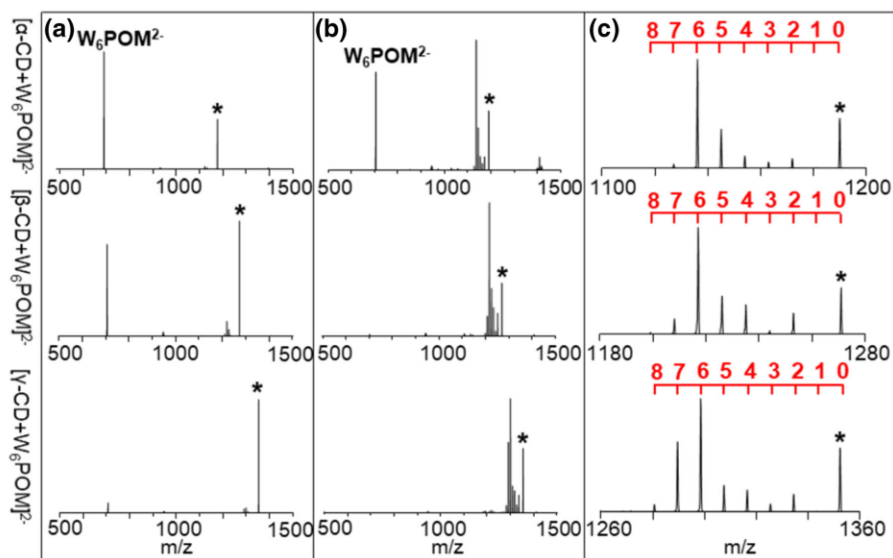


Figure 3. (a) HCD (CE = 45) and (b) low-energy CID (CE = 17) spectra of Lindqvist CD- W_6POM complexes. The precursor ion signal in each spectrum is marked with an asterisk. (c) Expanded m/z range of the spectra in panel (b) showing multiple water loss peaks. The red ruler on top of each spectrum shows the corresponding number of water losses

that of CD- $W_{12}POM$ complexes, which has been discussed in detail in the previous section. The presence of an abundant W_6POM^{2-} fragment produced by direct dissociation of $[\alpha\text{-CD} + W_6POM]^{2-}$ in the low-energy CID spectrum is consistent with the relatively weak binding between the smaller $\alpha\text{-CD}$ cavity and W_6POM^{2-} anion.

Direct dissociation of $[\alpha\text{-CD} + W_6POM]^{2-}$ is observed in competition with losses of multiple water molecules from the complex (pathway 3 in Scheme 2), which is the only pathway in low-energy CID spectra of $[\beta\text{-CD} + W_6POM]^{2-}$ and $[\gamma\text{-CD} + W_6POM]^{2-}$ anions (Figure 3b). Water losses also are observed as lower-abundance peaks in HCD spectra of CD- W_6POM complexes. Figure 3c shows regions of the low-energy CID spectra of CD- W_6POM complexes containing the water loss pattern observed as a distribution of peaks spaced by 9 m/z units ($z=2$). For all three complexes, the most abundant fragment, $[\text{CD} + W_6POM - 6H_2O]^{2-}$, corresponds to the loss of six water molecules. Interestingly, very low signal was obtained for a fragment ion corresponding to a single water loss and loss of three water molecules. Similar fragmentation patterns were observed in low-energy CID spectra acquired at different excitation voltages (Figure 4) indicating that the observed losses of multiple water molecules are not sequential but rather occur in parallel. Loss of seven water molecules becomes more abundant for the $[\gamma\text{-CD} + W_6POM]^{2-}$ complex.

Further excitation of the fragment ions produced via loss of either single or multiple water molecules from $[\gamma\text{-CD} + W_6POM]^{2-}$ in an MS^3 experiment (Figure S3) results in additional losses of water molecules. The preference for the overall

loss of 6 water molecules is clearly observed in the MS^3 experiments. MS^3 of $[\gamma\text{-CD} + W_6O_{19} - 6H_2O]^{2-}$ shows abundant losses of one and two water molecules and a minor peak corresponding to three water losses. Despite the preference for the loss of six water molecules in the MS^2 experiment, an overall loss of up to ten water molecules was observed in the MS^3 spectra.

The observed loss of multiple water molecules is not limited to W_6POM^{2-} . Low-energy CID spectra of CD- Mo_6POM complexes shown in Figure 5 contain similar multiple water loss patterns. However, in contrast with CD- W_6POM , CD- Mo_6POM complexes predominantly lose five water molecules, with a single water loss almost absent in the spectra. In addition, we observed an abundant pair of fragments, $HM_4O_{13}^-$ and $[\text{CD} + Mo_2O_6 - H - H_2O]^-$, as confirmed by high-resolution MS experiments. The latter is most likely produced via a loss of one water molecule from the $[\text{CD} + Mo_2O_6 - H]^-$ anion. Similarly, $HW_4O_{13}^-$ fragment ion is present as a minor peak in the spectrum of CD- W_6POM . However, the complementary anion undergoes more substantial dehydration forming a distribution of $[\text{CD} + W_2O_6 - H - xH_2O]^-$ ($x=1, 2, 3$) fragments with two and three water losses as the dominant species (Figure S4). This observation is consistent with the greater extent of water loss from the CD- W_6POM as compared to CD- Mo_6POM .

Simultaneous loss of multiple water molecules is an unusual pathway in low-energy CID. We propose that this pathway is initiated by a proton transfer from the CD to the W_6POM^{2-} anion. Proton transfer is a dominant pathway in

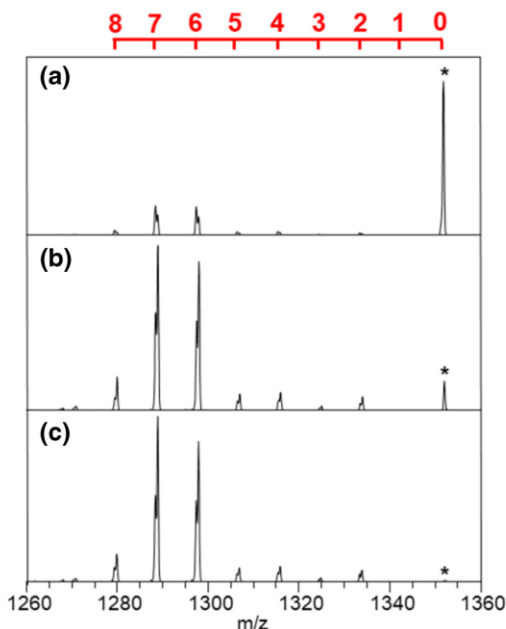


Figure 4. A region of low-energy CID spectra of $[\gamma\text{-CD} + \text{W}_6\text{POM}]^{2-}$ showing multiple water losses at (a) CE = 16, (b) CE = 19, and (c) CE = 22. The precursor ion signal in each spectrum is marked with an asterisk. The red ruler on top of the panel shows the corresponding number of water losses

dissociation of Keggin CD- W_{12}POM discussed earlier. However, for the Keggin CD- W_{12}POM complex, proton transfer is followed by the separation of $[\text{CD} - \text{H}]^-$ and $\text{HW}_{12}\text{POM}^{2-}$. Comparison of the gas-phase basicities of $\text{W}_{12}\text{POM}^{3-}$ (374–385 kcal/mol) [65] and $\text{W}_6\text{POM}^{2-}$ (335–347 kcal/mol) [68] indicates that proton transfer from CD (Bronsted acidity 325–327 kcal/mol) [66] to $\text{W}_{12}\text{POM}^{3-}$ is more exothermic than to $\text{W}_6\text{POM}^{2-}$, which could promote the separation of fragments formed through pathway 1. The absence of the $\text{HW}_6\text{O}_{19}^-$ fragment in the CID spectra of CD- W_6POM complexes could be explained by assuming that the separation of $[\text{CD} - \text{H}]^-$ and $\text{HW}_6\text{O}_{19}^-$ does not efficiently compete with other dissociation pathways.

In order to rationalize simultaneous losses of multiple water molecules from the complex, we assume that $\text{HW}_6\text{O}_{19}^-$ or $\text{HMo}_6\text{O}_{19}^-$ formed through the proton transfer step decompose into several smaller fragments. We propose that POM fragments formed in this initial step subsequently attack the CD cage thereby forming covalent bonds to the host molecule and eliminating multiple water molecules. The anionic product of this dissociation pathway is a derivatized CD. MS^n experiments (data not shown) demonstrate that this species undergoes subsequent loss of several water molecules followed by losses of hydrocarbon fragments. However, no losses of W-containing neutral molecules were observed in these

experiments. These results confirm that POM fragments form strong covalent bonds with CD thereby yielding an unusual CD derivative.

The observed distribution of water losses from the complex may be attributed to the presence of multiple pathways for the covalent attachment of metal oxide fragments to the CD. Meanwhile, the difference between the preferred number of water losses from the CD- W_6POM and CD- Mo_6POM likely indicates the differences in either the type or reactivity of the fragments of HMo_6POM^- in comparison with HW_6POM^- .

The formation of the $\text{HMo}_4\text{O}_{13}^-$ and $[\text{CD} + \text{Mo}_2\text{O}_6 - \text{H} - \text{H}_2\text{O}]^-$ pair of fragments could be rationalized using the same mechanism. However, in this case, only one covalent bond is formed between the CD and Mo_2O_6 fragment releasing one water molecule. In contrast, up to three water molecules are released by covalent bond formation between CD and W_2O_6 fragment, which indicates that W_2O_6 is more reactive than Mo_2O_6 . This finding is in agreement with the more efficient water loss from CD- W_6POM as compared to CD- Mo_6POM . However, this pathway is only observed as a minor dissociation channel for CD- W_6POM , which is consistent with the higher exothermicity of the proton transfer from the CD (Bronsted acidity 325–327 kcal/mol) [66] to $\text{Mo}_6\text{POM}^{2-}$ (gas-phase basicity in the range of 342–355 kcal/mol) [68] as compared to $\text{W}_6\text{POM}^{2-}$ (gas-phase basicity in the range of 335–347 kcal/mol) [68].

H/D Exchange and ^{18}O Exchange Experiments

It is reasonable to assume that a majority of water losses involve hydroxyl groups of the CD host molecule. In order to obtain additional insights into the types of hydrogen and oxygen atoms involved in the process, we carried out H/D exchange (HDX) and ^{18}O exchange experiments using $[\gamma\text{-CD} + \text{W}_6\text{POM}]^{2-}$ as a representative species. Experimental CID spectra of the complexes were rationalized using statistical simulations.

HDX experiments were performed by diluting the stock solution of $[\gamma\text{-CD} + \text{W}_6\text{POM}]^{2-}$ complex in a deuterated solvent. The extent of HDX was controlled by varying the solvent composition. Specifically, a very limited extent of HDX of the hydroxyl groups of $\gamma\text{-CD}$ was observed using CD_3OD as a solvent. In contrast, more extensive HDX was observed in a $\text{CD}_3\text{OD}/\text{D}_2\text{O}$ mixture. $\gamma\text{-CD}$ has 24 labile hydrogens of the hydroxyl groups available for HDX [69]. Each of the (α -1,4)-linked α -D-glucopyranose units on the CD structure contains one primary and two secondary hydroxyl groups on the outer rim and inner cavity of CD, respectively. The primary hydroxyl groups are flexible and often involved in intermolecular hydrogen bonding. Meanwhile, the 16 secondary hydroxyl groups on the inner CD surface are connected by intramolecular hydrogen bonds, which determine the rigidity of the CD cavity in the condensed phase [69]. More than 16 exchanges were previously observed in gas-phase HDX experiments of $\gamma\text{-CD}$ indicating that the exchange is not limited to the primary hydroxyl groups [70]. The remaining hydrogen atoms in $\gamma\text{-CD}$ on the C-H sites

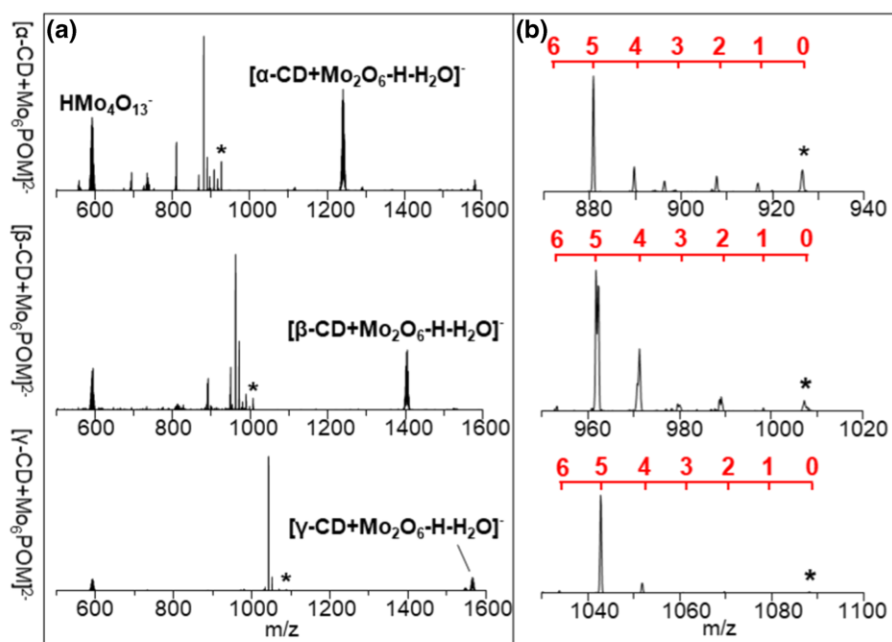


Figure 5. (a) Low-energy CID spectra of Lindqvist CD- Mo_6POM complexes at $\text{CE} = 17$. The precursor ion signal in each spectrum is marked with an asterisk. (b) Expanded m/z range of the spectra showing multiple water loss peaks. The red ruler on top of each spectrum shows the corresponding number of water losses

of the glucopyranose units are not exchangeable due to their lower acidity.

In the condensed phase, $\text{W}_6\text{POM}^{2-}$ is deeply embedded into the CD cavity with the eight primary hydroxyl groups pointing away from the complex thereby optimizing the interactions with solvent molecules in solution or with other complexes in the crystalline phase [59]. However, little is known about the structure of the $[\gamma\text{-CD} + \text{W}_6\text{POM}]^{2-}$ complex in the gas phase. The HDX experiments described herein were designed to probe whether only the secondary or all of the hydroxyl groups are involved in the observed water losses.

An ESI-MS spectrum of a solution of $[\gamma\text{-CD} + \text{W}_6\text{POM}]^{2-}$ in 50:50 (v/v) $\text{CD}_3\text{OD}/\text{D}_2\text{O}$ solvent analyzed 3 h after mixing is shown in Figure S5. We observe a series of peaks ranging from $m/z = 1296$ to $m/z = 1320$ arising from the isotopomers of $[\gamma\text{-CD} - \text{H}]^-$ produced by HDX. The distribution is centered at $m/z = 1312$ corresponding to 16 exchanged hydrogens (Figure S5). In addition, an isotopic envelope of $[\gamma\text{-CD} + \text{W}_6\text{POM}]^{2-}$ is observed in a range of $m/z = 1351$ – 1365 . The center of the isotopic envelope of $[\gamma\text{-CD} + \text{W}_6\text{POM}]^{2-}$ after HDX is shifted to $m/z = 1360$ from $m/z = 1352$ for the original complex corresponding to an average exchange of 16 hydrogens.

We systematically examined MS^2 of the isotopic peaks of $[\gamma\text{-CD} + \text{W}_6\text{POM}]^{2-}$ from this distribution using an isolation window of 1 m/z . The m/z range corresponding to multiple water losses in the low-energy CID spectrum of $m/z = 1365$ from the high m/z side of the isotopic distribution is shown in

Figure 5a. Each of the features in this region contains a distribution of isotopic peaks originating from a combined loss of H_2O , HDO , and D_2O due to the partial exchange of hydrogens with deuterium atoms.

The observed isotopic distributions of water losses from partially exchanged $[\gamma\text{-CD} + \text{W}_6\text{POM}]^{2-}$ complexes may be rationalized using the following model. We assume that (1) the complex has a similar distribution of hydrogen and deuterium atoms as the $[\gamma\text{-CD} - \text{H}]^-$ detected in the ESI-MS spectrum and (2) loss of a single or multiple water molecules is a random single-step process. The latter assumption is supported by the non-sequential loss of multiple water molecules discussed earlier. First, we calculate the distribution of deuterium atoms in a selected isotopic peak of the complex. Next, we use a hypergeometric distribution to predict the number of deuterium atoms incorporated into the water molecules eliminated from this isotopic peak of the complex in CID. Finally, we compare the simulated distribution with the experimental CID data.

In the first step, we calculate all possible combinations of the isotopes of the partially exchanged $\gamma\text{-CD}$ and $\text{W}_6\text{POM}^{2-}$ that have an m/z in the ± 0.5 m/z window selected in the CID experiment. This generates a predicted distribution of hydrogen and deuterium atoms in the isolated precursor ion.

In the second step, we calculate the probability of deuterium incorporation into the products using a hypergeometric distribution by considering two scenarios: (1) when all of the 24

hydroxyl groups participate in the reaction and (2) only 16 randomly selected hydrogen or deuterium atoms can be incorporated into the products. The second scenario represents a situation when only the secondary hydroxyl groups participate in the reaction. Knowing the total number of hydrogen and deuterium atoms in the pool (N), we calculate the probability of incorporating k deuterium atoms into n water losses (n is in the range of 1–8). This probability is given by the hypergeometric distribution in Eq. (1):

$$C(p, k) = \frac{p!}{k!(p-k)!} \cdot \frac{(N-p)!}{(2n-k)!(N-p-2n+k)!} \cdot \frac{(N)!}{(2n)!(N-2n)!} \quad (1)$$

where p represents the total number of available deuterium atoms in the pool. We note that Eq. (1) is also used to calculate the initial distribution of deuterium atoms in the second scenario described earlier, in which we limited the number of available hydrogen or deuterium atoms to 16. The calculated distributions of possible neutral losses from $m/z = 1365$ when either 24 or 16 hydroxyl groups participate in the reaction are shown in Figure 6b, c, respectively. We observe a similar bell-shaped isotopic pattern for each of the multiple water loss features in both of the simulated spectra. However, the simulated distribution in Figure 6c demonstrates a distinct shift in the center of m/z in each of the multiple water loss features with respect to the experimental isotopic distribution. The deviation of the center of m/z obtained from the simulation and the experimental value increases gradually with an increase in the number of water losses. In contrast, the experimental results are in a good agreement with the simulation, in which all of the 24 hydroxyl groups are assumed to be involved in the water loss channel (Figure 6b). We conclude that all of the 24 hydroxyl groups are involved in the observed water losses. It is unlikely that W_6POM^{2-} interacts with all the 24 hydroxyl groups prior to collisional excitation. The lack of selectivity towards specific types of hydroxyl groups in CD participating in the water loss indicates that the initial gas-phase structure of the complex may not be the determining factor in the mechanism of this fragmentation pathway.

A similar approach was used to examine fragmentation of ^{18}O -exchanged $[\gamma\text{-CD} + W_6POM]^{2-}$ anions. In these experiments, the complex was generated using the one-pot synthesis in $H_2^{18}O$. The incorporation of ^{18}O atoms into W_6POM^{2-} was confirmed using ESI-MS (Figure S6). We observe that the isotopic pattern of CD remains the same in $H_2^{16}O$ and $H_2^{18}O$ indicating that oxygen atoms of $\gamma\text{-CD}$ do not participate in the ^{18}O exchange. Meanwhile, the center of the isotopic distribution of W_6POM^{2-} shifts from $m/z = 704$ to $m/z = 722$ corresponding to the incorporation of 18 ^{18}O atoms into W_6POM^{2-} . Similarly, the center of the isotopic distribution of $[\gamma\text{-CD} + W_6POM]^{2-}$ complex is shifted from $m/z = 1352$ to $m/z = 1370$ confirming the same extent of ^{18}O exchange in the complex.

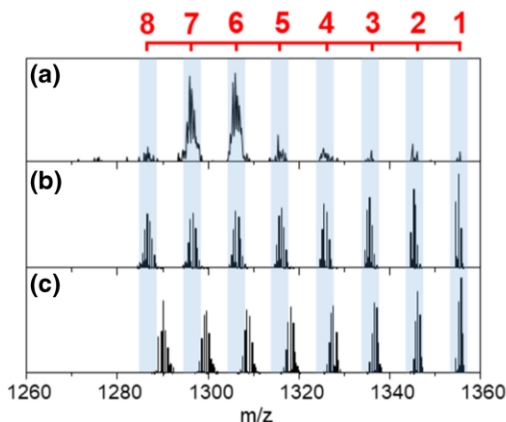


Figure 6. Experimental (a) and simulated (b, c) distributions of water losses from $m/z = 1365$ isolated from the isotopic pattern of deuterium-exchanged $[\gamma\text{-CD} + W_6POM]^{2-}$. Panel (b) shows a simulated spectrum obtained assuming that all of the 24 $-\text{OH}$ groups are available for the water loss channel; panel (c) shows a simulated spectrum obtained assuming that only 16 $-\text{OH}$ groups participate in the water loss channel. The red ruler shows the corresponding number of water losses

MS^2 spectra of the isotopic peaks of $[\gamma\text{-CD} + W_6POM]^{2-}$ from this distribution were acquired using an isolation window of $0.5\ m/z$. Figure 7a shows the low-energy CID spectrum of $m/z = 1369.5$ in the m/z range containing water loss fragments. The most abundant isotopic signal in each of the water loss features corresponds to losses of $H_2^{18}O$ molecules, which indicates that oxygen atoms of W_6POM^{2-} participate in this reaction.

We rationalize the observed isotopic distribution of multiple water losses from ^{18}O -exchanged $[\gamma\text{-CD} + W_6POM]^{2-}$ using the same statistical modeling described earlier. Three scenarios are considered in these simulations: (1) only 19 oxygen atoms of W_6POM^{2-} participate in the reaction and (2) 35 oxygen atoms of both W_6POM^{2-} and 16 primary hydroxyl groups of $\gamma\text{-CD}$ can be incorporated into the reaction product; (3) 43 oxygen atoms of both W_6POM^{2-} and all 24 hydroxyl groups of $\gamma\text{-CD}$ are involved in the process.

The calculated distributions of possible water losses from $m/z = 1369.5$ in the above-described scenarios are shown in Figure 7b–d, respectively. The simulated water loss spectrum shown in Figure 7b is in good agreement with the experimental result, showing substantial incorporation of ^{18}O into the neutral products. In contrast, simulated water loss spectra (Figure 7c, d) deviate from the experimental spectrum in both the center of m/z and shape of the isotopic distribution. These results indicate that oxygen atoms of W_6POM^{2-} are predominantly incorporated into the water molecules produced in this reaction.

Based on the results of HDX and ^{18}O exchange experiments, we conclude that the multiple water losses in the low-

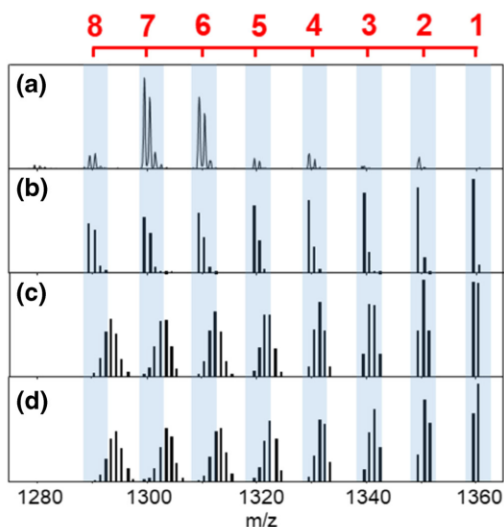


Figure 7. Experimental (a) and simulated (b–d) distributions of water losses from $m/z = 1369.5$ isolated from the isotopic pattern of ^{18}O -exchanged $[\gamma\text{-CD} + \text{W}_6\text{POM}]^{2-}$. (b–d) Simulated spectra obtained assuming that different number of oxygen atoms participate in the water loss channel: (b) only the oxygen atoms of $\text{W}_6\text{POM}^{2-}$; (c) a total of 35 oxygen atoms of both $\text{W}_6\text{POM}^{2-}$ and 16 secondary hydroxyl groups of $\gamma\text{-CD}$; (d) a total of 43 oxygen atoms of $\text{W}_6\text{POM}^{2-}$ and all 24 hydroxyl groups of $\gamma\text{-CD}$. The red ruler shows the corresponding number of water losses

energy CID spectra of $\text{CD-M}_6\text{POM}$ ($M = \text{Mo}, \text{W}$) complexes are composed of H atoms from the hydroxyl groups of CD and O atoms of $\text{M}_6\text{POM}^{2-}$. The observed fragmentation pathway may be rationalized assuming that the initial proton transfer from CD to $\text{M}_6\text{POM}^{2-}$ results in dissociation of HM_6POM^- producing reactive metal oxide species. These species subsequently undergo multiple condensation reactions with the hydroxyl groups of CD eliminating water molecules. Dehydration reactions between alcohols and multinuclear transition metal oxides in the gas phase resulting in a loss of one water molecule have been previously reported [71–73]. The reaction mechanism involves deprotonation of an alcohol by a metal oxide followed by alkoxo ligand substitution resulting in elimination of a water molecule [74]. Isotopic labeling experiments have confirmed that the oxygen atom in the resulting alkylated metal oxide product originates from the alcohol, which is consistent with our results [71]. It has been demonstrated that W-containing metal oxides are more reactive towards alcohol dehydration than their Mo-containing analogs [71]. The enhanced reactivity of W-containing metal oxides may be used to rationalize the more efficient water loss from $\text{CD-W}_6\text{POM}$ as compared to $\text{CD-Mo}_6\text{POM}$ observed in this study [75].

Conclusion

We report a systematic investigation of the gas-phase fragmentation pathways of host-guest complexes of CDs (α -, β -, and γ -CD) and small POMs (Keggin $\text{W}_{12}\text{POM}^{3-}$, Lindqvist $\text{W}_6\text{POM}^{2-}$ and $\text{Mo}_6\text{POM}^{2-}$). We observe three major fragmentation pathways under high-energy and low-energy CID conditions: proton transfer from CD to POM, direct dissociation, and a series of multiple water losses from the complex. The major dissociation channel is determined by the cavity diameter of the CD, the size of the complex, and gas-phase basicity and structural stability of the POM anion. In particular, proton transfer from CD to POM followed by the separation of $[\text{CD} - \text{H}]^-$ and $\text{HW}_{12}\text{POM}^{2-}$ in $\text{CD-W}_{12}\text{POM}$ complexes is a major channel observed in the low-energy CID spectra and attributed to the higher gas-phase basicity and stability of the $\text{W}_{12}\text{POM}^{3-}$ anion. In contrast, direct dissociation is more pronounced in HCD indicating that this is an entropically favorable pathway associated with a higher threshold energy than the proton transfer channel. An unusual fragmentation pathway observed in low-energy CID experiments of $\text{CD-W}_6\text{POM}$ and $\text{CD-Mo}_6\text{POM}$ complexes corresponds to multiple water losses from the complex. These water losses are found to occur in parallel as competing channels and are attributed to covalent coupling of the fragments of Lindqvist POM to CD accompanied by elimination of multiple water molecules upon collisional excitation. This covalent bond formation efficiently competes with other dissociation channels of the $\text{CD-W}_6\text{POM}$ and $\text{CD-Mo}_6\text{POM}$ host-guest complexes in the gas phase. The results presented in this study demonstrate the unique proton-mediated reactivity of transition metal oxide clusters for covalent modification of the macrocyclic host molecule via supramolecular gas-phase ion chemistry. Future experiments will examine the properties of the derivatized CD produced in the gas phase by depositing them onto surfaces for preparing unconventional condensed-phase materials [76–78].

Acknowledgements

The authors thank Dr. Youyun Zhou (Southern University of Science and Technology, China) for the valuable discussions. The authors also thank Jessica Townsend for the help in the graphic design. J. W. acknowledges support from a Feodor Lynen Fellowship of the Alexander von Humboldt Foundation.

References

1. Lehn, J.M.: Supramolecular chemistry—scope and perspectives molecules, supermolecules, and molecular devices (Nobel Lecture). *Angew. Chem. Int. Ed. Eng.* **27**, 89–112 (1988)
2. Steed, J.W., Turner, D.R., Wallace, K.: *Core Concepts in Supramolecular Chemistry and Nanochemistry*. Wiley, Hoboken (2007)
3. Vögtle, F., Weber, E.: *Host Guest Complex Chemistry Macrocycles: Synthesis, Structures, Applications*. Springer Science & Business Media, Berlin (2012)

4. Brown, C.J., Toste, F.D., Bergman, R.G., Raymond, K.N.: Supramolecular catalysis in metal-ligand cluster hosts. *Chem. Rev.* **115**, 3012–3035 (2015)
5. Jiao, Y., Tang, B., Zhang, Y., Xu, J.F., Wang, Z., Zhang, X.: Highly efficient supramolecular catalysis by endowing the reaction intermediate with adaptive reactivity. *Angew. Chem.* **130**, 6185–6189 (2018)
6. Zhang, D.S., Gao, Q., Chang, Z., Liu, X.T., Zhao, B., Xuan, Z.H., Hu, T.L., Zhang, Y.H., Zhu, J., Bu, X.H.: Rational construction of highly tunable donor-acceptor materials based on a crystalline host-guest platform. *Adv. Mater.* **30**, 1804715 (2018)
7. Qu, D.-H., Wang, Q.-C., Zhang, Q.-W., Ma, X., Tian, H.: Photosensitive host-guest functional systems. *Chem. Rev.* **115**, 7543–7588 (2015)
8. Mao, D., Liang, Y., Liu, Y., Zhou, X., Ma, J., Jiang, B., Liu, J., Ma, D.: Acid-labile acyclic cucurbit [n] uril molecular containers for controlled release. *Angew. Chem. Int. Ed.* **56**, 12614–12618 (2017)
9. Ma, X., Zhao, Y.: Biomedical applications of supramolecular systems based on host-guest interactions. *Chem. Rev.* **115**, 7794–7839 (2014)
10. Chandler, D.: Interfaces and the driving force of hydrophobic assembly. *Nature*. **437**, 640 (2005)
11. Schneider, H.J.: Binding mechanisms in supramolecular complexes. *Angew. Chem. Int. Ed.* **48**, 3924–3977 (2009)
12. Assaf, K.I., Nau, W.M.: The chaotropic effect as an assembly motif in chemistry. *Angew. Chem. Int. Ed.* **57**, 13968–13981 (2018)
13. Kaabel, S., Adamson, J., Topić, F., Kiesilä, A., Kalenius, E., Öeren, M., Reimund, M., Prigorenko, E., Löökene, A., Reich, H.J.: Chiral hemicucurbit [8] uril as an anion receptor: selectivity to size, shape and charge distribution. *Chem. Sci.* **8**, 2184–2190 (2017)
14. Gibb, C.L., Gibb, B.C.: Anion binding to hydrophobic concavity is central to the salting-in effects of Hofmeister chaotropes. *J. Am. Chem. Soc.* **133**, 7344–7347 (2011)
15. Assaf, K.I., Ural, M.S., Pan, F., Georgiev, T., Simova, S., Rissanen, K., Gabel, D., Nau, W.M.: Water structure recovery in chaotropic anion recognition: high-affinity binding of dodecaborate clusters to γ -cyclodextrin. *Angew. Chem. Int. Ed.* **54**, 6852–6856 (2015)
16. Sullivan, M.R., Yao, W., Tang, D., Ashbaugh, H.S., Gibb, B.C.: The thermodynamics of anion complexation to nonpolar pockets. *J. Phys. Chem. B.* **122**, 1702–1713 (2018)
17. Assaf, K.I., Gabel, D., Zimmermann, W., Nau, W.M.: High-affinity host-guest chemistry of large-ring cyclodextrins. *Org. Biomol. Chem.* **14**, 7702–7706 (2016)
18. Assaf, K.I., Hennig, A., Peng, S., Guo, D.-S., Gabel, D., Nau, W.M.: Hierarchical host-guest assemblies formed on dodecaborate-coated gold nanoparticles. *Chem. Commun.* **53**, 4616–4619 (2017)
19. Warneke, J., Jenne, C., Bernarding, J., Azov, V.A., Plaumann, M.: Evidence for an intrinsic binding force between dodecaborate dianions and receptors with hydrophobic binding pockets. *Chem. Commun.* **52**, 6300–6303 (2016)
20. Bachecker, T., Schmid, P., Renaudineau, S., Diat, O., Proust, A., Pfitzner, A., Bauduin, P.: Polyoxometalates in the Hofmeister series. *Chem. Commun.* **54**, 1833–1836 (2018)
21. Naskar, B., Diat, O., Nardello-Rataj, V.R., Bauduin, P.: Nanometer-size polyoxometalate anions adsorb strongly on neutral soft surfaces. *J. Phys. Chem. C.* **119**, 20985–20992 (2015)
22. Pang, H.-j., Peng, J., Zhang, C.-j., Li, Y.-g., Zhang, P.-p., Ma, H.-y., Su, Z.-m.: A polyoxometalate-encapsulated 3D porous metal-organic pseudo-rotaxane framework. *Chem. Commun.* **46**, 5097–5099 (2010)
23. Cao, H.-L., Cai, F.-Y., Huang, H.-B., Karadeniz, B., Lü, J.: Polyoxometalate-cucurbituril molecular solid as photocatalyst for dye degradation under visible light. *Inorg. Chem. Commun.* **84**, 164–167 (2017)
24. Fang, X., Kögerler, P., Isaacs, L., Uchida, S., Mizuno, N.: Cucurbit [n] uril-polyoxoanion hybrids. *J. Am. Chem. Soc.* **131**, 432–433 (2008)
25. Goel, T., Baroah, N., Mallia, M.B., Bhasikuttan, A.C., Mohanty, J.: Recognition-mediated cucurbit [7] uril-heptamolybdate hybrid material: a facile supramolecular strategy for $99m$ Tc separation. *Chem. Commun.* **52**, 7306–7309 (2016)
26. Ishii, Y., Takenaka, Y., Konishi, K.: Porous organic-inorganic assemblies constructed from Keggin polyoxometalate anions and calix [4] arene- Na^+ complexes: structures and guest-sorption profiles. *Angew. Chem.* **116**, 2756–2759 (2004)
27. Tian, A., Lin, X., Ying, J., Zhang, J., Lin, H., Liu, G., Zhao, D., Li, N., Wang, X.: Self-assembly of a molecular crown as a structural analogue of calix [4] arene to modify Keggin anions. *Dalton Trans.* **42**, 9809–9812 (2013)
28. Su, P., Prabhakaran, V., Johnson, G.E., Laskin, J.: In situ infrared spectroelectrochemistry for understanding structural transformations of precisely defined ions at electrochemical interfaces. *Anal. Chem.* **90**, 10935–10942 (2018)
29. Prabhakaran, V., Lang, Z., Clotet, A., Poblet, J.M., Johnson, G.E., Laskin, J.: Controlling the activity and stability of electrochemical interfaces using atom-by-atom metal substitution of redox species. *ACS Nano.* **13**, 458–466 (2018)
30. Martín-Sabi, M., Soriano-López, J., Winter, R.S., Chen, J.-J., Vilà-Nadal, L., Long, D.-L., Galán-Mascarós, J.R., Cronin, L.: Redox tuning the Weakley-type polyoxometalate archetype for the oxygen evolution reaction. *Nat. Catal.* **1**, 208 (2018)
31. Szejtli, J.: Introduction and general overview of cyclodextrin chemistry. *Chem. Rev.* **98**, 1743–1754 (1998)
32. Montes-García, V., Pérez-Juste, J., Pastoriza-Santos, I., Liz-Marzán, L.M.: Metal nanoparticles and supramolecular macrocycles: a tale of synergy. *Chem. Eur. J.* **20**, 10874–10883 (2014)
33. Engel, S., Möller, N., Ravoo, B.J.: Stimulus-responsive assembly of nanoparticles using host-guest interactions of cyclodextrins. *Chem. Eur. J.* **24**, 4741–4748 (2018)
34. Zhang, P., Mejjide Suárez, J., Driant, T., Derat, E., Zhang, Y., Ménand, M., Roland, S., Sollogoub, M.: Cyclodextrin cavity-induced mechanistic switch in copper-catalyzed hydroboration. *Angew. Chem.* **129**, 10961–10965 (2017)
35. Li, H., Meng, B., Chai, S.-H., Liu, H., Dai, S.: Hyper-crosslinked β -cyclodextrin porous polymer: an adsorption-facilitated molecular catalyst support for transformation of water-soluble aromatic molecules. *Chem. Sci.* **7**, 905–909 (2016)
36. Jing, J., Szarapak-Jankowska, A., Guillot, R., Pignot-Paintrand, I., Picart, C., Auzély-Velty, R.: Cyclodextrin/paclitaxel complex in biodegradable capsules for breast cancer treatment. *Chem. Mater.* **25**, 3867–3873 (2013)
37. Zhou, J., Yu, G., Huang, F.: Supramolecular chemotherapy based on host-guest molecular recognition: a novel strategy in the battle against cancer with a bright future. *Chem. Soc. Rev.* **46**, 7021–7053 (2017)
38. Wu, Y., Shi, R., Wu, Y.-L., Holcroft, J.M., Liu, Z., Frascioni, M., Wasielewski, M.R., Li, H., Stoddart, J.F.: Complexation of polyoxometalates with cyclodextrins. *J. Am. Chem. Soc.* **137**, 4111–4118 (2015)
39. Moussawi, M.A., Leclerc-Laronze, N., Floquet, S., Abramov, P.A., Sokolov, M.N., Cordier, S., Ponchel, A., Monflier, E., Bricout, H., Landy, D.: Polyoxometalate, cationic cluster, and γ -cyclodextrin: from primary interactions to supramolecular hybrid materials. *J. Am. Chem. Soc.* **139**, 12793–12803 (2017)
40. Moussawi, M.A., Haouas, M., Floquet, S., Shepard, W.E., Abramov, P.A., Sokolov, M.N., Fedin, V.P., Cordier, S., Ponchel, A., Monflier, E.: Nonconventional three-component hierarchical host-guest assembly based on Mo-blue ring-shaped giant anion, γ -cyclodextrin, and Dawson-type polyoxometalate. *J. Am. Chem. Soc.* **139**, 14376–14379 (2017)
41. Zhang, B., Guan, W., Yin, F., Wang, J., Li, B., Wu, L.: Induced chirality and reversal of phosphomolybdate cluster via modulating its interaction with cyclodextrins. *Dalton Trans.* **47**, 1388–1392 (2018)
42. Yang, P., Zhao, W., Shkurenko, A., Belmabhou, Y., Eddaoudi, M., Dong, X., Alshareef, H.N., Khashab, N.M.: Polyoxometalate-cyclodextrin metal-organic frameworks: from tunable structure to customized storage functionality. *J. Am. Chem. Soc.* **141**, 1847–1851 (2019)
43. Stuckart, M., Izarova, N.V., van Leusen, J., Smekhova, A., Schmitz-Antoniak, C., Bamberger, H., van Slageren, J., Santiago-Schübel, B., Kögerler, P.: Host-guest-induced environment tuning of 3d ions in a polyoxopalladate matrix. *Chem. Eur. J.* **24**, 17767–17778 (2018)
44. Gabelica, V., Galic, N., De Pauw, E.: On the specificity of cyclodextrin complexes detected by electrospray mass spectrometry. *J. Am. Soc. Mass Spectrom.* **13**, 946–953 (2002)
45. Schalley, C.A.: Supramolecular chemistry goes gas phase: the mass spectrometric examination of noncovalent interactions in host-guest chemistry and molecular recognition. *Int. J. Mass Spectrom.* **194**, 11–39 (2000)
46. Weimann, D.P., Schalley, C.A.: Host-guest chemistry of self-assembling supramolecular capsules in the gas phase. *Supramol. Chem.* **20**, 117–128 (2008)
47. Qi, Z., Heinrich, T., Moorthy, S., Schalley, C.A.: Gas-phase chemistry of molecular containers. *Chem. Soc. Rev.* **44**, 515–531 (2015)

48. Lebrilla, C.B.: The gas-phase chemistry of cyclodextrin inclusion complexes. *Acc. Chem. Res.* **34**, 653–661 (2001)
49. Penn, S.G., He, F., Lebrilla, C.B.: Peptides complexed to cyclodextrin fragment rather than dissociate when subjected to blackbody infrared radiation. *J. Phys. Chem. B.* **102**, 9119–9126 (1998)
50. Vrkic, A.K., O'Hair, R.A., Lebrilla, C.B.: Unusual covalent bond-breaking reactions of β -cyclodextrin inclusion complexes of nucleobases/nucleosides and related guest molecules. *Eur. J. Mass Spectrom.* **9**, 563–577 (2003)
51. Ma, X., Wei, Z., Xiong, X., Jiang, Y., He, J., Zhang, S., Fang, X., Zhang, X.: Gas-phase fragmentation of host-guest complexes between β -cyclodextrin and small molecules. *Talanta.* **93**, 252–256 (2012)
52. Bakhtiar, R., Kaifer, A.: Mass spectrometry studies on the complexation of several organometallic complexes by α - and β -cyclodextrins. *Rapid Commun. Mass Spectrom.* **12**, 111–114 (1998)
53. Fan, Y., Lu, S., Cao, J.: A novel inorganic-organic hybrid complex between polyoxometalate and cyclodextrin: synthesis, structure and catalytic activity. *Int. J. Mass Spectrom.* **435**, 163–167 (2019)
54. Fan, Y., Zhang, Y., Jia, Q., Cao, J., Wu, W.: The stabilizing role of cyclodextrins on Keggin phosphotungstic acid by complexation unveiled by electrospray mass spectrometry. *Mass Spectrom. Lett.* **6**, 13–16 (2015)
55. Julian, R.R., May, J.A., Stoltz, B.M., Beauchamp, J.: Molecular mouse-traps: gas-phase studies of the covalent coupling of noncovalent complexes initiated by reactive carbenes formed by controlled activation of diazo precursors. *Angew. Chem. Int. Ed.* **42**, 1012–1015 (2003)
56. Julian, R.R., May, J.A., Stoltz, B.M., Beauchamp, J.: Biomimetic approaches to gas phase peptide chemistry: combining selective binding motifs with reactive carbene precursors to form molecular mousetraps. *Int. J. Mass Spectrom.* **228**, 851–864 (2003)
57. Schaefer, M.: Supramolecular crown ether adducts in the gas phase: from molecular recognition of amines to the covalent coupling of host/guest molecules. *Angew. Chem. Int. Ed.* **42**, 1896–1899 (2003)
58. Lee, T.-C., Kalenius, E., Lazar, A.I., Assaf, K.I., Kühnert, N., Grün, C.H., Jänis, J., Scheman, O.A., Nau, W.M.: Chemistry inside molecular containers in the gas phase. *Nat. Chem.* **5**, 376 (2013)
59. Falaise, C., Moussawi, M.A., Floquet, S., Abramov, P.A., Sokolov, M.N., Haouas, M., Cadot, E.: Probing dynamic library of metal-oxo building blocks with γ -cyclodextrin. *J. Am. Chem. Soc.* **140**, 11198–11201 (2018)
60. Klempner, W.G.: Tetrabutylammonium isopolyoxometalates. *Inorg. Synth.* **27**, 74–85 (1990)
61. Fetterolf, D., Yost, R.-A.: Energy-resolved collision-induced dissociation in tandem mass spectrometry. *Int. J. Mass Spectrom. Ion Phys.* **44**, 37–50 (1982)
62. Wells, J.M., McLuckey, S.A.: Collision-induced dissociation (CID) of peptides and proteins. *Methods Enzymol.* **402**, 148–185 (2005)
63. Bayat, P., Gatineau, D., Lesage, D., Marhabaie, S., Martinez, A., Cole, R.B.: Investigation of activation energies for dissociation of host-guest complexes in the gas phase using low-energy collision induced dissociation. *J. Mass Spectrom.* **54**, 437–448 (2019)
64. Vinokur, N., Ryzhov, V.: Using collision-induced dissociation with corrections for the ion number of degrees of freedom for quick comparisons of relative bonding strength. *J. Mass Spectrom.* **39**, 1268–1274 (2004)
65. Ganapathy, S., Fournier, M., Paul, J., Delevoye, L., Guelton, M., Amoureux, J.: Location of protons in anhydrous Keggin heteropolyacids $H_3PMo_{12}O_{40}$ and $H_3PW_{12}O_{40}$ by 1H $\{^{31}P\}/^{31}P$ $\{^1H\}$ REDOR NMR and DFT quantum chemical calculations. *J. Am. Chem. Soc.* **124**, 7821–7828 (2002)
66. Li, Z., Couzjin, E.P., Zhang, X.: Intrinsic properties of α -cyclodextrin complexes with benzoate derivatives in the gas phase: an experimental and theoretical study. *J. Phys. Chem. B.* **116**, 943–950 (2012)
67. Jenne, C., Keßler, M., Warneke, J.: Protic anions $[H(B_{12}X_{12})]$ ($X = F, Cl, Br, I$) that act as Brønsted acids in the gas phase. *Chem. Eur. J.* **21**, 5887–5891 (2015)
68. Li, S., Dixon, D.A.: Molecular and electronic structures, Brønsted basicities, and Lewis acidities of group VIB transition metal oxide clusters. *J. Phys. Chem. A.* **110**, 6231–6244 (2006)
69. Price, N.P.: Oligosaccharide structures studied by hydrogen–deuterium exchange and MALDI-TOF mass spectrometry. *Anal. Chem.* **78**, 5302–5308 (2006)
70. Kellersberger, K.A., Dejsupa, C., Liang, Y., Pope, R.M., Dearden, D.V.: Gas phase studies of ammonium–cyclodextrin compounds using Fourier transform ion cyclotron resonance. *Int. J. Mass Spectrom.* **193**, 181–195 (1999)
71. Waters, T., O'Hair, R.A., Wedd, A.G.: Catalytic gas phase oxidation of methanol to formaldehyde. *J. Am. Chem. Soc.* **125**, 3384–3396 (2003)
72. Llusar, R., Sorribes, I., Vicent, C.: Electrospray ionization based methods for the generation of polynuclear oxo- and hydroxo group 6 anions in the gas-phase. *J. Clust. Sci.* **20**, 177–192 (2009)
73. Harris, B.L., Waters, T., Khairallah, G.N., O'Hair, R.A.: Gas-phase reactions of $[VO_2(OH)_2]$ and $[V_2O_5(OH)]$ with methanol: experiment and theory. *J. Phys. Chem. A.* **117**, 1124–1135 (2012)
74. Jackson, P., Fisher, K.J., Willett, G.D.: The catalytic activation of primary alcohols on niobium oxide surfaces unraveled: the gas phase reactions of Nb_5O_{15} clusters with methanol and ethanol. *Chem. Phys.* **262**, 179–187 (2000)
75. Waters, T., O'Hair, R.A., Wedd, A.G.: Gas-phase reactivity of heterobimuclear oxometalate anions $[CrMoO_8(OR)]$, $[CrWO_8(OR)]$, and $[MoWO_8(OR)]$ ($R = H, tBu$). *Inorg. Chem.* **44**, 3356–3366 (2005)
76. Laskin, J., Johnson, G.E., Warneke, J., Prabhakaran, V.: From isolated ions to multilayer functional materials using ion soft-landing. *Angew. Chem. Int. Ed.* **57**, 16270–16284 (2018)
77. Warneke, J., McBriarty, M.E., Riechers, S.L., China, S., Engelhard, M.H., Apra, E., Young, R.P., Washton, N.M., Jenne, C., Johnson, G.E., Laskin, J.: Self-organizing layers from complex molecular anions. *Nat. Commun.* **9**, 1889 (2018)
78. Su, P., Hu, H., Warneke, J., Belov, M.E., Anderson, G.A., Laskin, J.: Design and performance of a dual-polarity instrument for ion soft landing. *Anal. Chem.* **91**, 5904–5912 (2019)

Mass Spectrometry

Preparative Mass Spectrometry Using a Rotating-Wall Mass Analyzer

Pei Su, Hang Hu, Daisy Unsihuay, Di Zhang, Tiziano Dainese, Rosa E. Diaz, Jongsu Lee, Don K. Gunaratne, Haiyan Wang, Flavio Maran, Jianguo Mei, and Julia Laskin*

Abstract: The design of functional interfaces is central to both fundamental and applied research in materials science and energy technology. We introduce a new, broadly applicable technique for the precisely controlled high-throughput preparation of well-defined interfaces containing polyatomic species ranging from small ions to nanocrystals and large protein complexes. The mass-dispersive deposition of ions onto surfaces is achieved using a rotating-wall mass analyzer, a compact device which enables the separation of ions using low voltages and has a theoretically unlimited mass range. We demonstrate an efficient deposition of singly charged $Au_{144}(SC_4H_9)_{60}$ ions (33.7 kDa), which opens up exciting opportunities for the structural characterization of nanocrystals and their assemblies using transmission electron microscopy. Our approach also enables the high-throughput deposition of mass-selected ions from multicomponent mixtures, which is of interest to the controlled preparation of surface gradients and rapid screening of molecules in mixtures for a specific property.

The deposition of well-defined polyatomic species onto surfaces is a powerful approach for the precisely controlled preparation of interfaces for materials design and synthesis.^[1] Mass spectrometry (MS) is a powerful preparative tool due to its ability to generate mass- and charge-selected polyatomic ions in the gas phase and deposit them onto surfaces under controlled conditions.^[2] Gentle deposition of ions on surfaces with or without the retention of charge in a process referred to as ion soft-landing^[3] helps preserve the structure and, in

specific cases, the reactivity of the ion.^[4] Furthermore, the ability to control surface coverage, spot size, and pattern makes ion soft-landing particularly advantageous for the preparation of coatings, thin films, and the selective doping of materials.^[5] Ion soft-landing has been employed to prepare protein and peptide arrays,^[6] nanocluster-based catalysts,^[7] electrochemical interfaces,^[8] self-organizing layers,^[9] as well as optical^[10] and magnetic thin films.^[11]

A majority of preparative MS instruments utilize quadrupole^[12] and lateral time-of-flight analyzers^[13] as mass-filtering devices. Despite the significant advances in soft-landing instrumentation,^[14] mass filtering limits the deposition to one species at a time and requires specialized high-voltage electronics. The broader application of preparative MS will benefit from the development of simple, low-cost, and compact instruments. Ambient soft-landing systems have been developed to address this need and improve the scalability of the technique.^[15] However, the ability to deposit mass-selected ions in a high-throughput manner is still limited. Furthermore, mass-filtering devices traditionally used in soft-landing experiments are limited to lower-mass ions ($m/z < 4000$), which hinders their application to nanomaterials design and protein-structure characterization.

Herein, we address some of these limitations by introducing a straightforward approach for mass-selected ion deposition using a rotating-wall mass analyzer (RWMA, Figure 1A). A RWMA enables the dispersive deposition of ions with different m/z ratio onto distinct locations on a surface by separating them in space. This device has a theoretically unlimited mass range and enables the deposition of ions originating from multicomponent mixtures onto substrates in a high-throughput manner. Although RWMAs have been previously employed as mass analyzers,^[16] they are used as a preparative device for the first time in this study. RWMAs are well-suited for applied research since they separate ions using low radio-frequency (rf) voltages ($\leq 10 V_0$, p) and kHz frequencies provided by inexpensive waveform generators, making ion soft-landing accessible to the broader scientific community. Furthermore, the small size of RWMAs is advantageous to the development of miniature preparative MS instrumentation.

A RWMA is comprised of a cylinder segmented lengthwise into eight identical arc-shaped electrodes (Figure 1A). A constant-strength rotating electric field is constructed by applying sinusoidal waveforms of identical frequency and amplitude to the eight electrodes with a sequential 45° phase shift between the adjacent electrodes (Figure 1B). The rotating electric field has the same frequency as that of the sinusoidal waveforms. When a continuous ion beam collimated using an einzel lens is transferred through the RWMA, ions of different m/z ratio are separated into concentric rings

* P. Su, H. Hu, D. Unsihuay, J. Lee, Prof. J. Mei, Prof. J. Laskin
Department of Chemistry, Purdue University
560 Oval Drive, West Lafayette, IN 47907 (USA)
E-mail: jlaskin@purdue.edu

D. Zhang, Prof. H. Wang
School of Materials Engineering, Purdue University
701 W. Stadium Avenue, West Lafayette, IN 47907 (USA)

Dr. T. Dainese, Prof. F. Maran
Department of Chemistry, University of Padova
1, Via Marzolo, Padova 35131 (Italy)

Dr. R. E. Diaz
Birk Nanotechnology Center, Discovery Park, Purdue University
1205 W. State St., West Lafayette, IN 47907 (USA)

Dr. D. K. Gunaratne
Physical Science Division, Pacific Northwest National Laboratory
P.O. Box 999, MSIN K8-88, Richland, WA 99352 (USA)

Prof. H. Wang
School of Electrical and Computer Engineering, Purdue University
465 Northwestern Avenue, West Lafayette, IN 47907 (USA)

Supporting information and the ORCID identification number(s) for the author(s) of this article can be found under:
<https://doi.org/10.1002/anie.202000065>.

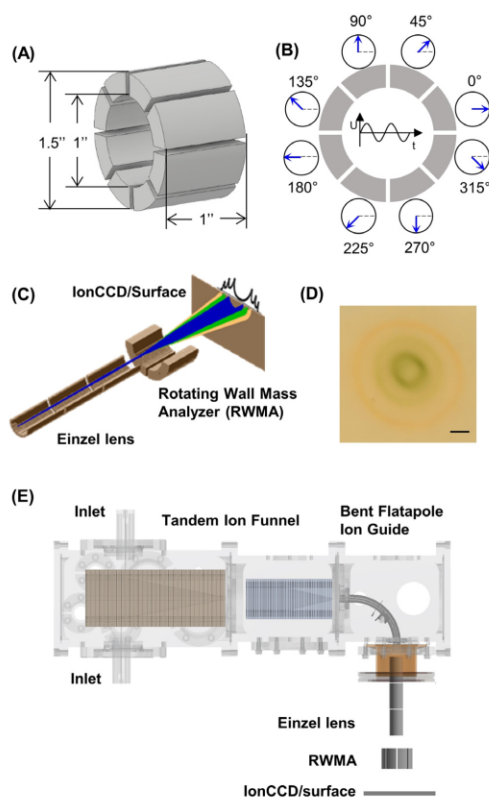


Figure 1. A) Schematic drawing of the rotating-wall mass analyzer (RWMA). B) Diagram showing the phases of the sinusoidal rf waveforms applied to the eight electrodes. C) Schematic drawing extracted from SIMION simulations illustrating the dispersive separation of ions based on their m/z ratio using a RWMA. A beam containing a mixture of three dyes ($m/z = 253$: yellow, 330: green, and 470: blue) produced by ESI is collimated using an einzel lens, separated using a RWMA, and collected on the IonCCD/surface. The three dyes are separated into distinct rings and detected as three pairs of signals on the one-dimensional profile of the IonCCD (black trace). D) Optical image of a surface containing soft-landed yellow/green/blue dyes dispersed by a RWMA ($f = 100$ kHz, $V_{0-p} = 10$ V) into three rings. Scale bar: 2 mm. E) Schematic diagram of the ion-soft-landing setup used in this study. Details of the high-flux ESI interface are provided in ref. [4e].

(Figure 1 C). Ion-beam characterization prior to deposition is performed using a one-dimensional position-sensitive IonCCD detector^[17] positioned perpendicular to the RWMA with its center aligned with the instrument axis. When a ring-shaped ion beam of a specific m/z ratio is detected using an IonCCD, it generates a pair of peaks symmetrically located around the center of the detector. The IonCCD detector is subsequently replaced by a collector surface for ion soft-landing experiments.

Ion-trajectory simulations for three dyes of different m/z ratio (Figure 1 C) using the SIMION software and a photo-

graph of the experimentally obtained deposition spot (Figure 1 D) show three concentric rings of different radii; the corresponding IonCCD profile is shown as a black trace in Figure 1 C. The dimensions of the RWMA (Figure 1 A) were optimized using SIMION simulations to facilitate the separation of hyperthermal (< 100 eV) ions. The device was subsequently coupled to a high-transmission electrospray-ionization (ESI) interface described in a previous study (Figure 1 E).^[4e] The ESI interface generates a collimated ion beam of ≈ 2 mm diameter with a well-defined kinetic energy and can be readily tuned for the transmission of ions over a broad mass range. Although in this study, the RWMA was operated at a pressure of $5 \times 10^{-5} - 1 \times 10^{-4}$ torr, we estimate, based on mean-free-path calculations, that in its current configuration, the device can be operated at a pressure of up to 1×10^{-3} torr. A higher pressure may affect the separation performance due to collisions of the ions with background gas molecules.

An analytical equation [Eq. (10) in Section S2 of the Supporting Information] is used to predict the radius of the deposition ring. The radius is determined by the m/z ratio and kinetic energy of the ion, the frequency and amplitude of the rotating electric field, and the distance between the RWMA and the surface. The frequency of the rotating electric field determines the m/z range for which the best separation is achieved. For example, we used $f = 70 - 100$ kHz for $m/z < 1000$ and $f = 7 - 10$ kHz for $m/z > 10000$. SIMION simulations were used to optimize the distances between the RWMA, einzel lens, and surface necessary to maintain a well-defined rotating electric field. A distance of 0.5" between the RWMA and einzel lens is used to prevent a substantial field penetration into the device (Figure S3, Supporting Information). Minimal perturbation of the rotating electric field is obtained when the surface is positioned at least 0.5" away from the RWMA. The actual position of the surface is selected based on the desired radius of the separated ion beam. We note that the experimentally measured radius of the ring deviates from its predicted value due to a quadratic decay of the field outside of the RWMA (Figure S3). The effective length and average strength of the rotating field can be calibrated using a model compound (Supporting Information, Section S4); the resulting values are subsequently used to predict the deposition radius for a particular ionic species.

The ability of RWMA to separate high-mass ions using low rf amplitudes is demonstrated using an atomically precise $\text{Au}_{144}(\text{SC}_4\text{H}_9)_{60}$ cluster (33.7 kDa) as a model system.^[18] Owing to its distinct electrochemical,^[18] optical,^[19] biological,^[20] and catalytic properties,^[21] $\text{Au}_{144}(\text{SR})_{60}$ (Figure 2 A) is one of the most widely studied thiolated gold clusters. Previous studies employed ESI-MS to determine the composition of atomically precise $\text{Au}_{144}(\text{SR})_{60}$ clusters;^[22,23] structural characterization was performed using scanning transmission-electron microscopy (STEM),^[24] nuclear magnetic resonance,^[22] single-crystal X-ray diffraction,^[25] and theoretical calculations.^[22,24,26] In this experiment, we do not attempt to separate this cluster from a mixture, but rather demonstrate that a specific charge state of the $\text{Au}_{144}(\text{SR})_{60}$ cluster may be deposited onto a surface for subsequent structure determination. Furthermore, the high-flux deposition of

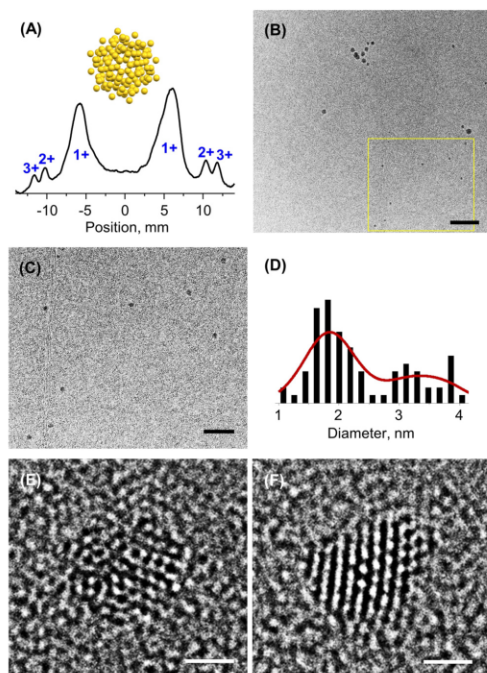


Figure 2. A) Gold-atom arrangement in $\text{Au}_{144}(\text{SCH}_2\text{Ph})_{60}^{2+}$ and the IonCCD beam profile showing $\text{Au}_{144}(\text{SC}_4\text{H}_9)_{60}^{n+}$ ($n=1,2,3$) separated by a RWMA at $f=7$ kHz, $10 V_{0-p}$ when the IonCCD was positioned $1''$ after the RWMA. The charge states of $\text{Au}_{144}(\text{SC}_4\text{H}_9)_{60}^{n+}$ are labelled on top of the peaks. B) TEM images of $\text{Au}_{144}(\text{SC}_4\text{H}_9)_{60}^{n+}$ deposited onto a graphene-coated Cu grid acquired at 300 kV acceleration voltage. Scale bar: 20 nm. C) Expanded view of an area of the TEM image highlighted by the yellow square in panel (B) containing monodisperse $\text{Au}_{144}(\text{SC}_4\text{H}_9)_{60}^{n+}$ clusters. Scale bar: 10 nm. D) Cluster-size distribution extracted from the TEM image in (B). E) Representative HRTEM image of an individual $\text{Au}_{144}(\text{SC}_4\text{H}_9)_{60}^{n+}$ cluster acquired at 300 kV acceleration voltage. F) HRTEM image of the cluster shown in (E) after electron-beam irradiation. Scale bar: 1 nm.

cluster ions reported in this study provides a direct path for the preparation of cluster-based multilayered assemblies.

In these experiments, cationic $\text{Au}_{144}(\text{SC}_4\text{H}_9)_{60}^{n+}$ clusters produced by ESI were separated using the RWMA operating at $f=7$ kHz and $V_{0-p}=10$ V. We obtained almost 1 nA of ion current for $\text{Au}_{144}(\text{SC}_4\text{H}_9)_{60}^{n+}$ clusters on a surface positioned after the RWMA. The kinetic energy of the ions entering the RWMA was 35 eV per elementary charge. The IonCCD mounted $1''$ away from the RWMA showed two major peaks corresponding to singly charged $\text{Au}_{144}(\text{SC}_4\text{H}_9)_{60}^{+}$ ions ($m/z=33.7k$; Figure 2 A). Additionally, we observed minor signals of $\text{Au}_{144}(\text{SC}_4\text{H}_9)_{60}^{2+}$ ($m/z=16.9k$) and $\text{Au}_{144}(\text{SC}_4\text{H}_9)_{60}^{3+}$ ($m/z=11.2k$) at larger radii, which agrees with previously reported charge-state distributions of $\text{Au}_{144}(\text{SR})_{60}$ in ESI-MS.^[22,23] The results obtained at different frequencies of the rotating field are shown in Figure S4. The experimentally observed radii of $\text{Au}_{144}(\text{SC}_4\text{H}_9)_{60}^{n+}$ cations are consistent with the simulated

values (Figure S5). Furthermore, in Figure S6, we show the ability to separate the charge-state distribution of Apoferritin (480 kDa), a cage-like protein complex extensively studied by cryogenic electron microscopy^[46] and native MS.^[27]

We used the same conditions to deposit singly charged $\text{Au}_{144}(\text{SC}_4\text{H}_9)_{60}^{+}$ clusters onto a graphene-coated TEM copper grid. A specially-designed TEM-grid holder was used to position the grid within the ring-shaped $\text{Au}_{144}(\text{SC}_4\text{H}_9)_{60}^{+}$ ion beam (Figure S7). To ensure gentle deposition, the kinetic energy of the cluster was reduced to ≈ 3 eV by biasing the grid. Both TEM (Figure 2 B,C) and STEM (Figure S8) images confirm that a substantial fraction of $\text{Au}_{144}(\text{SC}_4\text{H}_9)_{60}^{n+}$ clusters are deposited uniformly as dimensionally intact species with the expected diameter of ≈ 1.8 nm.^[25] The bimodal cluster-size distribution (Figure 2 D) indicates that some of the clusters aggregate on the TEM grid, as also seen in Figure 2 B. The aggregation is likely driven by the mobility of the $\text{Au}_{144}(\text{SC}_4\text{H}_9)_{60}^{n+}$ clusters on the TEM grid at room temperature and could be either induced by the electron beam or thermal processes on the surface.^[24] A similar bimodal size distribution has been previously reported for $\text{Au}_{25}(\text{S}(\text{CH}_2)_2\text{Ph})_{18}$ clusters drop-cast onto TEM grids.^[28]

A representative high-resolution TEM (HRTEM) image of an individual $\text{Au}_{144}(\text{SC}_4\text{H}_9)_{60}^{n+}$ cluster is shown in Figure 2 E. The observed cluster core is consistent with the known icosahedral structure of $\text{Au}_{144}(\text{SR})_{60}$.^[25] However, we cannot rule out a possible beam-induced rearrangement of the cluster. Indeed, a substantially different face-centered-cubic (fcc)-like gold core arrangement was observed for the same cluster after several frame shots (Figure 2 F). Additional HRTEM images are shown in Figure S9. The observed rearrangement is attributed to the acceleration voltage used in the study. It has been shown that radiation damage of $\text{Au}_{144}(\text{SC}_2\text{H}_4\text{Ph})_{60}$ clusters may be minimized using a lower acceleration voltage of 80 kV.^[23] Regardless, the apparent low level of background noise in the sample prepared by ion soft-landing results in the enhanced image contrast observed in HRTEM experiments. The use of a RWMA substantially expands the range of ion-soft-landing applications in nanocluster research, bringing it to the boundary between nanoclusters and nanocrystals. The uniform deposition of $\text{Au}_{144}(\text{SC}_4\text{H}_9)_{60}^{n+}$ clusters onto TEM grids enabled by this technique is particularly advantageous for their structure determination using low-electron-dose HRTEM single-particle reconstruction^[29] and STEM-nanobeam electron diffraction.^[24,30]

Separation and simultaneous deposition of ions with different m/z ratios by spreading them onto a surface based on their m/z value is another important attribute of RWMAs. This capability facilitates the high-throughput deposition of species present in multicomponent mixtures, which is of interest to the rapid screening of their mass- or size-dependent properties. We note that when mass filtering is employed in preparative mass-spectrometry experiments focused on separating and screening components of mixtures, the experimental throughput is determined by the complexity of the mixture. In contrast, mass-dispersive devices such as RWMAs enable a simultaneous deposition of all components onto distinct locations on a surface determined by their m/z ratio. Additionally, mass-dispersive soft-landing of mixtures

may be used to prepare physical and chemical gradients on surfaces.^[31]

Polymer surfaces with a wettability gradient have been used in biomedical research for protein adsorption and cell adhesion.^[32] In this study, we prepared a wettability gradient by spreading hydrophilic polyacrylamide (PAM) oligomers onto a hydrophobic fluorinated self-assembled monolayer (FSAM) surface. In this experiment, different oligomers are deposited onto different rings on the surface. We expect that the hydrophilicity of the surface manifested by a decrease in the contact angle will increase with the length of the hydrophilic oligomer. Traditionally, contact-angle measurement between a surface and a water droplet is used to evaluate the hydrophilicity or hydrophobicity of a surface. Hydrophilic surfaces are characterized by contact angles $< 90^\circ$ and hydrophobic surfaces display contact angles $> 90^\circ$. A negative-mode ESI-MS spectrum of PAM ($M_n = 1500$) shown in Figure 3A contains deprotonated oligomer anions spaced by $m/z = 71$.^[33] A mixture of PAM oligomers was separated using a RWMA operated at $f = 70$ kHz and $V_{0-p} = 10$ V. The IonCCD positioned at a distance of $2''$ from the RWMA showed an eagle-wing-like beam profile composed of multiple rings corresponding to the oligomer series (Figure 3B). The prepared surface was analyzed by spatially resolved nanospray-desorption electrospray-ionization (nano-DESI) MS.^[34] In this experiment, described in detail elsewhere,^[35] line scans were acquired across the deposition area, providing information on the spatial localization of individual oligomers. The resulting profile of the spatial distribution of the oligomers is shown in Figure 3C. The total oligomer signal (black trace) is consistent with the IonCCD profile (Figure 3B), confirming the spatial separation of oligomeric species on the surface based on their m/z ratio. As expected, the diameter of the ring decreases with an increase in the m/z ratio of the oligomer. The mass resolution of the RWMA was determined by taking the ratio of the deposition radius of an individual component and the FWHM of the peak observed in the nano-DESI profile. Based on the observed profiles, we estimate that in this configuration, the mass resolution of the RWMA is $m/\Delta m = 5-10$. This value is somewhat lower than the mass resolution of preparative mass spectrometers used in nanocluster research ($m/\Delta m = 20-50$).^[12a,13a] The mass resolution of RWMA can be improved using a more tightly focused ion beam.

The presence of the wettability gradient on the surface containing the PAM oligomers was confirmed using contact-angle measurements (Figure 4A). Small water droplets ($1 \mu\text{L}$) were placed on the surface from the edge to the center, where PAM oligomers of increased length were deposited. We observed that the contact angle of the surface decreases with an increase in the oligomer size, indicating a gradual increase in the hydrophilicity of the surface. Further evidence of the wettability gradient was inferred from nano-DESI experiments. Specifically, we observed that the peak width of the nano-DESI profiles of individual oligomers increases with oligomer size (Figure S10). This broadening of the individual profiles is attributed to an increase in the size of the liquid bridge when it is brought in contact with the more hydrophilic part of the surface containing larger oligomers.

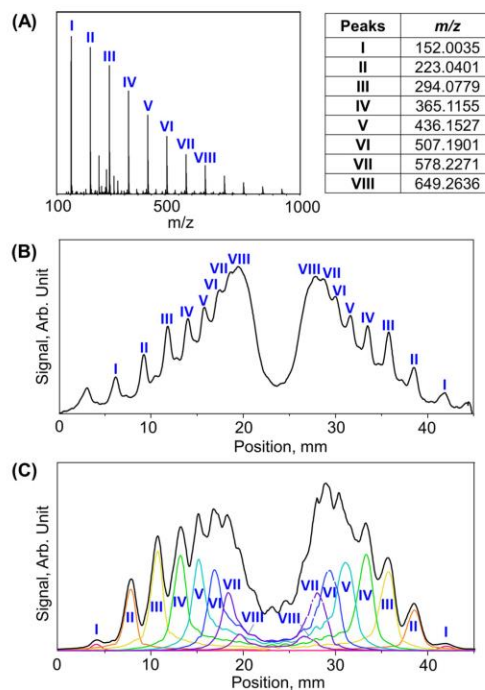


Figure 3. A) Negative-mode ESI-MS spectrum of PAM ($M_n = 2500$); m/z ratios of the major oligomers observed in the spectrum (I to VIII) are listed in the table, B) IonCCD beam profile of the PAM oligomers with a RWMA operating at $f = 70$ kHz, $V_{0-p} = 10$ V with the IonCCD positioned $2''$ after the RWMA; peaks corresponding to different oligomers are marked. C) Nano-DESI line scan along the deposition region showing extracted ion signals for different oligomers (colored lines) and the total ion signal (black line).

This observation is consistent with the contact-angle measurements.

In another experiment, we generated a different wettability gradient by depositing hydrophobic polydimethylsiloxane (PDMS) oligomers onto a hydrophilic bare gold surface. We anticipated an increase in hydrophobicity from the edge to the center of the surface where longer PDMS oligomers were deposited. The positive-mode ESI-MS spectrum of PDMS ($M_n \approx 580$) contains ammonium adducts of PDMS oligomers separated by $m/z = 74$ (Figure S11). Figure S12 shows the IonCCD beam profile of the mixture of PDMS oligomers separated using a RWMA operated at frequency of $f = 50$ kHz and amplitude of $V_{0-p} = 10$ V. Figure 4B shows the contact angles of the prepared surface from the edge to the center, where longer-chain PDMS oligomers were deposited. As expected, the deposition of PDMS oligomers of longer chain length results in an increased hydrophobicity of the surface.

In conclusion, we present a straightforward approach for the high-flux and high-throughput deposition of intact mass-

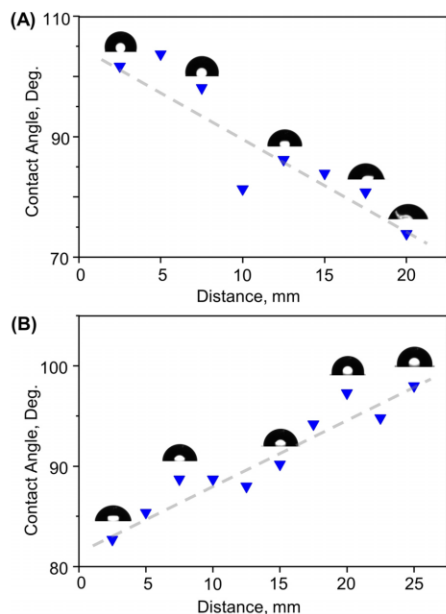


Figure 4. Contact angles of A) a hydrophobic FSAM surface covered with hydrophilic PAM oligomers and B) a hydrophilic gold surface covered with hydrophobic PDMS oligomers. The x coordinate of the plot corresponds to the distance between the point of measurement and the edge of the surface. The grey dashed lines are shown to guide the eye.

selected ions using the RWMA device powered by inexpensive electronics. We demonstrate the ability of this device to separate high-mass ions in space and disperse them onto surfaces for further characterization. The new technique opens up intriguing opportunities for the purification of well-defined nanoclusters and protein complexes on surfaces for structural determination using modern electron-microscopy techniques. Additionally, high-throughput ion soft-landing of multicomponent mixtures enables the design of surface gradients and a rapid screening of the individual components for a particular property (for example, catalytic activity, optical or magnetic properties, or biological activity). Although we demonstrated the capabilities of RWMAs using ions generated by ESI, this device can be readily coupled to other ionization sources. The small size, ease of operation, and a theoretically unlimited mass range of RWMAs make them particularly appealing for the development of miniaturized ion soft-landing instrumentation and its dissemination to the broad scientific community.

Acknowledgements

The authors thank the Electron Microscopy Core at Purdue University for the assistance provided with the high-resolu-

tion TEM experiments. We also thank Prof. R. Graham Cooks (Purdue University), Prof. Rob Whetten (University of Northern Arizona), Dr. Grant Johnson (Pacific Northwest National Laboratory), Dr. Matthias Zeller, and Dr. Wenpeng Zhang (Department of Chemistry, Purdue University) for helpful discussions, as well as Dr. Fan Pu and Ke Chen (Department of Chemistry, Purdue University) for providing the PAM samples and help with contact-angle measurements.

Conflict of interest

The authors declare no conflict of interest.

Keywords: electron microscopy · gold nanoclusters · high throughput · mass spectrometry · surface preparation

How to cite: *Angew. Chem. Int. Ed.* **2020**, *59*, 7711–7716
Angew. Chem. **2020**, *132*, 7785–7790

- [1] a) R. E. Palmer, R. Cai, J. Vernieres, *Acc. Chem. Res.* **2018**, *51*, 2296–2304; b) J. Laskin, G. E. Johnson, J. Warneke, et al., *Angew. Chem. Int. Ed.* **2018**, *57*, 16270–16284; *Angew. Chem.* **2018**, *130*, 16506–16521; c) J. Vernieres, S. Steinhauer, J. Zhao, et al., *Adv. Sci.* **2019**, 1900447; d) T. Kaposi, S. Joshi, T. Hoh, et al., *ACS Nano* **2016**, *10*, 7665–7674.
- [2] a) G. Verbeck, W. Hoffmann, B. Walton, *Analyst* **2012**, *137*, 4393–4407; b) S. Rauschenbach, M. Ternes, L. Harnau, et al., *Annu. Rev. Anal. Chem.* **2016**, *9*, 473–498.
- [3] a) G. E. Johnson, Q. Hu, J. Laskin, *Annu. Rev. Anal. Chem.* **2011**, *4*, 83–104; b) G. E. Johnson, D. Gunaratne, J. Laskin, *Mass Spectrom. Rev.* **2016**, *35*, 439–479; c) J. Cyriac, T. Pradeep, H. Kang, et al., *Chem. Rev.* **2012**, *112*, 5356–5411.
- [4] a) V. Grill, J. Shen, C. Evans, et al., *Rev. Sci. Instrum.* **2001**, *72*, 3149–3179; b) B. Gologan, Z. Takáts, J. Alvarez, et al., *J. Am. Soc. Mass. Spectrom.* **2004**, *15*, 1874–1884; c) F. Mazzei, G. Favero, M. Frasconi, et al., *Anal. Chem.* **2008**, *80*, 5937–5944; d) K. D. D. Gunaratne, V. Prabhakaran, A. Andersen, et al., *Phys. Chem. Chem. Phys.* **2016**, *18*, 9021–9028; e) P. Su, H. Hu, J. Warneke, et al., *Anal. Chem.* **2019**, *91*, 5904–5912; f) J.-N. Longchamp, S. Rauschenbach, S. Abb, et al., *Proc. Natl. Acad. Sci.* **2017**, *114*, 1474–1479; g) V. A. Mikhailov, T. H. Mize, J. L. Benesch, et al., *Anal. Chem.* **2014**, *86*, 8321–8328; h) N. Thontasen, G. Levita, N. Malinowski, et al., *J. Phys. Chem. C* **2010**, *114*, 17768–17772.
- [5] a) V. Prabhakaran, B. L. Mehdi, J. J. Ditto, et al., *Nat. Commun.* **2016**, *7*, 11399; b) G. Dubey, R. Urcuyo, S. Abb, et al., *J. Am. Chem. Soc.* **2014**, *136*, 13482–13485; c) A. Li, Y. Zi, H. Guo, et al., *Nat. Nanotechnol.* **2017**, *12*, 481.
- [6] a) Z. Ouyang, Z. Takáts, T. A. Blake, et al., *Science* **2003**, *301*, 1351–1354; b) P. Wang, J. Laskin, *Angew. Chem. Int. Ed.* **2008**, *47*, 6678–6680; *Angew. Chem.* **2008**, *120*, 6780–6782; c) P. Wang, O. Hadjar, J. Laskin, *J. Am. Chem. Soc.* **2007**, *129*, 8682–8683.
- [7] a) A. Halder, L. A. Curtiss, A. Fortunelli, et al., *J. Chem. Phys.* **2018**, *148*, 110901; b) J. Ustarroz, I. M. Ornelas, G. Zhang, et al., *ACS Catal.* **2018**, *8*, 6775–6790; c) M. J. Cuddy, K. P. Arkill, Z. W. Wang, et al., *Nanoscale* **2014**, *6*, 12463–12469; d) Y. X. Zhao, M. M. Wang, Y. Zhang, et al., *Angew. Chem. Int. Ed.* **2019**, *58*, 8002–8006; *Angew. Chem.* **2019**, *131*, 8086–8090; e) S. Vajda, M. G. White, *ACS Catal.* **2015**, *5*, 7152–7176; f) E. C. T'yo, S. Vajda, *Nat. Nanotechnol.* **2015**, *10*, 577; g) M.-A. Ha, E. T. Baxter, A. C. Cass, et al., *J. Am. Chem. Soc.* **2017**, *139*, 11568–11575.

- [8] a) V. Prabhakaran, G. E. Johnson, B. Wang, et al., *Proc. Natl. Acad. Sci.* **2016**, *113*, 13324–13329; b) P. Su, V. Prabhakaran, G. E. Johnson, et al., *Anal. Chem.* **2018**, *90*, 10935–10942.
- [9] a) J. Warneke, M. E. McBriarty, S. L. Riechers, et al., *Nat. Commun.* **2018**, *9*, 1889; b) S. Rauschenbach, G. Rinke, N. Malinowski, et al., *Adv. Mater.* **2012**, *24*, 2761–2767; c) G. Rinke, S. Rauschenbach, S. Schrettl, et al., *Int. J. Mass Spectrom.* **2015**, *377*, 228–234; d) S. Abb, N. Tarrat, J. Cortés, et al., *Angew. Chem. Int. Ed.* **2019**, *58*, 8336–8340; *Angew. Chem.* **2019**, *131*, 8424–8428.
- [10] a) T. Lünskens, P. Heister, M. Thämer, et al., *Phys. Chem. Chem. Phys.* **2015**, *17*, 17541–17544; b) S. Rauschenbach, R. Vogelgesang, N. Malinowski, et al., *ACS Nano* **2009**, *3*, 2901–2910.
- [11] a) P. Erler, P. Schmitt, N. Barth, et al., *Nano Lett.* **2015**, *15*, 4546–4552; b) F. Paschke, P. Erler, V. Enekel, et al., *ACS Nano* **2019**, *13*, 780–785; c) S. Kahle, Z. Deng, N. Malinowski, et al., *Nano Lett.* **2012**, *12*, 518–521.
- [12] a) S. Baker, S. Thornton, A. Keen, et al., *Rev. Sci. Instrum.* **1997**, *68*, 1853–1857; b) S. Rauschenbach, F. L. Stadler, E. Lunedei, et al., *small* **2006**, *2*, 540–547; c) C. Zhang, H. Tsunoyama, H. Akatsuka, et al., *J. Phys. Chem. A* **2013**, *117*, 10211–10217; d) K. D. D. Gunaratne, V. Prabhakaran, Y. M. Ibrahim, et al., *Analyst* **2015**, *140*, 2957–2963; e) A. Majumdar, D. Köpp, M. Ganeva, et al., *Rev. Sci. Instrum.* **2009**, *80*, 095103.
- [13] a) B. Von Issendorff, R. Palmer, *Rev. Sci. Instrum.* **1999**, *70*, 4497–4501; b) C. Roy, B. Sebok, S. Scott, et al., *Nat. Catal.* **2018**, *1*, 820.
- [14] a) W.-P. Peng, M. P. Goodwin, Z. Nie, et al., *Anal. Chem.* **2008**, *80*, 6640–6649; b) P. S. Mayer, F. Tureček, H.-N. Lee, et al., *Anal. Chem.* **2005**, *77*, 4378–4384; c) R. Palmer, L. Cao, F. Yin, *Rev. Sci. Instrum.* **2016**, *87*, 046103; d) M. A. Röttgen, K. Judai, J.-M. Antonietti, et al., *Rev. Sci. Instrum.* **2006**, *77*, 013302; e) H. Hartmann, V. Popok, I. Barke, et al., *Rev. Sci. Instrum.* **2012**, *83*, 073304.
- [15] a) A. K. Badu-Tawiah, C. Wu, R. G. Cooks, *Anal. Chem.* **2011**, *83*, 2648–2654; b) J. Hou, Q. Zheng, A. K. Badu-Tawiah, et al., *Chem. Commun.* **2016**, *52*, 13660–13663; c) G. E. Johnson, V. Prabhakaran, N. D. Browning, et al., *Batteries & Supercaps* **2018**, *1*, 97–101; *Supercaps* **2018**, *1*, 97–101.
- [16] a) J. Clemmons, F. Herrero, *Rev. Sci. Instrum.* **1998**, *69*, 2285–2291; b) M. Nojima, Y. Anai, M. Hotta, et al., *J. Vac. Sci. Technol. B Nanotechnol. Microelectron.* **2016**, *34*, 03H132.
- [17] a) O. Hadjar, G. Johnson, J. Laskin, et al., *J. Am. Soc. Mass Spectrom.* **2011**, *22*, 612–623; b) G. E. Johnson, O. Hadjar, J. Laskin, *J. Am. Soc. Mass Spectrom.* **2011**, *22*, 1388–1394.
- [18] R. W. Murray, *Chem. Rev.* **2008**, *108*, 2688–2720.
- [19] a) M. Hesari, Z. Ding, *Acc. Chem. Res.* **2017**, *50*, 218–230; b) M. Zhou, C. Zeng, Y. Chen, et al., *Nat. Commun.* **2016**, *7*, 13240; c) I. Guryanov, F. Polo, E. V. Ubyvok, et al., *Chem. Sci.* **2017**, *8*, 3228–3238.
- [20] L. Becucci, R. Guidelli, F. Polo, et al., *Langmuir* **2014**, *30*, 8141–8151.
- [21] a) W. Li, Q. Ge, X. Ma, et al., *Nanoscale* **2016**, *8*, 2378–2385; b) S. Das, A. Goswami, M. Hesari, et al., *Small* **2014**, *10*, 1473–1478.
- [22] T. Dainese, M. Agrachev, S. Antonello, et al., *Chem. Sci.* **2018**, *9*, 8796–8805.
- [23] H. Qian, R. Jin, *Nano Lett.* **2009**, *9*, 4083–4087.
- [24] D. Bahena, N. Bhattarai, U. Santiago, et al., *J. Phys. Chem. Lett.* **2013**, *4*, 975–981.
- [25] N. Yan, N. Xia, L. Liao, et al., *Sci. Adv.* **2018**, *4*, eaat7259.
- [26] O. Lopez-Acevedo, J. Akola, R. L. Whetten, et al., *J. Phys. Chem. C* **2009**, *113*, 5035–5038.
- [27] A. C. Leney, A. J. Heck, *J. Am. Soc. Mass Spectrom.* **2017**, *28*, 5–13.
- [28] A. Venzo, S. Antonello, J. A. Gascón, et al., *Anal. Chem.* **2011**, *83*, 6355–6362.
- [29] M. Azubel, J. Koivisto, S. Malola, et al., *Science* **2014**, *345*, 909–912.
- [30] J. Liu, N. Jian, I. Ornelas, et al., *Ultramicroscopy* **2017**, *176*, 146–150.
- [31] a) J. Genzer, R. R. Bhat, *Langmuir* **2008**, *24*, 2294–2317; b) M. B. Wijesundara, E. Fuoco, L. Hanley, *Langmuir* **2001**, *17*, 5721–5726.
- [32] M. S. Kim, G. Khang, H. B. Lee, *Prog. Polym. Sci.* **2008**, *33*, 138–164.
- [33] M. Neffliu, A. Venter, R. G. Cooks, *Chem. Commun.* **2006**, 888–890.
- [34] P. J. Roach, J. Laskin, A. Laskin, *Analyst* **2010**, *135*, 2233–2236.
- [35] J. Laskin, B. S. Heath, P. J. Roach, et al., *Anal. Chem.* **2012**, *84*, 141–148.

Manuscript received: January 2, 2020

Revised manuscript received: February 18, 2020

Accepted manuscript online: February 28, 2020

Version of record online: March 19, 2020

Principles of Operation of a Rotating Wall Mass Analyzer for Preparative Mass Spectrometry

Pei Su, Michael F. Espenship, and Julia Laskin*


 Cite This: *J. Am. Soc. Mass Spectrom.* 2020, 31, 1875–1884


 Read Online

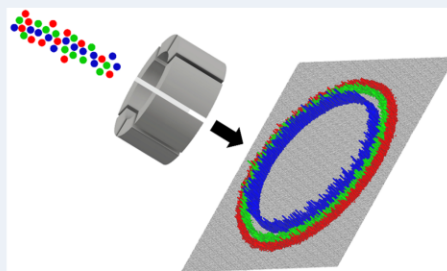
ACCESS |


 Metrics & More


 Article Recommendations


 Supporting Information

ABSTRACT: In this contribution, we describe the principles of operation of a rotating wall mass analyzer (RWMA), a mass-dispersive device for preparative mass spectrometry. Ions of different m/z are spatially separated by RWMA and deposited onto ring-shaped areas of distinct radii on a surface. We use a combination of an analytical equation for predicting the radius of the deposition ring and SIMION simulations to understand how to optimize the experimental conditions for the separation of multicomponent mixtures. The results of these simulations are compared with the experimental data. We introduce a universal mass calibration procedure, based on a series of polyacrylamide ions, which is subsequently used to predict the deposition radii of unknown analytes. The calibration is independent of the polarity, kinetic energy, and charge state of the ion as demonstrated by assigning m/z values of different analytes including multiply charged ubiquitin ions. We demonstrate that mass resolution of the RWMA is affected by the width and kinetic energy distribution of the ion beam. The best mass resolution obtained in this study is $m/\Delta m = \sim 20$. Preparative mass spectrometry using RWMA provides the advantages of simplicity, compactness, and low fabrication cost, which are particularly promising for the development of miniaturized instrumentation. The results presented in this work can be readily adapted to preparative separation of a variety of charged species of interest to the broad scientific community.



INTRODUCTION

Ion soft landing is a preparative mass spectrometry technique that enables the intact deposition of hyperthermal (<100 eV) polyatomic ions onto surfaces.^{1–4} The ability to select ions with well-defined mass, charge, and kinetic energy, along with precise control over size, shape, and position of the ion beam in the deposition process, distinguishes ion soft landing from traditional synthetic and surface preparation approaches.^{5–7} Different projectile ions including molecular ions, noncovalent complexes, clusters, and ionic fragments generated in the gas phase have been used in soft-landing studies both to address the fundamental questions related to ion–surface interactions and to enable applications of hyperthermal beams.^{8–14} Ion soft landing has been employed in selective modification of polymer films,¹⁵ doping of carbon-based materials,^{16,17} nanocluster catalysts,^{18–22} along with preparation of biomolecular substrates and coatings,^{23–25} optical and magnetic thin films,^{26–29} two-dimensional materials,³⁰ electrochemical interfaces,^{31,32} self-organizing layers,^{33,34} and supramolecular assemblies.

Since the first soft-landing instrument was implemented by Cooks and co-workers in 1977,³⁷ significant advances have been achieved in preparative mass spectrometry instrumentation. In particular, a variety of mass spectrometers^{38,39} have been used in preparative separation of ions. Due to their compatibility with continuous ion sources, quadrupole mass filters^{3,40,41} and lateral

time-of-flight mass analyzers^{42,43} have been widely employed in ion soft-landing instruments. Despite substantial improvement in mass range and ion transmission, mass-filtering devices transmit only one m/z at a time, which limits the experimental throughput in the preparative separation of multicomponent mixtures. In contrast, mass-dispersive devices such as sector⁴⁴ and distance-of-flight mass spectrometers⁴⁵ enable spatial separation and simultaneous deposition of ions of different m/z on a surface, which is beneficial to the throughput of ion soft-landing experiments.

Aside from innovations in mass analyzers, the development of high-flux ion sources has shifted the focus of ion soft-landing research from investigations of isolated ions to two-dimensional architectures and multilayered ionic assemblies.^{13,46–48} In particular, the matrix assembly cluster source (MACS) has been developed to produce milliampere-scale currents for the generation of size-controlled nanoclusters.^{49,50} Meanwhile,

Received: April 22, 2020

Revised: July 27, 2020

Accepted: July 30, 2020

Published: July 30, 2020



nanoampere-range ion currents have been achieved using electrospray ionization (ESI) coupled to a dual electrodynamic ion funnel system.^{51,52} The ability to generate high-intensity ion beam provides a direct path to the implementation of mass-dispersive devices in preparative mass spectrometry, which will enable high-flux deposition of ions onto a relatively large surface area.

In a recent work, we presented a mass-dispersive device, a rotating wall mass analyzer (RWMA), which enables simultaneous deposition of multiple ions on a surface by separating different m/z in space.⁵³ An RWMA enables high-throughput purification and deposition of ions from multicomponent mixtures onto the same substrate. This capability is of interest to the rapid screening of individual components for a specific physical and chemical property and generating surface gradients.⁵³ More strikingly, RWMA allows the transmission and separation of ions in an unlimited mass range using low radio frequency (rf) voltages ($\leq 10 V_{p-p}$) produced by inexpensive waveform generators. We have previously demonstrated that the RWMA enables separation and deposition of an atomically precise thiolated gold cluster, $Au_{144}(SC_4H_9)_{60}$ (33.7 kDa) in its +1, +2, and +3 charge states.^{53,54}

Although the concept of the RWMA was first developed for separating atomic ions in an analytical spacecraft mass spectrometer in the 1990s,^{55,56} the performance and capability of this device as a mass analyzer for preparative purposes have not yet been fully explored. Herein, we present a systematic study of the RWMA employed specifically for ion soft-landing experiments using a combination of experiments and simulations. We present a modified analytical equation for predicting the deposition radius for a specific m/z and discuss factors that affect the separation of multicomponent mixtures. In addition, we have developed a universal mass calibration of the RWMA using a series of oligomer ions. Finally, we present a systematic study of the factors affecting mass resolution of the RWMA. Although the performance characteristics of the RWMA are discussed in the context of hyperthermal ion deposition, the same principles of operation can be used for the separation of higher-kinetic-energy ions for other types of applications.

METHOD

The RWMA constructed in our laboratory is composed of a stainless steel cylinder (1.5" outer diameter, 1" inner diameter, 1" length) segmented lengthwise into eight arc-shaped electrodes (Figure 1b). The length of the RWMA was selected to facilitate the separation of hyperthermal ions (≤ 100 eV). The eight electrodes are connected to eight identical sinusoidal rf voltages generated using four dual-channel Rigol DG1022Z arbitrary waveform generators (Beaverton, OR). Typically, we use sinusoidal waveforms with a frequency in the range 5–100 kHz and $\leq 10 V_{0-p}$ amplitude. A constant-strength rotating electric field is constructed by applying the rf voltages to the eight electrodes with a 45° phase shift between each waveform (Figure 1a).⁵⁵ The four waveform generators are synchronized to lock the phases of the waveforms using the following procedure: First, the function generators are connected through the 10 MHz in/out ports using BNC cables. Next, one of the function generators is designated as the internal clock, to which the other three units are synchronized. To construct the rotating field, the frequency and amplitude of each waveform are first selected; then, one of the waveforms is designated as the reference phase (start phase = 0°). The initial phases of the

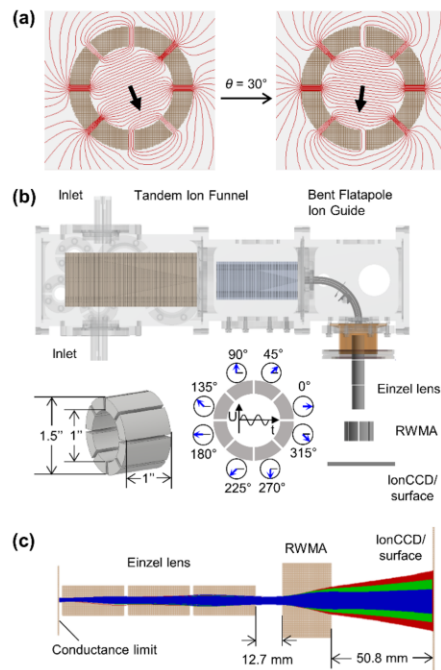


Figure 1. (a) Cross-section view of the RWMA from SIMION simulations showing the equipotential lines (red) at $\theta = 0^\circ$ and $\theta = 30^\circ$. The black arrows indicate the direction of the electric field. The equipotential lines inside the RWMA are evenly spaced indicating that a homogeneous rotating field is constructed in the central region of the RWMA. (b) Schematic drawing of the ion soft-landing instrument composed of a high-transmission ESI interface, an einzel lens, the RWMA, and an IonCCD/surface. The left bottom corner shows the schematic drawing of the RWMA fabricated in our lab, and a diagram showing the phases of the sinusoidal rf waveforms applied to the eight electrodes. This panel is adopted from ref 52 and presented here for clarity. (c) Cross-sectional view of the electrode geometry used in SIMION simulations including a conductance limit plate, einzel lens, RWMA, and IonCCD/surface. The red, green, and blue traces indicate the ion trajectories of 12 000 ions of $m/z = 253.2$, $m/z = 329.2$, $m/z = 470.3$, respectively, at a kinetic energy of 20 eV.

remaining waveforms are adjusted accordingly (start phase = 45°, 90°, 135°, 180°, 225°, 270°, 315°) by monitoring them on an oscilloscope (Figure 1b).

The instrument configuration for ion soft-landing experiments using the RWMA described in our previous study⁵² is shown in Figure 1b. It is composed of a high-transmission ESI interface described elsewhere,⁵² einzel lens, RWMA, and IonCCD (OI Analytical, Pelham, AL) detector/collector surface. Briefly, ions produced using ESI are transferred through the dual ion funnel system and subjected to collisional focusing in the bent flatpole. The ion beam is subsequently transferred into the high-vacuum region (5×10^{-5} Torr), focused by the einzel lens (three 12.7 mm long cylinders spaced by 0.65 mm gaps), spatially separated using the RWMA, and collected on a detector/surface. The rf and dc voltage settings of the high-transmission ESI interface used in this study are similar to the

ones reported in our previous publication.⁵⁷ Typical rf levels for high-pressure funnel (HPF), low-pressure funnel (LPF), and bent flatpole are ~ 270 , ~ 135 , and ~ 400 V, respectively. Typical DC settings for positive and negative ions are 376/–385 V (inlet), 384/–400 V (HPF Repeller In), 333/–355 V (HPF Repeller Out), 332/–354 V (HPF Funnel In), 164/–150 V (HPF Funnel Out), 163/–149 V (LPF Funnel In), 28/–28 V (LPF Lens), and 32/–32 V (LPF Funnel Out), respectively. Typical voltages on the einzel lens are 10/–15/10 V and –10/18/–10 V for positive and negative ions, respectively, and need to be adjusted according to the flatpole bias in a specific experiment to achieve the best focusing. IonCCD profiles were obtained using 50 ms integration time.⁵⁸

Fitting of the ion beam profiles was carried out in Excel using a sum of Lorentzian distributions. The peak positions were first defined, and the peak intensities and widths were optimized by minimizing the sum of squares of deviations between the experimental and simulated data points to obtain the best-fit curves. For the determination of the fwhm of the peaks, three replicates of ion beam profiles were collected in the experiments to obtain statistically significant results.

Ion trajectories were simulated using SIMION 8.0.4 software package (Scientific Instrument Services, Ringoes, NJ). We used the Lua macro to generate the geometry of the electrodes and the time-dependent electric field in the potential array. The size of the grid unit in the potential array was defined as 0.3175 mm to enhance the smoothness of the electrode surfaces. Two electrode geometries were considered. In the first electrode geometry, the ion beam was generated at the conductance limit, focused by the einzel lens, dispersed by the RWMA, and deposited on an IonCCD/surface (Figure 1c). This geometry represents the experimental setup used in our study. In the second electrode geometry used to study the intrinsic properties of the device, an isolated RWMA was constructed, with two mesh grids positioned at the entrance and the exit of the RWMA to terminate the rotating field (Figure S1). For each m/z , a group of 12 000 ions was produced with a birth step of 0.01 μ s between each ion. The product of the birth step and the number of replicate ions should be equal to or greater than one rf period to create a full ring pattern on the collector plate. Ion beams with different fwhm's were created using a 2D Gaussian distribution. The kinetic energy spread of the ion beam was represented by a Gaussian kinetic energy distribution of varying width.

The kinetic energy distribution (KED) of the ions was measured using a stainless steel plate mounted 12.7 mm away from the einzel lens. The plate was connected to the picoammeter and biased, which allowed us to apply the retarding voltage to the collector plate while measuring the ion current. A stainless steel mesh (part 9230TS1, McMaster Carr, Elmhurst, IL) kept at 0 V was mounted ~ 2 mm in front of the plate to maintain a uniform electric field close to the plate. Ion current detected on the plate was measured as a function of the retarding voltage. Each data point was acquired by averaging the ion current for 10 s. The integrated retarding potential curve was obtained by plotting the ion current as a function of the retarding voltage. KED was obtained by taking a first derivative of the retarding potential plot.

Polyacrylamide (PAM, $M_p = 2700$, $M_w = 3200$, $M_n = 2500$) was kindly provided by Dr. Fan Pu and Prof. R. Graham Cooks (Department of Chemistry, Purdue University) and was used as the calibration standard. The PAM oligomer solution used for ESI was prepared by dissolving the powder in 9:1 methanol:H₂O (v/v) to a final concentration of 100 μ M. Poly-

(dimethylsiloxane), hydride terminated (PDMS, $M_n = 580$), was purchased from Sigma-Aldrich (St. Louis, MO). PDMS oligomer solution used for ESI was prepared by dissolving the PDMS in methanol/toluene = 70%/30% with 10 mM ammonium acetate to a final concentration of 100 μ M. The solution of ubiquitin from bovine erythrocytes ($\geq 98\%$ purity, Sigma-Aldrich) used for ESI-MS was prepared at a concentration of ~ 0.05 mg mL⁻¹ in a solvent of methanol/H₂O/CH₃COOH/glycerol = 49%/49%/1%/1%. Three organic dyes, 2-[4-(dimethylamino)styryl]-1-ethylpyridinium (DASPE⁺, $m/z = 253.2$), malachite green (MG⁺, $m/z = 329.2$), and Victoria blue B (VBB⁺, $m/z = 470.3$) were purchased from Sigma-Aldrich. For the soft-landing experiments, a solution containing all three dyes at the same concentration (45 μ M each) was prepared by dissolving the dyes in methanol. ESI-MS analyses were performed using an LTQ XL linear ion trap mass spectrometer (Thermo Fisher Scientific GmbH, Bremen, Germany). Samples were introduced into the inlet by direct infusion through a fused silica capillary (50 μ m ID, 150 μ m OD) at a flow rate of ~ 0.5 μ L min⁻¹. Typical mass spectrometer conditions on the LTQ for the positive and negative ionization modes were as follows: electrospray voltage, ± 3 kV; capillary temperature, 300 °C; capillary voltage, ± 10 V; tube lens, ± 20 V; scan range, 100–2000 m/z . High-resolution mass spectra were acquired on an Agilent 6560 IM Q-TOF (Santa Clara, CA) mass spectrometer through direct infusion under the following instrument conditions: electrospray voltage, ± 4 kV; capillary temperature, 325 °C; m/z range, 100–3200.

RESULTS AND DISCUSSION

Analytical Expression for the Deposition Radius. The concept of using a rotating electric field for mass separation was first introduced by Clemmons et al., who described the theory and principles of operation of the RWMA as an analytical mass spectrometer.⁵⁵ In contrast, in this contribution, we provide a detailed description of the RWMA used exclusively as a mass-dispersive device for ion soft-landing experiments. In these experiments, a continuous ion beam with well-defined beam size and kinetic energy distribution (KED) is directed into the RWMA along the instrument axis (defined by the central axis of the RWMA cylinder, Figure 2a). Ions of different m/z are radially dispersed by the rotating field. After exiting the rotating

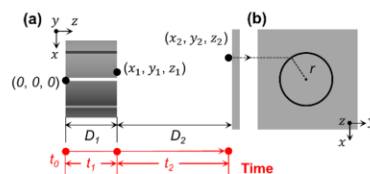


Figure 2. (a) Schematic diagram of the RWMA and a collector plate used to derive eq 1. The ion entering the RWMA at $(0, 0, 0)$ at time t_0 along the cylinder's central axis is radially dispersed by the rotating field and exits the RWMA at (x_1, y_1, z_1) . The length of this region and time the ion spends in this region are denoted as D_1 and t_1 , respectively. Next, the ion travels through the field-free region along its velocity vector attained at (x_1, y_1, z_1) and lands onto the collector plate at (x_2, y_2, z_2) . The length of this region and time the ion spends in this region are denoted as D_2 and t_2 , respectively. (b) Projection of the collector plate perpendicular to the central axis showing the ring deposition pattern formed by a continuous ion beam; r is the radius of the ring.

field region, ions drift with a constant velocity in the field-free region until they hit the surface. When the collector plate is mounted at a specific distance, D_2 , behind the RWMA, ions of different m/z are collected onto distinct ring-shaped areas of different radii (Figure 2b). The radius of the ring depends on the m/z and kinetic energy of the ion, frequency and amplitude of the rotating electric field, and distance between the surface and the RWMA. Equation 1 presents an analytical equation for predicting the radius for a specific ion:

$$R = \sqrt{x_2^2 + y_2^2} = \frac{zE}{m\omega^2} \sqrt{2(1 + \omega^2 t_1^2 + \omega^2 t_2^2)(1 - \cos \omega t_1) + \omega t_1(\omega t_1 - 2 \sin \omega t_1)} \quad (1)$$

where

$$f = \frac{\omega}{2\pi} t_1 = D_1 \sqrt{\frac{m}{2E_k}} \quad t_2 = D_2 \sqrt{\frac{m}{2E_k}}$$

where m , z , and E_k are the mass, charge state, and kinetic energy of the ion, E and f are the amplitude and frequency the rotating field, and D_1 and D_2 are the lengths of the rotating field and field-free region, respectively. A similar expression in polar coordinates was presented by Clemmons et al.⁵⁵

It is evident from eq 1 that the radius of the ring is proportional to the amplitude of the rotating field, E . Furthermore, we found that the radius increases linearly with the length of the field-free region, D_2 (Figure S2). It is also clear that there is a strong dependence of the radius on m/z , E_k , and f . In order to better understand this dependence, we show in Figure 3a the calculated value of the deposition radius as a function of m/z assuming the same kinetic energy per charge (35 eV/charge) and the same charge state (± 1) for all the m/z . This represents the scenario of spreading singly charged ions generated from oligomer mixtures onto a surface. We observe that, at 70 and 90 kHz, the radius decreases gradually with an increase in m/z in the presented m/z range. In contrast, the curves at higher frequencies start to “fold” at higher m/z meaning that, beginning from some m/z referred to as the turning point, the radius increases with an increase in m/z . The turning point is seen to shift toward lower m/z with an increase in the frequency of the rotating field. Folding of the curve results in an overlap in the radii of different m/z ions and failure of ion separation in the folded m/z range. The calculated radii of $m/z = 200, 400, 600,$ and 800 are extracted from the plots in Figure 3a and reconstructed as simulated mass spectra at different frequencies in Figure 3b. We observe that, at 70–110 kHz (black, red, and blue spectra), the four peaks are properly ordered as the radii decrease with m/z . Furthermore, we find that the peaks of the same series of ions are farther separated at 90 kHz than at 70 kHz. This is consistent with the larger slope of the r vs m/z curve at higher frequencies (Figure 3a), which indicates that the resolution for separation of ions in a specific m/z range can be improved by adjusting the frequency to an optimal value. However, at frequencies above 110 kHz, the order of the rings changes with m/z 800 observed at a larger radius than m/z 600 at 130 kHz (green spectrum) and at a larger radius than both m/z 600 and m/z 400 at 150 kHz (purple spectrum). Clearly, for this m/z range, the RWMA must be operated at a frequency of the rotating field below 110 kHz.

We provide a qualitative explanation for the observed trend. The extent of radial dispersion depends on the time the ion spends in the rotating field, which is determined by ion's m/z

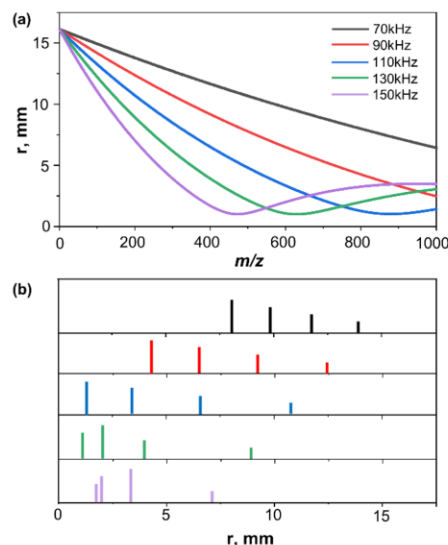


Figure 3. (a) Plots of the deposition radius as a function of m/z for singly charged ions of the same E_k (35 eV) and at several frequencies of the rotating field shown in different colors. (b) Simulated RWMA mass spectra containing four signals ($m/z = 200, 400, 600,$ and 800) extracted from the plots shown in panel a at different frequencies shown using the same color coding as in panel a. The heights of the bars in the simulated spectra indicate the m/z .

and kinetic energy. At lower rotating field frequencies, ions in the presented m/z range are ejected from the rotating field region within the first rf period. In this case, each m/z is dispersed into a ring with a distinct radius, which is inversely proportional to m/z . In contrast, at higher frequencies, higher- m/z ions that spend a longer time in the field are subjected to an additional radial dispersion from the second rf period. As a result, some of the radii correspond to more than one m/z , which is detrimental to the mass-dispersive ion separation. A similar effect may be achieved by decreasing the kinetic energy of the ions. To avoid this folding, for a particular kinetic energy of the ion beam, the frequency of the rotating field is selected such that the m/z range of interest leaves the RWMA within one rf period.

Calibration. Equation 1 is derived assuming that the rotating field is confined within the physical dimensions of the RWMA. However, the field strength along the instrument axis extracted from SIMION simulations shown in Figure S3 displays a penetration of the rotating field into the field-free region. This indicates that ions exiting the RWMA are still being influenced by the field. As a result, the experimentally observed deposition radius deviates from the radius calculated using eq 1. To correct for this deviation, we established a calibration procedure using a series of polyacrylamide (PAM) oligomers as the calibrants. Negative-mode ESI of PAM ($M_n = 1500$) produces deprotonated oligomer anions spaced by $m/z = 71$ (Figure S4 and Table S1).⁵⁹ The m/z values of the PAM oligomers used for the calibration are listed in Table S1. In a typical calibration procedure, IonCCD is mounted at a desired distance from the RWMA, and the radii of the PAM calibrant ions are extracted

from the IonCCD profile with the RWMA operating at a desired frequency and amplitude. The experimentally determined radii of the oligomers are compared with the values predicted by the analytical equation. The initial rotating electric field strength is calculated using eq 1 assuming that the field is confined to the physical dimensions of the RWMA (i.e., the field length, D_1 , equals 25.4 mm). The sum of squares of deviations between the calculated and experimentally determined radii is subsequently minimized using the GRG nonlinear algorithm provided by Excel's Solver with the strength and length of the rotating field being the only adjustable parameters. This calibration procedure is similar to the "Simplex Optimization" in time-of-flight mass spectrometry.⁶⁰ During the optimization, the total distance ($D_1 + D_2$) is kept constant. In the calibration carried out with $f = 70$ kHz, $V_{0-p} = 10$ V, and IonCCD at a distance of 50.8 mm from the RWMA, with the PAM anions traveling through the RWMA at a kinetic energy of 35 eV/charge, the optimal length of the field was found to be $D_1 = 44.1$ mm, which is longer than the length of the RWMA. In addition, the optimized field strength of $E = 705$ V m⁻¹ is lower than the maximum field strength of 740 V m⁻¹ extracted from the SIMION simulation (Figure S3). These findings are in agreement with our hypothesis that the penetration of the rotating field outside of the RWMA causes the observed deviation between the predicted and experimental radii and that the effective field length and field strength must be calibrated to obtain accurate peak assignments based on the experimentally measured radii.

Next, we generated a calibration curve using eq 1 and the optimized parameters obtained from the calibration procedure. Figure 4 shows the calibration curves of the deposition radii, r , as

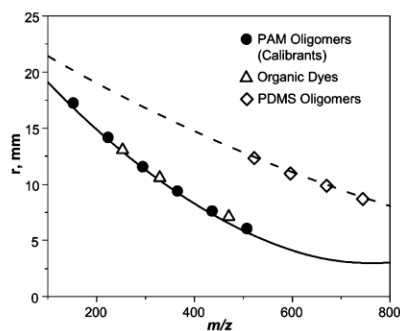


Figure 4. Plots of the calibrated deposition radii vs m/z at $f = 70$ kHz (solid) and $f = 50$ kHz (dashed). The experimental data points are shown for PAM calibrants (filled circles), organic dyes (open triangles), and PDMS oligomers (open diamonds). The r values were calculated using eq 1 using the effective rotating field strength (E) and length of the field (D_1) obtained from the calibration.

a function of m/z at $f = 70$ kHz (solid) and $f = 50$ kHz (dashed) at an ion kinetic energy of 35 eV/charge. The curves were obtained using the calibrated rotating field strength ($E = 705$ V m⁻¹) and length ($D_1 = 44.1$ mm). The radii of the PAM calibrant ions used for the calibration are labeled as filled circles in Figure 4b. The performance of the calibration was examined using different types of charged analytes with the same instrument configuration. Specifically, we measured ion beam profiles for two multicomponent mixtures using the RWMA with the IonCCD positioned 50.8 mm away from the analyzer. The first

mixture is composed of organic dyes generating singly charged ions, and the second mixture generates singly charged ammonium adducts of PDMS oligomers.⁶¹ The kinetic energy of the ions was 35 eV. The rotating field frequencies employed for dispersion of the dyes and the PDMS oligomers were 70 and 50 kHz, respectively. The experimentally determined radii are shown in Figure 4 and Table S2. We observe a ~2% relative error of the calculated radii from the experimental values for the PDMS oligomers (Table S2). This demonstrates that the same calibration parameters can be used for different frequencies of the rotating field and for ions of both polarities.

In the field of mass spectrometry, mass calibration is commonly conducted using a polynomial curve fitting, in which calibrant ions are selected to cover the m/z range of interest. Mass calibration of high m/z species typically requires a series of high m/z calibrant ions. In contrast, we find that mass calibration of the RWMA conducted using the low- m/z PAM oligomers can be used for a much broader m/z range of interest independent of the charge state and kinetic energy of the ions. In this experiment, we generated multiply charged ubiquitin (8.6 kDa) ions using ESI of an acidified solution. Figure 5a shows an

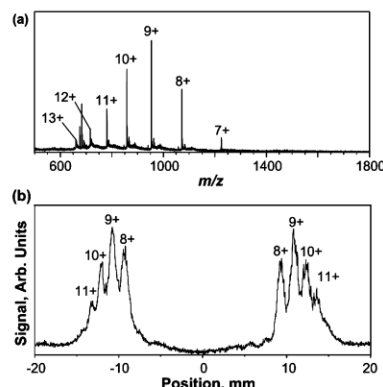


Figure 5. (a) ESI mass spectrum of 5 μ M ubiquitin in 49:49:1:1 methanol/ H_2O / CH_3COOH /glycerol (v/v/v/v) showing a distribution of charge states ranging from +7 to +13. (b) IonCCD profile of ubiquitin ions separated by the RWMA operated at a frequency of $f = 40$ kHz. The charge state assignment of each peak is labeled in the profile.

LTQ mass spectrum of a 5 μ M ubiquitin in 49:49:1:1 methanol/ H_2O / CH_3COOH /glycerol (v/v/v/v). We observe a distribution of charge states ranging from 7+ to 13+, with 9+ showing the highest abundance.⁶² The same solution was used to generate an ion beam in the soft-landing instrument for the RWMA separation. [We note that the ESI interfaces of the LTQ and our custom-designed soft-landing instrument are quite different. As a result, the abundances of the individual charge states are likely different on the two instruments.] The resulting IonCCD beam profile acquired with the rotating field of $f = 40$ kHz at a distance of 50.8 mm from the exit of the RWMA and the kinetic energy of 30 eV/charge is shown in Figure 5b. We observe several pairs of peaks symmetrically located around the center of the x axis ($x = 0$) corresponding to different charge states of ubiquitin. In particular, four pairs of peaks with decreasing radii were assigned to +11, +10, +9, and +8 charge states. The experimentally obtained radii were subsequently

compared with the predicted values using the calibrated parameters listed in Table S3. We find a good match between the predicted and experimental radii indicating the robustness of the calibration procedure and accurate charge state assignments. The relative errors of the calibration are $\sim 0.7\%$.

Based on these results, it is reasonable to conclude that the same calibration parameters obtained using PAM oligomers can be readily adapted to other ion mixtures independent of the polarity, charge state, kinetic energy of the ions, and the frequency of the rotating field. In addition, because the effective field strength and length are independent of m/z , it is reasonable to assume that the calibration parameters obtained using low- m/z PAM can be used to predict the radii of high- m/z ions. Our previously reported results for 33.7 kDa $\text{Au}_{144}(\text{SC}_4\text{H}_9)_{60}$ ions are consistent with this assertion.⁵⁷

Mass Resolution. In mass spectrometry, mass resolution is defined as the ratio of m/z and full-width-at-half-maximum (fwhm) of the peak in a mass spectrum. Similarly, mass resolution of the RWMA is determined by the spatial separation of the individual components and is calculated by taking the ratio of the deposition radius (r) to the width of the ring (Δr). We estimate mass resolution of this device based on the ion beam profile obtained from the IonCCD, in which the ring is detected as a pair of peaks separated by a distance corresponding to the diameter of the ring. The radius of the ring is determined from the measured separation distance between the two peaks, and the width of the ring corresponds to the fwhm of the individual peak. Mass resolution of the RWMA in its current configuration was experimentally determined using a standard mixture containing three organic dyes. Specifically, a beam containing positively charged DASPE⁺ (m/z 253.2), MG⁺ (m/z 329.2), and VBB⁺ (m/z 470.3) was separated using the RWMA operated at $f = 70$ kHz, $10 V_{0-p}$ with the IonCCD positioned at a distance of 2" from the device. Typical ion beam profiles acquired at kinetic energies ranging from 20 to 50 eV are shown in Figure 6a. Three pairs of peaks symmetrically located around the center of each profile are assigned to the three singly charged dyes, with lower m/z corresponding to peaks at larger radii. The profiles were subsequently fitted with sums of Lorentzian distributions, from which the fwhm values were extracted (Figure S5). Figure 6b shows the fwhm and mass resolution of the peaks of the dyes obtained by averaging the values of fwhm from three repeated measurements and from both the left and right side of the profiles. From this experiment, we conclude that the upper limit of mass resolution ($m/\Delta m$) of ~ 20 is achievable for the RWMA in its current configuration, which is comparable to the mass resolution of mass analyzers typically used in nanocluster research ($m/\Delta m = 20-50$).⁴²

In addition, we observe that, for all the ions, peak width decreases with an increase in kinetic energy. In fact, a similar trend in the beam width was obtained when the rotating field was switched off, with a higher-energy ion beam showing a narrower profile (data not shown). This is attributed to the known difficulty in focusing of lower-energy ion beams. Furthermore, the VBB⁺ peak is slightly broader than peaks of MG⁺ and DASPE⁺ at all kinetic energies, while the peak widths of MG⁺ and DASPE⁺ are similar.

In the following, we carried out a set of SIMION simulations to reproduce the realistic experimental conditions. In the electrode geometry, we implemented a conductance limit plate and einzel lens in front of the RWMA (Figure 1c). In each simulation scenario, the ion beam containing the three dyes was produced at the conductance limit plate and sent through the

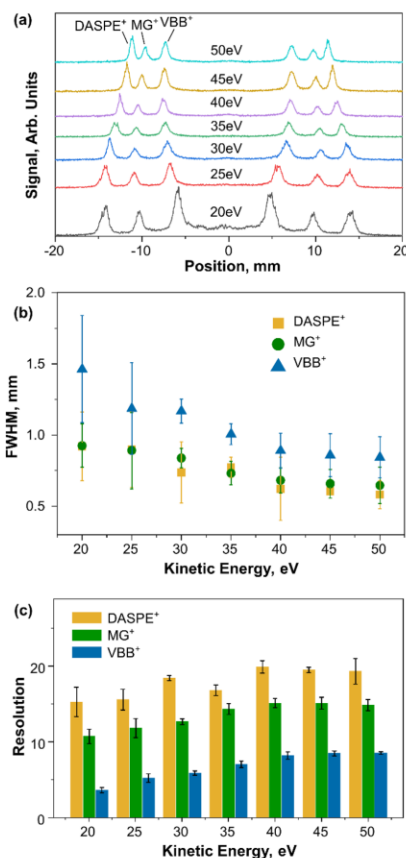


Figure 6. (a) IonCCD profile of a mixture of the three dyes acquired using RWMA operated at $f = 70$ kHz, $10 V_{0-p}$ at different kinetic energies. (b) fwhm's of the peaks in the profiles shown in panel a, and (c) corresponding values of mass resolution.

einzel lens and RWMA to the collector plate. The locations of the individual ion splats on the collector plate positioned 2" away from the RWMA were recorded for 12 000 ions of each m/z . The distances between the ion landing locations and the center of the surface were subsequently extracted and used to construct histograms (bin width = 0.01 mm) of the deposition ring radii. The histograms were fitted with Gaussian distributions, and the fwhm's were extracted as the simulated fwhm's of the deposition rings. Due to the physical restrictions of the instrument, we cannot measure the width of the beam at the conductance limit. However, the kinetic energy distribution (KED) of the beam can be measured using a retarding potential method described in detail in the Methods section. In particular, we measured the KED of the ion beam at a distance of 12.7 mm out of the einzel lens where the RWMA is typically positioned. The mean KED and fwhm measured experimentally are 18.6 and 1.6 eV, respectively, for the flatpole bias of 20 V, and 48.1 and 1.8 eV, respectively, for the flatpole bias of 50 V (Figure S6). These values were used as the initial beam conditions in

SIMION simulations. Due to the unknown initial width of the beam at the conductance limit, we performed a series of simulations with different initial beam widths ranging from 0.5 to 2 mm (filled circle distribution) to cover a broad range of possible scenarios. For each beam width, we systematically adjusted the voltage on the second element of the einzel lens to achieve the best focusing on the surface. Figure 7 shows the

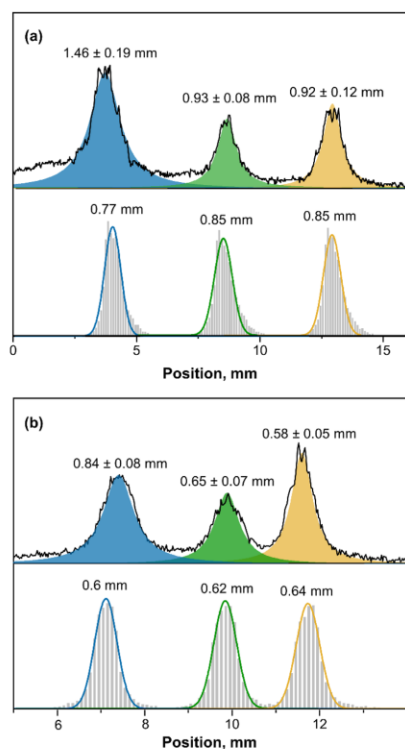


Figure 7. Experimental beam profiles (top black trace) and the corresponding profiles generated using SIMION simulations (light gray bars) of the three dyes at kinetic energies of 20 (a) and 50 eV (b). Yellow, green, and blue areas/curves on the top/bottom of each panel represent Lorentzian profiles obtained from the best fit of the underlying peaks of DASPE⁺ (m/z 253.2), MG⁺ (m/z 329.2), and VBB⁺ (m/z 470.3), respectively.

optimal simulated distributions of the deposition radii for beam kinetic energies of 20 and 50 eV. The experimental ion beam profiles and the corresponding Lorentzian curve fitting results are shown for comparison. The best matches between the simulated and experimental beam profiles were obtained using the initial beam width of 1 and 0.7 mm for beam kinetic energies of 20 and 50 eV, respectively. The einzel lens voltages providing best focusing in the simulations were 1.2 V/−50 V/1.2 V and 25.5 V/−25 V/25.5 V for 20 and 50 eV ion beams, which are in close agreement with the experimentally obtained voltages of 1.2 V/−40.1 V/1.2 V and 25.5 V/−22.6 V/25.5 V for 20 and 50 eV ion beams, respectively. At both kinetic energies, the simulated widths of the deposition rings are similar for all the m/z .

Based on the simulation results discussed above, we conclude that the focusing conditions of the einzel lens have a pronounced effect on the mass resolution of the RWMA. However, it is not clear from these simulations how the mass resolution is affected by the two important intrinsic parameters of the ion beam, the fwhm and KED. In the following, we describe a series of SIMION simulations with an isolated RWMA configuration shown in Figure S1 to understand how the rotating field affects the width of the deposition ring. In particular, we generated ion beams of DASPE⁺ (m/z 253.2) of different widths in the source (fwhm of 0.5, 1, 1.5, and 2 mm along with 0 mm corresponding to a point source) with the KED of fwhm of 0.2 eV, 1 and 2 eV centered at 20 eV/charge. The results of the simulations are summarized in Figure 8. We observe that the width of the

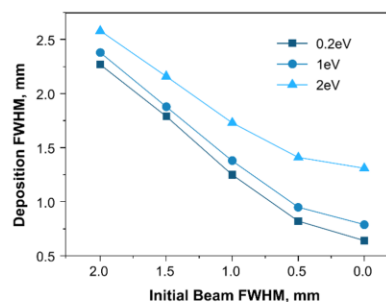


Figure 8. Simulated fwhm of the deposition ring of DASPE⁺ (m/z 253.2) with Gaussian-shaped KEDs of 0.2, 1, and 2 eV fwhm centered at 20 eV/charge and various initial beam widths (0, 0.5, 1, 1.5, and 2 mm).

deposition ring decreases with a decrease in both the beam width and fwhm of the KED. However, the observed trend is strongly dependent on the width of the KED. In particular, for a relatively narrow KED (fwhm of 0.2 and 1 eV), the width of the deposition ring shows a near proportional decrease with a decrease in the initial beam width. In contrast, for a broader KED (fwhm of 2 eV), the extent of decrease in the width of the deposition ring is not as pronounced especially when the initial beam is very narrow. These results indicate a substantial deterioration of the device performance with an increase in the KED spread. It follows that an improvement in mass resolution of the RWMA may be achieved only by narrowing both the beam width and KED simultaneously.

Based on the SIMION simulations, we conclude that both the initial width and KED of the ion beam have a pronounced effect on mass resolution of the RWMA. Higher mass resolution can be obtained using a narrow parallel ion beam with a narrow KED. A narrow ion beam can be generated using either two einzel lenses or a collisional multipole with a small conductance limit aperture. Meanwhile, the narrow KED can be obtained by minimizing the acceleration gradient at the exit of the collisional flatpole in our existing instrument. In addition, it has been demonstrated that an ion beam with a narrow KED of ~0.2 eV can be generated by extending the collisional multipole into the high vacuum region⁶³ or by employing an exponential lens^{64,65} to eliminate the kinetic energy spread of the ion beam.

CONCLUSION

In conclusion, we present the performance of a mass-dispersive device, RWMA, for ion soft-landing research. Ions of different

m/z traveling through the device are separated onto distinct rings of different radii on a surface. We present an analytical expression for predicting the deposition radius of ions. The separation performance for ions in a different range of m/z and kinetic energy can be optimized by adjusting the frequency of the rotating electric field. In addition, we describe a universal calibration of the device using a series of polyacrylamide ions to obtain a reliable prediction of the deposition radii for unknown analytes. Moreover, ion trajectory simulations and experiments demonstrate that mass resolution of the device can be improved by minimizing the width and kinetic energy spread of the ion beam. The use of RWMA greatly reduces the complexity and cost of preparative mass spectrometry instrumentation due to the moderate vacuum requirement ($<10^{-3}$ Torr) and simple electronics. These characteristics of the RWMA make it a promising candidate for the development of inexpensive and transportable preparative mass spectrometers.⁶⁶ Such affordable ion deposition systems would facilitate the use of preparative mass spectrometry in applications in photonics, memory storage, molecular electronics, catalysis, and biology.

■ ASSOCIATED CONTENT

Supporting Information

The Supporting Information is available free of charge at <https://pubs.acs.org/doi/10.1021/jasms.0c00140>.

Ion deposition radius as a function of distance from the entrance of RWMA; ESI-MS of PAM oligomers; and major peak list (PDF)

■ AUTHOR INFORMATION

Corresponding Author

Julia Laskin – Department of Chemistry, Purdue University, West Lafayette, Indiana 47907, United States; orcid.org/0000-0002-4533-9644; Email: jlaskin@purdue.edu

Authors

Pei Su – Department of Chemistry, Purdue University, West Lafayette, Indiana 47907, United States; orcid.org/0000-0001-6148-0181

Michael F. Espenship – Department of Chemistry, Purdue University, West Lafayette, Indiana 47907, United States; orcid.org/0000-0003-1174-3347

Complete contact information is available at: <https://pubs.acs.org/doi/10.1021/jasms.0c00140>

Notes

The authors declare no competing financial interest.

■ ACKNOWLEDGMENTS

We thank Prof. R. Graham Cooks (Purdue University) for helpful discussions and Dr. Fan Pu (Department of Chemistry, Purdue University) for providing the PAM samples.

■ REFERENCES

- (1) Cyriac, J.; Pradeep, T.; Kang, H.; Souda, R.; Cooks, R. Low-energy ionic collisions at molecular solids. *Chem. Rev.* **2012**, *112*, 5356–5411.
- (2) Johnson, G. E.; Gunaratne, D.; Laskin, J. Soft- and reactive landing of ions onto surfaces: Concepts and applications. *Mass Spectrom. Rev.* **2016**, *35*, 439–479.
- (3) Rauschenbach, S.; Stadler, F. L.; Lunedei, E.; Malinowski, N.; Koltsov, S.; Costantini, G.; Kern, K. Electrospray Ion Beam Deposition of Clusters and Biomolecules. *Small* **2006**, *2*, 540–547.

- (4) Verbeck, G.; Hoffmann, W.; Walton, B. Soft-landing preparative mass spectrometry. *Analyst* **2012**, *137*, 4393–4407.

- (5) Johnson, G. E.; Hu, Q.; Laskin, J. Soft landing of complex molecules on surfaces. *Annu. Rev. Anal. Chem.* **2011**, *4*, 83–104.

- (6) Rauschenbach, S.; Vogelgesang, R.; Malinowski, N.; Gerlach, J. W.; Benyoucef, M.; Costantini, G.; Deng, Z.; Thontasen, N.; Kern, K. Electrospray Ion Beam Deposition: Soft-Landing and Fragmentation of Functional Molecules at Solid Surfaces. *ACS Nano* **2009**, *3*, 2901–2910.

- (7) Palmer, R. E.; Cai, R.; Vernieres, J. Synthesis without solvents: The cluster (nanoparticle) beam route to catalysts and sensors. *Acc. Chem. Res.* **2018**, *51*, 2296–2304.

- (8) Grill, V.; Shen, J.; Evans, C.; Cooks, R. G. Collisions of ions with surfaces at chemically relevant energies: instrumentation and phenomena. *Rev. Sci. Instrum.* **2001**, *72*, 3149–3179.

- (9) Laskin, J.; Johnson, G. E.; Prabhakaran, V. Soft landing of complex ions for studies in catalysis and energy storage. *J. Phys. Chem. C* **2016**, *120*, 23305–23322.

- (10) Vajda, S.; White, M. G. Catalysis applications of size-selected cluster deposition. *ACS Catal.* **2015**, *5*, 7152–7176.

- (11) Heiz, U.; Bullock, E. Fundamental aspects of catalysis on supported metal clusters. *J. Mater. Chem.* **2004**, *14*, 564–577.

- (12) Halder, A.; Curtiss, L. A.; Fortunelli, A.; Vajda, S. Perspective: Size selected clusters for catalysis and electrochemistry. *J. Chem. Phys.* **2018**, *148*, 110901.

- (13) Weippert, J.; Hauns, J.; Bachmann, J.; Greisch, J.-F.; Narita, A.; Müllen, K.; Böttcher, A.; Kappes, M. M. Oligomerization of Dehydrogenated Polycyclic Aromatic Hydrocarbons on Highly Oriented Pyrolytic Graphite. *J. Phys. Chem. C* **2020**, *124*, 8236–8246.

- (14) Rauschenbach, S.; Ternes, M.; Harnau, L.; Kern, K. Mass Spectrometry as a Preparative Tool for the Surface Science of Large Molecules. *Annu. Rev. Anal. Chem.* **2016**, *9*, 473–498.

- (15) Wijesundara, M. B. J.; Fuoco, E.; Hanley, L. Preparation of Chemical Gradient Surfaces by Hyperthermal Polyatomic Ion Deposition: A New Method for Combinatorial Materials Science. *Langmuir* **2001**, *17*, 5721–5726.

- (16) Prabhakaran, V.; Mehdi, B. L.; Ditto, J. J.; Engelhard, M. H.; Wang, B.; Gunaratne, K. D. D.; Johnson, D. C.; Browning, N. D.; Johnson, G. E.; Laskin, J. Rational design of efficient electrode-electrolyte interfaces for solid-state energy storage using ion soft landing. *Nat. Commun.* **2016**, *7*, No. 11399.

- (17) Dubey, G.; Urcuyo, R.; Abb, S.; Rinke, G.; Burghard, M.; Rauschenbach, S.; Kern, K. Chemical Modification of Graphene via Hyperthermal Molecular Reaction. *J. Am. Chem. Soc.* **2014**, *136*, 13482–13485.

- (18) Ha, M.-A.; Baxter, E. T.; Cass, A. C.; Anderson, S. L.; Alexandrova, A. N. Boron Switch for Selectivity of Catalytic Dehydrogenation on Size-Selected Pt Clusters on Al₂O₃. *J. Am. Chem. Soc.* **2017**, *139*, 11568–11575.

- (19) Tyo, E. C.; Vajda, S. Catalysis by clusters with precise numbers of atoms. *Nat. Nanotechnol.* **2015**, *10*, 577–588.

- (20) Zhao, Y.-X.; Wang, M.-M.; Zhang, Y.; Ding, X.-L.; He, S.-G. Activity of Atomically Precise Titania Nanoparticles in CO Oxidation. *Angew. Chem., Int. Ed.* **2019**, *58*, 8002–8006.

- (21) Ustarroz, J.; Ornelas, I. M.; Zhang, G.; Perry, D.; Kang, M.; Bentley, C. L.; Walker, M.; Unwin, P. R. Mobility and Poisoning of Mass-Selected Platinum Nanoclusters during the Oxygen Reduction Reaction. *ACS Catal.* **2018**, *8*, 6775–6790.

- (22) Humphrey, J. J. L.; Kronberg, R.; Cai, R.; Laasonen, K.; Palmer, R. E.; Wain, A. J. Active site manipulation in MoS₂ cluster electrocatalysts by transition metal doping. *Nanoscale* **2020**, *12*, 4459–4472.

- (23) Ouyang, Z.; Takáts, Z.; Blake, T. A.; Gologan, B.; Guymon, A. J.; Wiseman, J. M.; Oliver, J. C.; Davison, V. J.; Cooks, R. G. Preparing Protein Microarrays by Soft-Landing of Mass-Selected Ions. *Science* **2003**, *301*, 1351–1354.

- (24) Blake, T. A.; Ouyang, Z.; Wiseman, J. M.; Takáts, Z.; Guymon, A. J.; Kothari, S.; Cooks, R. G. Preparative Linear Ion Trap Mass Spectrometer for Separation and Collection of Purified Proteins and

- Peptides in Arrays Using Ion Soft Landing. *Anal. Chem.* **2004**, *76*, 6293–6305.
- (25) Wu, X.; Delbianco, M.; Anggara, K.; Michnowicz, T.; Pardo-Vargas, A.; Bharate, P.; Sen, S.; Pristl, M.; Rauschenbach, S.; Schlickum, U.; Abb, S.; Seeberger, P. H.; Kern, K. Imaging single glycans. *Nature* **2020**, *582*, 375–378.
- (26) Kahle, S.; Deng, Z.; Malinowski, N.; Tonnoir, C.; Forment-Aliaga, A.; Thontasen, N.; Rinke, G.; Le, D.; Turkowski, V.; Rahman, T. S.; Rauschenbach, S.; Ternes, M.; Kern, K. The Quantum Magnetism of Individual Manganese-12-Acetate Molecular Magnets Anchored at Surfaces. *Nano Lett.* **2012**, *12*, 518–521.
- (27) Paschke, F.; Erler, P.; Enenkel, V.; Gragnaniello, L.; Fonin, M. Bulk-Like Magnetic Signature of Individual Fe₄H Molecular Magnets on Graphene. *ACS Nano* **2019**, *13*, 780–785.
- (28) Erler, P.; Schmitt, P.; Barth, N.; Imler, A.; Bouvron, S.; Huhn, T.; Groth, U.; Pauly, F.; Gragnaniello, L.; Fonin, M. Highly Ordered Surface Self-Assembly of Fe₄ Single Molecule Magnets. *Nano Lett.* **2015**, *15*, 4546–4552.
- (29) Lünskens, T.; Heister, P.; Thämer, M.; Walenta, C. A.; Kartouzian, A.; Heiz, U. Plasmons in supported size-selected silver nanoclusters. *Phys. Chem. Chem. Phys.* **2015**, *17*, 17541–17544.
- (30) Vats, N.; Wang, Y.; Sen, S.; Szilagy, S.; Ochner, H.; Abb, S.; Burghard, M.; Sigle, W.; Kern, K.; van Aken, P. A.; Rauschenbach, S. Substrate-Selective Morphology of Cesium Iodide Clusters on Graphene. *ACS Nano* **2020**, *14*, 4626–4635.
- (31) Su, P.; Prabhakaran, V.; Johnson, G. E.; Laskin, J. In Situ Infrared Spectroelectrochemistry for Understanding Structural Transformations of Precisely Defined Ions at Electrochemical Interfaces. *Anal. Chem.* **2018**, *90*, 10935–10942.
- (32) Prabhakaran, V.; Johnson, G. E.; Wang, B.; Laskin, J. In situ solid-state electrochemistry of mass-selected ions at well-defined electrode-electrolyte interfaces. *Proc. Natl. Acad. Sci. U. S. A.* **2016**, *113*, 13324–13329.
- (33) Warneke, J.; McBriarty, M. E.; Riechers, S. L.; China, S.; Engelhard, M. H.; Aprà, E.; Young, R. P.; Washon, N. M.; Jenne, C.; Johnson, G. E. Self-organizing layers from complex molecular anions. *Nat. Commun.* **2018**, *9*, No. 1889.
- (34) Rauschenbach, S.; Rinke, G.; Malinowski, N.; Weitz, R. T.; Dinnebir, R.; Thontasen, N.; Deng, Z.; Lutz, T.; de Almeida Rollo, P. M.; Costantini, G.; Harnau, L.; Kern, K. Crystalline Inverted Membranes Grown on Surfaces by Electrospray Ion Beam Deposition in Vacuum. *Adv. Mater.* **2012**, *24*, 2761–2767.
- (35) Kaposi, T.; Joshi, S.; Hoh, T.; Wiengarten, A.; Seufert, K.; Paszkiewicz, M.; Klappenberger, F.; Eciya, D.; Dordević, L.; Marangoni, T.; Bonifazi, D.; Barth, J. V.; Auwärter, W. Supramolecular Spangling, Crocheting, and Knitting of Functionalized Pyrene Molecules on a Silver Surface. *ACS Nano* **2016**, *10*, 7665–7674.
- (36) Rinke, G.; Rauschenbach, S.; Schrettl, S.; Hoheisel, T. N.; Blohm, J.; Gutzler, R.; Rosei, F.; Frauenrath, H.; Kern, K. Soft-landing electrospray ion beam deposition of sensitive oligoynes on surfaces in vacuum. *Int. J. Mass Spectrom.* **2015**, *377*, 228–234.
- (37) Franchetti, V.; Solka, B. H.; Baitinger, W. E.; Amy, J. W.; Cooks, R. G. Soft landing of ions as a means of surface modification. *Int. J. Mass Spectrom. Ion Phys.* **1977**, *23*, 29–35.
- (38) Louris, J. N.; Cooks, R. G.; Syka, J. E. P.; Kelley, P. E.; Stafford, G. C.; Todd, J. F. Instrumentation, applications, and energy deposition in quadrupole ion-trap tandem mass spectrometry. *Anal. Chem.* **1987**, *59*, 1677–1685.
- (39) Mikhailov, V. A.; Mize, T. H.; Benesch, J. L. P.; Robinson, C. V. Mass-Selective Soft-Landing of Protein Assemblies with Controlled Landing Energies. *Anal. Chem.* **2014**, *86*, 8321–8328.
- (40) Hartmann, H.; Popok, V. N.; Barke, L.; Oeynhaus, V. v.; Meiwes-Broer, K.-H. Design and capabilities of an experimental setup based on magnetron sputtering for formation and deposition of size-selected metal clusters on ultra-clean surfaces. *Rev. Sci. Instrum.* **2012**, *83*, 073304.
- (41) Tsunoyama, H.; Shibuta, M.; Nakaya, M.; Eguchi, T.; Nakajima, A. Synthesis and Characterization of Metal-Encapsulating Si₁₆ Cage Superatoms. *Acc. Chem. Res.* **2018**, *51*, 1735–1745.
- (42) von Issendorff, B.; Palmer, R. E. A new high transmission infinite range mass selector for cluster and nanoparticle beams. *Rev. Sci. Instrum.* **1999**, *70*, 4497–4501.
- (43) Roy, C.; Sebok, B.; Scott, S. B.; Fiordaliso, E. M.; Sørensen, J. E.; Bodin, A.; Trimarco, D. B.; Damsgaard, C. D.; Vesborg, P. C. K.; Hansen, O.; Stephens, I. E. L.; Kibsgaard, J.; Chorkendorff, I. Impact of nanoparticle size and lattice oxygen on water oxidation on NiFeO_xH_y. *Nat. Catal.* **2018**, *1*, 820–829.
- (44) Mayer, P. S.; Tureček, F.; Lee, H.-N.; Scheidemann, A. A.; Olney, T. N.; Schumacher, F.; Strop, P.; Smrcina, M.; Pátek, M.; Schirlin, D. Preparative Separation of Mixtures by Mass Spectrometry. *Anal. Chem.* **2005**, *77*, 4378–4384.
- (45) Enke, C. G.; Ray, S. J.; Graham, A. W.; Dennis, E. A.; Hieftje, G. M.; Carado, A. J.; Barinaga, C. J.; Koppenaal, D. W. Distance-of-Flight Mass Spectrometry: A New Paradigm for Mass Separation and Detection. *Annu. Rev. Anal. Chem.* **2012**, *5*, 487–504.
- (46) Laskin, J.; Johnson, G. E.; Warneke, J.; Prabhakaran, V. From Isolated Ions to Multilayer Functional Materials Using Ion Soft Landing. *Angew. Chem., Int. Ed.* **2018**, *57*, 16270–16284.
- (47) Cuddy, M. J.; Arkill, K. P.; Wang, Z. W.; Komsa, H.-P.; Krashennikov, A. V.; Palmer, R. E. Fabrication and atomic structure of size-selected, layered MoS₂ clusters for catalysis. *Nanoscale* **2014**, *6*, 12463–12469.
- (48) Tsunoyama, H.; Zhang, C.; Akatsuka, H.; Sekiya, H.; Nagase, T.; Nakajima, A. Development of High-flux Ion Source for Size-selected Nanocluster Ions Based on High-power Impulse Magnetron Sputtering. *Chem. Lett.* **2013**, *42*, 857–859.
- (49) Palmer, R. E.; Cao, L.; Yin, F. Note: Proof of principle of a new type of cluster beam source with potential for scale-up. *Rev. Sci. Instrum.* **2016**, *87*, 046103.
- (50) Cai, R.; Cao, L.; Griffin, R.; Chansai, S.; Hardacre, C.; Palmer, R. E. Scale-up of cluster beam deposition to the gram scale with the matrix assembly cluster source for heterogeneous catalysis (propylene combustion). *AIP Adv.* **2020**, *10*, 025314.
- (51) Gunaratne, K. D. D.; Prabhakaran, V.; Ibrahim, Y. M.; Norheim, R. V.; Johnson, G. E.; Laskin, J. Design and performance of a high-flux electrospray ionization source for ion soft landing. *Analyst* **2015**, *140*, 2957–2963.
- (52) Su, P.; Hu, H.; Warneke, J.; Belov, M. E.; Anderson, G. A.; Laskin, J. Design and Performance of a Dual-Polarity Instrument for Ion Soft Landing. *Anal. Chem.* **2019**, *91*, 5904–5912.
- (53) Su, P.; Hu, H.; Unsuhay, D.; Zhang, D.; Dainese, T.; Diaz, R. E.; Lee, J.; Gunaratne, D. K.; Wang, H.; Maran, F.; Mei, J.; Laskin, J. Preparative Mass Spectrometry Using a Rotating-Wall Mass Analyzer. *Angew. Chem., Int. Ed.* **2020**, *59*, 7711–7716.
- (54) Dainese, T.; Agrachev, M.; Antonello, S.; Badocco, D.; Black, D. M.; Fortunelli, A.; Gascón, J. A.; Stener, M.; Venzo, A.; Whetten, R. L.; Maran, F. Atomically precise Au₁₄₄(SR)₆₀ nanoclusters (R = Et, Pr) are capped by 12 distinct ligand types of 5-fold equivalence and display gigantic diastereotopic effects. *Chem. Sci.* **2018**, *9*, 8796–8805.
- (55) Clemmons, J. H.; Herrero, F. A. Mass spectroscopy using a rotating electric field. *Rev. Sci. Instrum.* **1998**, *69*, 2285–2291.
- (56) Orsini, S.; Livi, S.; Torkar, K.; Barabash, S.; Milillo, A.; Wurz, P.; Di Lellis, A.; Kallio, E. SERENA: A suite of four instruments (ELENA, STROFIO, PICAM and MIPA) on board BepiColombo-MPO for particle detection in the Hermean environment. *Planet. Space Sci.* **2010**, *58*, 166–181.
- (57) Su, P.; Hu, H.; Unsuhay, D.; Zhang, D.; Dainese, T.; Diaz, R. E.; Lee, J.; Gunaratne, D. K.; Wang, H.; Maran, F.; Mei, J.; Laskin, J. Preparative Mass Spectrometry Using a Rotating-Wall Mass Analyzer. *Angew. Chem., Int. Ed.* **2020**, *59*, 7711.
- (58) Hadjar, O.; Johnson, G.; Laskin, J.; Kibelka, G.; Shill, S.; Kuhn, K.; Cameron, C.; Kassan, S. IonCCD for Direct Position-Sensitive Charged-Particle Detection: from Electrons and keV Ions to Hyperthermal Biomolecular Ions. *J. Am. Soc. Mass Spectrom.* **2011**, *22*, 612–623.
- (59) Nefliu, M.; Venter, A.; Cooks, R. G. Desorption electrospray ionization and electrosonic spray ionization for solid- and solution-phase analysis of industrial polymers. *Chem. Commun.* **2006**, 888–890.

- (60) Christian, N. P.; Arnold, R. J.; Reilly, J. P. Improved Calibration of Time-of-Flight Mass Spectra by Simplex Optimization of Electrostatic Ion Calculations. *Anal. Chem.* **2000**, *72*, 3327–3337.
- (61) Chen, X.; Raab, S. A.; Poe, T.; Clemmer, D. E.; Larriba-Andaluz, C. Determination of Gas-Phase Ion Structures of Locally Polar Homopolymers Through High-Resolution Ion Mobility Spectrometry-Mass Spectrometry. *J. Am. Soc. Mass Spectrom.* **2019**, *30*, 905–918.
- (62) Hu, Q.; Laskin, J. Secondary Structures of Ubiquitin Ions Soft-Landed onto Self-Assembled Monolayer Surfaces. *J. Phys. Chem. B* **2016**, *120*, 4927–4936.
- (63) Moision, R. M.; Armentrout, P. B. An electrospray ionization source for thermochemical investigation with the guided ion beam mass spectrometer. *J. Am. Soc. Mass Spectrom.* **2007**, *18*, 1124–1134.
- (64) Vestal, M. L.; Blakley, C. R.; Ryan, P. W.; Futrell, J. H. New crossed-beam apparatus for the study of ion–molecule collision processes. *Rev. Sci. Instrum.* **1976**, *47*, 15–26.
- (65) O'Connor, P. J.; Leroi, G. E.; Allison, J. Understanding ion deceleration lenses: what are the simplicity/performance trade-offs? *J. Am. Soc. Mass Spectrom.* **1991**, *2*, 322–335.
- (66) Ouyang, Z.; Cooks, R. G. Miniature Mass Spectrometers. *Annu. Rev. Anal. Chem.* **2009**, *2*, 187–214.